Ultramafic and mafic rock types from Choiseul, Santa Isabel and santa Jorge (Northeastern Solomon Islands): origins and significance

Thomas Berly

Ultramafic and mafic rock types from Choiseul, Santa Isabel and San Jorge (Northeastern Solomon Islands): origins and significance

Thomas Berly

Thesis submitted for the degree of Doctor of Philosophy

PhD in Cotutelle between the Australian National University (Canberra, Australia) and the Université Joseph Fourier (Grenoble, France)

14 December 2005

In the memory of Henriette Lapierre

Declaration.

All of the work presented in this thesis is my own, except where otherwise acknowledged. Some of the ideas presented have benefited from discussions with my supervisors, advisors and other colleagues, but all interpretations and conclusions are my own.

Thomas Berly

Supervisors, Examiners and Advisers

Supervisors:

- **Professor Richard Arculus**
  Department of Earth and Marine Sciences, Australian National University (Canberra, Australia)

- **Professor Henriette Lapierre**
  "Laboratoire de Géodynamique des Chaînes Alpines", Université Joseph Fourier (Grenoble, France)

Examiners:

- **Dr Ian Parkinson**
  Department of Earth Sciences, The Open University (Milton Keynes, England)

- **Dr Georges Ceuleneer**
  Dynamique terrestre et planétaire, Centre National de Recherche Scientifique (Toulouse, France)

Advisers

- **Dr Jörg Hermann**
  Research School of Earth Sciences, Australian National University (Canberra, Australia)

- **Dr Carl Spandler**
  Research School of Earth Sciences, Australian National University (Canberra, Australia)

Acknowledgements

This PhD study has been a long journey and there are many people that I would like to thank for their direct/indirect involvement and contribution to my thesis work. Although they cannot be thanked individually, I really appreciate their help.

I wish to express my gratitude to my supervisors Richard Arculus and Henriette Lapierre for giving me the opportunity to undertake this PhD project. Many thanks to Richard for providing financial support towards research and living expenses.

I would like to say a "big thank" to my advisors Jörg Hermann and Carl Spandler.
I really enjoyed the numerous discussions and debates with Carl while he was a PhD student and subsequently as my advisor. I believe that Carl is a brilliant geologist and I wish him well for his future career in research.
Jörg was literally my mentor throughout the course of my PhD. He always made time to talk about any problems, crazy ideas or weird models. His expertise and knowledge are invaluable. He is a great source of inspiration and motivation. Jörg was instrumental to the success of my PhD. Thanks for your unlimited patience and understanding.

The examiners are gratefully acknowledged for having the patience to read my thesis.

Thanks to all the staff from "everywhere around the world".
In the Solomon Islands, I would like to thank the field staff of the Geological Survey of the Solomon Islands (Honiara) for their invaluable field support; in particular Cromwell Qopoto, Stanley Basi, Andrew Mason and Watson Satokana.
In France, many thanks to Olivier Bruguier, Delphine Bosch, Francine Keller, Claudine Meugniot, Claudie and François Sénebier, Pierre Brunel and Philippe Telouk.
In Switzerland, thanks to François Bussy and Jean Hernandez
In England, I am indebted to Ian Parkinson for the Re/Os work.
And of course in Australia, thank you to Steve Eggins, Charlotte Allen, John Vickers, Tony Phimphisane, John Seeley, Ulrich Senff, Shane Paxton, Nick Ware, Frank Brink, Terry Mernagh and Chris Foudoulis. Special mention to Brian Harrold and Maree Coldrick who were so helpful with solving problems.

To my fellow PhD and honours students over the past six years (Carl, Greg, Davide, Helen, Juan-Pablo, Silvano, Al, Herman, Cromwell, Will, Rob, Kurt, Sarah) and of course my office mates (Macca, Luke and the Kiwi Marty). As mates and colleagues, you provided plenty of advice as well as fun and distractions when needed.

I'm most grateful to the ANU administration and especially John Hooper for contributing to implement the cotutelle scheme at the ANU. Special thanks to the French Embassy and especially Alain Moulet for his constant support and interest for the cotutelle scheme.

I would like to thank the "Ministère des Affaires Etrangères" (France) and the "Région Rhône-Alpes" (France) for their financial support.
The French Embassy is also gratefully acknowledged for its financial support throughout my PhD and for giving me the experience of working for this well respected institution for almost years. During this period, I had the occasion to meet many tremendous people in the vast world of Science and Technology.

To my dear Australian and French friends who were so supportive. Paul, thanks for keeping me fit. To Javier and Luisa for being good neighbours and friends. To Sylvain (mon jumeau) for simply being my best friend.

I'd also like to especially thank my family and adopted family who have always encouraged me throughout the course of my PhD. In particular my parents, for their constant and precious support.

Last but certainly not least, my beautiful fiancée Charisse. Thank you for your unconditional support. There is no doubt that without you, I wouldn't have done it. We make a real good team.

Table of Contents

CHAPTER 2: GEOLOGY AND GEOCHEMISTRY OF THE "SIRUKA ULTRAMAFICS": EVIDENCE FOR FLUID METASOMATISM IN AN ISLAND ARC SETTING

CHAPTER 3: SUPRA-SUBDUCTION ZONE PYROXENITES FROM SAN JORGE AND SANTA ISABEL (SOLOMON ISLANDS): A METASOMATIC ORIGIN

CHAPTER 4: MINERAL TRACE ELEMENT COMPOSITIONS, STUDY OF FLUID INCLUSIONS AND WHOLE ROCK RE/OS SYSTEM: INDICATIONS OF A COMPLEX SLAB-DERIVED METASOMATIC ORIGIN FOR THE SAN JORGE/SANTA ISABEL PYROXENITES (SOLOMON ISLANDS).

CHAPTER 5: ORIGIN AND NATURE OF THE MAFIC COMPLEXES OF THE SANTA ISABEL, SAN JORGE AND CHOISEUL ISLANDS: EVIDENCE FROM MINERALOGICAL AND GEOCHEMICAL CHARACTERISTICS

CHAPTER 6: CONSEQUENCES OF THE OJP-ARC COLLISION

ABSTRACT

The Solomon Islands are a NW- to SE-trending double chain of islands, the older basement of which was formed by SW-directed subduction of the Pacific Plate beneath the Indo-Australian Plate between the Eocene and Early Miocene. When the Ontong Java Plateau (OJP) collided with the Solomon arc, a polarity reversal of subduction occurred leading to NE-directed subduction of the Indo-Australian Plate beneath the Solomon arc. Due to OJP-arc collision, thin fault slices of peridotites, pyroxenites, gabbros, and basalts are now exposed on SE Santa Isabel and neighbouring San Jorge as well as on Choiseul. Some pillow lavas have been identified on the basis of geochemical characteristics as of OJP provenance but the origins of the ultramafic rocks remain uncertain.

The Siruka Ultramafics or Choiseul Peridotites are largely exposed in Southeastern Choiseul (Eastern Solomons) as a coherent thrust sheet. These peridotites are among the freshest reported oceanic peridotites, and mainly comprise tectonised harzburgites with rare pyroxenites. The harzburgites are characterised by olivine with high Fo (89-93) contents, high magnesium (100*Mg/(Mg+Fe)(Mg#)>90) pyroxenes that are depleted in Al_2O_3 (<4 wt%), and low rare earth element abundances; all these features are consistent with a refractory origin for the Choiseul Peridotites. Whole rock and clinopyroxene middle (M)REE-heavy (H)REE data are consistent with melting in the garnet peridotite facies followed by melting in the spinel field. Although exposed in an island arc setting, the harzburgites have many features in common with abyssal peridotites. Compositions of most spinel span the moderately-depleted to depleted end of the abyssal peridotite range. In addition, the bulk of the calculated oxygen fugacities (fO_2s) averages 0.31 $\log_{10}$ units below the fayalite-magnetite-quartz (FMQ) buffer, comparable to the relatively reduced environments in which abyssal peridotites are formed. On the other hand, whole rock and clinopyroxene are also characterised by variable large ion lithophile element (LILE), Sr, and Pb enrichments. Reaction of these peridotites is inferred with a metasomatising fluid enriched in LILE, Sr and Pb relative to the REE. Some samples can contain relatively high Cr# spinel and have high fO_2s (up to 1.26 $\log_{10}$ units >FMQ) equivalent to those reported for supra-subduction zone (SSZ) peridotites. As a result, the Choiseul Peridotites are interpreted to have two-stage origins: 1. ocean-ridge residual harzburgites formed beneath an ocean ridge; 2. infiltration by a reactive fluid or melt released from a subducted slab underneath the pre-Miocene basement of Choiseul.

The San Jorge and Santa Isabel pyroxenites are associated in the field with harzburgites, dunites, and sometimes incorporated into serpentine massifs (NW San Jorge). These pyroxenites are remarkably fresh, coarse-grained rocks ranging from orthopyroxenite, websterite to clinopyroxenite depending on modal proportion of clinopyroxene relative to orthopyroxene. Olivine and spinel occur rarely and only in small proportions. Secondary phases include mainly amphibole (hornblende to tremolite), serpentine, magnetite, Fe-Ni-sulfide, and occasionally a compositionally distinctive clinopyroxene and chlorite. However, these retrograde assemblages are limited suggesting the pyroxenites were exhumed rapidly to the surface. Pyroxenes are characterised by high Mg# (0.85-0.94 for cpx and 0.83-0.91 for opx) and low Al_2O_3 contents (< 3.6 wt%) which are all coincident with a mantle origin in a SSZ environment. Two-pyroxene thermometry gives a large

range of equilibration temperatures between 800 and 1050°C indicating the pyroxenites originated in a relatively cold environment. The assemblage cpx-opx-sp-ol requires 0.7<equilibration pressures<1.7 GPa. Whole rock (analysed by solution- and laser ablation (LA ICP-MS) and mineral trace element abundances (determined by LA ICP-MS) shows: 1. cpx dominates the whole rock budget for REE and other lithophile elements; 2. there is variable depletion in light (L)REE relative to middle (M)REE and flat to convex M to heavy (H)REE; 3. overall REE abundances are low. Primitive mantle-normalised multi-element diagrams of pyroxene and whole rock are marked by variable enrichments in Cs, Ba, Pb, and Sr, which are known to be mobile in subduction zone environments. These geochemical characteristics combined with the multi-generational network of veins and replacement textures, wherein mantle orthopyroxene relics occur amongst an orthopyroxene-clinopyroxene assemblage exclude an origin as arc cumulates but rather the result of reaction between a peridotite and a metasomatic agent (aqueous fluid and/or melt). Geochemical similarities between the orthopyroxenites and the websterites are consistent with derivation from the same metasomatic process. In contrast, the clinopyroxenites are the only pyroxenites having spinel exsolution within the clinopyroxene, yielding higher temperatures of formation (>1050°C). Their clinopyroxene has unusual high TiO_2 contents coupled with high Mg# and Cr_2O_3 contents compared to clinopyroxene from the websterites. This indicates the clinopyroxenites were formed in hotter conditions from a more primitive source compared to the other pyroxenites.

Mineral trace element geochemistry combined with the study of fluid inclusions is crucial for determining the nature and composition of the metasomatising agent involved in formation of the pyroxenites. The results of this work indicate the metasomatising agent was enriched in LILE, Sr, Pb, and CO_2+H_2O and to a lesser extent LREE, which is typically the geochemical signature of subducted slab-derived fluids. Formation of opx and cpx requires the metasomatising agent to carry a significant solute load including Ca, Fe, and Si. It is therefore likely that the metasomatising agent was a hydrous melt. Re-Os isotopic study reveals that the $^{187}Os/^{188}Os$ for the pyroxenites are high compared to abyssal peridotites, and interpreted to be the result of ingress of sediment-derived radiogenic Os to a relatively unradiogenic mantle source. This complex metasomatic process, involving hydrous melts derived from the sediments, is likely to have resulted in the formation of various pyroxenites.

A large variety of mafic rock types are exposed on Choiseul and Santa Isabel/San Jorge. They include volcanic rocks (basalts and andesites), schists, and gabbroic rocks with variable degrees of deformation, metamorphism, and alteration. Their chemical compositions are highly variable ranging from back arc basin basalt (BABB)- to arc- to OJP-like affinities. In detail, the San Jorge and Santa Isabel gabbros are gabbronorites and represent medium- to high-pressure arc cumulates with variable amounts of trapped liquid. On Santa Isabel, the gabbros are in fault contact with OJP-related basalts which mainly outcrop north of the KKKFS but also are found south of this fault system. An OJP-related schist is also exposed on San Jorge. With the exception of this sample, the volcanic sequence on San Jorge is sparse with only a Fe-Ti MORB-type basalt and a boninitic-like sample. Conversely, the volcanic cover of Choiseul is volumetrically

dominant and includes the geochemically similar Voza lavas and Choiseul Schists. Another unit, the Oaka Metamicrogabbros are not cumulates but represent frozen melts. All these formations have typical BABB affinities. The juxtaposition of arc-like and BABB-like cumulates and volcanic rocks are interpreted as portions of an arc-backarc crust.

Unraveling the origins of the different petrogenetic suites exposed on Choiseul, Santa Isabel, and San Jorge is crucial for understanding of the tectonic and magmatic processes resulting from the OJP-arc collision. Even if the mechanism of accretion remains difficult to determine, the key issue for this study has been the identification of a complete SSZ-ophiolite comprising an entire arc mantle-cumulate-volcanic lavas sequence. The study of the exhumed portions of the mantle wedge has crucial implications for understanding the nature and composition of fluids released during dehydration processes of the slab, the mechanism of transport of these slab-derived fluids migrating through the mantle and more generally the composition of the mantle wedge.

RÉSUMÉ

Chapitre 1: introduction et préambule

Les îles Salomon se situent dans l'océan pacifique, au nord-est de l'Australie. Elles forment une double chaine d'îles, incluant, au total, six îles principales qui sont, du nord au sud: Choiseul, New Georgia, Santa Isabel, Guadalcanal, Malaita et Makira. Leur histoire géologique est très complexe et intimement liée au plateau océanique d'Ontong Java (OJP).

OJP est le plus grand ($1{,}86*10^{6}$ km^{2}= superficie de l'Alaska) et le plus volumineux des provinces volcaniques (LIPs) comptabilisant un volume total estimé à $5*10^{7} km^{3}$. La formation des 40 km de croûte océanique s'est faite en deux épisodes volcaniques très courts (< 3 Ma chacun), datés à 122 Ma et 90 Ma (datation Ar-Ar sur basaltes), probablement liés au fonctionnement du point chaud de Louisville (42°S 159°W). Depuis sa formation, OJP a dérivé passivement avec la plaque pacifique avant de rentrer en collision avec l'arc volcanique des îles Salomon issu de la subduction de la plaque pacifique sous la plaque indo-australienne. Cette collision a induit le blocage de la subduction à vergence sud et la naissance d'une nouvelle subduction à vergence nord de la plaque indo-australienne sous l'arc Salomon. Cette jeune subduction a créé une nouvelle chaîne volcanique (5 Ma), située plus au sud, dont fait partie l'archipel "New Georgia". D'autre part, cette collision a aussi entrainé l'obduction en écaille de roches ultramafiques (péridotites et pyroxénites) et mafiques (gabbros, roches volcaniques et schistes) qui affleurent sur l'île de Choiseul et au sud de Santa Isabel ainsi qu'à San Jorge. Des basaltes en coussins sont mis à l'affleurement au sud-ouest de Santa Isabel. Ce sont des tholeiites pauvres en K présentant des spectres de terres rares (REE) relativement plats caractéristiques des basaltes échantillonnés lors des programmes de forage ODP (Ocean Drilling Program). Ces basaltes représentent les parties supérieures du plateau océanique obducté sur l'arc Salomon lors de la collision OJP-arc. Toutefois l'origine des autres roches volcaniques et des roches mafiques et ultramafiques de Choiseul, Santa Isabel et San Jorge reste incertaine. Ces terrains peuvent provenir de la lithosphère océanique, du plateau océanique Ontong Java et/ou de l'arc Salomon. Cette étude met l'accent sur l'importance de reconnaître et d'identifier la nature des terrains qui sont juxtaposés sur ces îles afin de préciser leurs origines. Les caractéristiques pétrologiques, minéralogiques, géochimiques (minéraux et roches totales) et isotopiques sont présentées et discutées dans cette thèse. Le premier chapitre a le mérite d'étudier en détail le contexte géologique relativement compliqué des îles Salomon. Chapitre 2 décrit précisément la pétrologie, la mineralogie et la géochimie des péridotites de Choiseul. Le chapitre 3 focalise sur l'étude pétrographique et les analyses géochimiques roches totales des pyroxénites de San Jorge et de Santa Isabel permettant de jeter des bases solides pour des études plus ciblées (chapitre 4) sur la géochimie des phases minérales (en particulier le pyroxène), des inclusions fluides et la géochimie isotopique du couple Re/Os. Les roches ultrabasiques à basiques (gabbros et basaltes) de Choiseul, Santa Isabel et San Jorge sont étudiées ensemble dans le chapitre 5. Enfin un modèle est proposé (chapitre 6) pour expliquer la formation et l'exhumation des roches ultramafiques et mafiques en relation avec la collision entre OJP et l'arc salomonais.

Chapitre 2: Géologie et géochimie des roches ultramafiques de Siruka (peridotites de Choiseul)

A Choiseul, les péridotites affleurent uniquement dans le sud-est de l'île et particulièrement à Siruka (d'où le nom des roches ultramafiques de Siruka). Ce sont essentiellement des harzburgites et des dunites qui sont plus ou moins altérées et déformées et à texture porphyroclastique, voire mylonitique.
Les minéraux primaires sont exclusivement l'olivine, le pyroxène (orthopyroxène et clinopyroxène) et le spinel tandis que les minéraux secondaires incluent surtout le serpentine mais aussi moins fréquemment l'amphibole et la chlorite. L'olivine est omniprésente (69-79%) sous forme de large porphyroclastes souvent altérés en serpentine. Des porphyroclastes d'orthopyroxène peuvent être présents en forte proportion (jusqu'à 25%). A l'inverse, le clinopyroxène est très rare (3-7%) et apparait sous forme de porphyroclastes de petite taille (< 0.5mm), de néoblastes de forme anhédrale ou d'exsolutions dans les cristaux d'orthopyroxène. Le spinel forme des porphryclastes d'aspect globuleux qui ne représentent qu'en moyenne 0.4-1.1 % de proportion minérale des péridotites. En terme de composition, l'olivine est très magnésienne (Fo= 89-93) tout comme les pyroxènes qui sont également riches en Mg avec des Mg# supérieurs à 90. De plus, les pyroxènes sont aussi caractérisés par des teneurs relativement basses en Al_2O_3 (< 3 wt%). Les valeurs en Cr# et le Mg# du spinel sont globalement similaires à celles déterminées pour le spinel typique des péridotites abyssales. Certains cristaux de spinel, montrant des Cr# élevés (0.58) pour des Mg# relativement bas (50), sont plutôt caractéristiques du spinel des péridotites d'arc.
Les données thermométriques sont obtenues à partir des différents géothermomètres disponibles sur les couples clinopyroxène-orthopyroxène et olivine-spinel. Ces températures d'équilibration ont des valeurs très variables comprises entre 652 et 1032°C. A noter que les péridotites contenant l'amphibole et la chlorite montrent des températures d'équilibration plus faibles que les autres. Les fugacités en oxygène calculées à partir du couple olivine-spinel sont très variées (-1.04 unité log à + 1.26 unité log). Toutefois la majorité des péridotites ont des fugacités en oxygène négatives suggérant que les péridotites proviennent d'un milieu réducteur. Toutefois les péridotites, incluant de l'amphibole et de la chlorite en relative abondance, sont plus oxidées avec des fugacités en oxygène comparables à des péridotites d'arc.
Les analyses géochimiques des péridotites en éléments majeurs montrent des teneurs élévées en magnésium qui sont négativement corrélées aux concentrations en SiO_2, Fe_2O_3, AL_2O_3 et CaO (wt %) indiquant que ces péridotites représentent des restites. Le caractère résiduelle de ces péridotites est aussi mis en évidence par les spectres de terres rares (REE) de roches totales, qui sont très appauvris en terres rares légères (LREE). De plus, ces spectres se caractérisent par une forte pente entre les terres rares moyennes (MREE) et lourdes (HREE) montrant que la fusion, à l'origine de ces restites, a débuté (1-8% de fusion partielle) dans le domaine de stabilité des péridotites à grenat, puis a continué (11-21% de fusion partielle) dans le domaine de stabilité des péridotites à spinel. Les spectres élargis de roches totales indiquent des enrichissements sélectifs en Rb, Ba, Cs, Pb et Sr, éléments connus pour être mobiles dans les processus d'altération et de métamorphisme. Toutefois ces enrichissements sont aussi détectés dans les analyses du

clinopyroxène de ces péridotites. Le fait que ces enrichissements soient présents à la fois dans les données géochimiques de la roche totale et du clinopyroxène est un argument de poids pour conclure que ces enrichissements ne sont pas attribués à des processus dits secondaires.
Le caractère très réfractaire des péridotites, la fusion débutant dans le domaine de stabilité des péridotites à grenat ainsi que le rapport Cr# peu élévé du spinel et la valeur moyenne négative de la fugacité d'oxygène suggèrent que ces péridotites sont similaires aux péridotites abyssales, bien qu'étant mises en place dans un milieu océanique. Toutefois, les spectres élargis de roche totale et du clinopyroxène (normalisés au manteau primitif) montrent conjointement des enrichissements sélectifs en Rb, Ba, Cs, Pb et Sr qui sont typiques des magmas des zones de subduction. De plus la présence de néoblastes anhédrales de clinopyroxène et d'amphibole dans certains échantillons et le caractère oxidé couple avec des valeurs élévées en Cr# pour le spinel de certains échantillons sont des arguments solides pour dire que ces péridotites ont intéragi avec des fluides. Par conséquent, il est suggéré que les roches ultramafiques de Choiseul soient issues, dans un premier temps, d'un processus de fusion au niveau d'une dorsale, suivi d'un possible métasomatisme par des fluides probablement provenant de la plaque océanique pacifique subductée.

Chapitre 3: étude pétrologique, minéralogique et géochimique des pyroxénites de San Jorge et de Santa Isabel

A la différence de Choiseul, les pyroxénites de San Jorge et de Santa Isabel sont omniprésentes et coexistent avec des péridotites. Ces pyroxénites forment fréquemment des veines ou des dykes de taille variable (quelques centimètres à un mètre) traversant des blocs de dunites ou/et harzburgites. Ces veines pyroxénitiques sont globalement riches en clinopyroxène tandis que les orthopyroxénites se trouvent plutôt en massifs. Généralement, des galets de pyroxénites ont été échantillonés, parfois inclus dans des massifs de serpentine (comme au nord de San Jorge) et de manière générale, les pyroxénites sont remarquablement fraîches. Le clinopyroxène et l'orthopyroxène varient en proportion aboutissant à une large variété d'orthopyroxénite (G1), de webstérite (G2) et de clinopyroxénite (G3). Olivine et spinel sont peu fréquents. La texture de ces pyroxénites est variable (granoblastique à porpyroclastique). Dans certains échantillons, on peut observer des textures d'imprégnation avec des cristaux d'orthopyroxène "squeletiques", ayant la même orientation et qui sont parsemés dans une masse recristallisée de clinopyroxène et d'orthopyroxène. Ces minéraux, de forme bizarre, sont interprétés comme des reliques mantellaires d'orthopyroxène. Les phases secondaires incluent l'amphibole (hornblende à trémolite), la serpentine, la magnétite, les sulphures de fer et de nickel et occasionellement une seconde generation de clinopyroxène (CpxII) ainsi que la chlorite. Néanmoins ces phases sont présentées en faible proportion indiquant les pyroxénites ont été exhumées rapidement. Un trait commun à toutes ces pyroxénites est la présence de nombreuses inclusions fluides en trainée parfois traversant plusieurs grains.
La géochimie des pyroxénites en éléments majeurs reflète étroitement leur mineralogie. Par example, les G2-webstérites et les G3-clinopyroxénites sont riches en CaO (> 13wt

%) tandis que la teneur en CaO est faible (< 5 wt%) pour les orthopyroxénites. Les clinopyroxénites se démarquent des autres pyroxénites par des valeurs en Ti plus élévées (TiO_2> 0.14 wt%) comparer aux orthopyroxénites et webstérites (0.02 < TiO_2 < 0.12 wt%). Par contre, les pyroxénites ont toutes en commun un Mg# élévé (> 0.82) et une concentration en Al peu importante (Al_2O_3< 3.5 wt%). En règle générale, les orthopyroxénites (G1) et les clinopyroxénites (G3) sont beaucoup plus magnésiennes (Mg#> 0.89) que les webstérites (0.82 < Mg# < 0.91). Cette tendance se retrouve dans la composition des pyroxènes qui sont caractérisés par des valeurs élevées du Mg# (comprises entre 83 et 94), avec les G1- et G3-pyroxènes plus magnésiens que les G2-pyroxènes, mais tous sont relativement pauvres en Al (Al_2O_3< 3.6 %). Ces caractéristiques géochimiques sont fréquemment observées pour des pyroxènes mantelliques des zones de subduction. Les données thermométriques obtenues sur les couples clinopyroxène-orthopyroxène indiquent que les pyroxénites ont été équilibrées à des températures relativement basses entre 800°C et 1050°C.
Les pyroxénites sont charactérisées par de faibles concentrations en terres rares (REE) et des appauvrissements variables en terres rares légères (LREE) de même ordre que pour les péridotites de Choiseul. Les spectres élargis normalisés au manteau primitif des pyroxénites (roche totale) montrent des enrichissements variables en éléments lithophiles tels que Ba, Cs, Rb, Sr and Pb. Ces éléments sont très mobiles lors de processus d'altération et de métamorphisme. Toutefois, ces enrichissements persistent pour les roches les moins altérées indiquant certainement une origine primaire.
Les relations de terrain et les caractéristiques pétrologiques, minéralogiques et géochimiques révèlent que les différentes pyroxénites de Santa Isabel et de san Jorge ne représentent pas des cumulats de OJP. En effet, leurs températures de cristallisation relativement peu élevées, la cristallisition en veines ainsi que les textures de replacement où des reliques mantelliques d'orthopyroxène coexistent avec un assemblage de pyroxènes recristallisés impliquent ces roches ne sont pas des cumulats mais représentent plutôt des produits d'intéraction entre la péridotite et un liquide. Ce métasomatisme est certainement responsible d'enrichissements variables (observés dans les spectres élargis normalisés au manteau primitif de roche totale), en éléments lithophiles tels que Ba, Cs, Rb, Sr and Pb qui seraient transportés par le liquide. L'héritage mantellique de ces pyroxénites est bien démontré par leurs caractères très magnésiens, leurs faibles concentrations en terres rares (REE) et leurs appauvrissements variables en terres rares légères (LREE) comme pour les harzburgites de Choiseul. Ces données géochimiques couplées à la présence d'inclusions fluides primaires sont autant d'arguments qui réenforcent la possibilité d'un processus de métasomatisme impliquant un liquide infiltrant and réagissant avec le manteau.

Chapitre 4: étude approfondie (phases minerals, inclusions fluides et isotopes) des pyroxénites de San Jorge et de Santa Isabel

Dans le chapitre précédent, nous avons démontré que les pyroxénites n'étaient pas des cumulats mais résultaient de processus d'intéraction fluides-péridotites affectant le coin de manteau d'arc. De ce fait, l'étude approfondie des éléments traces des pyroxènes et en particulier du clinopyroxène nous permet d'expliquer le ou les mécanismes de

métasomatisme du manteau à l'aplomb d'une plaque subductée et de caractériser la composition et la nature de ces liquides.
Comme pour la roche totale, l'étude géochimique in-situ des pyroxènes (orthopyroxène et clinopyroxène) par LA ICP-MS montre des enrichissements en Ba, Cs, Rb, Sr and Pb par rapport aux terres rares lourdes mis en évidence dans les spectres élargis normalisés au manteau primitif. L'étude des inclusions fluides (primaires et secondaires) par LA ICP-MS révèle qu'une partie de ces enrichissements est dûe à la présence de ces inclusions fluides includes dans le pyroxène. Toutefois les analyses de grains de pyroxène complétement dépourvus d'inclusions fluides révèlent que le pyroxène reste riche en ces éléments lithophiles. Ceci confirme que ces enrichissements sont primaires et non liés à des processus d'altération et de métamorphisme. Par conséquent le liquide est riche en éléments lithophiles, ce qui est caractéristique des liquides libérés lors des processsus de dehydration de la plaque subductée et infiltrant le manteau de l'arc. Les inclusions fluides, représentant le liquide piégé lors ou juste après de la cristallisation du pyroxène, offrent aussi la possiblité d'étudier directement la composition du fluide. Nous avons déjà souligné que, par la technique du LA-ICPMS, les inclusions fluides jouent aussi un role important dans le budget des éléments traces de la roche totale en particulier pour des éléments tels que le Ba, Cs, Rb, Sr and Pb. L'utilisation du spectromètre Raman permet d'observer que ces fluides sont aussi riches en méthane (CH_4) et phases minéralogiques telles que l'amphibole et la calcite. Cet assemblage solide-gaz indique que ces inclusions étaient riches en CO_2 et H_2O avant décrépitation selon la reaction: mineral non hydraté + CO_2 et H_2O = amphibole + calcite. D'autre part il est aussi démontré que le liquide soit capable de transporter des terres rares légères au vu des analyses du clinopyroxène des pyroxénites comparés au clinopyroxène d'harburgites de type MORB. En résumé, il est clair que le liquide soit riche en Ba, Cs, Rb, Sr and Pb et mais aussi en CO_2 et H_2O et dans une moindre mesure en terres rares légères et soit capable de transporter des éléments tels que Ca, Fe et Si pour cristalliser le clinopyroxène et l'orthopyroxène en abondante proportion car tous ces éléments sont appauvris dans le manteau. Cette composition riche en éléments majeurs et traces implique que la nature du liquide formant les pyroxénites par métasomatisme est proche de celle d'un magma hydrate plutôt que d'une solution aqueuse. Mais quelle est la source de ce liquide? L'étude des rapports isotopiques de l'Os pour les pyroxénites sont supérieurs à ceux du manteau supérieur indiquant un enrichissement en Os radiogénique du manteau. Il est démontré que cet enrichissement peut être interprété par une contribution des sédiments subductés qui constituent un réservoir potential d'Os radiogénique ainsi que de CO_2 et H_2O et d'éléments lithophiles. Résumant les arguments avancés juqu'ici, il semblerait que la formation des pyroxénites soit liée à un complexe mécanisme d'intéraction d'un magma hydraté provenant de la fusion des sédiments de la plaque Pacifique subducté.
Pour comprendre la complexité de ce métasomatisme du manteau d'arc, il suffit de regarder, dans le détail, les similarités mais surtout les différences minéralogiques et géochimiques des différentes pyroxénites (G1, G2 et G3). Il semblerait que les G1-orthopyroxénites et les G2-webstérites dérivent d'un même processus transitoire et progressive d'intéraction fluides – manteau au vu des analyses géochimiques des pyroxènes et à la cristallisation de orthopyroxénites hybrides ayant des zones enrichies en clinopyroxène avec des caractéritiques similaires aux G2-webstérites. Toutefois, les G3-clinopyroxénites diffèrent radicalement des autres webstérites en étant plus magnésiennes

et ayant des températures de cristallisation beaucoup élévées. Par conséquent, il semblerait que le G3-clinopyroxénites dérivent d'un magma hydraté très primitif et problablement issu directement de la fusion du manteau profond interagissant avec le manteau-sous-arc (40km de profondeur) lors de sa remontée. Par contre les G1-orthopyroxénites et les G2-webstérites seraient issues de l'intéraction entre un magma hydraté provenant de la fusion des sédiments de la plaque subductée se déhydratant et le manteau sur-jacent à la plaque.

Chapitre 5: nature et origine des complexes mafiques des îles de Choiseul, de Santa Isabel et de San Jorge

Les Voza Lavas et les Choiseul Schists sont étroitement associés sur le terrain. Ces deux formations présentent une même histoire métamorphique avec les Choiseul Schists qui sont les équivalents minéralogiques des roches métamorphiques de la formation de Voza lavas. Leur données géochimiques (éléments majeurs et traces) sont identiques. Ces résultats montrent que les Voza Lavas et les Choiseul Schists constituent une seule unité géologique ayant subi différents degrés de métamorphisme et de déformation. D'autre part leurs rapports Nb/Zr supérieurs à 35, leurs spectres de terres rares appauvris en terres légères et leurs abundances en terres rares (voisins de 10 fois la valeur des chondrites) indiquent que ces deux formations sont des MORB. Toutefois les spectres élargis (normalisés au manteau primitif) sont marqués par des enrichissements variables en éléments lithophiles même pour les roches les moins altérées. Ceci indique que ces enrichissements sont primaires et que, par conséquent, ces deux formations ont une affinité d'arc. Les Oaka metamicrogabbros montrent des teneurs en éléments majeurs et traces identiques à celles des Voza lavas et des Choiseul Schists. Ces microgabbros sont interprétés comme étant des liquides magmatiques cristallisés ("frozen melts"). De part leur géochimie, il semblerait que les roches mafiques de Choiseul représentent les parties volcaniques supérieurs de bassins d'arrière-arc.
Contrairement à Choiseul, ce sont les gabbros qui prédominent à San Jorge et à Santa Isabel (sud de l'île). Ce sont essentiellement des gabbronorites (clinopyroxène ± orthopyroxène ± plagioclase) avec peu ou pas d'olivine. La texture de ces roches varie de microgabbros à des roches à gros grains voire pegmatitiques. Les pegmatites sont généralement en veines en contact avec les roches ultramafiques et ont été aussi observées à Choiseul. Dans ces roches pegmatitiques, l'amphibole, de type ferri-tschermakite, est d'origine magmatique alors que l'amphibole des autres gabbros est interprétée comme étant métamorphique. La présence d'amphibole magmatique suggère que ces pegmatites appartiennent à l'arc. Les autres gabbronorites sont divisés en deux groupes. Le premier groupe est caractérisé par des rapports Mg# élévés (Mg#= 80-89) et des spectres de terres rares relativement appauvris présentant des anomalies positives en Eu. Ces caractéristiques géochimiques indiquent que ces roches sont des cumulats. Le second groupe a des rapports Mg# moins élévés (Mg#= 50-80) et les spectres de terres rares sont relativement plats, sans anomalies en Eu indiquant la présence de magma piégé dans ces roches. Les deux groupes de gabbros ont des spectres élargis (normalisés au manteau primitif) avec des enrichissements en éléments lithophiles qui sont aussi présents dans les spectres élargis du clinopyroxène et plagioclase. Ceci indique que ces

gabbronorites ont une origine d'arc. La quasi-absence d'olivine et le caractère magnésium des pyroxènes suggèrent que les gabbronorites résultent de processus de cristallisation fractionée sous relativement haute pression à partir d'un liquide magmatique relativement magnésien.
Uniquement deux échantillons de roches volcaniques provenant de San Jorge ont été étudiés. Le premier est un basalte riche en Fe et en Ti qui présente les caractéristiques géochimiques de MORB. Le second échantillon est une andésite (SiO_2= 58%) relativement riche en MgO (5%) et pauvre en TiO_2 (0.5%). Le spectre de terres rares de cette roche est appauvri (< 1 fois la valeur des chondrites) et plat. Ces données impliquent que cette andésite a des caractères géochimiques d'une boninite. Les autres basaltes affleurant au sud de KKKFS sont en coussins. Ces basaltes sont caractérisés par des spectres de terres rares plats et des rapports ε Nd (5-6) similaires aux basaltes d'OJP mis à l'affleurement au nord de KKKFS. D'autre part, un schiste (échantillon 16.13) mis à l'affleurement au sud-ouest de San Jorge possède des caractères géochimiques identiques à ceux des basaltes d'OJP. Par consequent, il semblerait que ce schiste appartienne aussi à OJP. La mise en place de roches appartenant à OJP au sud-ouest de KKKFS suggère que le KKKFS ne représente pas une simple limite de terrain comme il est admis dans les modèles tectoniques d'accrétion OJP-arc.

Chapitre 6: conséquences de la collision OJP-arc sur la formation et l'exhumation des roches mafiques et ultramafiques de Choiseul, de Santa Isabel et de San Jorge

Avant la collision OJP-arc, la subduction de la plaque océanique sous les îles Salomon a eu pour conséquence de libérer des fluides dans le manteau d'arc dû à la déhydratation progressive de la plaque subductée. Ceci provoque la fusion partielle du manteau profond causant une remontée magmatique sous l'arc. Ce magma hydraté très primitif est transporté par des conduits jusqu'à la transition manteau-croûte (30-40 km de profondeur). A ce niveau, le magma continue son ascension vers la surface en interéagissant avec la péridotite environnante. Cette réaction magma-péridotite entraine la cristallisation de clinopyroxénites (G3) en remplacement de l'orthopyroxène mantellique. Les caractéristiques de ces clinopyroxénites sont de cristalliser en veines à des températures élévées (> 1000°C) et d'être en équilibre avec le manteau (Mg# élévés > 90). L'enrichissement en éléments traces du clinopyroxène par rapport au clinopyroxène des harzburgites provient du liquide échappé de la plaque subductée et enrichissant la source mantellique qui rentre en fusion.
La collision entre OJP et les îles Salomon est relativement complexe et vivement contreversé. Toutefois, sans rentré dans les débats, l'arrivée progressive du plateau océanique Ontong Java à proximité des îles Salomon a probablement, dans un premier temps, eu comme effet de ralentir la subduction de la pacifique sous l'arc salomonais vu l'énorme structure du plateau. Ceci provoque un accroissement important des températures de la plaque subductée avec, pour consequence, un changement radicale des processus de déhydratation de la plaque subductée. C'est ainsi que la plaque subductée devient abnormalement chaude, libérant des quantités importantes de liquide à faibles profondeurs. Dans ces conditions, ces liquides issus de la déhydratation des parties mafiques de la plaque océanique peuvent induire la fusion partielle des sédiments

subductés produisant un magma hydraté et de type granitique. Ce magma riche en éléments concentrés dans les sédiments (Rb, Ba, Sr, Cs, Pb, CO_2, H_2O et LREE) et qui n'est pas en équilibre avec la péridotite, s'échappe de la plaque pacifique en subduction dans le manteau sur-jacent par des canaux ou des dykes. Vu le très fort rapport liquide/roche, l'intéraction entre ce magma et le manteau péridotitique conduit à cristalliser, en veines, des webstérites (G2) caractérisées par des Mg# inférieurs aux valeurs mantelliques (90) mais plus riches en éléments traces. Au fur et à mesure de la percolation et après le front de cristallisation des webstérites, le magma commence à s'équilibrer avec le manteau environnant et devient moins riche en éléments relativement compatibles. D'autre part, le transport de ce magma devient pervasive infiltrant la péridotite plus diffusivement. A ce stade, l'intéraction liquide – péridotite a pour conséquence de cristalliser des orthopyroxénites (G1) totalement équilibrées avec le manteau. Le liquide résiduelle, résultant de cette réaction, infiltre et métasomatise un large volume du manteau de façon cryptique, donnant naissance aux péridotites de Choiseul. A noter que l'échantillon 16.13 provenant de San Jorge et qui a les affinities géochimiques d'une boninite, peut très bien représenter le magma issu de la fusion des sédiments subductés.

Une des conséquences de la collision OJP-arc est très bien documentée. Il s'agit de l'inversion de la polarité de la subduction sous les îles Salomon. Toutefois, l'exhumation des pyroxénites de San Jorge et Santa Isabel et des péridotites de Choiseul traduit aussi probablement une régime de compression plus accentué de la collision entre OJP et l'arc. Cette exhumation est enregistré par la recristallisation des pyroxénites et des péridotites avec l'apparition progressive des minéraux secondaires tels que l'amphibole et la serpentine lors de leur remontée vers la surface. Etant donné que la cristallisation de ces minéraux secondaires est limitée, il est possible que cette exhumation se soit produite très rapidement (<5 Ma) le long du plan de Benioff par des phénomènes tectoniques le long de longues failles de cisaillement et/ou transportés par des diapirs de serpentine.

L'exhumation partielle du coin du manteau à l'aplomb de la plaque subductée est probablement corrélée à l'épisode d'écaillage et d'obduction partielle de la lithosphère de l'arc. Cet processus engender un empilement complexe d'écailles provenant 1) du manteau sous jacent à l'arc compose de péridotites (les péridotites de Choiseul) et de clinopyroxénites associées (G3-clinopyroxénites); 2) de la partie profonde de la croûte de l'arc incluant les gabbronorites de San Jorge; 3) des parties superficielles de l'arc qui sont représentées essentiellement par des basaltes de type MORB avec les affinités d'arc (du type Voza lavas). Ces terrains forment, en fait, une séquence complète d'arc.

Résultant de l'accentuation du régime compressif de la collision, les terrains d'arc, comprenant les pyroxénites de San Jorge et Santa Isabel, les péridotites de Choiseul et les gabbros et basaltes des trois îles, sont juxtaposés, de manière très complexe, aux basaltes d'OJP qui sont, eux mêmes, obductés sur l'arc.

Conclusion:

En résumé, nos résultats montrent que la collision OJP-arc a pour consequence:

- La formation de pyroxénites qui est liée à l'intéraction de liquides (probablement des magmas hydratés) libérés de la plaque pacifique subductée dûe au blocage de la subduction par OJP;
- L'écaillage et l'exhumation d'un complexe ophiolitique d'arc ou de basin d'arrière arc incluant une séquence complète manteau- cumulat-roche volcanique.
- L'obduction de la croûte supérieure d'OJP représentée par les basaltes d'OJP sur l'arc (mais pas les parties profondes du plateau océanique).

Preamble

1 INITIAL PURPOSE OF THIS THESIS

1.1 Problematic

The Cretaceous submarine Ontong Java Plateau (OJP), in the western Pacific Ocean, is the most voluminous of the world's large igneous provinces (LIPs), and represents the largest known magmatic event on Earth (Coffin and Eldholm, 1994). LIPs are the products of basaltic volcanism on a scale and at an effusion rate not seen on Earth at the present time, and their formation may have had significant effects on the Earth's climate and biosphere (Coffin and Eldholm, 1994). After basalt and associated intrusive rock emplaced at spreading, LIPs are the most significant accumulations of mafic material on the Earth's surface (Mann and Taira, 2004). Commonly attributed to mantle plume or hotspots (Morgan, 1971), they presently account for 5-10% of the heat and are expelled from the mantle (Sleep, 1990). Despite their importance in studies of mantle dynamics and global environmental impact, only scarce data is available to explain the mantle processes involved in the formation of the LIPs (Coffin and Eldholm, 1994; Mamberti et al., 2004; Mann and Taira, 2004).

Recent studies (Coffin and Eldholm, 1994) reveal the potential for up to 30% partial melting to generate large volume of basalts in a short period (< 3 Ma) (Richards et al., 1989). Models based on 5-30% partial melting for OJP basalts imply that they have generated from the lower mantle (>670 km) (Figure 1). In addition, Campbell and Griffiths (1990) and Coffin and Eldholm (1991, 1994) indicate that plume heads giving rise to LIPs may be formed at the core-boundary. Studying the geochemical characteristics of LIPs (especially OJP) would therefore give the opportunity to assess the compositions of the lower mantle (even perhaps the core-mantle boundary origin) and to understand the melting processes involved in mantle plume. Despite the enormous size of the oceanic plateaus, very little is known about their overall structure and composition (Mamberti et al., 2004). So far, scientific oceanic drilling programs (ODP) have merely "scratched the surface of oceanic plateaus" as only the volcanic basement (basalts) and sediments were recovered (Mahoney et al., 1993). Lower parts of LIPs including oceanic plateaus are yet to be found (Neal et al., 1997). Speculations about the composition of their lower crustal body include granulite or eclogite facies (Furlong and Fountain, 1986; Wood, 1984) while other authors (i.e. Neal et al., 1997) argue for the presence of "hidden cumulates" with wehrilitic to pyroxenitic compositions including dunites, pyroxenites and gabbros. Investigating these rocks would help to comprehend the genesis and the geodynamics of the oceanic plateaus.

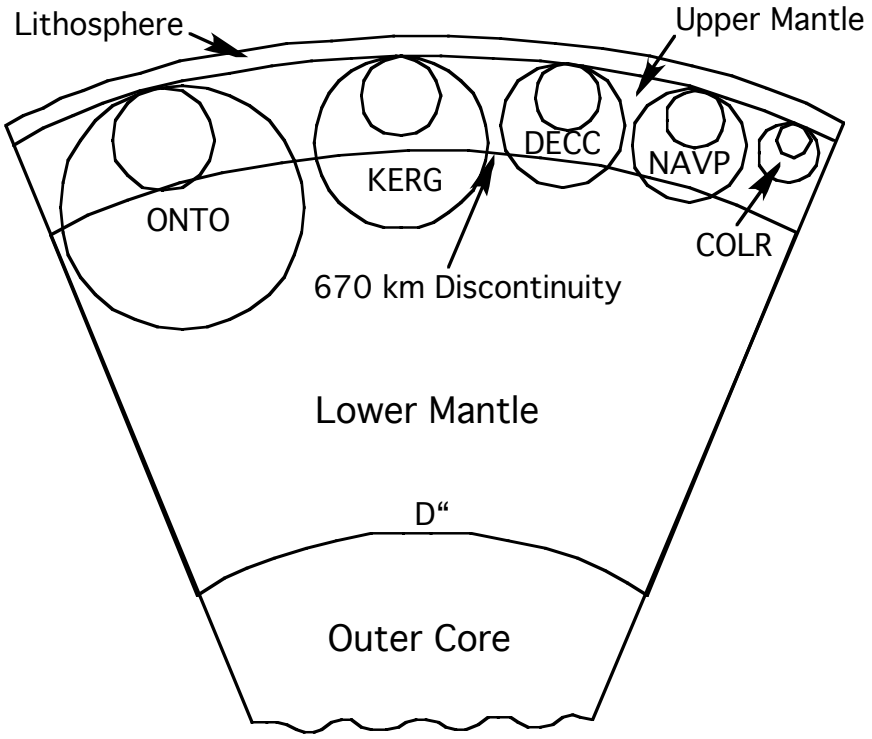

Fig. 1: Minimum and maximum spherical diameters in five LIPs calculated assuming 5% and 30% partial melting plotted on a cross section of the Earth (Coffin and Eldholm, 1994)
Abbreviations: ONTO: Ontong Java Plateau; KERG: Kerguelen Plateau; DECC: Deccan traps; NAVP: North Atlantic Volcanic Province; COLR: Columbia River basalts.

1.2 The choice of the Solomon Islands

Ontong Java Plateau is the biggest of the six largest oceanic plateaus in the world (Mann and Taira, 2004) which all constitute 54% of the total anomalous crust volume of all oceanic plateaus (Schubert and Sandwell, 1989). Fragments of the OJP are known to have obducted on the Solomon arc in the location of Santa Isabel (Tejada et al., 1996) and Malaita (Petterson et al., 1997). On Santa Isabel, they are intimately associated with gabbros, pyroxenites and peridotites, which are scattered along a major terrane boundary (KKKFS) whereas the Siruka Ultramafics are exposed as a coherent thrust sheet and are considered to be part of the Choiseul basement (Ridgway and Coulson, 1987). Similar rock assemblages have been interpreted as remnants of plume-generated oceanic plateaus accreted in the Caribbean Islands (Lapierre et al., 1997, 2000) and Ecuador (Mamberti et al., 2004). However compared to these accreted oceanic plateaus, the ultramafic and mafic rocks from San Jorge/Santa Isabel and Choiseul are remarkably fresh, less tectonised and are clearly exposed on the coasts of these islands.

1.3 Initial objectives of this study

Because drilling is technically difficult, logistically expensive and unlikely to reach lower parts (only the first 100m of volcanic sequence were sampled via this method), accreted oceanic plateaus represent therefore a great opportunity to scrutinize the structure and the

composition of oceanic plateaus. Based on the OJP origin of basalts found on Santa Isabel (north of KKKFS) (Tejada et al., 1996), the gabbros, pyroxenites and peridotites from San Jorge/Santa Isabel and Choiseul in close association with these basalts might represent a typical rock sequence from an oceanic plateau. However this remains to be demonstrated as the Solomon Islands are made of a collage of crustal units with complex geological histories due to the OJP-arc collision. If the volcanic rocks, gabbros and peridotites were to be cogenetically related to the OJP, the geochemical examination of gabbros representative of the OJP magma chamber would lead to determine the composition of the parental magmas of the OJP whilst the depleted peridotites would give an indication of the melting processes (degree, temperature and nature) of the mantle involved to generate the OJP.
The fate of oceanic plateaus on reaching subduction zones is contentious (Mann and Taira, 2004). Based on field and geochemical evidence of Archean greenstone belts (Polat and Kerrich, 1999), there is a growing consensus that the oceanic plateaus are major contributors to continents growth (Abbott, 1996; Albarède, 1996) where they are partially to totally accreted to the overiding plate subduction zones (Mann and Taira, 2004). Other models of accretion imply that the oceanic plateaus are totally subducted and do not contribute to the growth of continents Schubert and Sandwell, 1989). The distinction and recognition of the different terranes from Choiseul and San Jorge/Santa Isabel are therefore essential to unravel the accretion model of the OJP onto the arc as the interaction of the OJP with the Vitiaz subduction zone may provide a modern-day example of collage of terranes similar to the those of the greenstone belts (Tejada et al., 1996).

2 STRUCTURE & SUBJECT OF THIS THESIS

2.1 Structure

The main objective of this thesis is to unravel the origin and the nature of mafic and ultramafic rocks that were exhumed due the OJP-arc collision and are now exposed on the islands of Choiseul, Santa Isabel and San Jorge
Outlined in Chapter 1 is the general tectonic setting environment of the Solomon Islands suggested by previous works. This chapter recapitulates what we know about the history of the formation of the Ontong Java Plateau (OJP) and its collision with the Solomon Arc. Chapter 2 examines the petrology, mineralogy and geochemistry of the Siruka Ultramafics of Choiseul. Chapter 3 and 4 focus on the formation of a large variety of pyroxenites including orthopyroxenites, websterites and clinopyroxenites from Santa Isabel and San Jorge that generally occur as veins or dykes associated with peridotites. In detail, Chapter 3 describes the bulk-rock (major and trace elements) and mineral (major element) geochemistry combined with the field relationships, textural and petrological characteristics of these pyroxenites whereas Chapter 4 scrutinizes particularly the mineral trace element compositions together the bulk-rock Re/Os isotope geochemistry and study of the fluid inclusions to further understand the mechanism of formation of these pyroxene-rich rocks. Chapter 5 examines the mineralogical and geochemical characteristics of a large range of igneous or metamorphic rock types that are closely

associated with the ultramafic rocks from Choiseul, Santa Isabel and San Jorge. These data are used to recognize the different petrogenetic suites in order to unravel the complex juxtaposition of these mafic complexes. Based on the results presented in all of these chapters, Chapter 6 reveals the possible consequences and the implications of the OJP-arc collision on the formation and the exhumation of these ultramafic and mafic rocks from Choiseul, Santa Isabel and San Jorge.

2.2 Notes

The chapters aim to accommodate the study of the variety of rock types in only one region. To avoid repetition, the geological setting of the Solomon Islands and the geology of the islands (Choiseul, San Jorge and Santa Isabel) are largely described in Chapter 1 and only briefly referred in the other chapters. The analytical methods section is detailed in the Appendix 1, which includes the whole rock and mineral geochemistry (major and trace elements). Specific analytical methods could also be described in each chapter. Appendix 2 includes a large range of selected trace element compositions of clinopyroxene from the San Jorge and Santa Isabel (Solomon Islands) pyroxenites. Chapter 3 corresponds to an article "Supra-Subduction Zone pyroxenites from San Jorge and Santa Isabel (Solomon Islands)", which is currently under review (Journal of Petrology). This article has been slightly modified to fit with the other chapters of this thesis. It is referred throughout this thesis as "Berly et al., 2006" and is provided in the Appendix 3. Finally, Appendix 4 represents the final oral presentation, which was carried out at the University Joseph Fourier (Grenoble, France), in the "Dolomieu" room of the "Laboratoire de Géodynamique des Chaînes Alpines (LGCA)" on the Wednesday 14 December (2.30pm) in the presence of the jury.

A single reference list for the entire thesis is provided following Chapter 6. Organising the cited reference in this manner saves considerable space as many publications are cited more than once. It also helps the reader to easily access individual reference details.

The figures numbering includes two numbers: the first number indicates the chapter number and the second number is the actual number for the figure. For instance Fig. 1-2 refers to Figure n°2 of chapter 1. The same applies to tables numbering.

Note that the entire thesis (including the appendices) is available as an electronic copy (pdf. files) included on a CD in the back of this thesis.

2.3 Use of Acronyms

Acronyms used in this thesis are defined within each chapter. The list below provides the most commonly used acronyms.

General:

T: Temperature
P: Pressure

Opx: Orthopyroxene
Cpx: Clinopyroxene
WR: Whole rock
ANU: Australia National University
RSES: Research School of Earth Sciences
RSBS: Research School of Biological Sciences
LGCA: Laboratoire de Géodynamique des Chaînes Alpines
OJP: Ontong Java Plateau
LIP: Large igneous province(s)
KKKFS: Kia-Korigole-Kaipito Fault System
CST: Central Solomon terrain
SSTS: South Solomon trench system
NST: North Solomon trench
PNG: Papua New Guinea

Analytical:

XRF: X-ray Fluorescence
EDS: Energy dispersive spectrometry
WDS: Wavelength dispersive
SEM: Scanning electron microscope
EPMA: Electron MicroProbe Analyser
LA ICP-MS: Laser ablation inductively-coupled plasma spectrometer
MC-ICP-MS: Multi-collector inductively-coupled plasma spectrometer
LOI: Loss on ignition
GIS: Geological information system

Geochemical:

LILE: Large-ion lithophile element(s)
HFSE: High field strength element(s)
REE: Rare earth element(s)
LREE: Light rare earth element(s)
MREE: Middle rare earth element(s)
HREE: Heavy rare earth element(s)
OSMA: Olivine-spinel mantle array
FMQ: Fayalite-magnetite-quartz buffer

Rock types:

MORB: Mid ocean ridge basalt
NMORB: Normal mid ocean ridge basalt
EMORB: Enriched mid ocean ridge basalt
BABB: Back-arc basin basalt
OIB: Ocean island basalt
SSZ: Supra-subduction zone

List of Figures

CHAPTER 2:

CHAPTER 3:

List of Tables:

CHAPTER 5:

Chapter 1:
Geological background
of the Solomon Islands

1. REGIONAL SETTING OF THE SOLOMON ISLANDS

The Solomon Islands are located in the Pacific Ocean, northeast of Australia, between 155 30' and 170 30'E longitude and between 5 10' and 12 45'S latitude (Ridgway and Coulson, 1987 (Fig. 1-1). This scattered archipelago of mountainous islands and low-lying coral atolls stretches about 900 miles in a southeasterly direction from the Bougainville Island to the Santa Cruz Islands. The Solomon Islands form a linear NW-SE-trending double chain of islands separated in the centre by a narrow stretch of sea called the Slot (Petterson et al., 1997) (Fig. 1-1). The archipelago covers an area of about 249,000 square nautical miles while the land area is 28,446 sq. km, including six major islands and approximately 992 smaller islands, atolls and reefs. The six biggest islands are Choiseul, New Georgia, Santa Isabel, Guadalcanal, Malaita and Makira (also called San Cristobal) (Coleman, 1965) (Fig. 1-1).

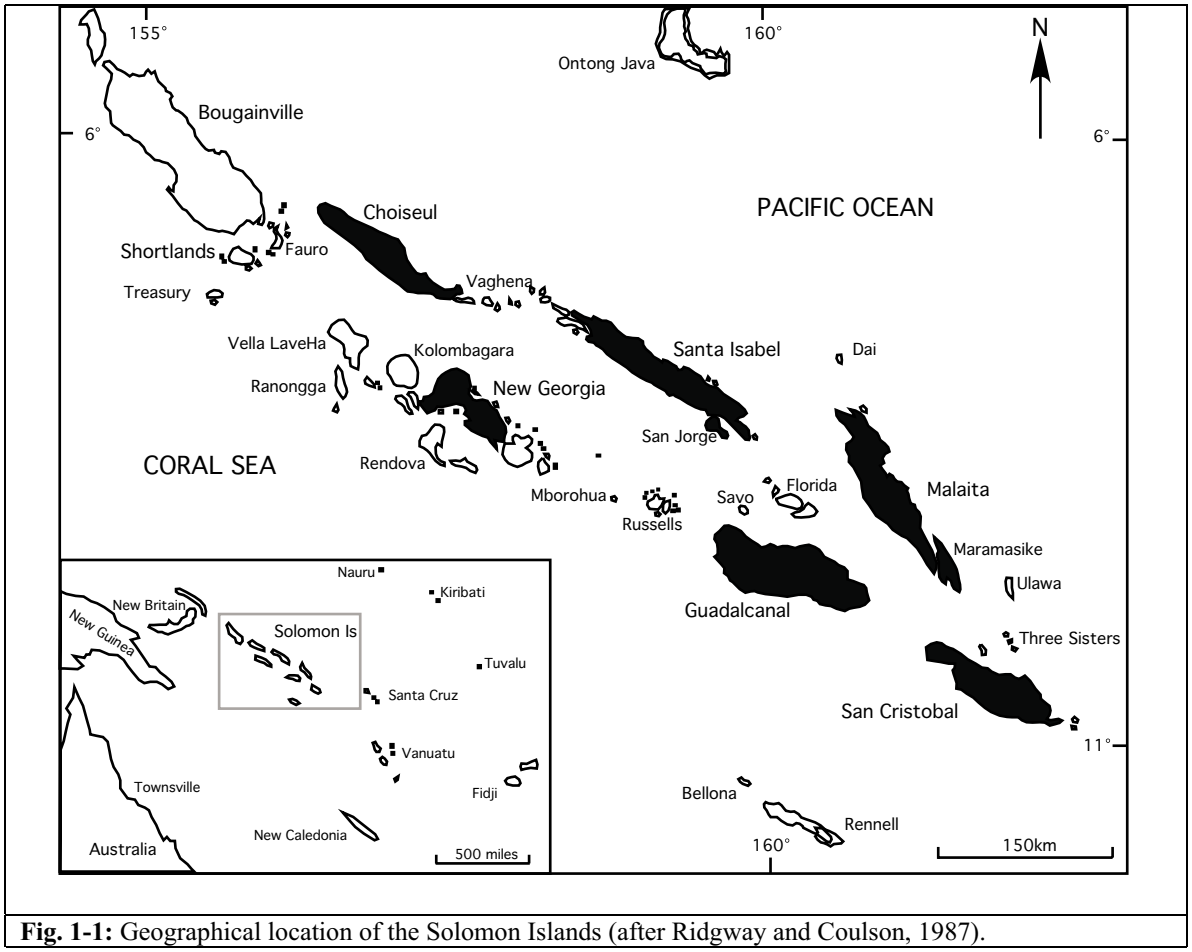

Fig. 1-1: Geographical location of the Solomon Islands (after Ridgway and Coulson, 1987).

2. THE ONTONG JAVA PLATEAU (OJP)

2.1. Large Igneous Provinces (LIPs)

The Ontong Java Plateau, located in the southwestern Pacific Ocean, is considered to be a giant oceanic plateau, which forms one of three main categories of mafic igneous provinces or LIPs (Coffin and Eldholm, 1991). The other two categories of LIPs include continental flood and volcanic passive margins (Coffin and Eldholm, 1994). The LIPs represent large-scale transient magmatism rooted deep in the Earth's mantle and therefore not controlled by lithospheric processes predicted by plate tectonic theory (Mann and Taira, 2004). Subcontinental scale-thick crust is produced with huge emplacements of predominantly mafic extrusive and intrusive rocks (Coffin and Eldholm, 1991). An estimation of 25 LIPs have formed since 250 Ma, which are now distributed worldwide (Fig. 1-2A) but most specifically in the Circum-Pacific region (Coffin and Eldholm, 1994) (Fig. 1-2B). Note that no major LIPs are forming today.

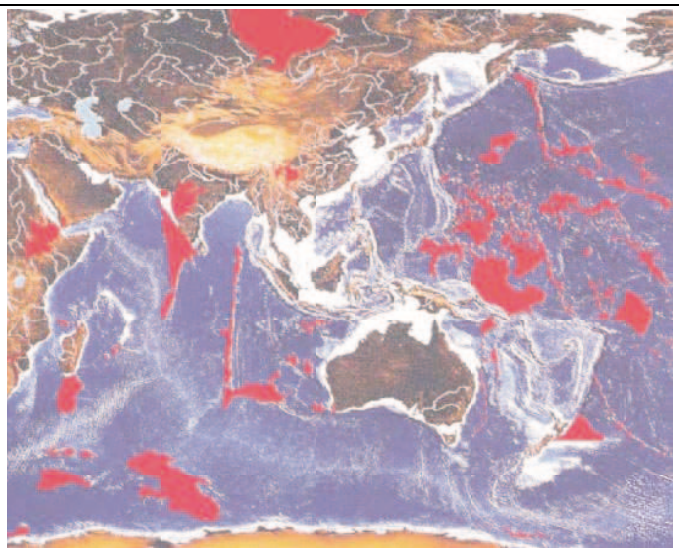

Fig. 1-2: Distribution of the large igneous provinces (LIPs) (emplaced since 250 Ma) of the Circum-Pacific region (in red) (after cover from Mahoney and Coffin, 1997). Note the location of the Ontong Java Plateau (OJP).

2.2. Characteristics and structure of OJP

OJP is defined by the 4000 m depth contour, adjacent to the > 4500 km deep Lyra, East Mariana, and Nauru ocean basins and bounded to the southwest by the >3000 m deep North Solomon Trench (Gladczenko et al., 1997). Morphologically, the OJP consists of two parts: the main plateau in the northwest and the eastern lobe or salient (Neal et al., 1997) (Fig. 1-3). The plateau surface rises to depths of 1700m in the central region of the main plateau but lies generally between 2-3km depth. The surface of the plateau appears to be relatively smooth although several seamounts like Ontong Java Atoll (the largest atoll in the world) occur (Berger et al., 1993; Kroenke, 1972).

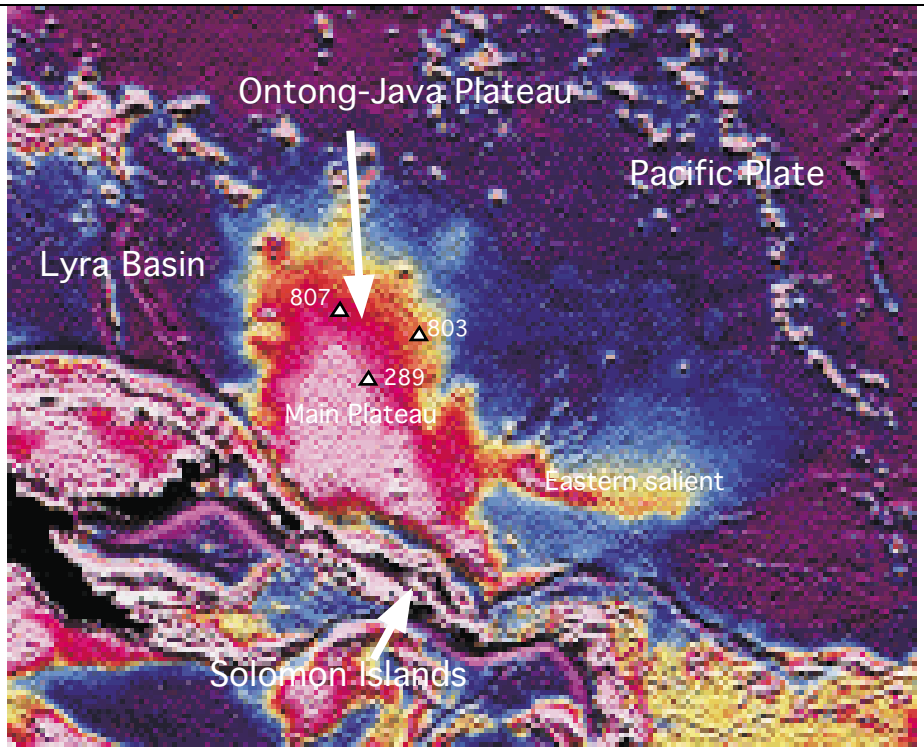

Fig. 1-3: Satellite-derived gravity map of the morphology of the Ontong Java Plateau (after Smith and Sandwell, 1995a,b and Neal et al., 1997).
OJP consists of two parts: the main plateau and eastern salient.
The locations of the drill sites (807, 803 and 289) are also shown as triangles.

The Alaska-size OJP is the world's largest oceanic plateau, covering an area of more than $1.86 * 10^6$ km^2 (Coffin and Eldholm, 1994) (Fig. 1-4). Furumoto et al. (1976) has estimated, using seismic and combined seismic-gravity, the crustal thickness of the OJP in the 30 - 43 km range with an estimated average around 36 km, comparable to the continental crusts (Christensen and Mooney, 1995). This translates to a volume of $>5 * 10^7$ km^3 and makes OJP the most voluminous LIPs (Neal et al., 1997).

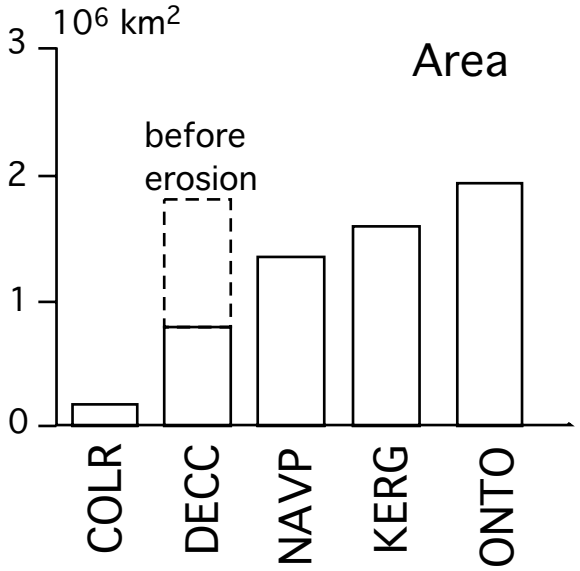

Fig. 1-4: LIP areas compared to each other (Coffin and Eldholm, 1994).
The OJP is largest of the LIPs covering $1.86*10^6$ km^2.

The OJP broadly has a similar crustal structure to 'normal' Pacific Ocean crust but each layer is abnormally thickened by up to a factor of 5 (Hussong et al., 1979; White et al., 1998). The upper crustal section comprises an upper basaltic lava-still pile with a pelagic sediment cover of > 1 km thick (Mayer et al., 1991). The OJP basement lavas were originally recovered from Ocean Drilling Project sites 209, 803 and 807 (Mahoney et al., 1993) on the high plateau (Fig. 1-3) and also identified outcropping on Malaita (Petterson et al., 1997) and Santa Isabel (Tejada et al., 1996). The origin of the dense lower crustal body with a velocity of 7.0-7.6 km/s remains controversial. Miura et al. (2004) agree that the lower crustal body represents a dense crustal root of garnet granulite or eclogite. However, Neal et al. (1997) suggest that the lower crustal body is wehrilitic to pyroxenite cumulate.

2.3. Origin and formation of the OJP

Like the other oceanic plateaus, OJP was formed by thermally induced "active" mantle plume where an inflated plume-head tailored by a narrow feeder conduit ("tail") develops, rifts the lithosphere (Coffin and Eldholm, 1994) (Fig. 1-5) and causes excessive magmatism (Campbell and Griffiths, 1990) in a geologically short period of less than 3 Ma (Richards et al., 1989).

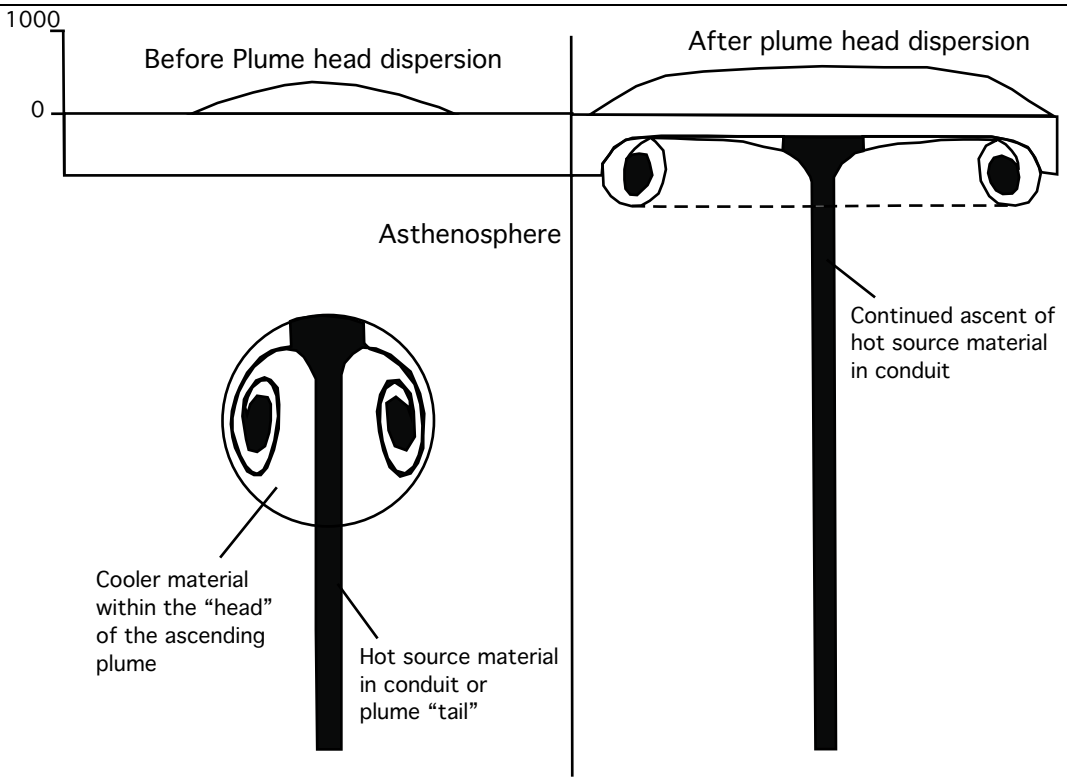

Fig. 1-5: Model for LIP generation and emplacement (after Coffin and Eldholm, 1994).
A) Thermally induced "active" mantle plume entraining mantle material during its ascent to the base of the lithosphere.
B) At the base of the lithosphere, the plume develops in a large transient head, rifting the lithosphere and causing excessive magmatism.

The ^{40}Ar-^{39}Ar ages of these OJP basalts dated from the OJP drillholes (Mahoney et al., 1993) and outcrops found on northern Santa Isabel and Malaita (Tejada et al., 1996) all suggest a bimodal distribution of ages with the first episode at 122±3 Ma and the second at 90 Ma. This means that most of the plateau was formed in these two relatively brief magmatic events related to mantle plume dynamics. Kroenke and Mahoney (1996) and Tejada et al. (1996) suggested that the 122 Ma event was significantly larger than the 90 Ma event. Therefore, the 122 Ma episode was at the origin of the construction of the main high plateau whereas the eastern salient was the result of the volcanic activity at 90 Ma (Neal et al., 1997) (Fig. 1-3).

These massive outpourings of basalt are at the origin of the undeformed Circum-Pacific Ontong Java Plateau, which was formed by mantle processes in the intraplate Pacific Ocean (Mann and Taira, 2004). However the original tectonic setting of the OJP emplacement is far to be resolved. According to the plate reconstruction of the OJP site at 125 Ma (Yan and Kroenke, 1993), the main plateau of OJP was formed at about 42°S, 159°W at the vicinity of a spreading center (Mahoney and Spencer, 1991; Winterer and Nakanishi, 1995) (Fig. 1-6). This location is approximately 1800 km distant from Louisville hotspot, indicating that OJP could be linked to this hotspot (Neal et al., 1997). The Vitiaz Trench has destroyed the portions of the Louisville hotspot older than 70 Ma (Mahoney and Spencer, 1991) and therefore no clear evidence exists to correlate

Louisville hotspot to the origin of OJP (Neal et al., 1997). In addition, Mayer and Tarduno, 1993) invoked that true polar wander of ≈10-15° should be executed to accommodate a Louisville hotspot origin for the OJP. Recent studies based on new tectonic reconstructions (Phinney et al., 1999) maintained the origin of the OJP at the Louisville hotspot.

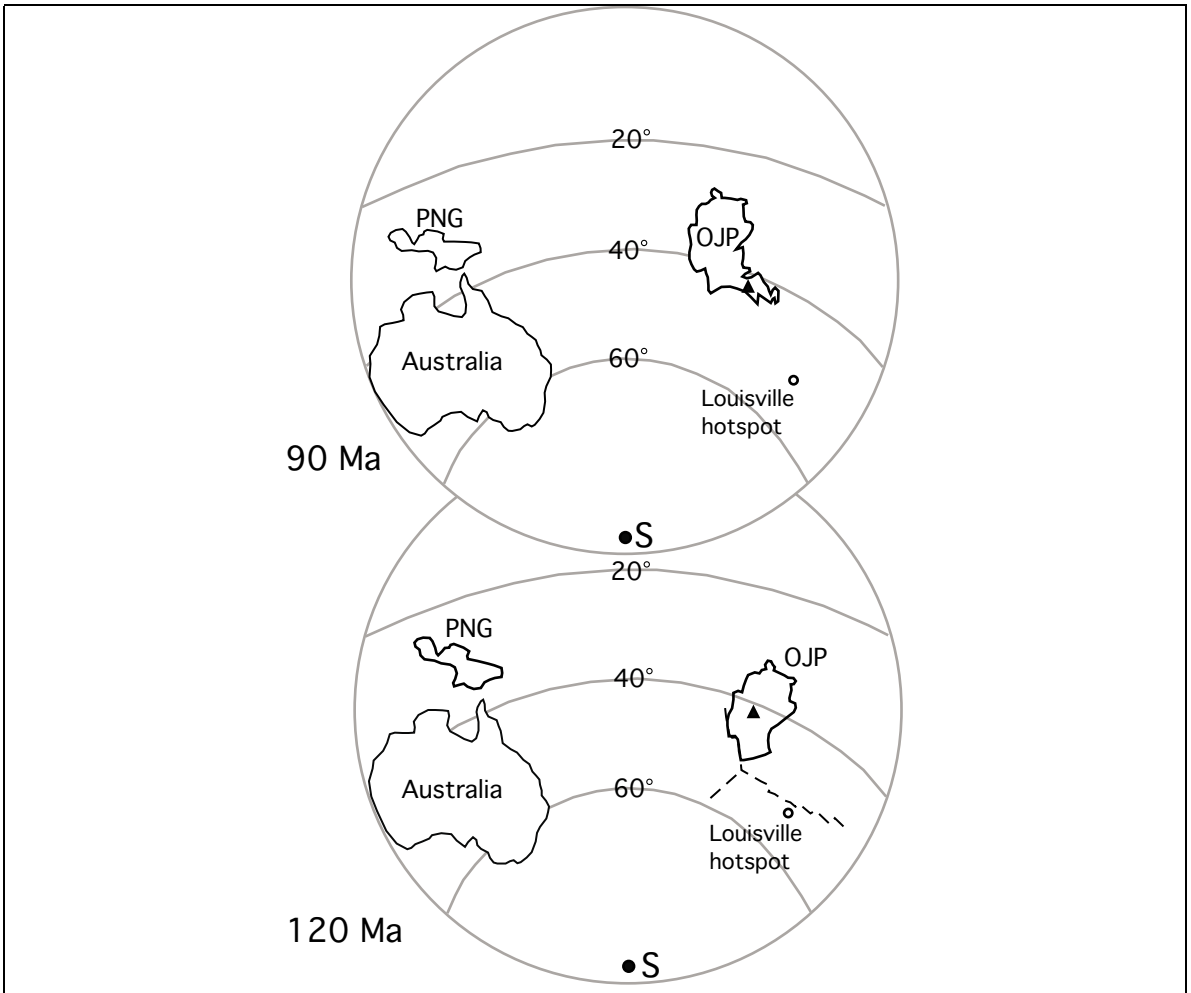

Fig. 1-6: Plate reconstruction (125-90 Ma) of the formation of the OJP (after Neal et al., 1997).
At 120 Ma, the main plateau is formed at the vicinity of a spreading centre nearby the Louisville hotspot. The triangle represents the inferred location of the OJP plume center beneath the crest of the high plateau.
At 90 Ma, the easter lobe is formed above the inferred plume center.
"S" represents the South Pole; OJP: Ontong Java Plateau; PNG: Papua New Guinea.

1.4. OJP Tectonic evolution (from 125 to ~ 30 Ma)

From when it was formed (125 Ma) until 100 Ma, OJP appears to be very close to the Pacific Plate Euler poles and moved relatively little (Petterson et al., 1993; Yan and Kroenke, 1993). Then from 100 to 85 Ma, the OJP moved steadily northward within the plate after change of plate motion occurring at 100 Ma (Yan and Kroenke, 1993). The 90 Ma event formed the eastern margin of the OJP when OJP passes approximately over the

position occupied by the high plateau during the 125 Ma episode (Neal et al., 1997) (Fig. 1-6).

From Aptian to Mid-Eocene, deep-water pelagic sedimentation was recorded on Malaita indicating an intra-oceanic environment (Petterson et al., 1997). During this period, OJP was passively carried northwards as part of the Pacific Plate (Fig. 1-7). Throughout the Eocene, the southwards-directed subduction of the Pacific Plate beneath the Australian Plate occurred at the North Solomon Island/Vitiaz Trench, which resulted in Stage 1-arc activity along a northeast-facing Solomon arc (Kroenke, 1984; Petterson et al., 1997).

Between 60 and 30 Ma, OJP passed directly over the Samoan hotspot (Yan and Kroenke, 1993) or possibly the Raratonga hotspot (Tejada et al., 1993) reflecting a subsequent plate motion change (Fig. 1-7). Younger series of Malaita were described by Tejada et al. (1996) and dated by ^{40}Ar-^{39}Ar at 44 Ma. These alkalic lavas are characterised by high vesicularity revealing a shallower –submarine eruptive setting (Petterson et al., 1997) and likely to be erupted from the Samoan hotspot are distinct to the OJP basalts. 44 Ma is also marked by a major change in Pacific plate motion (Fig. 1-7), which initiates a period of extension within the southern OJP. The development of basins allows the egress of magmas relating to both the eruption of volcanic alkaline rocks and intrusion of alnoites, accompanied by consequent intra-basin Eocene-Lower Miocene sedimentation (Neal et al., 1996).

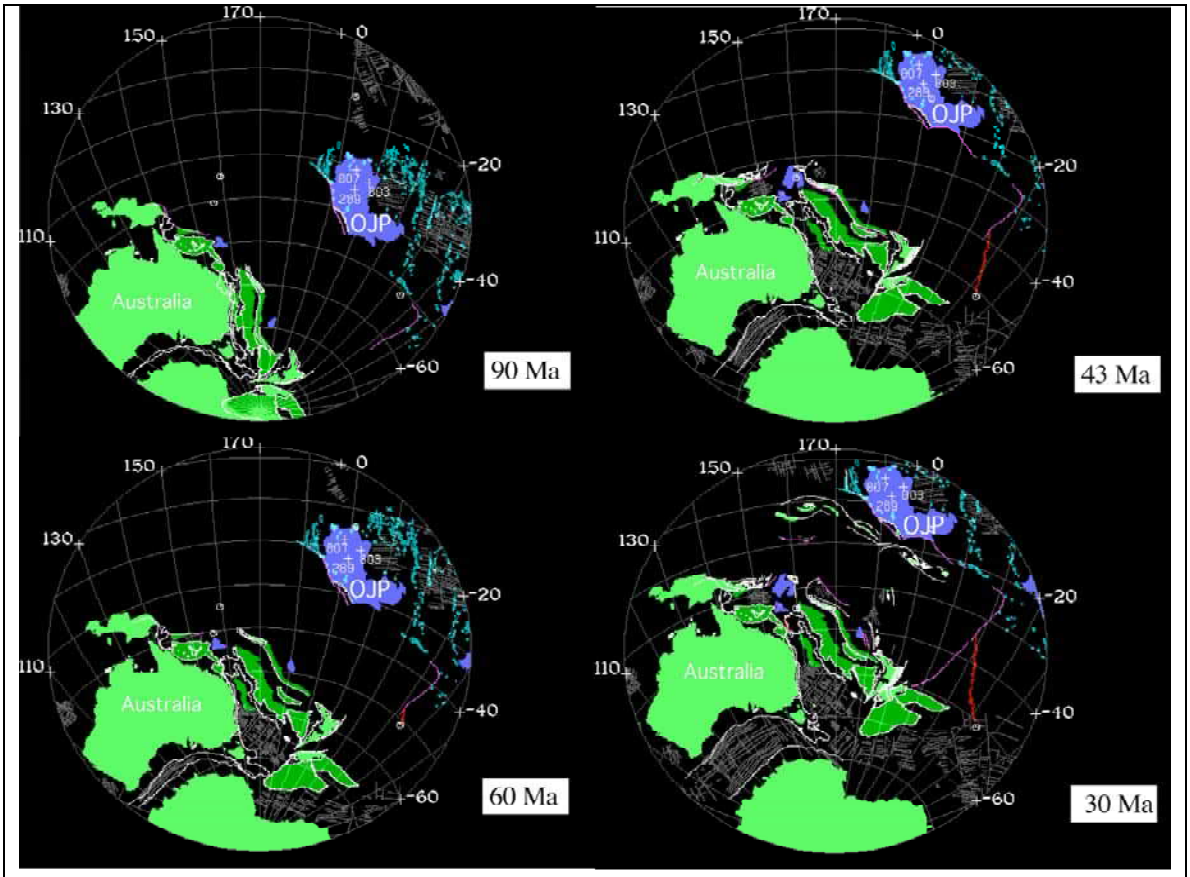

Fig. 1-7: Plate reconstruction of the Southwest Pacific 30-90 Ma (after Yan and Kroenke, 1993). See text for explanation.

3. TECTONIC MODELS OF OJP-SOLOMON ARC COLLISION

3.1. Timing of the OJP-Arc collision

Previous works (Kroenke and Sager, 1993; Petterson et al., 1997, 1999; Yan and Kroenke, 1993) (Fig. 1-8) suggested that the OJP arrived at the trench at 22 Ma (Early Miocene) in a "soft docking" event with no obvious record of associated deformation of the Solomon arc. The soft docking event of OJP, which was supported by a hiatus in Miocene arc volcanism (~ 20-15 Ma) and by plate reconstructions (Yan and Kroenke, 1993), was supposed to initiate the polarity reversal in the period ~12-6 Ma because the OJP was considered too thick to be subducted at the North Solomon trench (Fig. 1-8). According to the authors, this event was followed by a "hard docking" stage of the increased coupling between the OJP and the Solomon arc, which occurred at ~4-2 Ma (Fig. 1-8). This period coincides with an increasing compressional regime resulting in widespread deformational and uplift events evidenced in the formation of the Malaita anticlinorium (Petterson et al., 1997, 1999). In this scenario of OJP-arc collision, the workers assume that the North Solomon trench became inactive at the time of the first contact between the OJP and Solomon arc and Pacific-Australia motion was accommodated by the subduction of the Australian plate at the San Cristobal trench. This typical arc polarity reversal is well constrained by the dual inwardly dipping Benioff zones of the Pacific and Australian plates (Fig. 1-9) and is the reason that the Solomon Islands arc has been the focus of many seismic, geological and geophysical studies since it was first proposed by Kroenke (1972). However, there is a debate on whether or not the Pacific plate ceases completely to subduct underneath the Solomon arc while the new northeast-directed subduction of the Australian plate beneath the Solomon block along the SSTS is initiated during Late Miocene times (Petterson et al., 1999). Latest studies by Petterson et al. (1997, 1999) suggest the subduction at the Vitiaz trench in the vicinity of Solomon Islands have recommenced during the Mid Miocene (from ~15 Ma) and has continued intermittently and locally until present time based on the formation of Maetambe and Komboro volcanoes (Choiseul) (Ridgway and Coulson, 1987) and recent swath mapping data from Makira (Kroenke, 1995).

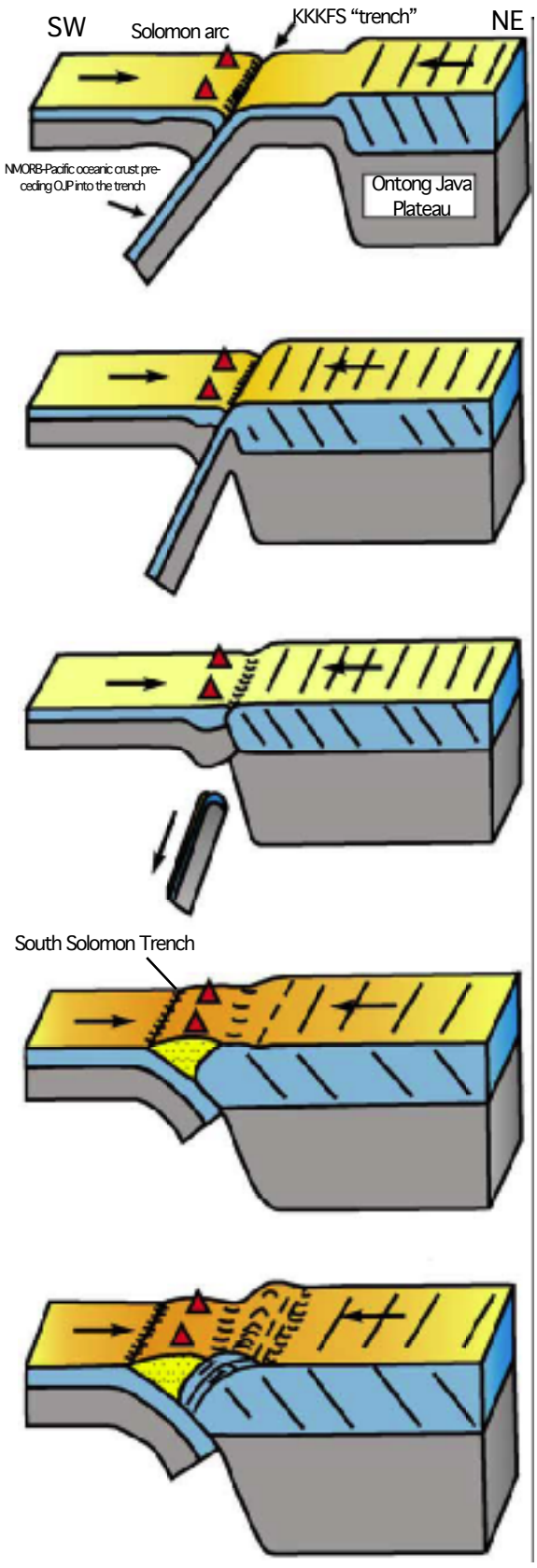

Yan and Kroenke, 1993 and Petterson et al, 1999

Eocene: initiation of SW-directed subduction of the Pacific Plate and formation of the Vitiaz- or "stage 1" -arc (equivalent to the Northern Melanesian arc)

~25-20 Ma: OJP docks with the trench during the phase of "sof-docking". Stage 1-volcanic activity ceases possibly due to steepening of the SW-dipping slab.

~20-15 Ma: Continued hiatus of Stage 1-volcanic activity. Inferred slab breakoff beneath the arc.

~12-6 Ma: NE subduction initiates along San Cristobal trench. South Solomons (Stage 2) arc volcanism.

~4-2: "Hard docking" of OJP leads to the formation of the Malaita and its eventual emergence above sea level. Subduction inferred to occur in a NE direction along the San Cristobal trench. Possible subduction along the North Solomon trench

Mann and Taira, 2004 Phinney et al, 2004 Cowley et al, 2004

Eocene: initiation of SW-directed subduction of the Pacific Plate and formation of the Vitiaz- or "stage 1" -arc (equvbalent to the Northern Melanesian arc)

~25-20 Ma: NE-facing subduction of the Pacific Plate underneath the Solomon arc along the present-day KKFS.

~5-0 Ma: Arrival of the OJP at the trench marked by the KKFS. NE Subduction initiation along San Cristobal trench. Subduction-accretion of upper parts of OJP forming the NE-vergent Malaita anticlinoriumand North Solomon trench whereas lower parts of OJP continues to subduct.

Fig. 1-8: Tectonic models for the evolution of the Solomon terrane juxtaposition. Interpretations for the timing of the major events by Yan and Kroenke (1993) and Petterson et al., 1999 are compared to those by Mann and Taira, 2004, Phinney et al., 2004 and Cowley et al., 2004.

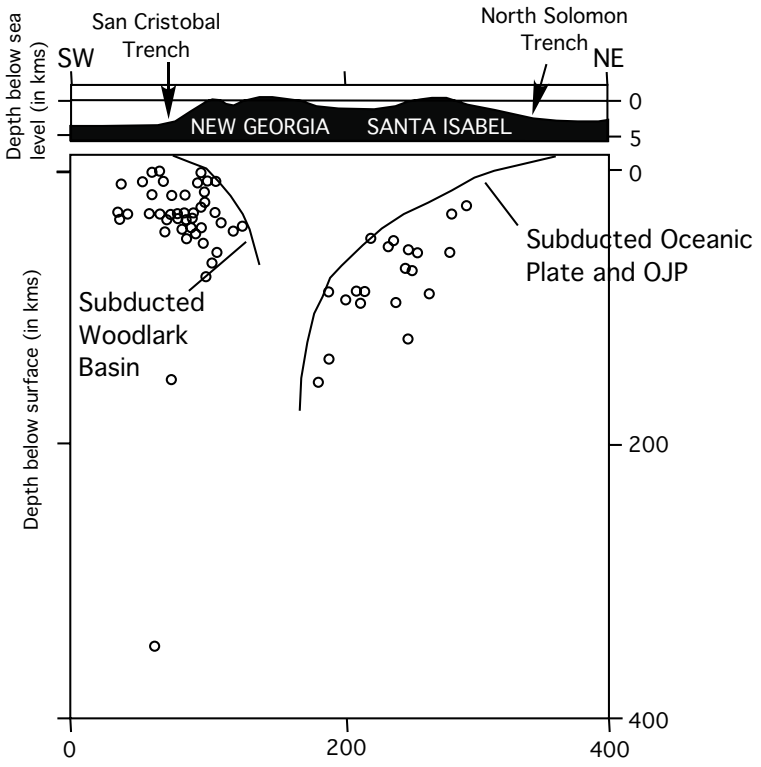

Fig. 1-9: Earthquake hypocenters (period 1963-1999) beneath the New Georgia-Santa Isabel transect (after Mann et al., 2004).
Northeast-dipping slab of Neogene (5-0 Ma) oceanic crust of the Woodlark basin at the San Cristobal Trench (underneath New Georgia) coexisting with the southwest-dipping slab of OJP and its Mesozoic adjacent oceanic crust at the North Solomon Trench (underneath Santa Isabel).
Note that present-day earthquakes indicate that OJP is subducting along the North Solomon Trench.

There are a lot of controversies about the timing of major events in the Ontong-Java-Solomon island arc convergent (Mann and Taira, 2004). Recent studies (Cowley et al., 2004; Man and Taira, 2004; Phinney et al., 2004), using new marine geophysical and onland geological data, found no evidence for an early Miocene tectonic "soft docking" event and concluded that the OJP converged on the Solomon arc only in the last 5 Ma and collided with the arc causing the accretion of the Malaita anticlinorium (Fig. 1-9). In this single tectonic event of OJP-arc convergence, the authors posit that the subduction occurred along the KKKFS (Kia-Korigole-Kaipito Fault System) (instead of the North Solomon Trench) until the arrival of the OJP at about 5 Ma (Fig. 1-9). The "choking" of this subduction caused the subduction zone to step seaward to form the present-day North Solomon trench.

3.2. Accretion models

The exact mechanism of accretion OJP-arc is still a subject of ongoing debate and research (Mann and Taira, 2004; Petterson et al., 1999). Few accretion models have been

tested to explain the presence of the OJP-related terranes obducted onto the arc from Malaita and Santa Isabel (Fig. 1-10). All of the models are essentially inferred from the onland geological data from the Malaita anticlinorium. Some authors (Mann and Taira, 2004; Petterson et al., 1999) show the OJP splitting in two with the upper parts "tectonic flakes" obducting and the lower parts subducting southwards on and beneath the arc (Fig. 1-10A). This mechanism is known as tectonic wedging (Oxburgh, 1972; Unruh et al., 1991). However this model is not supported by the geophysical data recently acquired by Mann and Taira (2004), Mann et al. (1998) and Phinney et al. (2004). Another obduction model "Active subduction-accretion of the uppermost crust of the OJP" (Mann and Taira, 2004; Petterson et al., 1999) is proposed where 4-10 km becomes detached from deeper OJP crust and forms a series of NE-directed imbricate structures with accompanying NE-vergent folds and NE-propagating faults (décollements) (Fig. 1-10B). In this model, the lower parts of the OJP are also thought to continue to subduct southwestwards underneath the Solomon arc.

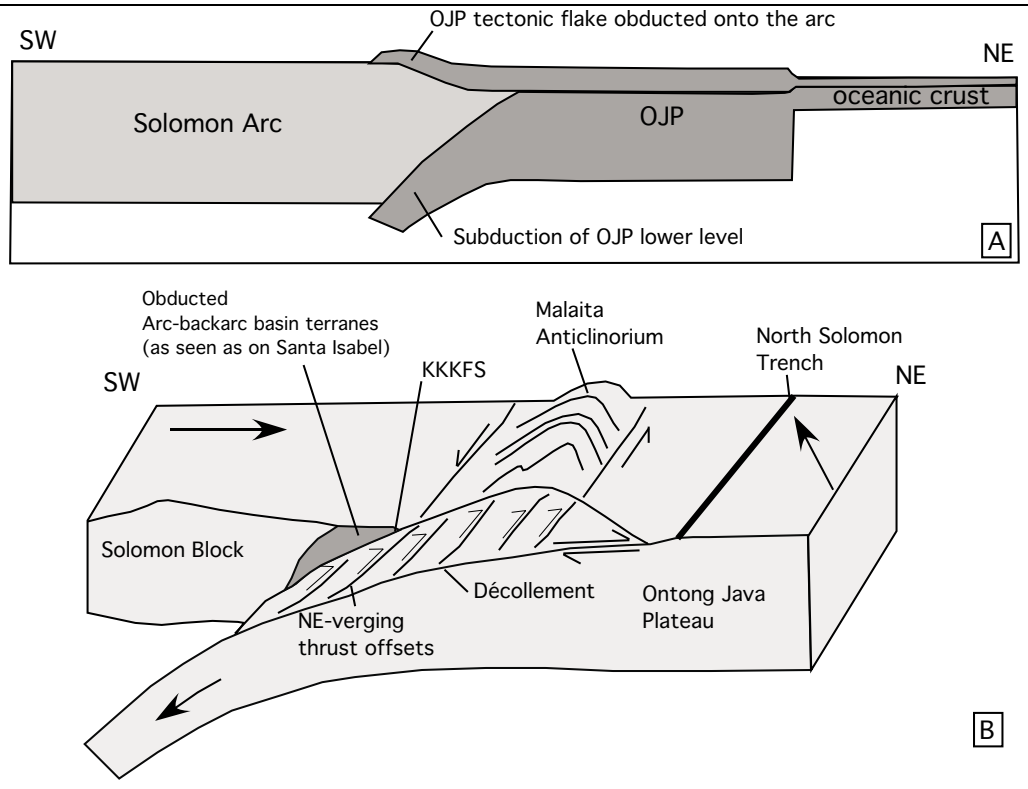

Fig. 1-10: Accretion models for the OJP-arc collision.
A) Schematic "Active flake tectonics" model for the obduction of the OJP (cartoon after Petterson et al., 1999). The solomon block acts as a triangular wedge that splits the OJP in two with the thin upper flake overriding the arc and the thick lower parts subducting southwards beneath the arc (Petterson et al., 1997; Mann and Taira, 2004).
B) Model of "Active subduction-accretion of the OJP uppermost crust" (cartoon after Petterson et al., 1999).
The increasing coupling between the OJP and the Solomon block result in the imbrication of NE-verging thrust sheets and related fault propagation folds forming a prism (Malaita Anticlinorium) (Petterson et al.,1999; Mann and Taira, 2004). The KKKFS represents a major terrane boundary, which was overthrusted deep arc basement over accreted OJP crust (Petterson et al., 1999).

4. PRESENT-DAY GEOLOGICAL FRAMEWORK OF THE SOLOMON ISLANDS

The islands of New Britain and Bougainville in Papua New Guinea, Solomon Islands and Vanuatu (formerly known as New Hebrides) are the components of the Greater Melanesian Arc System (Kroenke, 1984). The Solomon Islands consist of a linear, NW-SE-trending double chain of islands bounded by two trench systems, the Vitiaz Trench (northeast) and the South Solomon Trench System (SSTS) which marks the collision zone between the Australian and Pacific plates (Fig. 1-11). The complicated geological history of the Solomon Islands is caused in part by the collision between the OJP and the Solomon arc (Petterson et al., 1997). On the basis of different lithological assemblages, the Solomon Islands have been subdivided into several provinces (Coleman, 1960, 1965) or terrains (Petterson et al., 1999).

Coleman (1960) and Coleman and Packlam, 1976) have first described the geological province model (Fig. 1-11), dividing the Solomon Islands into three distinct provinces: 1) The Pacific Province to the east is represented by an uplifted, overthrusted and largely unmetamorphosed portion of OJP and forms the basement of Malaita, Ramos, Ulawa and north of the Kaipito-Korighole Fault System (KKKFS) on Santa Isabel; 2) The Central Province, adjacent to the Pacific Province on the southwest, includes variably metamorphosed Cretaceous and early Tertiary floor seafloor and remnants of the northeast-facing arc sequence that grew during the early to middle Tertiary above the then southwest-plunging Pacific Plate (prior to the arrival of the OJP from the east). The boundary between the Pacific and Central provinces is generally submerged except on Santa Isabel Island where it forms the KKKFS and 3) The Volcanic Province is characterised by an island arc sequence composed by young volcanic and intrusive rocks (<4 Ma), which are exposed along the southwestern flank of the Central Province.

According to Petterson et al. (1999), the Solomon terrains (Fig. 1-12) have a major Cretaceous-aged component and comprise: 1. a plume-related (OJP) terrain including Malaita, Ulawa, and the northeastern part of Santa Isabel; 2. a mid-ocean ridge basalt (MORB) terrain including much of Choiseul and Guadalcanal; 3. a hybrid terrain including both MORB and plume components forming Makira. Two stages of Tertiary arc development are recognized: Stage 1 from the Eocene to Early Miocene, including the Shortlands and southern part of Santa Isabel; Stage 2 from the Late Miocene to the present day, including the active volcanoes of the New Georgia Group and adjacent forearc.

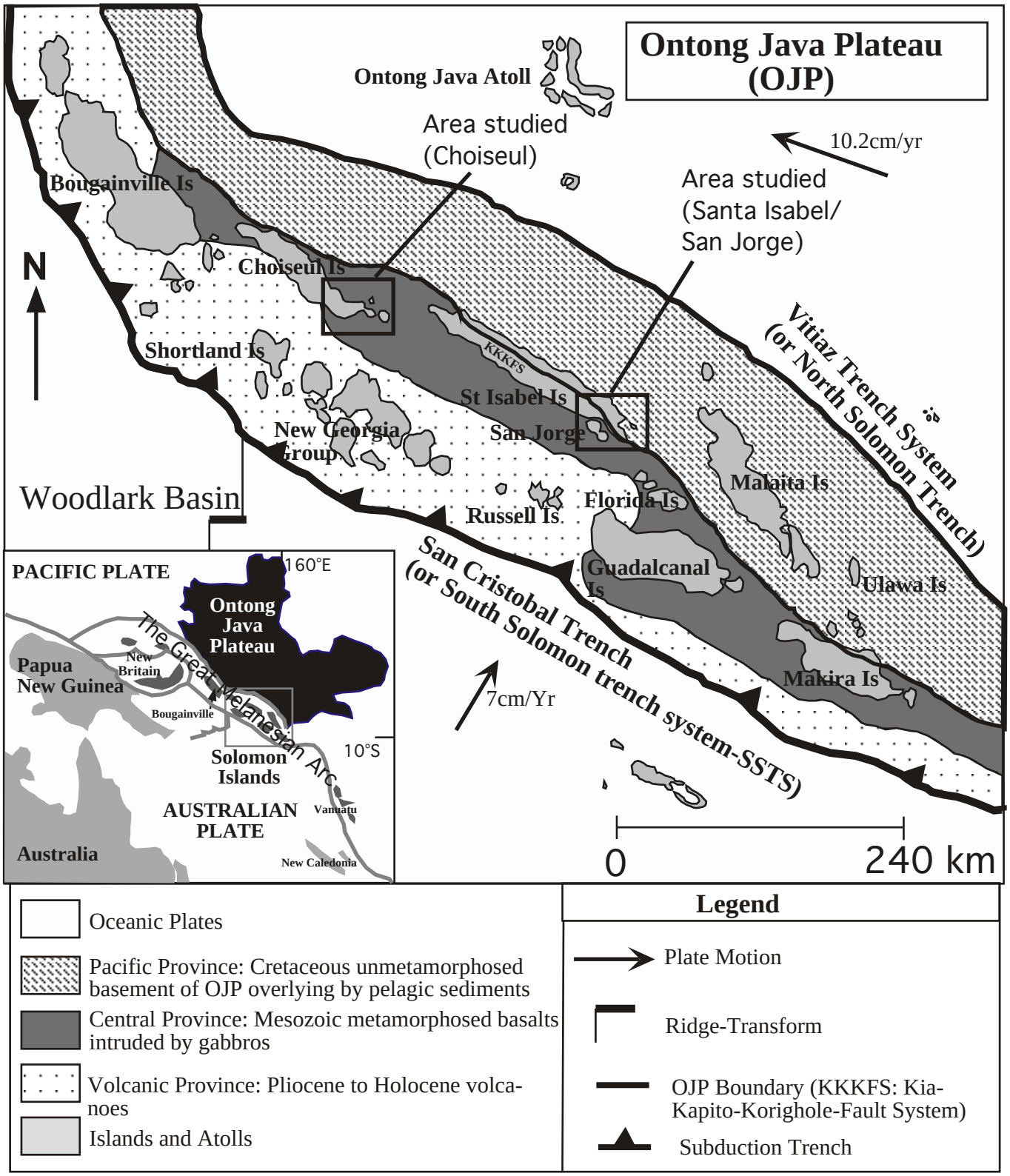

Fig. 1-11: Geological province model (Coleman, 1965) of Solomon Islands. Inset is a simplified map of the regional setting of the Great Melanesian Arc within the SW Pacific including the archipelago of the Solomon Islands.
Note the location of the areas studied for this thesis.

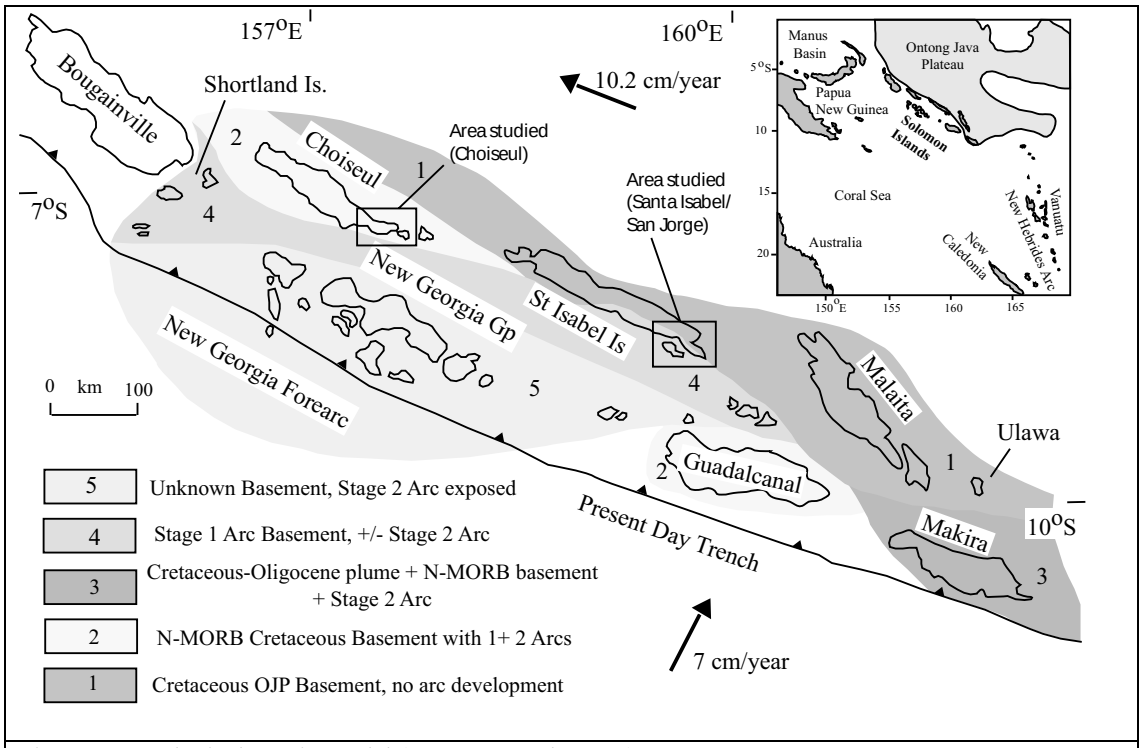

Fig. 1-12: Geological terrain model (Petterson et al., 1999).
Inset is a simplified map of the regional setting of the Solomon Islands.
Note the location of the areas studied for this thesis.

5. THE GEOLOGY OF CHOISEUL AND SAN JORGE/SANTA ISABEL AND ITS RELEVANCE TO GLOBAL GEOLOGICAL FRAMEWORK OF THE SOLOMON ISLANDS

5.1. Geology of Choiseul

Choiseul Island forms part of the NW-SE trending Solomon arc and shows pronounced elongation along this trend. Convergent plate-margin tectonics has dictated the structural development of the island, given rise to two distinct structural units: 1) the Pre-Miocene igneous and metamorphic basement complex and 2) the sedimentary and volcanic cover.
The distribution of rock types in the Choiseul Pre-Miocene basement is shown on the geological map of Choiseul (Fig. 1-13). The basement includes the Voza lavas and Choiseuls Schists, the Oaka Metamicrogabbro and Siruka Ultramafites (Ridgway and Coulson, 1987) .The Voza Lavas are the predominant formation of the Choiseul basement together with the Choiseul Schists. The Voza Lavas occur as pillowed, massive and brecciated basalts (Purvis and Kemp, 1975; Ridgway and Coulson, 1987) and can be divided into two groups: Group 1 - unmetamorphosed and low-grade rocks and Group 2 - more highly metamorphosed varieties (up to amphibolite facies). The Choiseul Schists (Fig. 1-13) are considered to be dynamothermally altered Voza Lavas, distinct from them by the presence of a tectonic fabric. Ridgway and Coulson (1987) considered that the Choiseul Schists were formed by deformation and metamorphism of parts of the original Voza lava sequence. The Oaka Metamicrograbbros are only locally exposed at the

southeast of Choiseul (Fig. 1-13). Occasionally altered, these microgabbros intruding the Voza Lavas are similar in mineralogy to Group 2 of the Voza lavas and both have comparable metamorphic history. The Siruka Ultramafites (Fig. 1-13) are almost all harzburgites, which have undergone varying degrees of serpentinisation. They form a large sheet lying on Choiseul Schists and Voza lavas with a generally subhorizontal contact (Coleman, 1960; Thompson, 1960) and are believed to be emplaced as a coherent thrust sheet, from the southeast on a subhorizontal plane in Late Miocene to Pleistocene times (Thompson, 1960).

The basement sequence of Choiseul is thought to represent an ophiolite complex with many of the characteristics of MORB, which has developed close to a subduction zone (Ridgway and Coulson, 1987). Unfortunately no radiometric age is available for the Choiseul basement sequence but stratigraphic and structural evidence suggest a probable Cretaceous age (Petterson et al., 1999; Ridgway and Coulson 1987). Petterson et al. (1999) concluded that basement sequence of Choiseul is representative of the SSMT.

The sedimentary and volcanic cover ranges in age from Miocene to Recent and in order of decreasing age (Ridgway and Coulson, 1987), they are Mole Formation (chiefly clastic sediments) (Early to Middle Miocene); Komboro and Maetambe Volcanics (Middle Miocene to Pleistocene); Vaghena Formation (calcareous and tuffaceous sediments) (Early Pliocene); Pemba Formation (calcareous sediments) (Early to Late Pliocene); Nukiki Limestone Formation (backreef and lagoonal deposits) (Pliocene); Holocene Deposits including alluvium, mangrove and freshwater swamp; backreef and lagoonal facies sediments and coralline reef limestones (Holocene). Petterson et al. (1997) inferred that stage 1-arc is represented by crystal- and lithic-rich turbidites from the Mole Formation whereas the Komboro and Maetambe Volcanics constitute the stage 2-arc sequence.

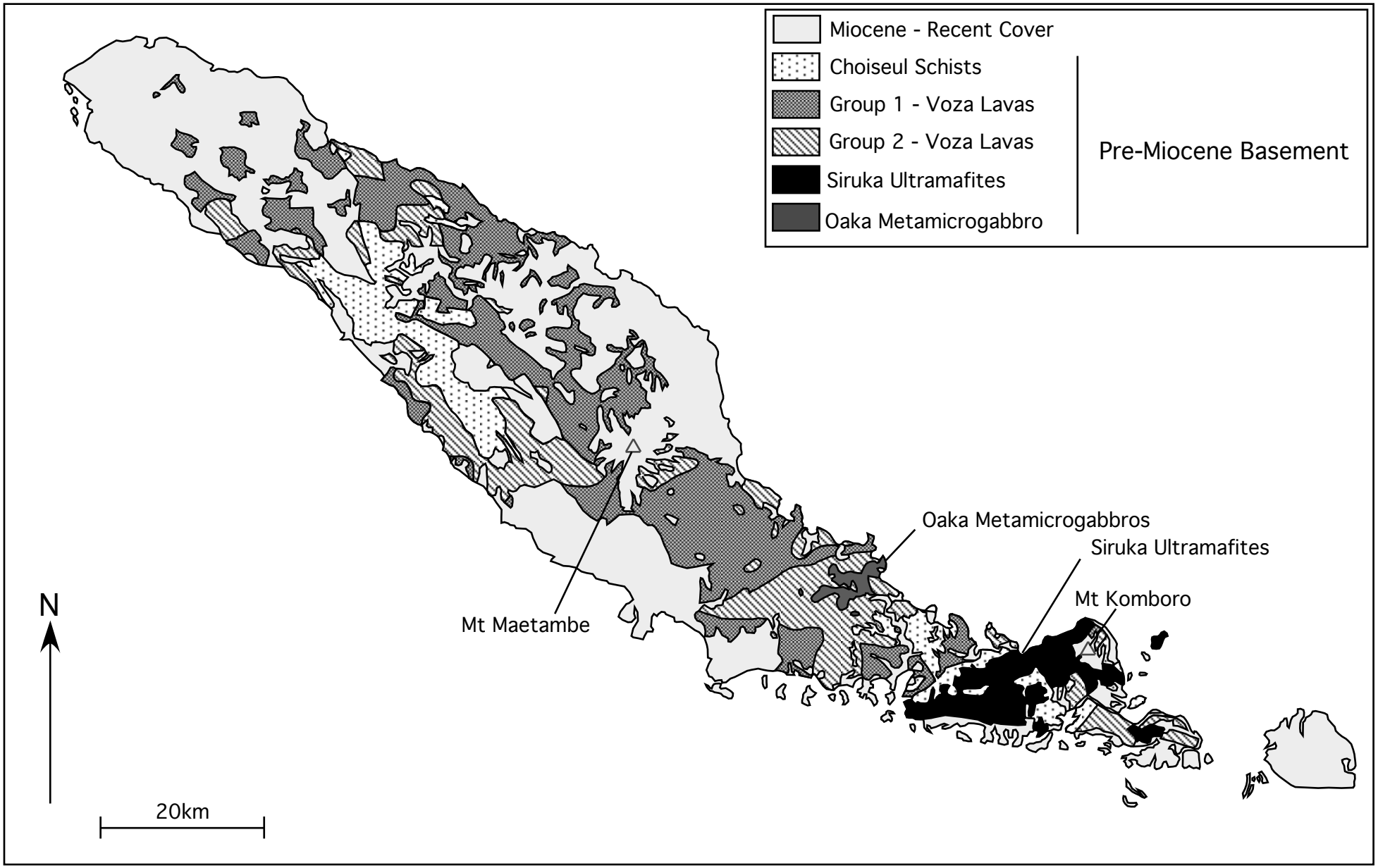

Fig. 1-13: Distribution of rock types in the Choiseul basement after Ridgway and Coulson, 1987.

5.2. Geology of Santa Isabel and San Jorge

The geology of Santa Isabel and San Jorge has been described by Hawkins and Barron (1991) and is shown in Figure 1-14.

The Kia-Korigole-Kaipito Fault System (KKKFS), which is known through seismic survey to extend offshore (Cowley et al., 1996), separates the Pacific Province to Central Province (Stanton, 1961). In the geological model of Petterson et al. (1999), the KKKFS marks a terrane boundary between the OJPT and the stage 1-arc sequence. At the North of KKKFS, the OJPT is made up of lavas known as Sigana Basalts, which are overlain by pelagic limestones and volcaniclastic sediments. The Sigana Basalts crop out as pillowed flows with rare alkalic dykes intruding the Sigana Basalts (the Sigana Alkalic Suite) (Tejada et al., 1996) (Fig. 1-14). The Sigana Basalts consist of low-K tholeiites that are petrologially and geochemically similar to lavas recovered by deep sea drilling of the OJP (Neal et al., 1997). The Sigana pillow-basalts are interpreted to be the OJP-related pillow lavas representing a flake of the OJP upper crust that was obducted onto the old Solomon arc as the result of the OJP-Solomon block collision (Petterson et al., 1997).

South of the KKKFS, the Central Province consists of pillowed and massive flows of basaltic to andesitic lavas (the San Jorge Volcanics), with associated micro- to medium-grained gabbros (the Kolose'eru Gabbros) and minor leucocratic rocks (Fig. 1-14), overlain by clastic sediments. All of these rock types are part of the Jajao Igneous Suite (Tejada et al., 1996) with ages in the range 62-46 Ma. The San Jorge Volcanics and the Kolose'eru Gabbros are both found on Santa Isabel (south of KKKFS) and San Jorge (Fig. 1-14). They are all petrographically, chemically, and isotopically distinct compared with the OJP Sigana basalts, and are suggested to be fragments of uplifted ocean floor formed in an arc – back-arc system (Tejada et al., 1996) representative of the stage 1-arc sequence (Petterson et al., 1999).

Along the KKKFS, thin fault-bound slices of peridotites are distributed on both sides of the fault system (Fig. 1-14)). The ultramafic rocks also crop out predominantly in the south of San Jorge and were termed San Jorge Ultramafites. In all locations, they consist of a series of elongate pods of more or less serpentinised harzburgites and dunites, cut by pyroxenite veins. Pyroxenites (orthopyroxenites and clinopyroxenites) can be found abundantly as pebbles making up the beaches (particularly on the southwest of San Jorge). The north part of San Jorge consists of a large domal mass of brecciated and flow-banded serpentine and serpentinous mud, analogous to the diapirs documented along the length of the Izu-Bonin-Mariana forearcs (Fig. 1-14) (Fryer et al., 1985). This serpentinite dome encloses blocks of very fresh pyroxenite as well as fresh to variably altered harzburgite at Rata Bay (Fig. 1-14).

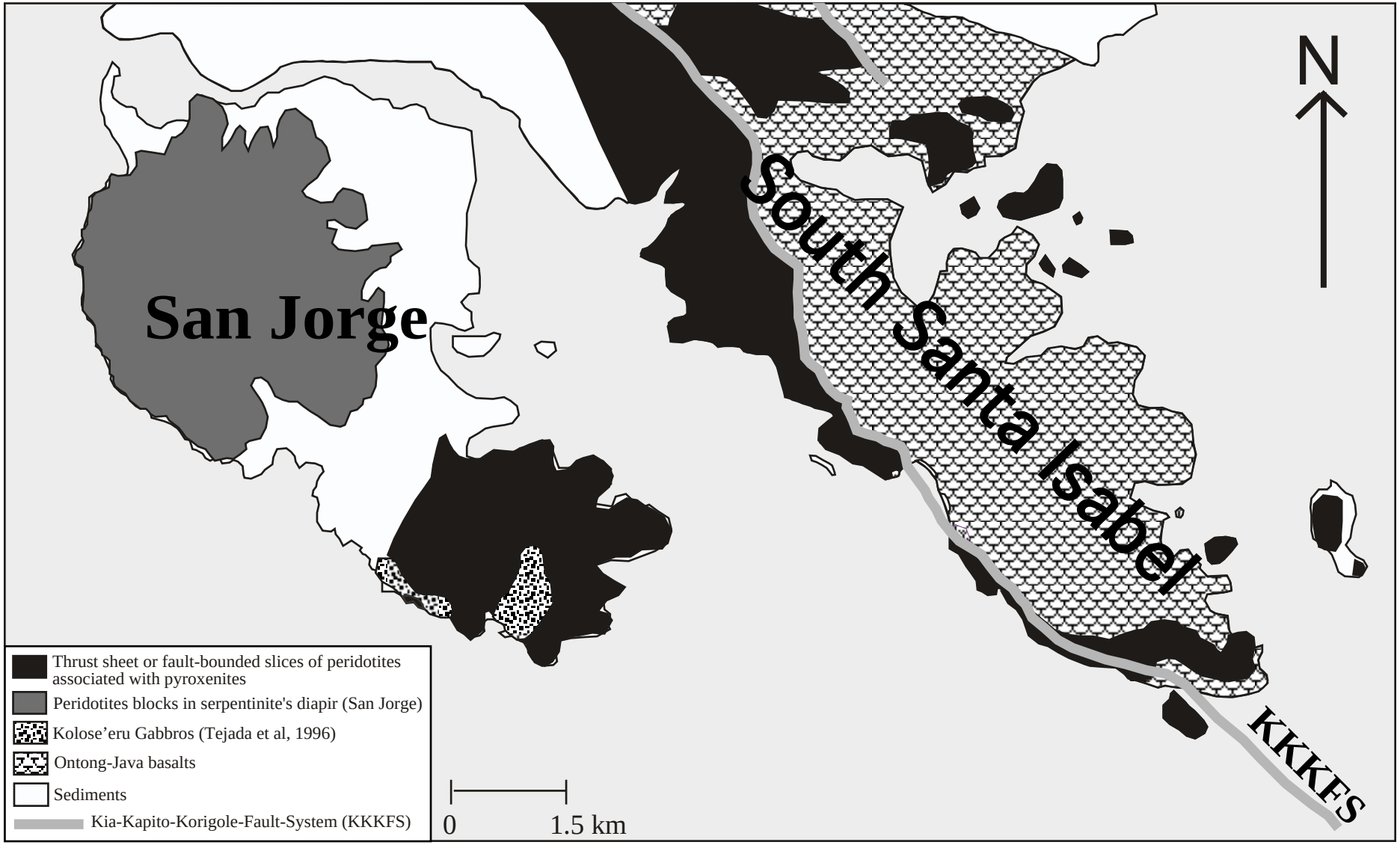

Fig. 1-14: Distribution of rock types in the Santa Isabel and San Jorge basements. (Map after Parkinson et al., 1997, pers. comm.)

Chapter 2:
Geology and geochemistry of the "Siruka Ultramafics": evidence for fluid metasomatism in an island arc setting

1 INTRODUCTION

Compared with most island arc systems in the world, there is a remarkable proportion of subaerially-exposed peridotite in the Solomon Islands. It is possible that the degree of exposure is related in some way to the collision of the Ontong Java Plateau (OJP) with the early Tertiary to Miocene arc system developed on the Australian Plate adjacent to the Vitiaz trench (Petterson et al., 1999). In this chapter, the origin of one of these peridotites, the "Siruka Ultramafics" in southeastern Choiseul, is examined through a study of the petrology, mineralogy and geochemistry of the component rock types. Our aim is to investigate the nature of melting and enrichment processes involved in the genesis of these peridotites in order to elucidate their tectonic setting. The mineralogy plus major and trace element geochemical characteristics of the Choiseul peridotites are compared with other peridotite suites from different geological environments (abyssal versus oceanic related peridotites). Finally, the exhumation process responsible for exposing these peridotites on the island of Choiseul is discussed.

2 GEOLOGICAL BACKGROUND AND SAMPLING LOCATION

The Solomons are bounded by two trench systems, the Vitiaz Trench (northeast) and the South Solomon Trench System (SSTS), which marks the collision zone between the Australian and Pacific plates. The complicated geological history of the Solomon Islands is caused in part by the collision between the OJP and the Solomon arc (Petterson et al., 1997) (see *Chapter 1*).

Coleman (1965) first described the geology of Choiseul and neighbouring small islands, followed by more detailed mapping by (Ridgway and Coulson, 1987). A simplified geological map of Choiseul and the location of the samples is shown in Figure 2-1. The pre-Miocene basement consists of several formations. The Voza Lavas and the Choiseul Schists form respectively an igneous and metamorphic basement to Choiseul with a gabbroic body (Oaka Metamicrogabbro) intruding the Voza Lavas in southeast of the island (Ridgway and Coulson, 1987) (Fig. 2-1). Another component is a complex ultramafic sheet commonly referred to as the "Siruka Ultramafics", first described by Coleman (1960) and further examined by Thompson (1960).

The Siruka Ultramafics or Choiseul peridotites are exposed in a 40 km by 16 km zone in southeastern Choiseul (Fig. 2-1), overlying the Choiseul Schists (Ridgway and Coulson, 1987). Thompson (1960) suggested they were emplaced as a coherent thrust sheet during the late Miocene. The exposed peridotites are predominantly harzburgites. In contrast to San Jorge and Santa Isabel Islands, pyroxenites are rare.

Here I present a compilation of analytical data resulting from two separate studies. The first study (based at the ANU) by Dr Ian J. Parkinson in 1992, examined twelve harzburgites (Ch1, Ch2, Ch3, Ch4, Ch5, Ch6, Ch7A, Ch7B, Ch7C, Ch7D, Ch8 and

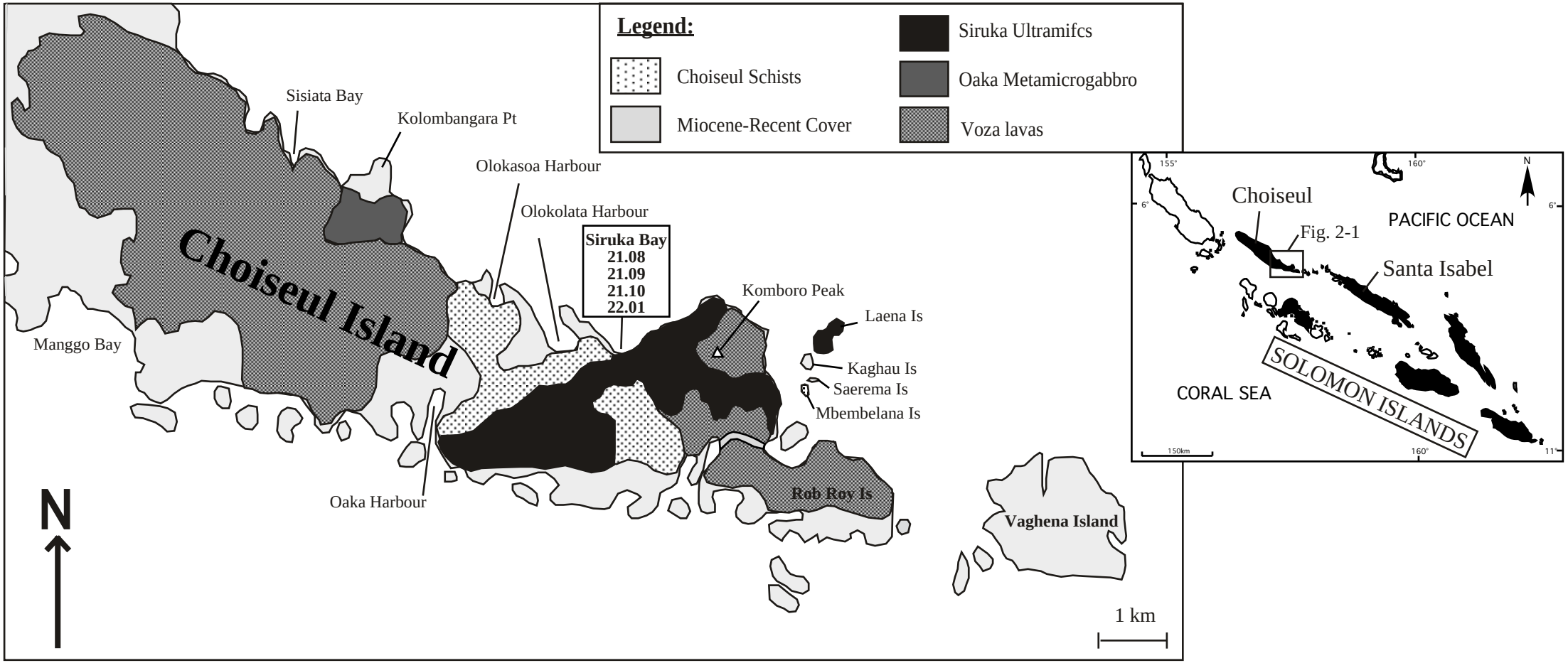

Fig. 2-1: Simplified geological map of southern part of Choiseul (after I. J. Parkinson, pers., comm.)

Ch10). The second commenced with field collections in May 1999; four peridotites (21.08, 21.09, 21.10 and 22.01) were recovered from Siruka Bay (Fig. 2-1) and analysed at the ANU together with further analyses of Ch10.

3 ANALYTICAL METHODS

The four whole rocks were analysed for major and trace element contents using respectively a XRF spectrometer (Department of Earth and Marine Sciences, ANU) and a solution ICP-MS (University of Montpellier, France).
Major element compositions for minerals were determined using a scanning electron microscope (SEM) housed at ANU and the trace element compositions of selected minerals were acquired in-situ by laser ablation, inductively-coupled plasma mass spectrometry (LA ICP-MS) at RSES (ANU).

4 PETROLOGY

The Choiseul peridotites have been affected by variable degrees of serpentinisation. They range from extremely fresh to highly serpentinised harzburgites. Modal abundances, calculated from bulk rock and mineralogical compositions in major elements, are presented in Table 2-1. The Choiseul peridotites are composed of ~ 69-79% olivine, ~ 18-25% orthopyroxene, ~ 3-7% clinopyroxene, and ~ 0.4-1.1% spinel. Exceptions to these ranges are Ch7B, Ch7D 21.08, which are highly sheared and contain higher orthopyroxene and lower modal olivine contents than these generalised ranges. In addition, three samples (21.08, Ch7A and Ch7C) have higher modal clinopyroxene contents compared to the other harzburgites.
The Siruka Ultramafics encompass a wide range of textures from coarse grained through porphyroclastic to mylonitic. The Ch10 and Ch7A samples have coarse-grained protogranular textures (nomenclature after Mercier and Nicolas, 1997) with olivine and orthopyroxene up to 5mm long and no obvious preferred orientation of the grains (Fig. 2-2A to C). Clinopyroxene is present in three morphologies: rare, ≤0.5 mm in length, altered and deformed, porphyroclastic grains (Type 1) (Fig. 2-2D); Type 2-clinopyroxene is characterised by small (≤ 100 μm) anhedral-shaped neoblasts of clinopyroxene within the matrix unassociated with orthopyroxene or spinel, and having globular or thin tails aspect (Fig. 2-2E); and Type 3-clinopyroxene occurs either as exsolution lamellae or discrete inclusions within the orthopyroxene porphyroclasts (Fig. 2-2F).
In larger clinopyroxene grains, orthopyroxene exsolution lamellae are possible (Fig. 2-2C). Small-size spinel found within interstices between olivine or orthopyroxene indicates that the deformation textures can be classified as “primary” (Mercier and Nicolas, 1997) (Fig. 2-2A). The other samples are characterised by porphyroclastic textures (Fig. 2-2D & Fig. 2-2F) and are highly sheared with a strong alignment of olivine and spinel porphyroclasts. Domains of smaller olivine neoblasts occur throughout these samples and substantial recrystallisation of olivine has also occurred (Fig. 2-2D). The spinel porphyroclasts are light reddish brown and generally occurs as highly irregular shape enclosing partly serpentinised tiny grains of olivine (Fig. 2-2D). Small discrete

Table 2-1: Petrological and mineralogical characteristics of the Choiseul peridotites (The Solomon Islands).

	Description			Primary Assemblage				Secondary Assemblage		
	Sample Number	Rock Type Peridotites	Texture	Ol (%)	Opx (%)	Cpx (%)	Sp (%)	Amph (%)	Chl (%)	Serp
This study	21.08	Cpx-rich Harzburgite	Strongly Sheared	67	21	7	0.5	Yes	-	Yes
	21.09	Harzburgite	Strongly Sheared	71	22	5	0.5	Yes	-	Yes
	21.10	Harzburgite	Strongly Sheared	74	20	5	0.9	Yes	Yes	Yes
	22.01	Harzburgite	Strongly Sheared	72	23	3	0.5	Yes	-	Yes
both	Ch 10	Harzburgite	Protogranular	77	18	4	0.7	Trace	-	Trace
Parkinson 's samples	Ch 1	Harzburgite	Mylonitic	77	17	5	0.7	Trace	-	Yes
	Ch 2	Harzburgite	Sheared	72	23	4	0.7	-	-	Yes
	Ch 3	Harzburgite	Strongly Sheared	74	21	4	0.7	-	-	Yes
	Ch 4	Harzburgite	Sheared	79	17	3	0.9	-	-	Yes
	Ch 5	Harzburgite	Strongly Sheared	74	22	3	0.5	-	-	Yes
	Ch 6	Harzburgite	Sheared	77	11	-	1.0	10	0.2	Yes
	Ch 7A	Cpx-rich Harzburgite	Protogranular	73	18	7	1.1	-	-	Trace
	Ch 7B	Harzburgite	Mylonitic	66	29	4	0.6	-	-	Yes
	Ch 7C	Cpx-rich Harzburgite	Sheared	69	25	6	0.8	-	-	Yes
	Ch 7D	Harzburgite	Sheared	59	35	-	0.4	4	1.5	Trace
	Ch 8	Harzburgite	Sheared	79	18	3	0.4	Trace	-	Yes

Numbers in % refer to the modal proportion of minerals for each sample. They were calculated based on the compositions of each mineral obtained by Microprobe.

List of Abbreviations:

Ol: Olivine; Opx: Orthopyroxenite; Cpx: Clinopyroxenite; Sp: Spinel; Amph: Amphibole; Chl: Chlorite; Serp: Serpentine.

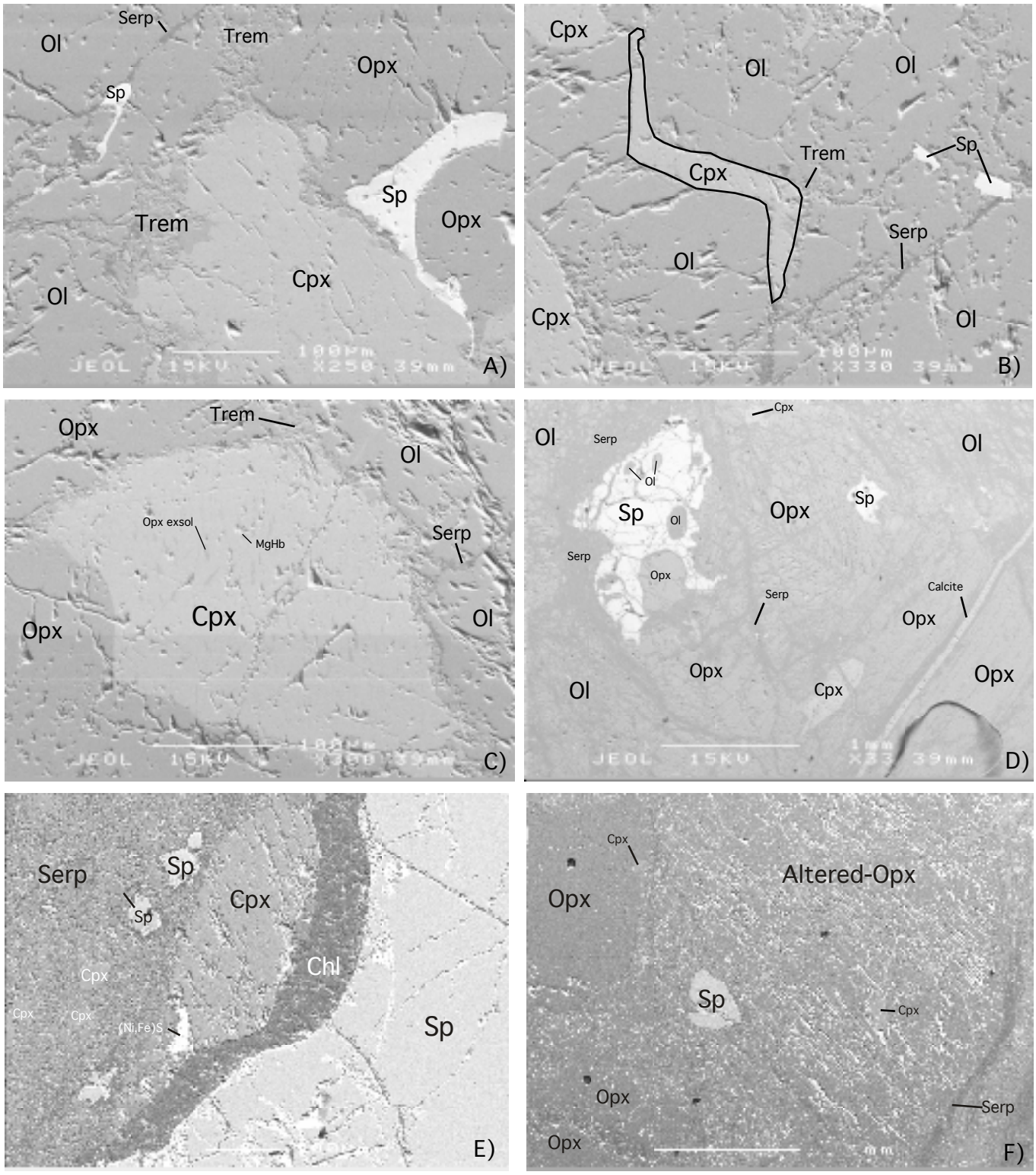

Fig. 2-2: Back-scattered SEM images of the Choiseul peridotites.
List of abbreviations: Cpx=clinopyroxene; Opx=orthopyroxene; Ol=Olivine; Sp=spinel; MgHb=magnesiohornblende; Trem=tremolite; exsol=exsolutions
A) Lobate spinel grain next to a clinopyroxene grain rimmed by tremolite. (sample Ch10).
B) Typical porphyroclastic texture (sample Ch10) with anhedral-shaped clinopyroxene grain. (sample Ch10).
C) Clinopyroxene grain with poikilitic aspect caused by the presence of magnesiohornblende blebs and orthopyroxene exsolutions. (sample Ch10).
D) Lobate spinel grains engulfing orthopyroxene and olivine small grains. A vein of calcite crosscutting all the minerals is obvious. (sample 21.09).
E) Development of chlorite on the rim of a spinel porphyroclast. Smaller grains of spinels and cpx are dissiminated amongst the serpentinised matrix. (sample 21.10)
F) Typical porphyroclastic texture with large orthopyroxene containing exsolution lamellae of clinopyroxene. (sample 21.10).

grains of anhedral spinel are also found in the matrix (Fig. 2-2E). Orthopyroxene is generally found as large porphyroclasts (up to 5 mm in length), which are either strained or lack peripheral recrystallisation into tiny neoblasts of olivine & orthopyroxene (Fig. 2-2F). Orthopyroxene neoblasts are commonly observed in the matrix (Fig. 2-2F). Small orthopyroxene grains also occur close to lobate spinel grains (Fig. 2-2D).
Two samples (Ch1 and Ch7B) have mylonitic textures with extremely fine-grained (<0.01 mm) olivine neoblasts. Orthopyroxene, clinopyroxene, and spinel grains also have substantially reduced grain-sizes in these samples. Alteration is both unusual and restricted in these peridotites. Less than 5 % serpentinisation is estimated for most samples with occasional chrysotile veins in the majority. There is more serpentine in the strongly sheared samples. In contrast, two samples (Ch7A and C10) with protogranular textures only contain trace of serpentine between grain boundaries. Tremolite occurs frequently as an interstitial phase rimming clinopyroxene, and is also occasionally observed within late serpentine veins. Magnesio-hornblende appears as small blebs (<10 μm) within clinopyroxene (Fig. 2-2C). In the porphyroclastic harzburgites, amphibole is also dispersed throughout the olivine matrix and is observed along the cleavage of orthopyroxene porphyroclasts where clinopyroxene has been exsolved. In the most altered samples (Ch6, Ch7D and 21.10), chlorite occurs in two places: around spinel grains forming prismatic splays (Fig. 2-2E) and within the olivine matrix. Rare late calcite veins crosscut the porphyroclasts and matrix of sample 21.09 (Fig. 2-2D).

5 MINERAL COMPOSITION

5.1 Olivine

Olivine compositions strictly range in 100*Mg/(Mg+Fe^{2+}) (Mg#) from 89 to 93. Representative olivine analyses are presented in Table 2-2. The most magnesian olivine (Fo_{93}) occurs in the coarse grained harzburgite (C10) and sample Ch7D, which has high orthopyroxene/olivine. Olivine enclosed in poikitically lobate spinel generally has higher Mg# (>91). Olivine crystals in porphyroclastic peridotites are unzoned and exhibit identical composition to the olivine neoblasts. Cr, Ca and Ti contents are below detection. In the plot of spinel Cr/(Cr+Al) (Cr#) against olivine Mg# for the Choiseul peridotites (Fig. 2-3), all the samples plot within the olivine-spinel mantle array (OSMA) of Arai (1994). Arai argues that the OSMA is a residual peridotite array and that cumulates plot off this trend to the right. In this case, the harzburgites can be inferred not to be cumulate in origin. All Choiseul peridotites plot in the overlap region between the abyssal peridotite field and the oceanic subduction zone peridotite field (Fig. 2-3). Ch7D, Ch8, Ch4 are part of the oceanic SSZ peridotites whereas Ch7A and Ch7B plot in the overlap region between passive margin peridotites and abyssal peridotites fields (Fig. 2-3).

Table 2-2: Representative olivine analyses for the Choiseul peridotites.

	Choiseul Peridotites (this study)												
Sample	2109-Px2	2109-Px9	2109-Px16	2109-13	2109-14	2109-15	2109-20	2110-Ol2	2110-Ol16	2110-8	Ch10-3	Ch10-19	Ch10-21
Grain	Neo	Neo	inc in sp	inc in sp	inc in sp	inc in sp	Neo	Neo	Neo	Neo	?	?	inc in sp
SiO_2	41.46	41.76	41.77	40.68	40.83	40.93	40.94	41.76	41.87	40.26	41.48	41.84	42.28
FeO*	8.77	9.59	7.96	9.98	10.32	9.85	9.35	9.19	9.03	10.22	8.81	8.44	6.94
MgO	49.31	49.21	50.98	49.6	49.34	49.6	50.12	50.13	50.51	48.98	49.52	49.99	51.48
Total	99.97	101.07	101.49	100.46	100.67	100.53	100.63	101.62	101.86	99.67	100.06	100.57	100.91
Mg#	0.9093	0.9015	0.9195	0.8986	0.8950	0.8998	0.9053	0.9068	0.9089	0.8952	0.9093	0.9135	0.9297

	Choiseul Peridotites (Parkinson's data)											
Sample	Ch 10	Ch 1	Ch 2	Ch 3	Ch 4	Ch 5	Ch 6	Ch 7A	Ch 7B	Ch 7C	Ch 7D	Ch 8
Grain	Core	Core	Core	Core	Core	Core	Core	Core	Core	Core	Core	Core
SiO_2	41.32	41.52	41.27	41.71	41.72	42.18	41.32	41.72	41.03	40.69	42.69	41.37
FeO*	8.29	9.06	9.11	9.32	9.41	9.51	8.63	9.41	9.58	9.21	8.27	9.23
MgO	49.51	49.37	50.28	51.54	49.89	52.24	49.99	49.89	50.09	50.35	50.78	50.84
Total	99.12	99.95	100.66	102.57	101.02	103.93	99.94	101.02	100.7	100.28	101.74	101.44
Mg#	0.9141	0.9066	0.9077	0.9079	0.9043	0.9073	0.9117	0.9043	0.9031	0.907	0.9163	0.9076

*Total iron as FeO.
List of abbreviations:
Neo=neoblasts; Porp=porphyroclasts; inc in sp=included in spinel.

Table 2-3: Representative spinel analyses for the Choiseul peridotites.

SPINEL	Choiseul peridotites (this study)										
Cr-Spinel	2108-1	2108-2	2108-3	2108-4	2108-7	2108-8	2108-9	2108-10	2108-11	2108-12	2109-1
TiO_2	0.05	0.05	0.04	0.04	0.05	0.05	0.04	0.04	0.03	0.05	0.04
Al_2O_3	37.64	37.08	37.29	42.64	39.15	43.17	39.95	36.85	40.09	37.48	36.75
Cr_2O_3	29.45	29.80	29.87	24.79	28.20	23.59	27.25	30.22	26.46	29.71	30.91
MgO	15.88	15.95	15.89	17.09	15.99	16.75	16.23	15.53	15.75	15.73	15.43
Fe_2O_3	2.16	2.30	2.00	1.23	2.22	1.83	1.84	1.98	1.94	2.10	1.99
FeO	12.71	12.34	12.59	11.45	12.97	12.16	12.47	13.05	13.06	12.91	13.56
Total	98.45	98.16	98.26	97.78	99.13	98.11	98.41	98.28	97.92	98.62	99.16
Mg#	0.690	0.697	0.693	0.727	0.687	0.711	0.699	0.679	0.683	0.685	0.670
Cr#	0.344	0.350	0.350	0.281	0.326	0.268	0.314	0.355	0.307	0.347	0.361
$Fe^{3+}/(Cr+Al+Fe^{3+})$	0.023	0.025	0.022	0.013	0.024	0.019	0.020	0.022	0.021	0.023	0.022
$Fe^{3+}/(Fe^{2+}+Fe^{3+})$	0.133	0.143	0.126	0.088	0.132	0.120	0.119	0.119	0.118	0.129	0.116

SPINEL	Choiseul peridotites (this study) (Continued)										
Cr-Spinel	2109-2	2109-3	2109-4	2109-5	2109-6	2109-7	2109-8	2109-9	2109-10	2109-11	2109-Px7
TiO_2	0.04	0.04	0.05	0.04	0.05	0.06	0.05	0.05	0.04	0.05	
Al_2O_3	36.51	39.10	37.00	40.53	35.25	34.56	35.52	37.19	36.82	36.65	36.84
Cr_2O_3	31.32	28.34	30.40	26.78	32.61	33.07	32.35	30.65	31.25	31.49	31.37
MgO	15.44	15.92	15.38	15.90	15.43	15.31	15.56	14.97	15.26	15.43	15.24
Fe_2O_3	1.84	2.00	2.18	1.60	2.04	1.90	2.03	1.21	1.82	1.72	1.13
FeO	13.43	13.05	13.56	13.12	13.25	13.29	13.07	14.17	13.95	13.50	14.13
Total	99.19	98.99	99.15	98.53	99.20	98.79	99.13	98.74	99.66	99.42	98.59
Mg#	0.672	0.685	0.669	0.683	0.675	0.673	0.679	0.653	0.661	0.671	0.658
Cr#	0.365	0.327	0.355	0.307	0.383	0.391	0.379	0.356	0.363	0.366	0.364
$Fe^{3+}/(Cr+Al+Fe^{3+})$	0.020	0.022	0.024	0.017	0.022	0.021	0.022	0.013	0.020	0.019	0.012
$Fe^{3+}/(Fe^{2+}+Fe^{3+})$	0.110	0.121	0.126	0.098	0.121	0.115	0.122	0.070	0.104	0.102	0.067

SPINEL	Choiseul peridotites (this study) (Continued)										
Cr-Spinel	2109-Px14	21.10-1	21.10-2	21.10-2	21.10-9	2110-Sp1	2110-Sp9	2110-Sp12	Ch10-1	Ch10-13	Ch10-20
TiO_2	0.07	0.06	0.06	0.05	0.05	0.08	0.05	0.01	0.05	0.02	bdl
Al_2O_3	34.08	32.93	34.45	33.63	35.53	31.21	39.25	36.04	31.87	32.64	32.45
Cr_2O_3	32.91	33.25	32.43	34.01	31.90	32.11	26.83	30.59	36.76	36.37	36.44
MgO	15.05	15.09	15.34	15.07	15.18	15.71	15.34	15.06	14.26	14.69	13.22
Fe_2O_3	1.71	2.61	2.69	2.08	2.53	5.14	2.10	2.14	1.00	1.27	0.33
FeO	13.64	12.68	12.98	13.40	13.73	11.62	14.03	13.99	14.95	14.61	16.67
Total	97.29	97.26	98.57	98.83	99.48	95.35	97.39	97.62	98.79	99.48	99.08
Mg#	0.663	0.680	0.678	0.667	0.664	0.707	0.661	0.657	0.6296	0.6418	0.5856
Cr#	0.393	0.404	0.387	0.404	0.376	0.408	0.314	0.363	0.4362	0.4278	0.4297
$Fe^{3+}/(Cr+Al+Fe^{3+})$	0.019	0.029	0.030	0.023	0.028	0.059	0.023	0.024	0.0112	0.0141	0.0037
$Fe^{3+}/(Fe^{2+}+Fe^{3+})$	0.102	0.157	0.156	0.123	0.142	0.285	0.119	0.121	0.0567	0.0727	0.0175

SPINEL	Choiseul peridotites (Parkinson's study)										
Cr-Spinel	Ch 1	Ch 2	Ch 3	Ch 4	Ch 5	Ch 6	Ch 7A	Ch 7B	Ch 7B	Ch 7C	Ch 7D
TiO_2	<0.08	<0.08	<0.08	<0.08	<0.08	<0.08	<0.08	<0.08	<0.08	<0.08	<0.08
Al_2O_3	31.28	31.57	33.99	29.4	33.2	33.77	38.33	37.67	43.89	34.42	21.85
Cr_2O_3	36.91	37.04	34.32	40.01	35.2	32	30.19	30.35	24.29	32.95	45.77
MgO	13.85	14.51	14.56	14.22	14.74	13.22	15.9	14.91	16.77	14.84	11.6
Fe_2O_3	2.53	1.66	2.26	1.6	1.83	3.89	1.35	2.29	1.89	2.23	2.72
FeO	16.07	14.45	15.37	15.12	14.69	17.22	13.49	15.2	13.29	14.49	17.7
Total	100.9	99.77	100.77	100.59	99.88	100.34	99.66	100.98	100.43	99.17	99.9
Mg#	0.606	0.642	0.628	0.626	0.641	0.578	0.677	0.636	0.692	0.646	0.539
Cr#	0.442	0.44	0.404	0.477	0.416	0.389	0.346	0.351	0.271	0.391	0.584
$Fe^{3+}/(Cr+Al+Fe^{3+})$	0.028	0.018	0.025	0.018	0.020	0.043	0.014	0.025	0.020	0.025	0.032
$Fe^{3+}/(Fe^{2+}+Fe^{3+})$	0.124	0.093	0.117	0.087	0.101	0.169	0.082	0.119	0.113	0.122	0.121

SPINEL	Choiseul peridotites (Parkinson's study)			
Cr-Spinel	Ch 7D	Ch 8	Ch 8	Ch 10
TiO_2	<0.08	<0.08	<0.08	<0.08
Al_2O_3	30.27	21.99	31.75	32.12
Cr_2O_3	35.62	45.25	34.38	37.28
MgO	12.8	12.32	13.52	15.45
Fe_2O_3	3.45	2.13	1.94	1.78
FeO	17	16.06	15.52	13.42
Total	99.35	98.1	97.37	100.47
Mg#	0.573	0.578	0.608	0.672
Cr#	0.441	0.58	0.421	0.438
$Fe^{3+}/(Cr+Al+Fe^{3+})$	0.039	0.025	0.022	0.019
$Fe^{3+}/(Fe^{2+}+Fe^{3+})$	0.154	0.107	0.101	0.106

*Fe_2O_3 calculated on the basis of 3 cations and 4 oxygens.

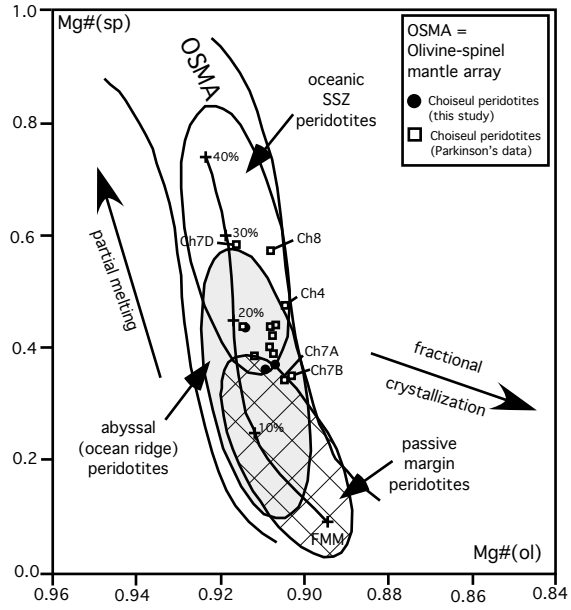

Fig. 2-3: Plot of spinel (sp) Cr# against olivine (ol) Mg# for the Choiseul peridotites showing the abyssal (ocean ridge) peridotite field of Dick and Bullen (1984), the supra-subduction zone peridotite field and passive continental margin field according to Pearce et al (2000), and the olivine-spinel mantle array (OSMA) and melting trend (marked by % melting) of Arai (1994). FMM=Fertile MORB mantle.

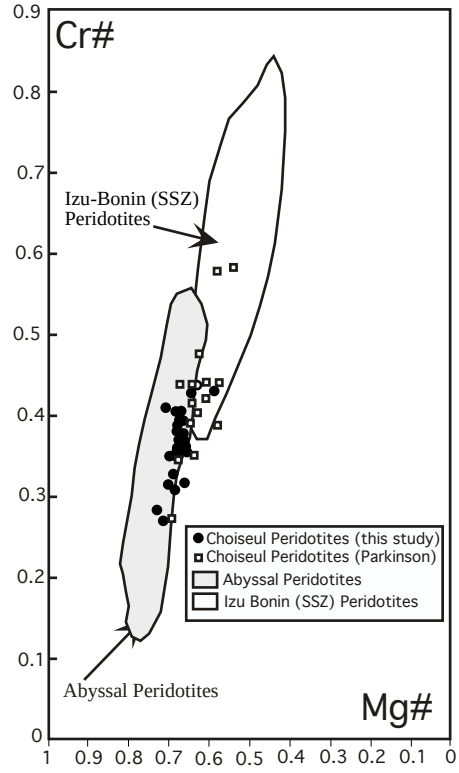

Fig. 2-4: Plot of Cr# versus Mg# for spinels of the Choiseul peridotites. The field for the abyssal peridotites is from Dick and Bullen (1984). Field of Izu Bonin (SSZ) peridotites is from Parkinson & Pearce, 1998.

5.2 Spinel

Representative spinel analyses are presented in Table 2-3. The spinel has a wide range in Cr# from 0.27 to 0.58 with the most Cr-rich samples in the clinopyroxene-poor samples. On the plot of Cr# versus Mg# (Fig. 2-4), the spinel plots at the moderately depleted to depleted end of the abyssal peridotite array of Dick and Bullen (1984). Some of the spinel grains have low Mg# and high Cr# falling within the field of the supra-subduction zone (SSZ) peridotites represented by the Izu-Bonin peridotites (Parkinson and Pearce, 1998) (Fig. 2-4).
$Fe^{3+}/(Fe^{3+}+ Cr + Al)$ ranges from 0.004 to 0.059 and $Fe^{3+}/\sum Fe$ between 0.12 and 0.285, reflecting wt% Fe_2O_3 contents of spinel ranging from 0.35 to 5.14 (Table 2-3). The broad variation in Fe_2O_3 contents is investigated more closely in the section on oxygen fugacity.

5.3 Orthopyroxene

Orthopyroxene compositions are shown in Table 2-4. They are magnesium with similar Mg# to the coexisting olivine (Mg# = 90 to 92). However, more variation exists in the orthopyroxene compositions. Al_2O_3 contents are relatively low ranging from 0.81 to 3.6 wt % (Fig. 2-5A). Orthopyroxene exsolution lamellae in clinopyroxene have the highest Al_2O_3 contents (3.6 wt %). Most samples have ≥2 wt % Al_2O_3 except two samples (Ch6 and Ch7D), which have Al_2O_3 < 1 wt %. These samples both contain substantial amounts of another aluminous phase, either amphibole or chlorite. CaO contents range broadly between 0.09 and 3.09 wt % but average 0.75 wt %. Small orthopyroxene neoblasts, found within embayments of lobate grained spinel, have lower Al_2O_3 contents compared to the orthopyroxene porphyroclasts (Table 2-4). Compositional zoning does occur within orthopyroxene porphyroclasts with CaO, Al_2O_3 and Cr_2O_3 decreasing towards the rims and Al_2O_3 and Cr_2O_3 being significantly depleted in orthopyroxene rims close to spinel grains.

5.4 Clinopyroxene

Clinopyroxene has a fairly restrictive range in Mg# of 0.928 – 0.956 with an average Mg# of 0.938 (see Table 2-5). This range of Mg# values is higher than coexisting olivine and orthopyroxene suggesting the parageneses are equilibrated (Gurney et al., 1979). The highest Mg# (0.956) belongs to one clinopyroxene included within a spinel. Al_2O_3 contents range from 0.73 to 4.00 wt % (Fig. 2-5B). Samples containing both aluminous chlorite and amphibole have the lowest aluminium contents. The Type 1 (clinopyroxene porphyroclasts) has systematically higher Al_2O_3 contents than Type 2 (clinopyroxene grains) (Fig. 2-5B). Type 1 clinopyroxene has >3 wt % Al_2O_3, whereas the Al_2O_3 contents for Type 2 are <3 wt % (Fig. 2-5B). The composition of the Type 3 clinopyroxene exsolution lamellae is higher in Al_2O_3 (~3.3 wt %).
Several samples such as Ch7A contain large clinopyroxene porphyroclasts that have striking compositional zoning in Al and Mg. No zoning exists for the Type 2 clinopyroxene.

Table 2-4: Representative orthopyroxene analyses for the Choiseul peridotites.

	Choiseul peridotites (this study)												
Sample	2109	2109	2109	2109	2109	2109	2109	2109	2109	2109	2109	2109	2109
Analysis	Px8	13	Px5	16	17	18	19	Px15	12	Px17	20	21	22
Type	next to sp	inc in sp	Neo	Neo	Neo	Neo	Neo	Porph	Porph	Porph	Porph	Porph	Porph
SiO_2	57.81	56.28	58.31	56.10	56.36	56.12	56.03	56.23	55.77	56.19	55.49	55.19	55.75
TiO_2	0.05	0.03	bdl	0.03	0.04	0.03	0.03	0.16	0.03	0.07	0.03	0.03	0.05
Al_2O_3	2.07	2.43	2.23	2.61	2.45	2.77	2.74	2.96	2.85	3.09	3.05	3.10	3.27
Cr_2O_3	0.58	0.76	0.37	0.56	0.56	0.59	0.62	0.71	0.65	0.90	0.78	0.79	0.69
FeO*	5.95	6.16	6.22	5.96	6.04	6.15	5.97	5.50	5.95	5.89	5.99	5.21	6.01
MnO	0.00	0.15	0.00	0.10	0.16	0.15	0.12	0.00	0.14	0.00	0.10	0.13	0.08
MgO	34.68	34.08	34.67	33.96	33.77	33.81	33.77	33.33	33.48	33.46	33.38	31.43	33.30
CaO	0.54	0.74	0.63	0.53	0.75	0.65	0.60	1.03	0.96	0.80	1.11	3.09	0.74
Na_2O	0.24	bdl	0.27	bdl	bdl	bdl	bdl	0.21	bdl	0.16	bdl	bdl	bdl
K2O	bdl	bdl	bdl	bdl	bdl	bdl	bdl	bdl	bdl	bdl	bdl	bdl	bdl
Σ	101.92	100.63	102.70	99.85	100.14	100.28	99.88	100.13	99.84	100.56	99.94	98.99	99.91
% En	90.30	90.43	89.79	90.30	89.58	89.96	90.00	89.70	89.68	89.61	89.80	85.93	89.50
% Fs	8.69	8.15	9.04	8.69	8.99	8.79	8.87	8.30	8.48	8.85	8.05	7.99	9.07
% Wo	1.01	1.42	1.17	1.01	1.43	1.25	1.14	1.99	1.84	1.54	2.15	6.08	1.44
Mg#	0.912	0.917	0.909	0.912	0.909	0.911	0.910	0.915	0.914	0.910	0.918	0.915	0.908

	Choiseul peridotites (this study) (continued)												
OPX	2109	2109	2109	21.1	2110	2110	2110	2110	2110	Ch10	Ch10	Ch10	Ch10
	23	24	25	4	5	6	7	Opx10	Opx14	2	9	12	24
Type	Porph	Porph	Porph	Neo	Neo	Neo	Neo	Porph	Porph	next to sp	exsol	Coarse G	Coarse G
SiO_2	56.11	55.23	55.70	56.00	56.19	55.77	55.63	56.22	57.32	57.07	55.67	57.29	56.82
TiO_2	0.03	0.03	0.02	0.02	0.03	0.02	0.02	0.03	0.00	0.04	0.01	0.07	
Al_2O_3	3.05	3.66	3.07	2.78	2.73	2.67	2.99	3.18	3.17	2.24	3.68	2.50	2.87
Cr_2O_3	0.70	0.78	0.72	0.63	0.58	0.59	0.63	0.92	0.91	0.38	1.08	0.64	0.85
FeO*	5.98	6.20	6.31	6.21	6.12	6.07	6.28	5.96	6.04	5.74	6.25	6.04	5.68
MnO	0.13	0.15	0.09	0.12	0.10	0.15	0.13	bdl	bdl	n.a.	n.a.	n.a.	n.a.
MgO	33.53	32.70	33.54	33.82	33.71	33.58	33.04	33.77	34.31	33.58	33.25	33.88	33.44
CaO	0.80	1.53	0.87	0.57	0.57	0.73	1.19	0.65	0.59	0.83	0.71	1.15	1.26
Na_2O	bdl	bdl	bdl	bdl	bdl	bdl	bdl	0.20	0.26	0.24	0.33	0.23	0.31
K2O	bdl	bdl	bdl	bdl	bdl	bdl	bdl	bdl	bdl	bdl	bdl	bdl	bdl
Σ	100.34	100.28	100.33	100.15	100.04	99.58	99.92	100.93	102.60	100.12	100.98	101.80	101.23
% En	89.50	88.42	89.85	90.15	89.76	89.92	88.70	89.86	90.00	89.79	89.22	88.94	89.10
% Fs	8.96	8.62	8.47	8.76	9.15	8.68	9.01	8.90	8.89	8.61	9.41	8.90	8.49
% Wo	1.54	2.97	1.68	1.09	1.10	1.40	2.29	1.24	1.11	1.60	1.37	2.17	2.41
Mg#	0.909	0.911	0.914	0.911	0.908	0.912	0.908	0.910	0.910	0.912	0.905	0.909	0.913

	Choiseul peridotites (Parkinson's study)												
OPX	Ch 1	Ch 2	Ch 3	Ch 4	Ch 5	Ch 6	Ch 7A	Ch 7A	Ch 7B	Ch 7C	Ch 7D	Ch 8	Ch 10
Type	Core	Core	Core	Core	Core	Core	Core	Rim	Core	Core	Core	Core	Core
SiO_2	56.56	56.20	55.37	57.21	56.76	56.39	56.20	57.68	55.58	55.43	57.39	56.73	56.03
TiO_2	bdl	bdl	bdl	bdl	bdl	bdl	bdl	bdl	bdl	bdl	bdl	bdl	bdl
Al_2O_3	2.48	2.59	2.96	2.36	2.38	0.82	2.93	1.75	3.05	2.63	0.81	1.76	2.25
Cr_2O_3	0.57	0.50	0.57	0.53	0.47	0.13	0.55	0.16	0.64	0.51	0.15	0.70	0.58
FeO*	5.82	6.08	6.01	5.94	6.16	5.87	6.09	5.98	6.36	6.17	5.71	6.04	5.74
MnO	bdl	bdl	bdl	bdl	bdl	bdl	bdl	bdl	bdl	bdl	bdl	bdl	bdl
MgO	33.96	34.31	34.12	34.19	35.64	34.44	33.31	34.46	33.79	34.41	34.63	34.26	33.40
CaO	0.32	0.60	0.35	0.39	0.64	0.09	0.59	0.22	0.51	0.27	0.29	0.63	0.90
Na_2O	bdl	bdl	bdl	bdl	bdl	bdl	bdl	bdl	bdl	bdl	bdl	bdl	bdl
K2O	bdl	bdl	bdl	bdl	bdl	bdl	bdl	bdl	bdl	bdl	bdl	bdl	bdl
Σ	99.71	100.28	99.38	100.62	102.05	97.74	99.67	100.25	99.93	99.42	98.98	100.12	98.90
% En	90.67	89.93	90.40	90.44	90.10	91.12	89.66	90.75	89.37	90.40	91.03	89.92	89.62
% Fs	8.72	8.94	8.93	8.82	8.74	8.71	9.20	8.84	9.46	9.09	8.42	8.90	8.64
% Wo	0.61	1.13	0.67	0.74	1.16	0.17	1.14	0.42	0.97	0.51	0.55	1.19	1.74
Mg#	0.912	0.906	0.910	0.911	0.912	0.913	0.907	0.911	0.905	0.909	0.915	0.910	0.912

*Total iron as FeO

List of Abbreviations:

bdl=below detection limit; n.a.=not analysed; next to sp=next to spinel; inc in sp=included in spinel; Neo=neoblast
Porph: porphyroclast; exsol=exsolution; Coarse G=coarse grain.

Table 2-5: Representative clinopyroxene analyses for the Choiseul peridotites.

Choiseul peridotites (this study)								
CPX	2109-Px4	2109-Px6	2109-Px13	2109-Px1	2110-Cpx6	2110-Cpx13	2110-Cpx13	Ch10-10
Type	Type 1	Type 1	Type 1	Type 1	Type 1	Type 1	Type 1	Type 1
SiO_2	52.57	53.53	52.97	52.28	53.91	52.93	52.93	53.55
TiO_2	0.14	0.14	0.02	0.17	0.17	0.04	0.04	bdl
Al_2O_3	3.51	3.21	3.21	3.47	3.37	3.68	3.68	3.07
Cr_2O_3	1.14	0.91	1.01	1.14	0.99	1.34	1.34	1.20
FeO	2.09	2.06	2.01	2.30	2.20	2.25	2.25	2.05
MnO	bdl	bdl	bdl	bdl	bdl	bdl	bdl	bdl
MgO	16.65	17.23	17.04	16.69	17.17	16.86	16.86	17.50
CaO	24.21	24.31	24.36	24.10	24.02	24.20	24.20	22.89
Na_2O	0.16	0.15	0.20	0.24	0.21	0.18	0.18	0.23
K_2O	bdl	bdl	bdl	bdl	bdl	bdl	bdl	bdl
Σ	100.47	101.54	100.82	100.39	102.04	101.48	101.48	100.49
% En	47.27	48.05	47.76	47.28	48.14	47.47	47.47	49.85
% Fs	3.33	3.22	3.16	3.66	3.46	3.55	3.55	3.28
% Wo	49.40	48.73	49.08	49.07	48.40	48.98	48.98	46.87
Mg#	0.93	0.94	0.94	0.93	0.93	0.93	0.93	0.94

Choiseul peridotites (this study) (continued)								
CPX	2109-15	2110-Cpx7	2110-Cpx11	Ch10-4	Ch10-18	2110-Cpx3	2110-Cpx15	Ch10-23
Type	Type 2	Type 2	Type 2	Type 2	Type 2	Type 2	Type 2	Type 3
SiO_2	52.87	55.27	54.28	54.39	53.92	54.22	54.34	53.38
TiO_2	0.06	0.06	0.16	0.07	0.12	0.10	0.07	0.14
Al_2O_3	2.63	0.73	2.48	2.75	2.06	2.81	2.55	3.39
Cr_2O_3	0.91	0.32	0.74	1.27	0.94	0.98	0.61	1.52
FeO	2.40	2.02	2.03	2.36	2.03	2.07	2.25	2.00
MnO	bdl	bdl	bdl	bdl	bdl	bdl	bdl	bdl
MgO	17.45	18.28	18.15	17.65	17.57	17.52	17.67	17.12
CaO	23.79	24.64	24.15	23.51	24.04	24.51	24.60	23.95
Na_2O	0.05	0.11	0.20	0.23	0.23	0.21	0.14	0.20
K_2O	bdl	bdl	bdl	bdl	bdl	bdl	bdl	bdl
Σ	100.19	101.43	102.19	102.23	100.91	102.42	102.23	101.70
% En	49.37	49.24	49.53	49.20	48.82	48.27	48.26	48.28
% Fs	2.25	3.05	3.11	3.69	3.16	3.20	3.45	3.16
% Wo	48.38	47.71	47.37	47.11	48.01	48.53	48.29	48.55
Mg#	0.956	0.942	0.941	0.930	0.939	0.938	0.933	0.938

Choiseul peridotites (Parkinson's study)								
CPX	Ch 1	Ch 2	Ch 3	Ch 4	Ch 5	Ch 6	Ch 7A	Ch 7A
Type	Core	Core	Core	Core	Core	Core	Core	Rim
SiO_2	53.45	52.12	54.00	53.28	53.41	53.06	51.85	53.43
TiO_2	bdl	bdl	bdl	bdl	bdl	bdl	bdl	bdl
Al_2O_3	2.56	3.22	2.12	2.68	2.66	1.17	4.00	1.99
Cr_2O_3	0.91	1.25	0.51	0.96	0.90	0.48	1.30	0.50
FeO	2.11	1.84	2.04	1.99	1.77	1.57	2.22	1.90
MnO	bdl	bdl	bdl	bdl	bdl	bdl	bdl	bdl
MgO	18.10	17.08	18.02	17.16	17.57	17.65	16.44	17.38
CaO	23.23	23.93	24.27	24.48	24.74	24.20	23.89	24.44
Na_2O	bdl	bdl	bdl	bdl	bdl	bdl	bdl	bdl
K_2O	bdl	bdl	bdl	bdl	bdl	bdl	bdl	bdl
Σ	100.48	99.46	100.96	100.55	101.05	98.13	99.69	99.63
% En	50.30	48.37	49.22	47.83	48.34	49.13	47.16	48.26
% Fs	3.29	2.92	3.13	3.11	2.73	2.45	3.57	2.96
% Wo	46.41	48.71	47.65	49.05	48.93	48.42	49.26	48.78
Mg#	0.939	0.933	0.940	0.939	0.947	0.953	0.930	0.942

Choiseul peridotites (Parkinson's study) (continued)						
CPX	Ch 7B	Ch 7B	Ch 7C	Ch 7D	Ch 8	Ch 10
Type	Core	Exsol	Exsol	Exsol	Core	Core
SiO_2	52.02	53.59	52.93	54.35	52.92	51.48
TiO_2	bdl	bdl	bdl	bdl	bdl	bdl
Al_2O_3	3.61	1.15	2.66	1.55	1.95	2.97
Cr_2O_3	1.04	0.20	0.89	0.82	1.01	0.94
FeO	2.02	1.90	2.09	2.02	2.19	2.05
MnO	bdl	bdl	bdl	bdl	bdl	bdl
MgO	16.77	17.95	16.89	18.88	17.97	16.81
CaO	23.66	24.26	24.00	23.68	24.95	23.06
Na_2O	bdl	bdl	bdl	bdl	bdl	bdl
K_2O	bdl	bdl	bdl	bdl	bdl	bdl
Σ	99.12	99.06	99.47	101.30	100.99	97.31
% En	48.04	49.24	47.83	50.98	48.39	48.67
% Fs	3.25	2.92	3.32	3.06	3.31	3.33
% Wo	48.72	47.84	48.85	45.96	48.30	48.00
Mg#	0.937	0.944	0.935	0.943	0.936	0.936

List of Abbreviations:
bdl= below detection limit; Exsol=exsolution
Clinopyroxene types: Type 1=porphyroclast; Type 2=small anhedral grain; Type 3: exsolution

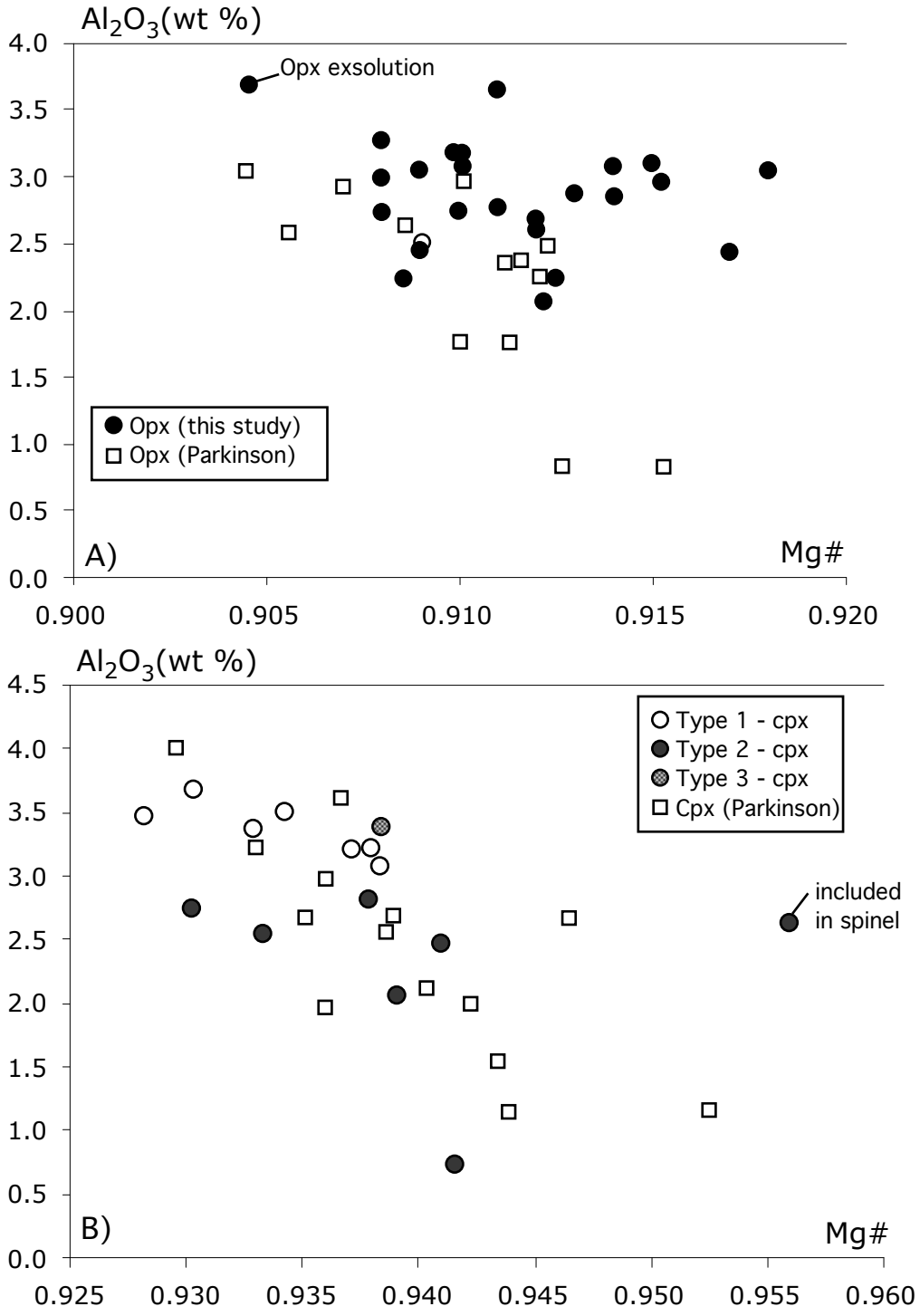

Fig. 2-5: Pyroxene compositional plots for the Choiseul peridotites.
List of abbreviations: Opx=orthopyroxene; Cpx: clinopyroxene.
A) Mg# versus Al_2O_3 wt% of orthopyroxene.
B) Mg# versus Al_2O_3 wt% of clinopyroxene. Type 1 - cpx represents the clinopyroxene porphyroclasts; Type 2 - cpx: the small anhedral grain of clinopyroxene; Type 3 - cpx are the exsolutions within orthopyroxene grains.

5.5 Amphibole

Two types of amphibole are present. Tremolite forms rims on the clinopyroxene grains (Fig. 2-2A) and also occurs in serpentinite veins, whereas magnesiohornblende forms blebs within the clinopyroxene grains (Fig. 2-2C). Representative amphibole analyses are presented in Table 2-6. Compositionally, the tremolite is magnesium-rich (Mg# ~0.95) and has appreciable Al_2O_3 contents ≤ 5 wt %, which is generally more aluminous than tremolites described in abyssal peridotites (Kimball, 1985). They are moderately low in Cr_2O_3 (< 1.1 wt %) and have low TiO_2 (< 0.17 wt %). In contrast, the magnesio-hornblende has lower Mg# (0.915) but higher Al_2O_3 (> 5 wt%) and Cr_2O_3 (> 2 wt %).

5.6 Chlorite

Representative chlorite compositions are listed in Table 2-7. Chlorite is highly aluminous (>7 wt %) ranging from being more aluminous than clinochlore to sub-aluminous. The most aluminous chlorite (>15 wt %) is associated with spinel grains whereas the sub-aluminous (<10 wt%) compositions are found next to serpentine minerals within the olivine matrix.

6 WHOLE ROCK COMPOSITION

6.1 Major elements

Whole rock major and trace element analyses are presented in Table 2-8. It is apparent from variable loss on ignition (LOI) values in this table that the peridotites have undergone different degrees of serpentinisation. The plot of MgO versus LOI (wt %) (Fig. 2-6A) demonstrates that the effect of serpentinisation is limited in terms of major elements with the exception of the most altered sample (21.08), which has lost significant MgO. This serpentinised sample (LOI >10 wt %) also has high Ca contents (CaO = 2.72 wt %) (Fig. 7B). The CaO contents of the other samples are insensitive to serpentinisation, averaging only 1.2 wt % (Fig. 2-6B).

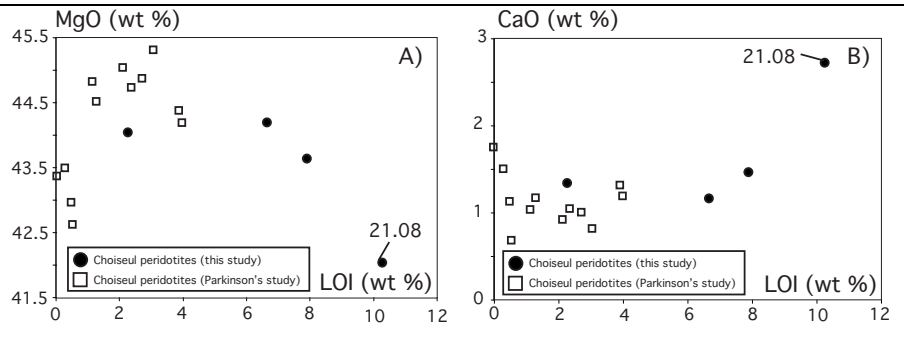

Fig. 2-6: Plots of MgO wt % (Fig. 2-6A) and CaO wt % (Fig. 2-6B) against Loss on ignition (LOI wt %) for the Choiseul peridotites.

Table 2-6: Representative amphibole analyses for the Choiseul peridotites.

	Choiseul peridotites (this study)										
Amphibole	2109-Px10	2109-Px11	2109-Px12	Ch10-5	Ch10-6	Ch10-7	Ch10-8	Ch10-14	Ch10-15	Ch10-17	Ch10-22
Type	tremolite	tremolite	tremolite	tremolite	tremolite	tremolite	tremolite	tremolite	tremolite	tremolite	Mg-Hb
SiO_2	56.93	58.19	56.31	56.16	56.17	56.6	57.14	57.36	55.15	53.49	51.12
TiO_2	0.03	0.17	0.09	0.01	0.09	0.08	0	0.14	0.13	0	0.08
Al_2O_3	1.95	0.99	3.25	2.23	2.76	2.36	2.6	2.24	3.51	4.31	5.68
Cr_2O_3	0.41	0.24	0.56	0.91	0.78	1	0.85	1.1	0.74	0.75	2.06
FeO tot	2.25	1.43	1.94	1.69	1.89	1.83	1.97	1.22	1.81	2.44	3.39
MnO	bdl	bdl	bdl	bdl	bdl	bdl	bdl	bdl	bdl	bdl	bdl
MgO	22.48	23.29	22.22	22.14	22.35	22.16	22.47	22.99	21.82	20.39	20.4
CaO	13.73	14.49	13.6	13.69	13.68	13.92	13.62	13.74	13.28	13.98	15.35
Na_2O	0.29	0.23	0.2	0.39	0.44	0.25	0.39	0.38	0.52	0.64	0.23
K_2O	bdl	bdl	bdl	bdl	bdl	bdl	bdl	bdl	bdl	bdl	bdl
Total	98.07	99.03	98.20	97.22	98.16	98.20	99.04	99.17	97.08	96.00	98.31
Mg#	0.947	0.967	0.959	0.959	0.955	0.956	0.953	0.971	0.956	0.937	0.915

	Choiseul peridotites (Parkinson's study)						
Amphibole	Ch1	Ch6	Ch6	Ch7D	Ch7D	Ch8	Ch10
Type	tremolite	Trem-Hb	tremolite	tremolite	tremolite	tremolite	tremolite
SiO_2	54.75	52.58	55.58	55.17	55.97	55.06	54.07
TiO_2	bdl	bdl	bdl	bdl	bdl	bdl	bdl
Al_2O_3	4.95	4.02	2.88	3.06	2.81	0.79	2.75
Cr_2O_3	0.24	0.45	0.78	0.69	0.47	0.25	1.06
FeO tot	2.35	3.17	2.49	2.04	2.15	2.26	1.72
MnO	bdl	bdl	bdl	bdl	bdl	bdl	bdl
MgO	21.61	22.04	23.55	21.79	22.42	25.11	22.24
CaO	13	11.13	11.74	12.86	12.89	10.95	13.41
Na_2O	bdl	0.83	0.51	bdl	bdl	bdl	0.17
K_2O	bdl	bdl	bdl	bdl	bdl	bdl	bdl
Total	96.4	94.18	96.53	95.61	96.69	94.42	96.81
Mg#	0.943	0.925	0.944	0.95	0.949	0.952	0.958

*Total iron as FeO
List of Abbreviations:
Mg-Hb=Magnesiohornblende; Trem-Hb=Tremolitic Hornblende.

Table 2-7: Representative chlorite analyses for the Choiseul peridotites.

Chlorite	21.10 (a)	Ch6 (b)	Ch6 (b)	Ch6 (b)	Ch7D (b)
Type	Chl	Chl	Chl	Chl	Chl
SiO_2	34.98	30.17	33.42	39.02	31.73
TiO_2	bdl	bdl	bdl	bdl	bdl
Al_2O_3	18.85	19.26	15.5	7.73	16.06
Cr_2O_3	n.a.	0.47	0.78	0.46	1.08
FeO	1.77	3.26	4.04	3.34	2.9
MnO	bdl	bdl	bdl	bdl	bdl
MgO	36.01	31.97	32.16	36.16	32.3
CaO	0.16	bdl	bdl	bdl	bdl
Na_2O	bdl	bdl	bdl	bdl	bdl
K_2O	bdl	bdl	bdl	bdl	bdl
Total	91.77	85.32	86.54	86.71	84.07
Mg#	0.973	0.943	0.934	0.951	0.952

(a) Choiseul peridotites (this study)
(b) Choiseul peridotites (Parkinson's study)
List of Abbreviations:
Chl=Chlorite; bdl=below detection limit; n.a.=not analysed
*Total iron as FeO

All the peridotites have a restricted range of composition with Mg# between 0.905 and 0.913. Good correlations exist between major oxides (SiO_2, total iron as Fe_2O_3*, Al_2O_3 and CaO) and Mg# which is used as an "index of depletion" (Fig. 2-7A). SiO_2, Al_2O_3, total iron as Fe_2O_3* and CaO all decrease with increasing Mg# (Fig. 2-7A). The bulk chemistry of Ch7D reflects its modified modal composition. Ch7D is characterised by its high SiO_2 and low Fe_2O_3* contents reflecting its elevated orthopyroxene content (Fig 2-7A). The low TiO_2 (0.003-0.02 wt %) together with Al_2O_3 (0.64-1.48 wt%) contents indicate that the peridotites are strongly depleted in magmaphile elements.

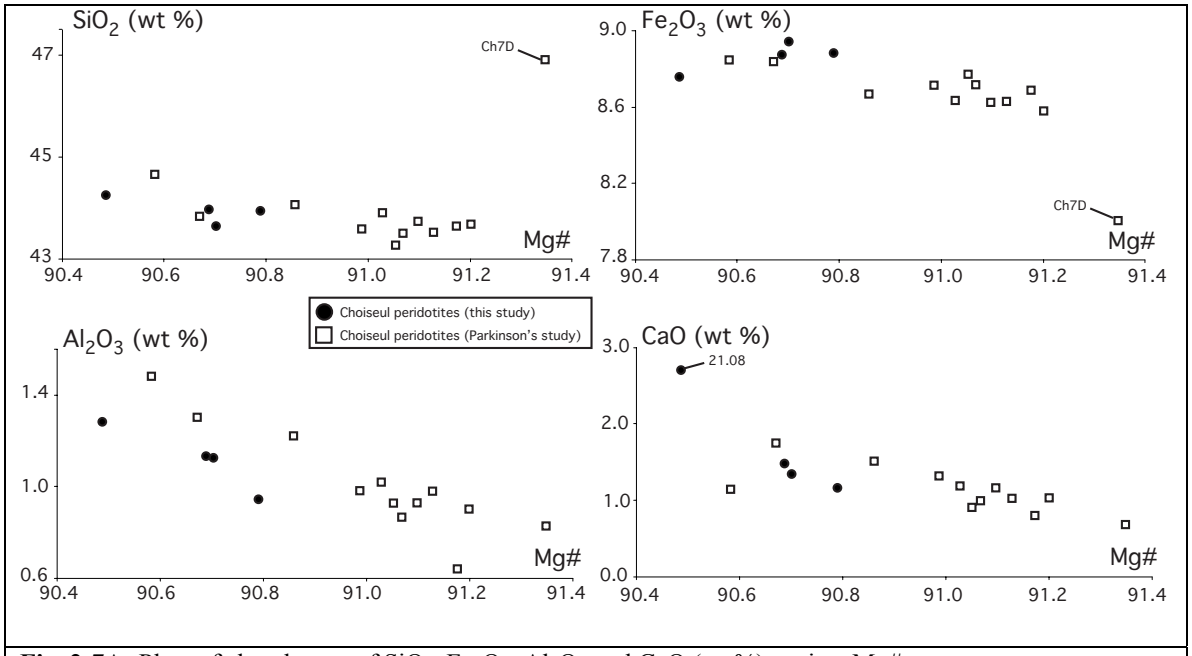

Fig. 2-7A: Plots of abundances of SiO_2, Fe_2O_3, Al_2O_3 and CaO (wt %) against Mg#.
The black dots define the data set of the Choiseul peridotites (this study) whereas the open squares refer to the dataset of Parkinson (pers. comm.) for the Choiseul peridotites.

Abundances of minor elements such as Sc, Ti, V, Cr and Ni are plotted against Mg# in Figure 2-7B. Ni, which is compatible during melting, has a positive trend consistent with known mineral-melt partitioning. Sample Ch7D is excluded from this good correlation having a low Ni content for its high Mg#, and reflecting orthopyroxene enrichment relative to olivine. Sc and V correlate negatively for Parkinson's samples. However, the Sc and V values for the 4 additional samples analysed here plot systematically below the Sc and Y values for Parkinson's samples for a given Mg#, suggesting an analytical error. Zn follows a similar trend when plotted against Mg# whereas Cu has a good negative correlation with Mg# (not plotted here). Cr and Co do not behave in any systematic manner with increasing bulk depletion. Frey et al. (1985) have also observed scattered Cr abundances in other ultramafic suites suggesting sampling scale problems. In the Cr versus Mg#, the highest Cr content belongs to sample 21.10 reflecting its high spinel proportion (0.9% of the whole rock) compared to other samples. The Co contents have a poor correlation partly because of some contamination during Parkinson's sample preparation.

Table 2-8: Whole rock major, minor and trace element compositions for the Choiseul peridotites.

	Choiseul peridotites (this study)				Choiseul peridotites (Parkinson's study)											
Samples	21.08	21.09	21.10	22.01	Ch 1	Ch 2	Ch 3	Ch 4	Ch 5	Ch 6	Ch 7A	Ch 7B	Ch 7C	Ch7 D	Ch 8	Ch 10
SiO_2	44.25	43.97	43.63	43.94	43.74	43.90	43.52	43.28	43.51	43.57	43.83	44.64	44.06	46.91	43.64	43.68
Al_2O_3	1.28	1.13	1.13	0.94	0.93	1.02	0.98	0.93	0.87	0.98	1.30	1.48	1.22	0.83	0.64	0.90
Fe_2O_3*	8.76	8.87	8.94	8.88	8.62	8.63	8.63	8.77	8.72	8.71	8.84	8.85	8.67	8.00	8.69	8.58
MnO	0.13	0.13	0.13	0.13	0.13	0.13	0.13	0.12	0.13	0.13	0.12	0.12	0.13	0.13	0.12	0.12
MgO	42.03	43.62	44.04	44.18	44.52	44.19	44.74	45.04	44.87	44.38	43.36	42.96	43.49	42.63	45.31	44.83
CaO	2.72	1.47	1.34	1.16	1.17	1.19	1.04	0.92	1.00	1.32	1.76	1.14	1.51	0.68	0.81	1.04
Na_2O	0.05	0.01	0.00	0.01	0.17	0.20	0.19	0.20	0.17	0.20	0.03	0.12	0.18	0.18	0.06	0.11
K_2O	0.00	0.00	0.00	0.00	0.00	0.00	0.00	0.01	0.00	0.02	0.00	0.00	0.00	0.00	0.00	0.00
TiO_2	0.01	0.01	0.01	0.01	0.02	0.02	0.02	0.01	0.01	0.01	0.02	0.01	0.01	0.01	0.01	0.00
P_2O_5	n.a.	n.a.	n.a.	n.a.	n.a.	n.a.	n.a.	n.a.	n.a.	n.a.	n.a.	n.a.	n.a.	n.a.	n.a.	n.a.
Cr_2O_3	0.45	0.45	0.48	0.42	0.36	0.41	0.43	0.37	0.38	0.38	0.43	0.36	0.41	0.36	0.41	0.40
NiO	0.30	0.30	0.31	0.31	0.34	0.33	0.33	0.33	0.33	0.32	0.31	0.30	0.32	0.28	0.32	0.32
S	0.03	0.03	0.01	0.02	0.00	0.00	0.00	0.01	0.00	0.00	0.00	0.01	0.00	0.00	0.00	0.01
LOI	10.27	7.90	2.27	6.68	1.26	3.97	2.34	2.09	2.69	3.88	0.00	0.47	0.26	0.52	3.04	1.13
Mg #	90.49	90.69	90.70	90.79	91.10	91.03	91.13	91.05	91.07	90.99	90.67	90.58	90.86	91.35	91.17	91.20
Li	n.a.	n.a.	n.a.	n.a.	1.85	1.71	2.35	2.23	2.24	2.28	n.a.	1.4	1.21	0.89	n.a.	1.27
Sc	12	13	13	12	14.1	13.5	13.3	12.2	12.3	14.6	16	17.1	15	13.1	12.4	14.2
Ti	49	45	45	30	30	50	38	33	34	34	48	49	45	30	38	44
V	41	40	45	33	46	46	42	37	38	45	52	59	49	41	34	42
Cr	2664	2642	3276	2442	2485	2773	2910	2530	2634	2593	2975	2438	2823	2481	2775	2716
Co	127	132	140	134	106	114	138	115	116	117	n.a.	117	104	96	n.a.	105
Ni	2090	2208	2302	2290	2667	2555	2563	2581	2572	2509	2456	2377	2502	2180	2516	2523
Cu	21	13	13	15	13	16	22	11	16	12	13	21	18	3	11	10
Zn	41	40	44	40	49	51	52	50	50	48	54	50	52	46	49	49
Ga	n.a.	n.a.	n.a.	n.a.	0.75	0.95	0.93	0.82	0.83	0.92	n.a.	1.36	1.01	0.94	n.a.	0.91
Rb	0.038	0.135	0.110	0.070	0.057	0.149	0.129	0.120	0.169	0.521	0.008	0.073	0.018	0.043	0.068	0.068
Sr	59.160	4.198	0.418	0.973	0.095	0.628	0.128	0.067	0.152	0.222	0.038	0.111	0.049	0.097	0.389	0.585
Y	0.143	0.138	0.132	0.137	0.204	0.209	0.153	0.129	0.132	0.218	0.367	0.243	0.287	0.088	0.064	0.177
Zr	0.041	0.021	0.021	0.048	0.149	0.232	0.139	0.129	0.106	0.163	0.162	0.128	0.111	0.338	0.159	0.116
Nb	0.007	0.003	0.005	0.009	0.007	0.013	0.016	0.013	0.015	0.022	0.004	0.022	0.004	0.004	0.005	0.004
Cs	0.002	0.011	0.008	0.008	0.006	0.014	0.009	0.009	0.016	0.041	0.001	0.016	0.001	0.004	0.009	0.008
Ba	0.335	0.370	0.275	0.436	0.566	0.243	0.132	0.116	0.146	0.179	0.016	0.165	0.126	0.154	0.317	0.313
La	0.004	0.005	0.003	0.009	0.037	0.029	0.017	0.048	0.023	0.027	0.002	0.055	0.011	0.011	0.007	0.020
Ce	0.004	0.021	0.003	0.014	0.038	0.064	0.034	0.032	0.046	0.055	0.003	0.060	0.021	0.021	0.010	0.044
Pr	0.000	0.002	0.001	0.003	0.004	0.006	0.003	0.002	0.003	0.006	0.000	0.005	0.002	0.002	0.001	0.003
Nd	0.002	0.007	0.002	0.007	0.015	0.027	0.009	0.008	0.013	0.020	0.001	0.018	0.007	0.005	0.003	0.010
Sm	0.003	0.004	0.003	0.007	bdl	bdl	0.002	bdl	bdl	0.004	0.001	0.003	bdl	bdl	0.001	bdl
Eu	0.001	0.002	0.001	0.002	0.001	0.001	bdl	0.000	0.001	0.001	0.001	0.000	0.000	bdl	0.000	0.001
Gd	0.007	0.008	0.007	0.007	0.005	0.008	0.003	0.003	0.005	0.008	0.006	0.007	0.008	0.002	0.001	0.006
Tb	0.002	0.002	0.002	0.002	0.002	0.003	0.001	0.001	0.001	0.002	bdl	0.002	0.003	0.001	bdl	0.002
Dy	0.023	0.021	0.021	0.019	0.014	0.021	0.014	0.009	0.011	0.022	0.029	0.023	0.028	0.007	0.005	0.018
Ho	0.007	0.006	0.006	0.007	0.005	0.007	0.005	0.004	0.004	0.008	bdl	0.009	0.009	0.003	0.002	0.006
Er	0.027	0.027	0.025	0.027	0.022	0.027	0.022	0.018	0.019	0.029	0.043	0.032	0.038	0.014	0.011	0.024
Yb	0.043	0.038	0.037	0.045	0.038	0.049	0.041	0.038	0.038	0.052	0.066	0.065	0.064	0.031	0.024	0.044
Lu	0.009	0.008	0.007	0.010	0.008	0.009	0.009	0.008	0.008	0.009	0.013	0.013	0.012	0.006	0.006	0.009
Hf	0.002	0.002	0.002	0.002	0.004	0.005	0.003	0.004	0.003	0.005	0.004	0.004	0.004	0.004	0.004	0.004
Ta	0.001	0.001	0.003	0.002	n.a.	n.a.	n.a.	n.a.	n.a.	n.a.	n.a.	n.a.	n.a.	n.a.	n.a.	n.a.
Pb	0.045	0.311	0.214	0.210	n.a.	n.a.	n.a.	n.a.	n.a.	n.a.	n.a.	n.a.	n.a.	n.a.	n.a.	n.a.
Th	0.001	0.006	0.001	0.001	0.003	0.004	0.005	0.004	0.006	0.015	0.004	0.008	0.002	0.001	0.006	0.003
U	0.235	0.031	0.004	0.012	0.001	0.001	0.001	0.001	0.002	0.008	0.000	0.001	0.001	0.001	0.002	0.002

*Total iron as Fe_2O_3

All major and minor elements are in wt %; all trace elements are in ppm. V, Cr, Co, Ni, Zn and Cu data were measured by XRF.

List of Abbreviations:

bdl: below detection limit; n.a.: not analysed

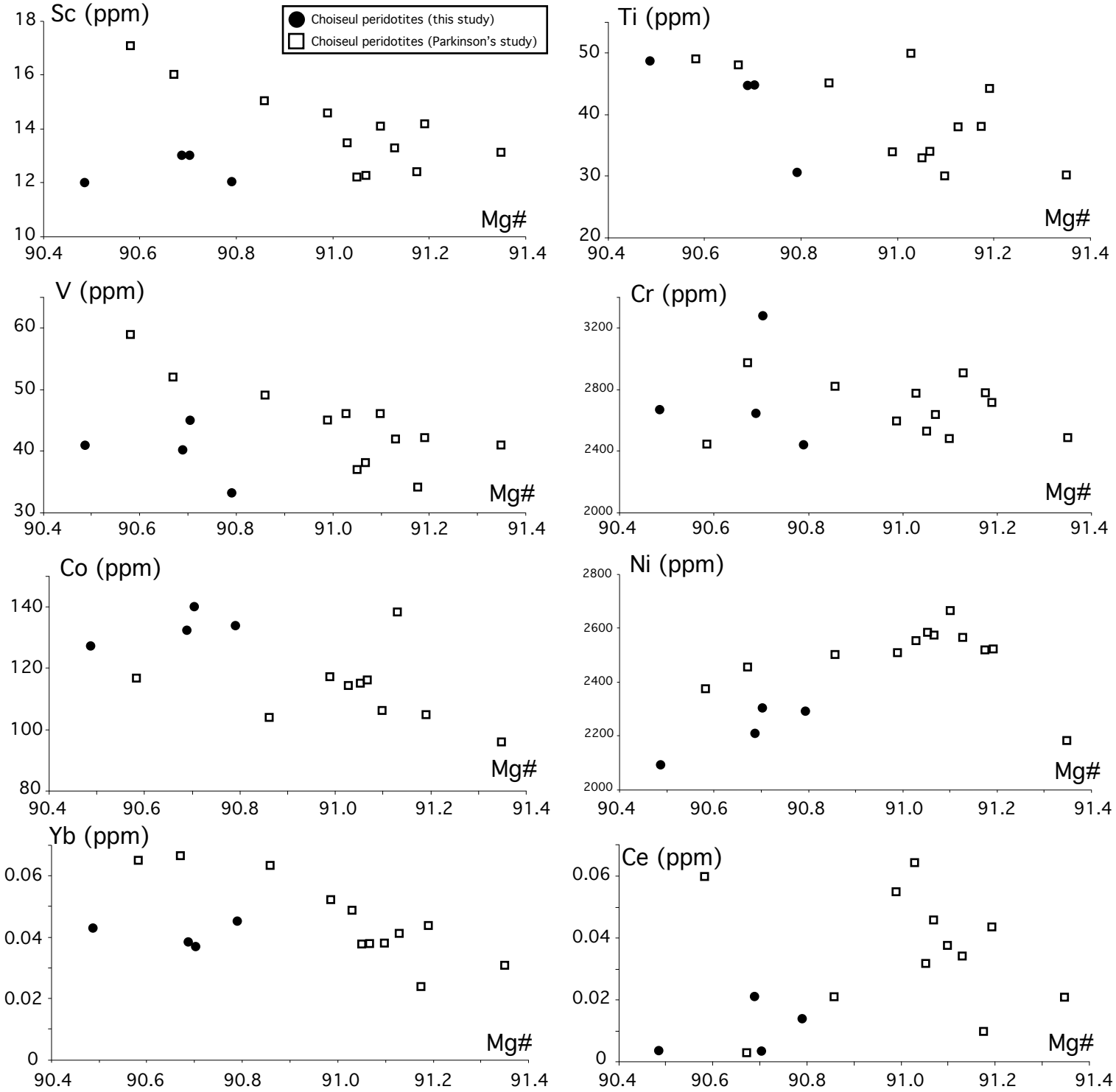

Fig. 2-7B: Plots of abundances of Sc, Ti, V, Cr, Co, Ni, Yb and Ce (ppm) against Mg#. The black dots define the data set of the Choiseul peridotites (this study) whereas the open squares refer to the dataset of Parkinson (pers. comm.) for the Choiseul peridotites.

6.2 Trace elements

Figure 2-8A shows the chondrite-normalised rare earth element (REE) abundances of all samples. The peridotites are all characterised by very low REE concentrations with heavy (H)REE ranging from 0.5 and 0.1 times chondrite, middle (M)REE concentrations < 0.1 times chondrite and light (L)REE concentrations between 0.01 and 0.25 times chondritic. The Choiseul peridotites have steep, linear, positive MREE-HREE profiles, which are similar to those of depleted abyssal peridotites or SSZ peridotites, and are indicative of high degrees of fractional melting (Pearce et al., 2000). The MREE-HREE gradients flatten out at Gd-Eu and then have flat to upward-inflected LREE patterns indicating a striking LREE enrichment giving a U-shaped aspect to the REE profiles. Although a cursory glance at the Figure 2-8A may suggest that the samples have negative Eu anomalies, in fact Eu is just the most depleted REE in the peridotites and is the most incompatible REE not to be enriched. The plot of Yb versus Mg# (Fig. 2-9) reveals that the Yb and more generally the HREE (not plotted here) have negative correlations with Mg# consistent with a residual origin for the peridotites. Moreover, Yb stays fairly constant with increasing LOI indicative of the HREEs low sensitivity to alteration (Fig. 2-9). In the plot of Ce versus LOI, no clear correlation can be distinguished suggesting that Ce enrichment is not due to alteration processes.

Primitive mantle-normalised multi-element diagrams of the Choiseul peridotites are presented in Figure 2-8B. These patterns are characterised by consistent positive Ti anomalies, variable negative Nb anomalies, strong large ion lithophile element (LILE) enrichments (Cs, Rb and Ba) and variable Pb and Sr positive anomalies. Ti is commonly enriched with respect to adjacent REE (Eu and Gd) (adjacent elements in terms of partitioning behaviour during melting of fertile peridotite), but slightly depleted relative to Er and Yb (the adjacent elements for melting of strongly residual peridotite). Nb has a variable negative anomaly in all samples even though there is some Nb contamination in all but two samples. The largest Nb anomalies are in the two samples milled in an agate TEMA. However, even in these samples, the Nb contents are elevated relative to its incompatibility.

The primitive mantle-normalised multi-element diagrams of the four samples of this study are marked by strong positive Sr anomalies relative to the neighbouring Pr and Nd. However the magnitude of this anomaly is variable in Parkinson's samples and can even be negative. Sample 21.08, which is the most altered sample (LOI > 10 wt %), also has high Sr and Ca contents (Fig. 2-7A and Fig. 2-9) typical of carbonate addition. Sample 21.09 is characterised by the presence of calcite veins explaining its high Sr content but not its CaO content which is very similar to other peridotites. This suggests that the high Sr content is not entirely due to carbonate addition and may be related to low temperature seafloor alteration. However, even if a weak correlation exists between the Sr and LOI for the samples moderately affected by alteration (Fig. 2-9), the Sr positive anomalies relative to neighbouring REE (Pr and Nd) persist in unaltered samples such as Ch7A and Ch10.

Striking positive Pb anomalies with respect to its adjacent REE (Ce and Pr) characterise the Choiseul peridotites. It should be noted that Pb was not measured in Parkinson's samples. The Sr and Pb anomalies give a spiked pattern on the left hand side of the multi-

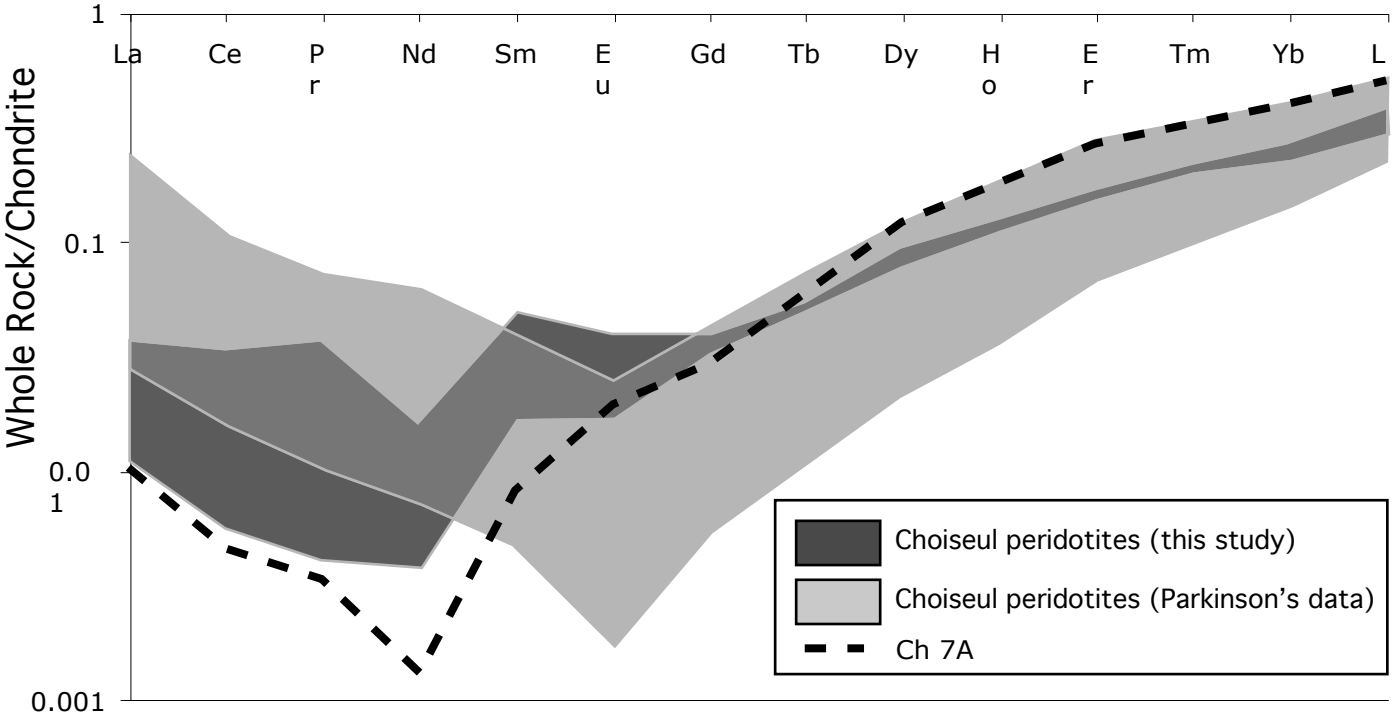

Fig. 2-8A: Chondrite-normalised whole rock REE patterns for the representative Choiseul peridotites. Chondrite normalising values are from Sun and McDonough (1989).

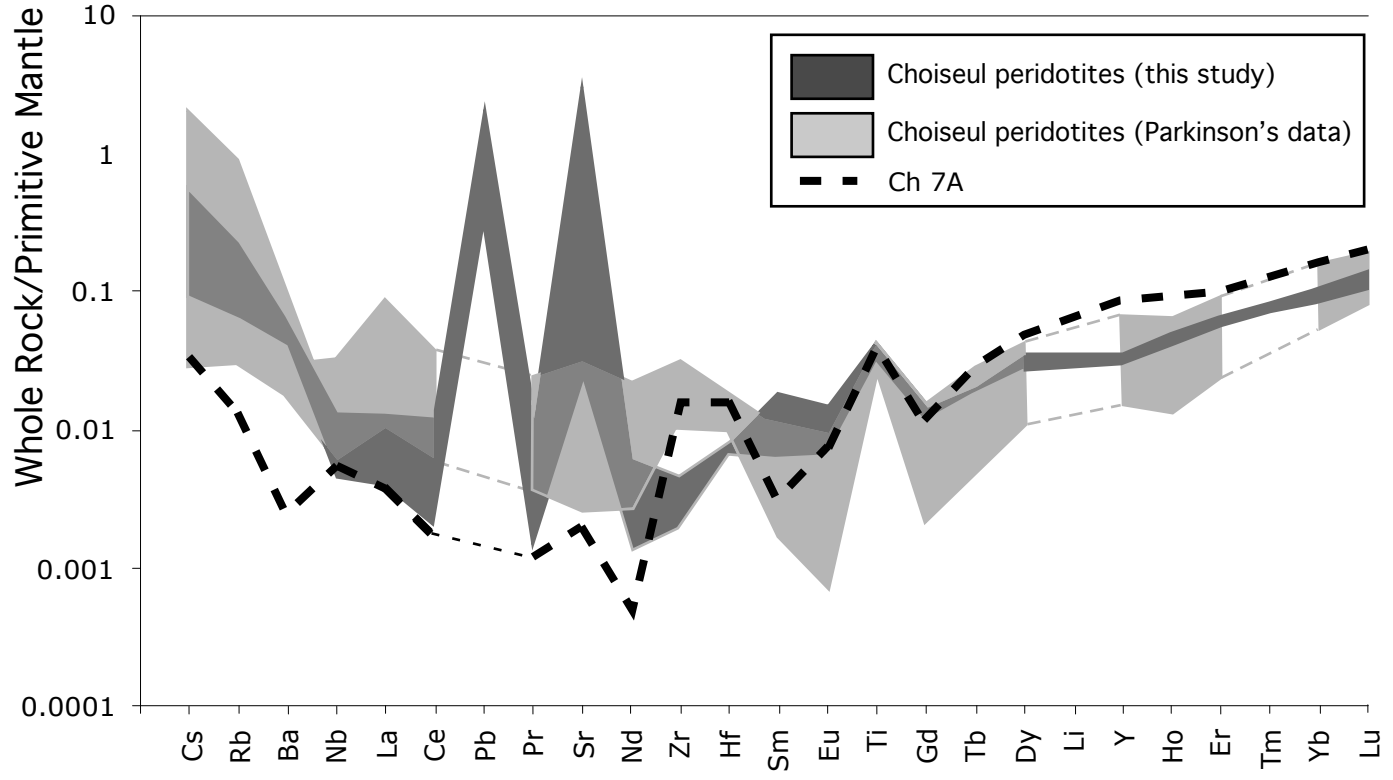

Fig. 2-8B: Primitive mantle-normalised whole rock multi-element patterns for the representative Choiseul peridotites. Primitive mantle normalising values are from Sun and McDonough (1989).

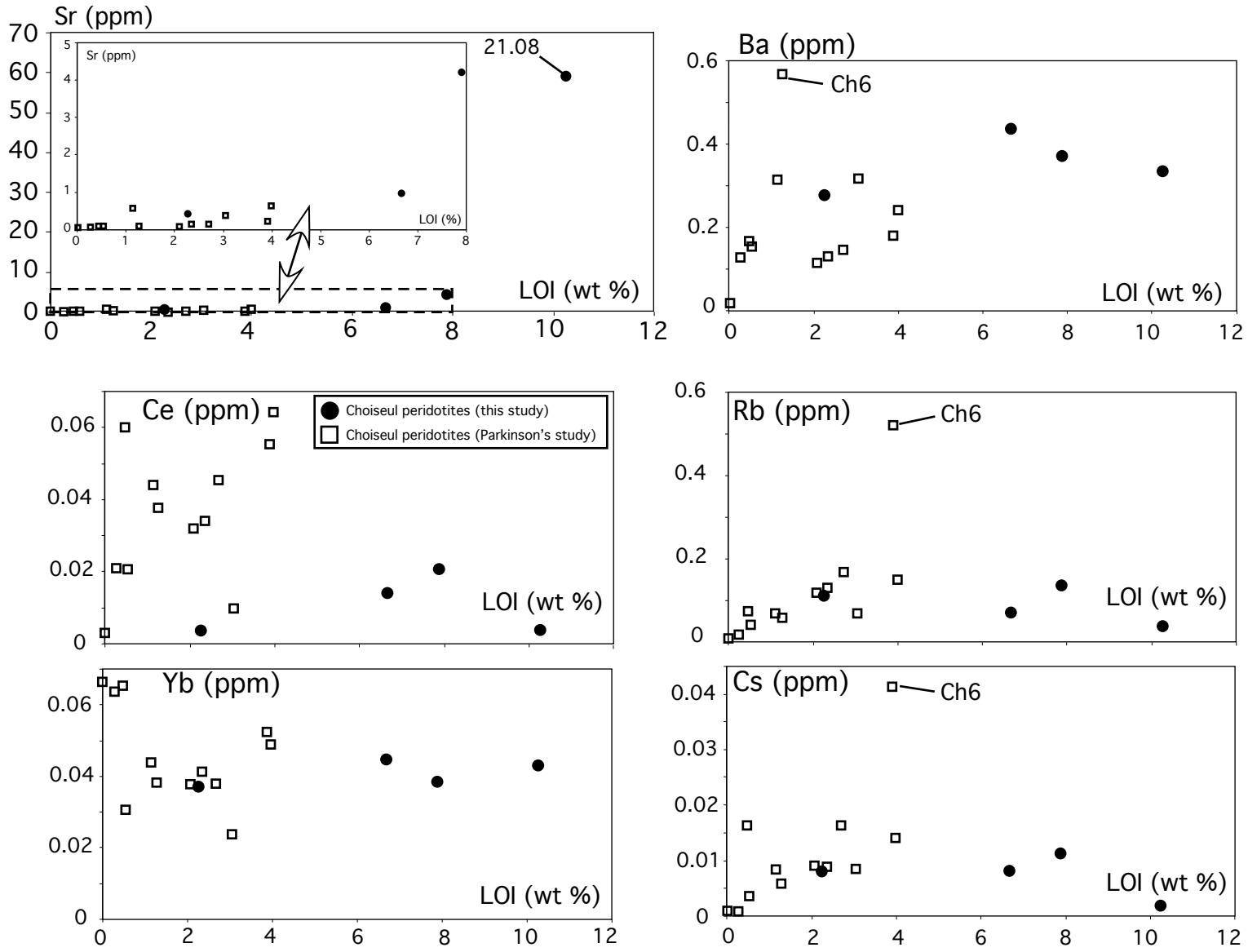

Fig. 2-9: Plots of various elements against loss on ignition (LOI) (wt %). Sr, Ba, Ce, Rb, Yb and Cs are in ppm. The black dots define the data set of the Choiseul peridotites (this study) whereas the open squares refer to the dataset of Parkinson (pers. comm.) for the Choiseul peridotites.

element diagrams. The Choiseul peridotites all show LILE enrichments (Cs, Rb and Ba) given the multi-elements plots the general "U-shape" (Fig. 2-8B). Plots of LILE against LOI (Fig. 2-9) reveal positive correlations for Ba. However, no convincing correlations exist between Cs, Rb, and LOI, with the most altered samples showing relative low Cs and Rb contents. In those plots (Fig. 2-9), Ch6 has consistently higher LILE contents compared to other samples with similar degrees of LOI, reflecting its high modal proportions of amphibole and chlorite. For sample Ch7A, which is the totally unaltered sample, Sr, Ba, Rb, and Cs contents are elevated over and above that expected if the element contents were controlled uniquely by melt depletion. Although some modifications of the LILE, Sr and Pb have occurred during low temperature alteration, the general "U-shape" with spiked pattern of the multi-element diagram is representative of primary trace element patterns in these peridotites.

7 CLINOPYROXENE GEOCHEMISTRY

In situ trace element analyses of clinopyroxene were carried out using the LA ICP-MS and are presented in Table 2-9. The chondrite-normalised REE diagrams of the clinopyroxene (Fig. 2-10A) are similar in all samples. As expected, the REE contents of the clinopyroxene are very low. All of the clinopyroxene has similar HREE contents to diopside from the most depleted abyssal peridotites (Johnson et al., 1990) but have more fractionated REE with $[Nd/Yb]_N$ ratios of 0.0015-0.0050 compared with 0.008-0.075 for abyssal peridotites. Whereas all the REE plots reveal sloping HREE to MREE profiles, the patterns from Dy to Sm are remarkably steep. The concentrations in LREE (La, Ce and Pr) are below the detection limit.

The primitive mantle-normalised multi-element profiles for the clinopyroxene are presented in Figure 2-10B. The patterns are marked by large Sr and Pb positive spikes. Sr concentrations in the clinopyroxene largely exceed those in abyssal peridotites with similar modal clinopyroxene and/or degrees of alteration whereas Pb is not commonly measured in clinopyroxene of the abyssal peridotites. This implies that the positive Sr and Pb anomalies in the bulk-rock multi-element profiles are in part primary although from mass-balance arguments, a component must be related to alteration. The clinopyroxene from the Choiseul peridotites is characterised by a variable LILE (Cs, Rb and Ba) enrichment that is slightly lower than the LILE enrichment in the whole rock (Fig. 2-8B). The negative Ba anomaly (relative to Rb), which is a common feature in most of the whole rocks, also manifests itself in the clinopyroxene data. This indicates that the whole rock data for these elements is representative of the primary composition of the peridotites. Nb concentrations in the clinopyroxene are elevated over and above the Nb contents in the whole rock (Fig. 2-8B). All of the clinopyroxene has similar positive Ti anomalies relative to adjacent Eu and Ti comparable with anomalies described for the whole rock data.

Table 2-9: Representative trace element analyses of clinopyroxene measured by LA ICP-MS for the Choiseul peridotites.

	Choiseul peridotites (this study)					Choiseul peridotites (Parkinson's sutdy)					
Sample	21.10	21.10	21.10	Ch10	Ch10	Ch 1	Ch 2	Ch 7a	Ch 7a	Ch 7a	Ch 10
Analysis	D1	D2	D8	M1	M3	Cpx 1-a	Cpx 2-a	Cpx 1-a	Cpx 1-c	Cpx 1-a	Cpx 3-a
Li	2.05	bdl	8.25	2.44	bdl	8.46	6.49	7.71	4.66	6.2	3.17
Sc	n.a.	n.a.	n.a.	n.a.	n.a.	54	60	57	65	52	57
Ti	384	371	384	321	338	n.a.	n.a.	n.a.	n.a.	n.a.	n.a.
V	n.a.	n.a.	n.a.	n.a.	n.a.	239	213	264	229	250	245
Ga	n.a.	n.a.	n.a.	n.a.	n.a.	2.71	1.63	4.44	1.81	3.63	3.44
B	8.48	8.67	8.81	10.02	10.56	n.a.	n.a.	n.a.	n.a.	n.a.	n.a.
Rb	0.0044	bdl	0.0355	0.0501	0.0638	0.105	0.119	0.087	0.08		0.064
Sr	0.0493	0.0267	0.0850	0.9409	2.1453	0.153	0.993	0.087	0.148	0.026	1.286
Y	3.6113	3.4240	3.3757	2.4704	2.3878	2.666	2.571	4.159	4.598	3.627	2.812
Zr	0.0938	0.0928	0.1101	0.0943	0.0944	0.026	0.043	bdl	0.062	0.017	0.017
Nb	0.0520	0.0536	0.0637	0.0668	0.0581	0.01	0.009	0.061	bdl	bdl	bdl
Cs	bdl	bdl	0.0020	0.0039	0.0083	n.a.	n.a.	n.a.	n.a.	n.a.	n.a.
Ba	0.0277	0.0029	0.0707	0.0977	1.1717	0.174	0.301	0.115	0.331	0.02	0.179
La	bdl	bdl	bdl	bdl	bdl	bdl	bdl	bdl	bdl	bdl	bdl
Ce	bdl	bdl	bdl	bdl	bdl	bdl	bdl	bdl	bdl	bdl	bdl
Pr	bdl	bdl	bdl	bdl	bdl	n.a.	n.a.	n.a.	n.a.	n.a.	n.a.
Nd	0.0036	0.0032	0.0022	0.0034	0.0063	bdl	bdl	bdl	bdl	bdl	bdl
Sm	0.0114	0.0126	0.0148	0.0088	0.0113	0.0035	0.0054	0.0308	0.0148		0.0174
Eu	0.0096	0.0095	0.0097	0.0100	0.0079	0.0053	0.0037	0.0261	0.0207	0.018	0.0152
Gd	0.1259	0.1189	0.1153	0.1121	0.0982	0.068	0.0601	0.1704	0.1845	0.1512	0.1047
Dy	0.4908	0.4715	0.4561	0.3581	0.3251	0.3082	0.3041	0.5712	0.6421	0.4718	0.3721
Ho	0.1446	0.1267	0.1290	0.0925	0.0936	n.a.	n.a.	n.a.	n.a.	n.a.	n.a.
Er	0.4964	0.4827	0.4583	0.3463	0.3343	0.3842	0.3594	0.5497	0.5974	0.4656	0.3678
Tm	0.0829	0.0771	0.0809	0.0546	0.0515	n.a.	n.a.	n.a.	n.a.	n.a.	n.a.
Yb	0.5942	0.5526	0.5408	0.4100	0.4163	0.4813	0.4614	0.6432	0.6716	0.5456	0.4568
Lu	0.0900	0.0826	0.0799	0.0693	0.0627	0.0786	0.0716	0.0956	0.1062	0.0809	0.0723
Hf	bdl	0.0042	0.0042	0.0037	0.0058	bdl	bdl	bdl	bdl	bdl	bdl
Pb	0.0251	0.0084	0.0157	0.0088	0.0177	bdl	bdl	bdl	bdl	bdl	bdl

All values are in ppm

List of Abbreviations:

n.a.=not analysed; bdl=below detection limit

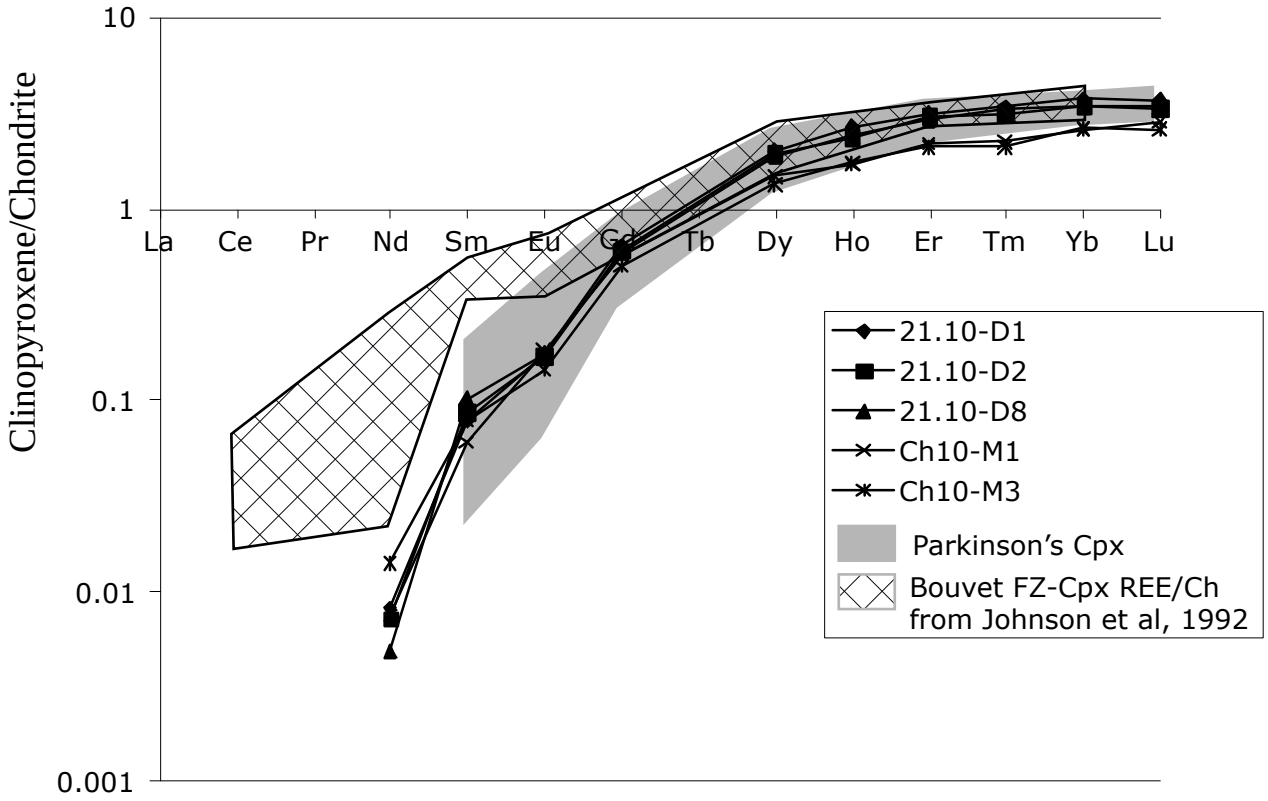

Fig. 2-10A: Chondrite-normalised REE diagrams for the clinopyroxenes from representative Choiseul peridotites. Reference is made to clinopyroxene (cpx) REE data from the Bouvet Fracture Zone (FZ) peridotites in Johnson et al., 1992. Chondrite normalising values are from Sun and McDonough (1989).

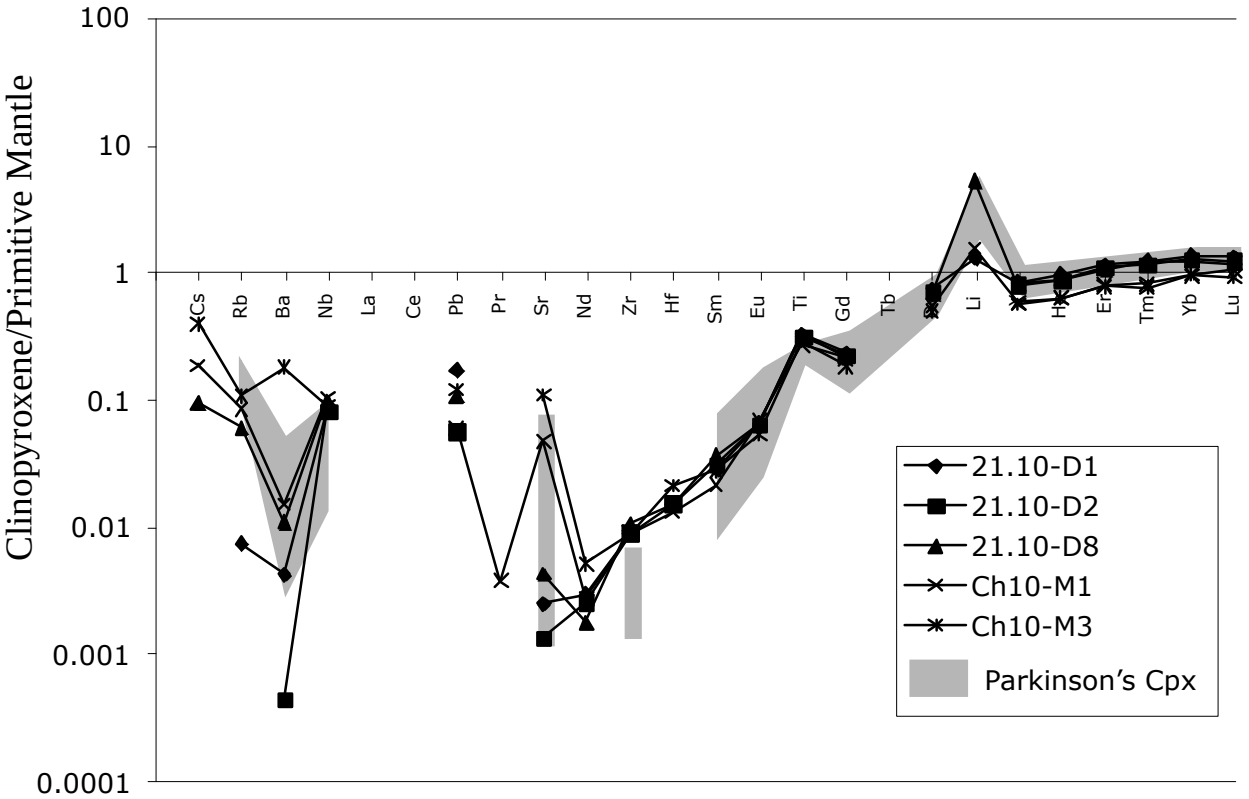

Fig. 2-10B: Primitive Mantle-normalised REE diagrams for the clinopyroxenes from representative Choiseul peridotites. Primitive mantle normalising values are from Sun and McDonough (1989).

8 GEOTHERMOBAROMETRY CHARACTERISTICS

8.1 Temperature

Temperatures calculated with "conventional" geothermometers record aspects of their solidus cooling history. Thermometers using the compositions of coexisting minerals were based on the two pyroxene thermometry of Wells (1977), Bertrand and Mercier (1985/86) and Brey and Köhler (1990), on the olivine and spinel Fe-Mg exchange thermometry of Balhaus et al. (1991) and on the Ca-in-Orthopyroxene thermometry of Brey and Köhler (1990). A wide range of temperatures calculated using these geothermometers is presented in Table 2-10 and Figure 2-11.

Temperatures calculated for coexisting olivine and spinel using Balhaus thermometer average 733°C, slightly lower than average temperature calculated for abyssal peridotites (~806°C) but greater than average temperature of 647°C calculated for the SSZ peridotites (Parkinson and Pearce, 1998). The low temperatures recorded by these peridotites compared to abyssal peridotites underline why the Choiseul peridotites plot on the right of the abyssal peridotite array in the Cr# versus Mg# spinel diagram because lower temperature isopleths extend to lower Mg# of spinel. The lowest temperature calculated using the Ballhaus thermometer belongs to Ch6, which contains a significant amount of amphibole and chlorite.

Fe-Mg exchange two-pyroxene thermometers give relatively homogeneous temperatures when compared to each other (Fig. 2-11). However, these thermometers yield a broad range in temperatures of equilibration between 652°C and 1032°C. The wide range in these samples results from various degrees of deformation and grain size variation within the samples. Deformation triggers sub-solidus re-equilibration increasing diffusion rates (Kramer and Seifert, 1991) while grain size reduction aids re-equilibration to persist to lower temperatures. Conversely, coarse-grained samples (such as C10) generally record higher temperatures (>1000°C). The samples containing amphibole and chlorite generally record the lowest temperatures while fresh peridotites have been re-equilibrated at 880°C on average. However, the occurrence of exsolution textures in porphyroclastic pyroxenes indicates higher temperatures of formation (> 1050°C).

8.2 Pressure

The only barometer available for spinel peridotite is the Ca-in-olivine barometer (Köhler and Brey, 1990). For the Choiseul peridotites, Ca is below the detection limit of ~45ppm by wave length dispersive EMP methods, so no pressures can be assessed. Moreover, Ca redistribution into clinopyroxene during sub-solidus cooling overprints any pressure information that can be extracted. The absence of plagioclase in the peridotite indicates that the recrystallisation must have occurred at $P > 0.6$ GPa (Seyler and Mattson, 1989). However the presence of spinel and the fact that garnet has not been found suggests a $P < 2.2$ GPa within the stability field of spinel.

Table 2-10: Temperatures (°C) calculated using a variety of geothermometers for the Choiseul peridotites.

	Samples	Wells	B&M	B&K	Ca in Opx	Ballhaus
(a)	21.09	878	813	732	1056	783
	21.10	900	853	777	926	807
	Ch10	990	1032	964	1086	722
(b)	Ch1	1001	1016	951	792	702
	Ch2	911	890	816	910	737
	Ch3	926	899	827	809	698
	Ch4	855	840	764	825	765
	Ch5	870	818	739	920	728
	Ch6	825	791	709	873	605
	Ch7A	903	901	828	907	736
	Ch7B	914	922	848	878	681
	Ch7C	871	880	806	765	721
	Ch7D	998	989	925	776	681
	Ch8	906	741	652	921	761
	Ch10	941	953	884	1004	763

(a): Choiseul peridotites (this study); (b): Choiseul peridotites (Parkinson's study)
Two-pyroxene thermometers of Well (1977), Brey and Kölher (1990) (BNK) and Bertrand and Mercier (1985/86) (B&M).
Ca-in-Opx thermometer of Brey and Köhler (1990). Fe-Mg exchange between olivine and spinel (Balhaus et al, 1991).

Table 2-11: Calculated oxygen fugacities using the Nell-Wood calibration for the Choiseul peridotites.

	Samples	Olivine Fo	Spinel (Cr#) Cr#	Spinel Fe3+/Fetot	Oxygen Fugacity Dlog FMQ)	Temperature T(°C)
(a)	21.09	0.900	0.383	0.107	-0.71	783
	21.10	0.895	0.404	0.118	-0.61	807
	Ch10	0.909	0.428	0.076	-1.04	722
(b)	Ch1	0.907	0.442	0.136	0.23	702
	Ch2	0.908	0.440	0.088	-0.83	737
	Ch3	0.908	0.404	0.119	-0.05	698
	Ch4	0.904	0.477	0.088	-0.94	765
	Ch5	0.907	0.416	0.104	-0.47	728
	Ch6	0.915	0.389	0.170	1.26	605
	Ch7A	0.904	0.346	0.080	-1.07	736
	Ch7B	0.903	0.351	0.118	-0.01	681
	Ch7C	0.907	0.391	0.123	-0.11	721
	Ch7D	0.916	0.584	0.124	0.33	681
	Ch8	0.908	0.580	0.111	-0.34	761
	Ch10	0.914	0.438	0.105	-0.58	763

(a): Choiseul peridotites (this study); (b): Choiseul peridotites (Parkinson's study)
Temperatures calculated using the olivine-spinel thermometer of Balhaus et al, 1991.

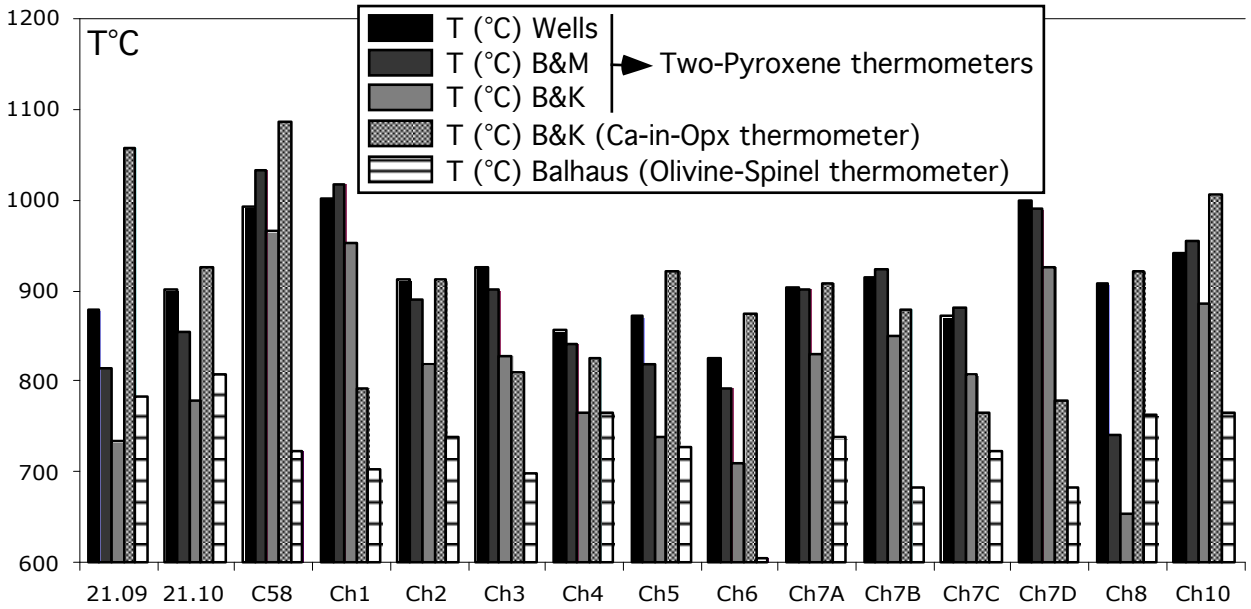

Fig. 2-11: Plots of representative temperatures (°C) calculated using a variety of geothermometers for the Choiseul Peridotites.
Two-pyroxene thermometers of Wells (1977), Bertrand and Mercier (B&M) (1985/86) and Brey and Kohler (B&K) (1990). Ca-in-Opx thermometer of Brey and Kohler (B&K) (1990). Fe-Mg exchange between olivine and spinel (Balhaus et al., 1991).

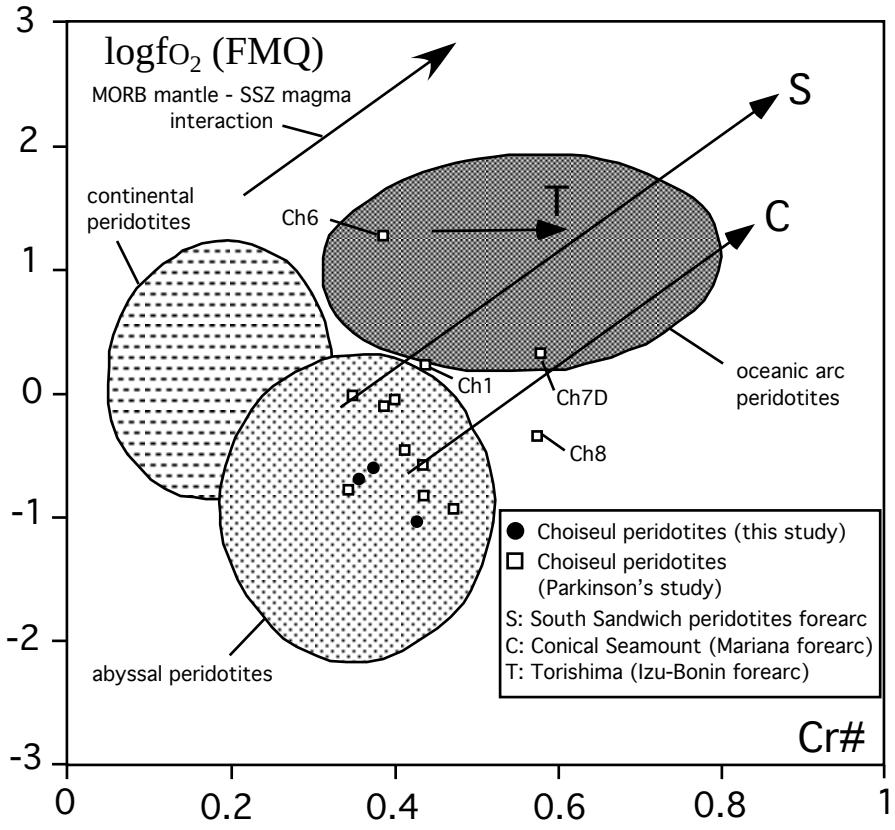

Fig. 2-12: Plot of $\log fO_2$ (FMQ) against Cr# of spinel for the Choiseul peridotites. Fields for abyssal peridotites, arc peridotites and continental peridotites are after Pearce et al., 2000. Reference is made to peridotite data from Conical Seamount (C) in Mariana Forearc and Torishima Forearc Seamount (T) in the Izu-Bonin forearc (Parkinson et al., 1998).

9 METAMORPHIC HISTORY

The Choiseul peridotites have undergone substantial sub-solidus re-equilibration related to a slow transport of these peridotites to the surface. This exhumation is recorded in minor retrograde assemblages.

Two types of amphibole have been found in the Choiseul peridotites. Magnesio-hornblende blebs occur mainly within clinopyroxene in the very fresh protogranular samples (i.e. C10). The flame-shaped magnesio-hornblende is generally very small (~ 10μm in length) but highly concentrated within the clinopyroxene, giving the crystal a poikilitic aspect (Fig. 2-2C). This type of amphibole is interpreted to be the high temperature alteration product of a hydrous fluid interaction with the clinopyroxene in the upper amphibolite facies, between the pyroxene breakdown (~825°C) and the upper limit of hornblende stability (>600°C).

Tremolite is a common phase in some peridotites but rarely exceeds 1% of the mode with the exception of Ch6 and Ch7D. Two types of tremolite are found. The first type is formed as an interstitial phase rimming the clinopyroxene (Fig. 2-2A and Fig. 2-2C) or distributed along the cleavage of orthopyroxene porphyroclasts replacing exsolved clinopyroxene. The relatively high Tschermak's substitution ($X_{Al,M1} = 0.185$) for this type of tremolite is consistent with formation in middle amphibole facies. This type of tremolite is believed to be of hydrothermal origin resulting from the hydration of the clinopyroxene (Kimball, 1985), according to the reaction:

$$5\ Mg_2Si_2O_6 + 4\ CaMgSi_2O_6 + 2\ H_2O = 2\ Ca_2Mg_5Si_8O_{22}(OH)_2 + 2\ Mg_2SiO_4$$

The second type of tremolite is dispersed within the peridotite matrix and frequently is associated with serpentine. This type of tremolite has limited Tschermak's substitution and is considered to have crystallised in greenschist and lower amphibole facies (Will et al., 1990).

Chlorite develops both on the rims of spinel (Fig. 2-2E) and within the olivine matrix. Chlorite forms in the greenschist facies by the reaction:

$$Mg_2SiO_6 + + MgAl_2O_4 + Mg_2SiO_4 + 4\ H_2O = Mg_5Al_2Si_3O_{10}(OH)_8$$

The most aluminous chlorite in the Choiseul peridotites has $X_{Al,M1} > 0.6$, which is higher than $X_{Al,M1} = 0.46$ calculated by Jenkins and Chernosky (1986) and considered to be the transition from "low grade" to "high grade" chlorite in ultramafic rocks (Will et al., 1990). The general decrease in $X_{Al,M1}$ from chlorite close to spinel to matrix chlorite can be interpreted as reflecting a decrease in metamorphic grade.

Serpentine is the product of hydration of olivine and can be found occasionally in the most altered samples. In these samples, veins of lizardite and chrysotile occur frequently (Fig. 3D), but no high temperature serpentine polymorph of antigorite has been found. In the fresh samples, serpentinisation forming lizardite is restricted to weathered surfaces.

10 OXYGEN FUGACITY

Oxygen fugacities (fO_2s) were determined using the methods of Nell and Wood (1991) and Balhaus et al. (1991), calibrated on the reaction:

$$6\ Fe_2SiO_4 + O_2 = 3\ Fe_2SiO_2O_6 + 2\ Fe_3O_4$$

These calibrations give fO_2s within the standards errors of 0.2-0.3 $\log_{10}$ units of each other, and are well suited to spinel peridotite containing Cr-rich spinel. Calculation depends on accurate analysis of the ferric ion content of spinel achieved during this study by the same method as Parkinson and Arculus (1999). Results, given in Table 2-11, are presented relative to the fayalite-magnetite-quartz (FMQ) buffer [$\Delta\log fO_2$(FMQ)] at the given temperature and pressure (in this case P = 1GPa).
Calculated fO_2s range over two $\log_{10}$ units from 1.04 units below to 1.26 log units above the FMQ buffer (Fig. 2-12). The bulk of the data average 0.31 $\log_{10}$ units below the FMQ buffer, indicating that Choiseul peridotites have an origin from a reduced environment. The most oxidized peridotite (Ch6) is the one, which has undergone metamorphism with introduction of water at high temperatures forming amphibole and chlorite.
Figure 2-12 shows a plot of $\Delta\log fO_2$(FMQ) against Cr# in spinel for the Choiseul peridotites. Fields of abyssal peridotites, continental peridotites and oceanic arc peridotites are after Parkinson et al. (1998) and Parkinson et al. (1999). The reference data from the Izu-Bonin and Mariana forearcs are from Parkinson et al. (1998) and Pearce et al. (2000). In this plot, it is worth noting the lack of correlation between $\Delta\log fO_2$(FMQ) and Cr# (spinel). It is also evident that the Choiseul data overlap the middle range for the abyssal peridotites with the exception of four samples Ch1, Ch6 Ch7A and Ch8. Three samples (Ch1, Ch7A an Ch6) have similar data to SSZ peridotites whereas sample Ch8 plots in between the abyssal peridotite and oceanic arc peridotite fields having high Cr# content in spinel.

11 DISCUSSION

11.1 Choiseul peridotites as residues of melting

From their modal mineralogy (Table 2-1), it is clear that the Choiseul peridotites are refractory. The predominant mantle rock type is harzburgite, dominated by olivine and orthopyroxene, and affected by variable degrees of deformation. To assess the degree of depletion for these peridotites, the geochemistry of clinopyroxene is typically used (Fisher et al., 1984). During partial melting in the spinel facies, clinopyroxene is rapidly consumed (Jaques and Green, 1980). As an indication, 15% of modal clinopyroxene remains in a fertile (unmelted peridotite) whereas after ~ 25 melting, the clinopyroxene phase is completely eliminated (Parkinson et al., 1998). In the Choiseul peridotites, clinopyroxene only occurs in small proportions (3-7 % modal proportion). Parkinson et al (1998) argue that clinopyroxene may persist to slightly higher degrees of melting if partial melting commences in the garnet field as it is a reaction product when garnet

breaks down to spinel. According to experimental results (Gaetani and Grove, 1998), clinopyroxene can also endure higher degree of partial melting during hydrous melting of a spinel peridotite. However the low clinopyroxene content of these peridotites is a strong indication that these harzburgites are very depleted. The porphyroclastic textures of some samples and the irregular shape of spinels, further indicate an origin as residual mantle that has undergone high-temperature deformation (Ohara et al., 2002).

Based on their geochemistry, the Choiseul peridotites are consistent with a residual origin. Mg# is negatively correlated with major oxides such as SiO_2, Al_2O_3, and total iron as Fe_2O_3, and some trace elements (Sc, V and Cu) (Fig. 2-7A and Fig. 2-7B). Ni, which is a compatible element, is positively correlated with Mg# (Fig. 2-7B). Similar correlations have been documented in other peridotite suites (Frey et al., 1985; Parkinson and Pearce, 1998; Quick, 1981; Sinigoi et al., 1980) and have been interpreted to result from variable degrees of partial melting of more fertile lherzolite. However, varying modal contents of minerals with same composition can also explain these correlations in element-MgO plots (Parkinson et al., 1998). The plots of Cr# of spinel versus Al_2O_3 and Yb contents in the whole rocks (Fig. 2-13) show good negative correlations between these elements indicating that variation in major element chemistry reflects varying degrees of melting and/or reaction rather than a difference in modal mineralogy.

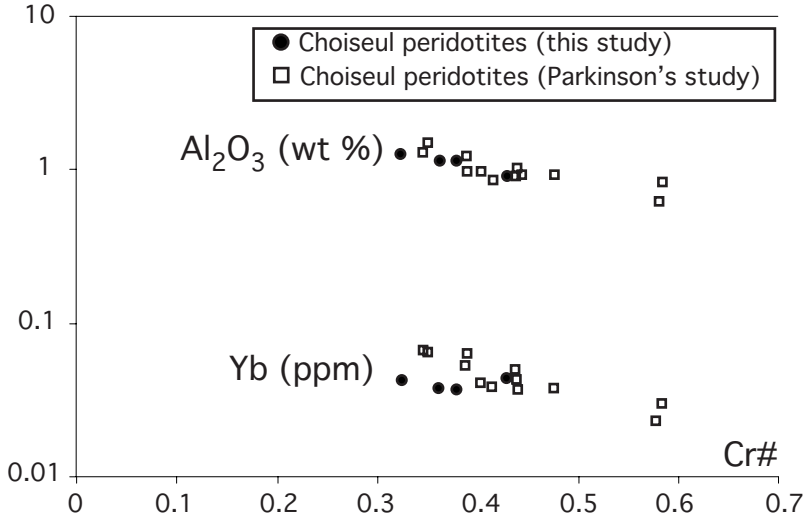

Fig. 2-13: Plots of Cr# of spinel against Al_2O_3 (wt%) and Yb (ppm) contents in the whole rock of the Choiseul peridotites.

Mineral composition gives further information on the melting process. The Fo content is a measure of total degree of melting as water does not affect the olivine-melt equilibria (Gaetani & Grove, 1998). The high Fo contents of olivine from the Choiseul peridotites (Table 2-2) suggest a high degree of melting. As melting proceeds, Mg# of pyroxene and Cr# of spinel increase whereas Al_2O_3 contents of spinel and pyroxene decrease. For the Choiseul peridotites, the pyroxenes are high magnesium (Mg# > 0.90) but low Al_2O_3 (< 4.00 wt %) whereas spinel has relatively high Cr#; all of these characteristics are indicative of a high degree of melting.

In summary, the petrological, mineralogical and geochemical characteristics of the Choiseul peridotites are consistent with an origin as a residual mantle.

11.2 Partial melting characteristics

The plot of spinel Cr# against olivine Mg# (Fig. 2-3) includes the spinel-lherzolite melting curve of Arai (1994). In this plot, all samples plot well within the OSMA array and lie along the melting trend between the values of 15% and 30% of partial melting. Most of the samples display high degrees of partial melting from 15 to 20 % with the exception of two samples (Ch7D and Ch8).
Figure 2-14 represents the diagram of the Cr# versus TiO_2 (wt %) in spinel in which a partial melting trend has been superimposed for ascertaining the degree of partial melting (Pearce et al., 2000). Low TiO_2 contents and moderate Cr# characterise most of the Choiseul spinel. The spinel lies close to the melting curve between 15% and 20%, consistent with the range of degree of partial melting assessed from the plot of spinel Cr# against olivine Mg#. However, it is not possible to confirm the high degrees of partial melting related to Ch7D and Ch8 because Parkinson (pers. comm.) did not measure Ti contents for these samples.
The degree of melting can also be quantified using the Ti-Yb covariations in whole rock mantle peridotites (Fig. 2-15). In this plot, the Choiseul samples lie along the theoretical fractional spinel lherzolite melting trends between the Izu-Bonin forearc samples (~ 23% partial melting; $\phi = 0$) and South Sandwich forearc samples (~ 18% partial melting; $\phi = 1$) (Pearce et al., 2000).
Modeling trace element concentrations in whole rock and clinopyroxene is a less ambiguous method for further elucidating the partial melting history of peridotites. These modeling calculations were carried out by Parkinson (pers. comm.) on some of the Choiseul peridotites. The rationale for the modeling is to match HREE-MREE section of the REE patterns as the MREE and HREE abundances in both clinopyroxene and whole rock are assumed to be unaffected by processes (i.e., metasomatism) other than melting. Fractional and batch melting were both calculated in the spinel facies for data comparison. Results of the melting modeling initiated in the garnet facies and followed by melting in the spinel facies are presented in Figure 2-16.
The modeling of the partial melting shows some interesting aspects about the Choiseul peridotites:

- Modeling parameters based on the clinopyroxene and whole rock REE calculations are very similar, signifying that clinopyroxene data is a good proxy for the whole data in term of REE;
- Steep HREE-MREE slope of the patterns is consistent with near-fractional melting rather than batch melting;
- LREE enrichment in whole rocks cannot be explained by melting modeling
- The overall amount partial melting varies only from 18-22%;
- The amount of melting in the garnet facies ranges from 1-7% with a lower amount of melting in the garnet facies correlating with a greater amount of partial melting in the spinel facies;
- The more depleted the peridotite, the less melting in the garnet facies is required;
- Less than 0.5% porosities are considered to illustrate the data.

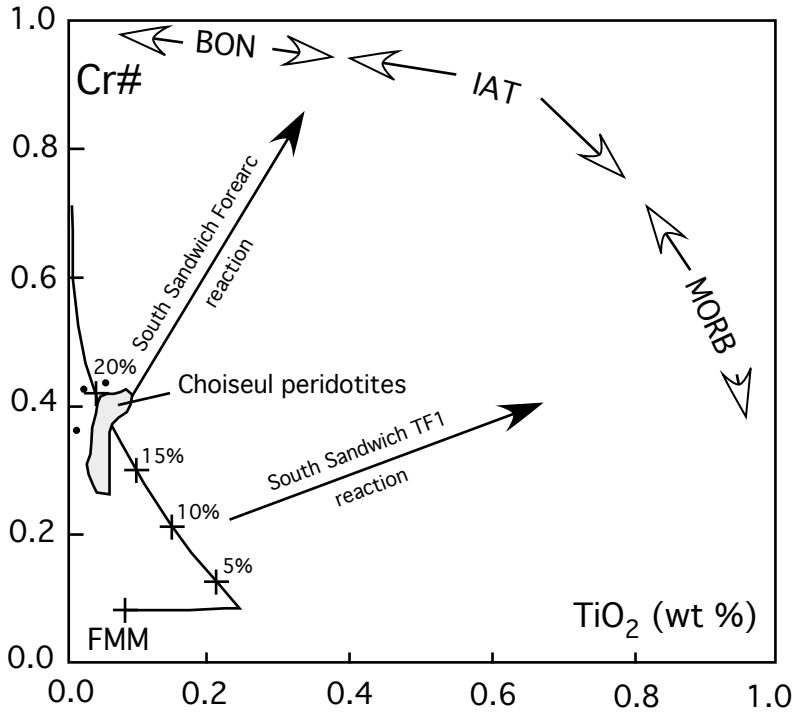

Fig. 2.14: Plot of Cr# against TiO_2 (wt %) for representative spinel of the Choiseul peridotites. Abbreviations are: FMM=Fertile MORB Mantle; BON=bonitites; IAT=island arc tholeiites; MORB: mid-ocean-ridge basalts.
Partial melting trends are after Pearce and al., 2000 and are annotated according to degree of melting. The South Sandwich Forearc reaction and the South Sandwich TF1 forearc are from Pearce et al., 2000 The TF1 peridotites result from the interaction between a relatively undepleted abyssal peridotite and a magma of MORB or MORB-IAT whereas the Forearc peridotites are explained by interaction of a harzburgite residual magma with a magma of depleted island arc tholeiite (BON).

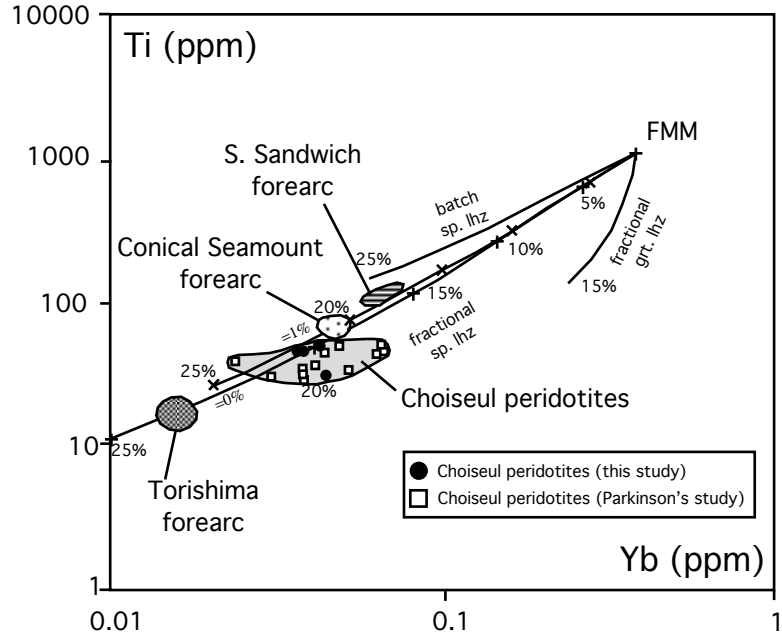

Fig. 2-15: Assessing the degrees of melting using Ti-Yb covariations in the Choiseul peridotites. Degrees of melting are annotated in %. FMM= Fertile MORB Mantle.
Partial melting trends after Pearce et al., 2000 using the coefficients of Parkinson and Pearce (1998). Peridotites from the Torishima forearc seamount, the Conical Seamount (Parkinson et al., 1998) and the South Sandwich forearc are shown for reference .

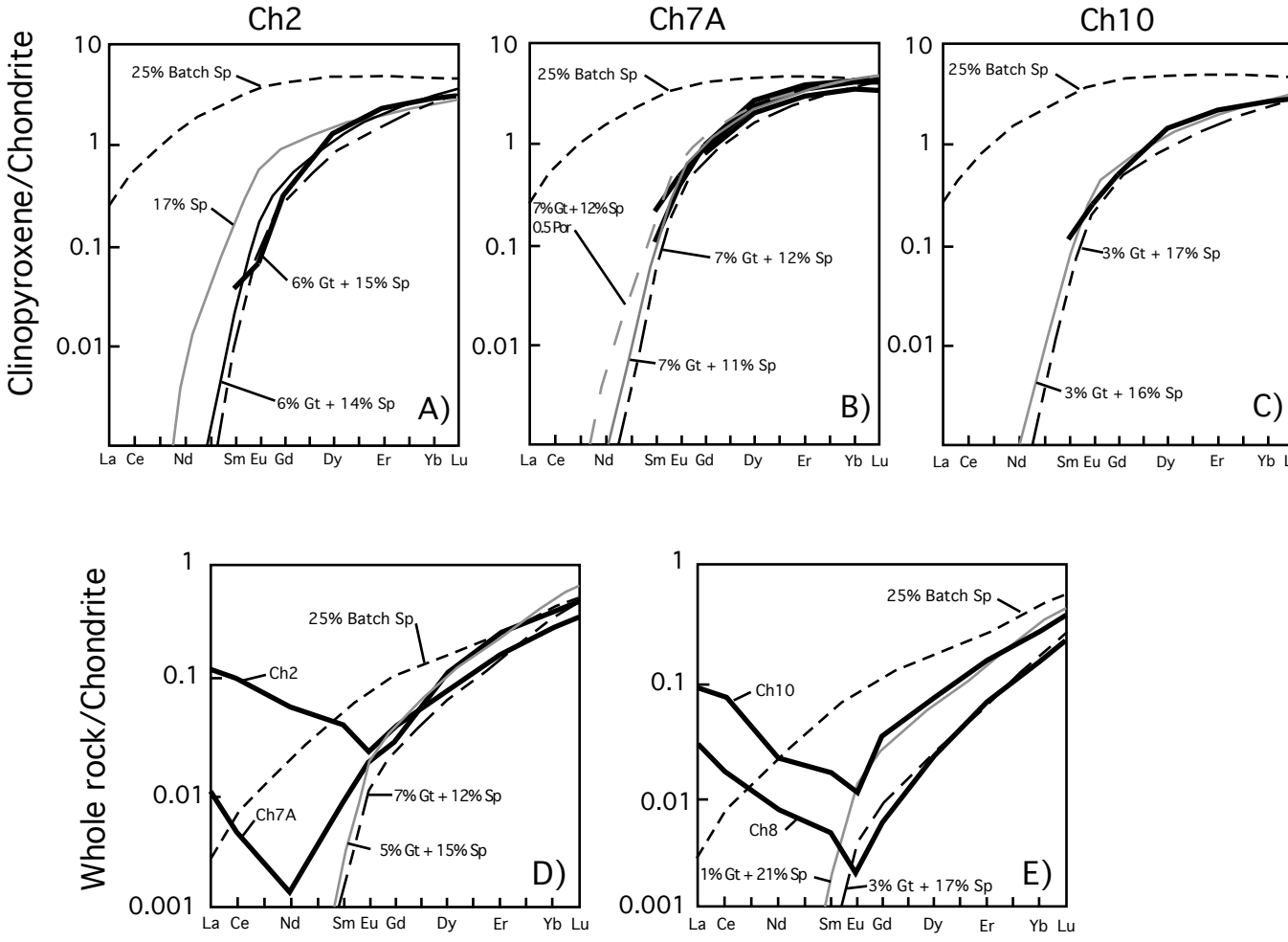

Fig. 2-16: Modeled REE patterns **A-C)** for clinopyroxene and **D-E)** for whole rock data.
All mineral partition data are from Hauri and Hart (1994). Initial modal composition encompasses 58% olivine, 25% orthopyroxene and 13.7% clinopyroxene. The melting mode is 10% olivine, 28% orthopyroxene, 60% clinopyroxene and 2% spinel. Modal composition in the garnet facies is calculated using the spinel mode and the new mode using the garnet-spinel reaction in Hauri and Hart (1994). Chondrite normalising values are from Sun and McDonough (1989).

11.3 Choiseul peridotites: MORB or SSZ or OJP-related?

Partial melting calculations denote that the Choiseul peridotites have undergone 1-8% partial melting in the garnet facies followed by 11-21% melting in the spinel field. Johnson et al. (1990) and Hauri and Hart (1994) argue that refractory abyssal peridotites commence their melting histories in the garnet field. In contrast, recent work (Parkinson et al., 1998) points out SSZ peridotites have undergone very high degrees of partial melting ranging from 15-25% with no evidence for any significant garnet residue in the melting process. The modeling by Neal et al. (1997) shows the OJP lavas resulted from 15-25% partial melting starting in the garnet stability field, similarly to the Choiseul peridotites. Based on the melting criteria alone, I could infer the Choiseul peridotites could possibly be related to OJP.

The average temperature of equilibration calculated for the Choiseul peridotites using the Balhaus thermometer (733°C) is slightly lower than the average temperature calculated for the abyssal peridotites (~ 806°C) but greater than average temperature of 647°C calculated for SSZ peridotites (Parkinson et al., 1998). Low olivine-spinel equilibration temperatures (Fig. 2-11) reflect the water-assisted diffusional re-equilibration in SSZ environments. This is consistent with the high degree of melting of the SSZ peridotites achieved not by exceptionally high upper mantle temperatures but H_2O-induced melting. In contrast, OJP-related peridotites would have much higher temperatures of equilibration (>1100°C) to account for high degree of partial melting. Therefore, moderate temperatures (~ 730°C) for relatively high degrees of melting exclude the Choiseul peridotites being related to the OJP.

To better constrain the tectonic setting of peridotites, many workers (Arai, 1994; Bonatti and Michael, 1989; Dick and Bullen, 1984) have used the composition of mineral phases. In the plot of Cr# versus Mg# (Fig. 2-3), most of the spinel plots at the moderately depleted end of the abyssal peridotite array defined by Dick and Bullen (1984). Note that some of the spinels (Ch8 and Ch7D) have higher Mg# and Cr# and plot within the SSZ peridotite field (Fig. 2-3). The plot of spinel Cr# versus Mg# of olivine outlines similar result with most of the peridotites plotting within the abyssal peridotite field and two samples (Ch8 and Ch7D) projecting within the SSZ peridotite field (Fig. 2-17A). The same conclusion is drawn from the spinel Cr# versus Al_2O_3 (wt %) in orthopyroxene (Fig. 2-17B) where Ch8 and Ch7D plot within the SSZ peridotite field distinct from the other peridotites which are abyssal peridotites-like. In this plot (Fig. 2-17B), the Choiseul peridotites exhibit a strong negative correlation between spinel Cr# and Al_2O_3 of orthopyroxene except for sample Ch6. This sample plots at low Al_2O_3 contents for a given Cr# indicating a redistribution of aluminium into the Al-rich phases (amphibole and chlorite). Clearly, the mineralogical compositions indicate that most of the Choiseul peridotites plot within the abyssal peridotite field. This does not necessarily mean that these peridotites are sub-ridge samples. Most convergent plate margin peridotites also seem to be very depleted but it is possible to have less depleted compositions from this type of setting. In contrast to the other Choiseul abyssal-like peridotites, Ch7D and Ch8 have obvious SSZ affinities.

The fO_2s are another line of evidence for tracking the petrogenesis of the Choiseul peridotites. For most of the Choiseul peridotites, fO_2s recorded by olivine-orthopyroxene-spinel equilibria are between 1.04 $\log_{10}$ units below to 0.23 $\log_{10}$ units above the FMQ

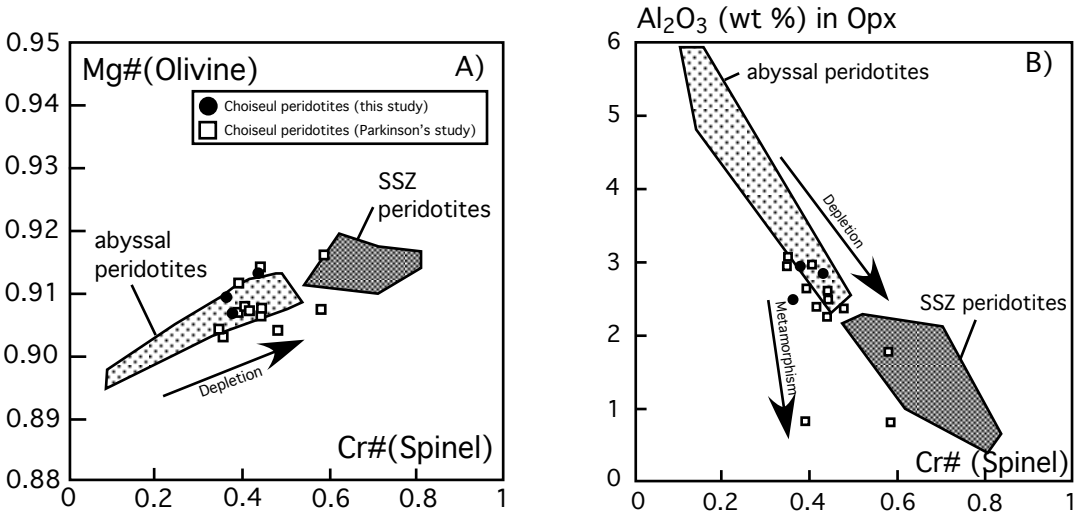

Fig. 2-17: Plots of Cr# in spinel versus A) Al_2O_3 (wt %) in orthopyroxene and B) Mg# in olivine for the Choiseul peridotites.
The black dots define the data set of the Choiseul peridotites (this study) whereas the open squares refer to the dataset of Parkinson (pers. comm.) for the Choiseul peridotites.
Reference is made to peridotites from abyssal peridotites (light stipple) and SSZ peridotites (heavy stipple) after Parkinson (pers. comm.), modified from Bonatti and Michael (1989).

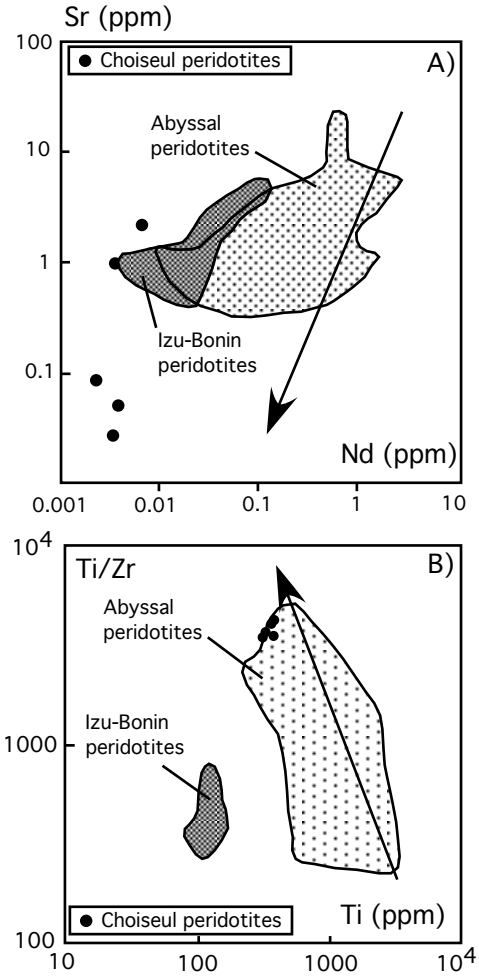

Fig. 2-18: Plot of A) Sr versus Nd and B) Ti/Zr versus Ti in clinopyroxene from the Choiseul peridotites.
Arrows indicate the direction of melt depletion from a fertile mantle source (Parkinson et al., 1998).
Reference is made to clinopyroxenes from Izu-Bonin peridotites and abyssal peridotites (Parkinson et al., 1998).

buffer (Fig. 2-12), overlapping the abyssal peridotite field. However, two samples (Ch7D and Ch6), which contain larger amounts of amphibole and chlorite, display high fO_2s reaching 1.26 $\log_{10}$ units above the FMQ buffer, plotting in the range of oceanic arc peridotites.
So with respect to the tectonic setting of the Choiseul peridotites, I can infer from the evidence outlined above that most samples have characteristics of abyssal peridotites with some samples featuring SSZ affinities.

11.4 Evidence for mantle interaction with a metasomatic fluid

The textures of the peridotites are indicative of high temperature fluid interaction accompanied by deformation. The Choiseul peridotites are variably tectonised and preserve evidence of shearing (Fig. 2-2). Very small anhedral-shaped grains of clinopyroxene (Type 2) (Fig. 2-2B and Fig. 2-2E) suggests a recrystallisation process linked to fluid-mantle interaction. The Type 2 clinopyroxene is found in all of the textural varieties of peridotite including those with protogranular texture (Fig. 2-2B) suggesting that the fluid infiltrates the mantle regardless of deformation intensity. This type of clinopyroxene is geochemically distinct from other clinopyroxene (Type 1). Type 2 has low Al_2O_3 contents (< 3 wt%) for high Mg# (Fig. 2-5B) comparable in composition to the arc-related clinopyroxene (Berly et al., 2006).
Magnesiohornblende blebs enclosed in the clinopyroxene grains are interpreted to result from the high temperature hydrous fluid interaction of the clinopyroxene in the upper amphibole facies. Based on their mineral compositions, tremolite and chlorite are considered to have a hydrothermal origin attesting to the presence of fluids during the exhumation of the peridotites.
Whole rock and clinopyroxene are also both characterised by variable LILE, Sr and Pb enrichments (Fig. 2-8B and Fig. 2-10B) even in the freshest peridotite samples, indicating that serpentinisation has a limited effect on the compositions of the peridotites for these elements. When compared to the Izu-Bonin peridotites (Parkinson et al., 1998), the primitive-mantle whole rock multi-element (Fig. 2-19B) and chondrite-normalised whole rock REE (Fig. 2-19A) patterns for the Choiseul peridotites exhibit similar enrichments in LILE, Sr, Pb and LREE, which are striking features in arc peridotites (Parkinson et al., 1998). Those enrichments are thought to result from peridotite interaction with an incompatible element-rich melt (Pearce et al., 2000). In addition to a SSZ-related origin, LILE, Sr and Pb are also all enriched in SSZ lavas (Hawkesworth et al., 1993; Maury et al., 1992).
The plot of Sr versus Nd for clinopyroxene (Fig. 2-18A) further demonstrates a SSZ signature for the Choiseul peridotites. Sr has similar distribution coefficient to Nd but is more enriched in a subduction component. Clinopyroxene from Choiseul peridotites is displaced from those in abyssal peridotites, trending towards high Sr contents, and plotting in the vicinity of the SSZ-related clinopyroxene. According to Alibert et al. (1994), high Sr contents together with Pb (specially in clinopyroxene) support the hypothesis of aqueous fluid released during the dehydration of subducted slab. The plot of Ti/Zr versus Ti (Fig. 2-18B) is also used to illustrate the SSZ affinity as Zr is enriched in the subduction component but Ti is not. Unlike the SSZ peridotites (Parkinson et al., 1998), Zr in clinopyroxene is not enriched with respect to clinopyroxene from the abyssal

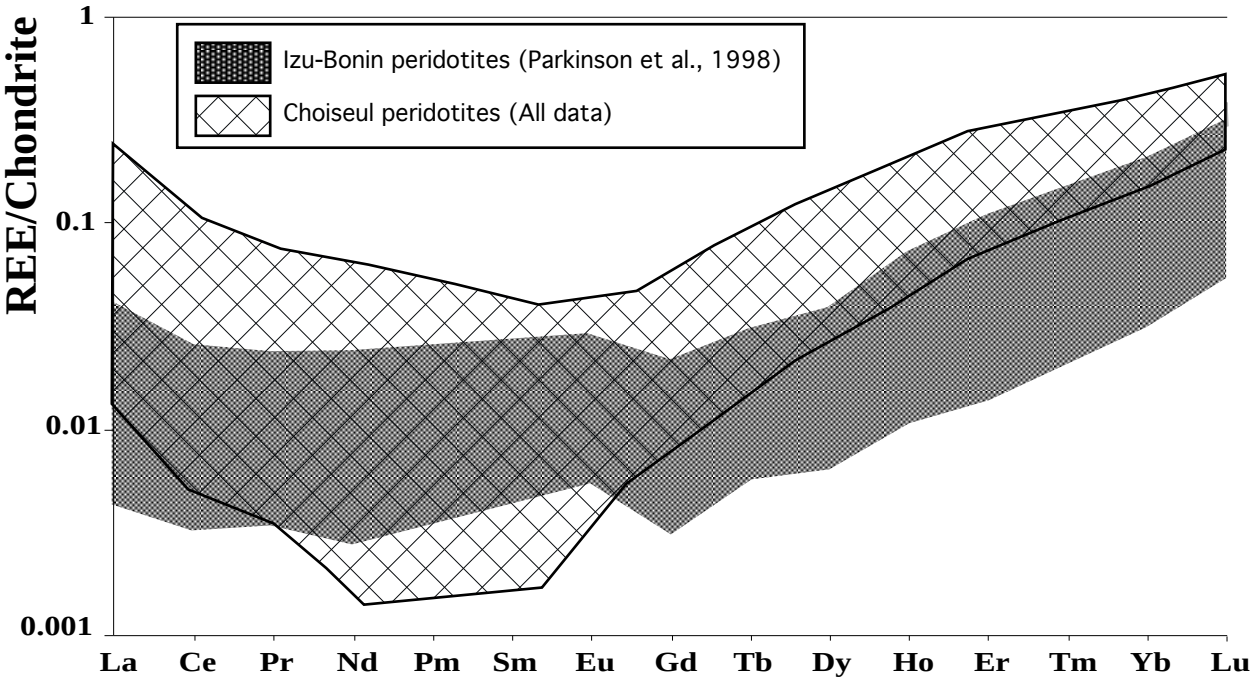

Fig. 2-19A: Chondrite-normalised whole rock REE patterns for the Choiseul peridotites and the Izu-Bonin peridotites (Parkinson et al., 1998).
In this diagram, the Choiseul peridotites field represent all Choiseul peridotites data including the ones from this study, Parkinson's study and Ch7A. Chondrite normalising values are from Sun and McDonough (1989).

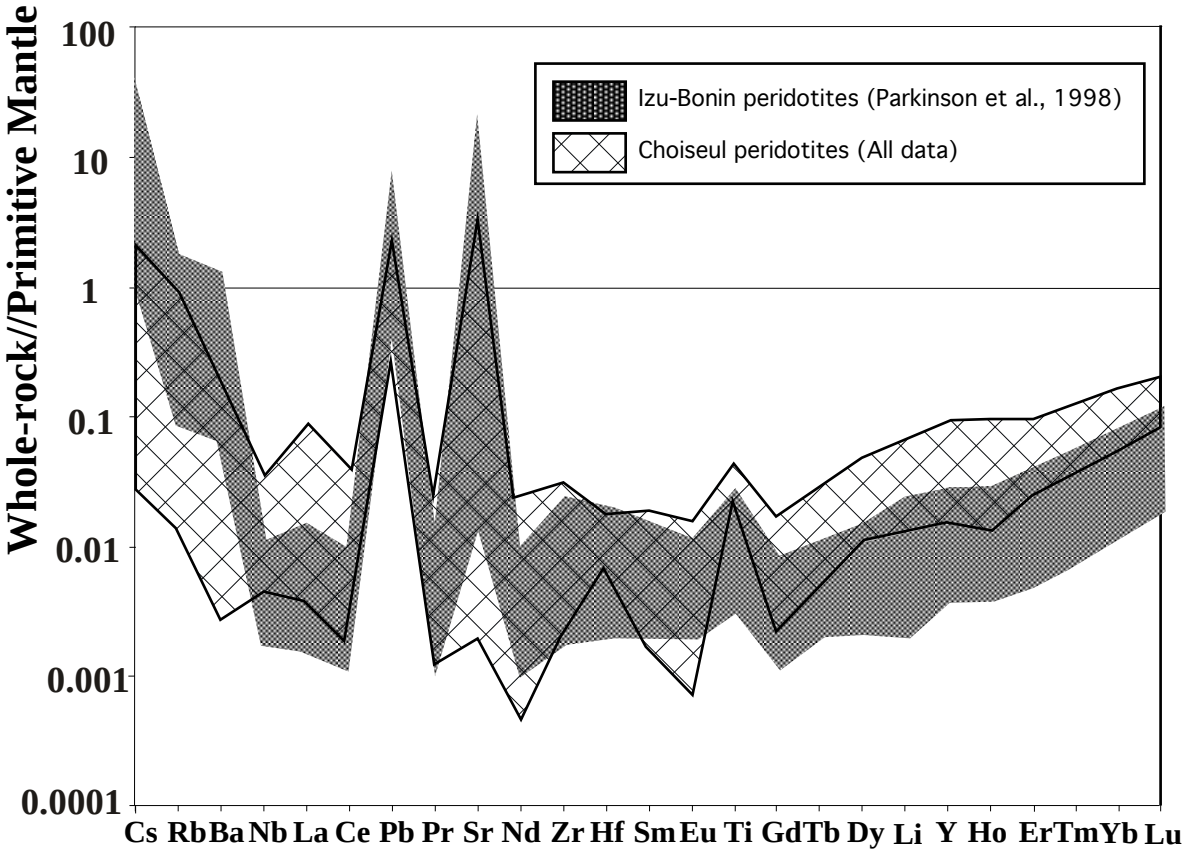

Fig. 2-19B: Primitive mantle-normalised whole rock multi-element patterns for the Choiseul peridotites and the Izu-Bonin peridotites (Parkinson et al., 1998).
In this diagram, the Choiseul peridotites field represent all Choiseul peridotites data including the ones from this study, Parkinson's study and Ch7A. Primitive mantle normalising values are from Sun and McDonough (1989).

peridotites (Fig. 2-18B). This does not mean that the Choiseul clinopyroxene lacks a SSZ signature but instead is consistent with metasomatism by an aqueous phase rather than by a silicate melt.

This assumption is further supported by the high orthopyroxene/olivine ratio of sample Ch7D compared to the other peridotites (Table 2-1). Olivine interacting with a Si-rich aqueous fluid forms orthopyroxene (Kelemen et al., 1992; Morishita et al., 2003). However, the introduction of H_2O-rich fluids from a subducted slab is claimed by some workers to trigger oxidation of the mantle wedge overlying the slab, and would shift the fO_2s towards values in excess of those of FMQ (Wood et al., 1990). This is not consistent with the reduced nature of many peridotites. However, the plot of fO_2s against Cr# in spinel (Fig. 2-12) shows that most of the Choiseul samples plot within the abyssal peridotite field but some are very close to the values corresponding to SSZ peridotites. The Choiseul peridotites have therefore undergone a small degree of oxidation. This is obvious even for the three samples (Ch1, Ch7D and Ch8), which exhibit clear evidence of interaction with a metasomatic agent. Their values in spinel Cr# and fO_2, which are distinct compared with other Choiseul samples, follow a trend interpreted by Pearce et al. (2000) as representing MORB mantle – SSZ magma interaction similarly to Mariana forearc and South Sandwich peridotites (Parkinson et al., 1998; Pearce et al., 2000). This feature is also apparent in the plot of Cr# versus TiO_2 (Fig. 2-14) where some of the spinel is intermediate between mid-ocean ridge or back arc mantle residues and island-arc magma with high fO_2s and high Cr#, high TiO_2 spinel.

The range of evidence outlined above demonstrates that metasomatic fluids infiltrated and reacted with the host peridotites at different stages of their tectonic histories. As a consequence, recrystallisation has occurred with evidence of newly formed clinopyroxene due to the circulation of fluid at high temperature. The presence of amphibole and chlorite are evidence that fluid percolation persisted during the cooling of the rocks when exhumed to the surface. In addition, the metasomatic fluid has also affected the composition of the original peridotites by slightly oxidising the spinel and re-forcing re-equilibration of the pyroxene.

The primary composition of the fluid can be ascertained by deciphering the geochemical data of the whole rock and the mineral phases. According to these data, the fluid was enriched in LILE, Sr, Pb and to a certain extent LREE. Metasomatic fluids with similar compositions have been described as interacting with peridotites in SSZ environments such as Mariana and Izu-Bonin forearcs (Parkinson et al., 1998) and South Sandwich forearc (Pearce et al., 2000). These authors concluded the metasomatic fluid involved was released from the subducted slab. During the dehydration of the subducted plate, the fluid oxidises the source regions of island arc basalts. The “re-enriched” mantle wedge undergoes high degrees of melting under hydrous conditions to generate SSZ lavas with typical arc compositions.

I argue that the Choiseul peridotites represent typical depleted MORB-type peridotites that have interacted with an aqueous liquid released from the subducted slab in a SSZ tectonic setting.

12 TECTONIC IMPLICATIONS

12.1 Formation of the peridotites

Prior to any subduction, the lithosphere in the Western Pacific had a MORB character and the mantle an "abyssal peridotite" composition (Fig. 2-20A). Note that in the absence of isotopic data, I do not know if this was of Indian or Pacific type. At about 43 million years ago, subduction of the Pacific Plate south-westwards along the Vitiaz Trench began. As a result, the subducted Pacific slab started releasing fluids into the overlying mantle region (Stern, 2002). The reaction between abyssal peridotites and the metasomatic agent would produce the Choiseul peridotites (Fig. 2-20B). The degree of reaction is difficult to assess, but the very depleted nature of these harzburgites means that only a small amount of reacting agent (<1%) would be required to alter the incompatible element contents of these rocks (Parkinson et al., 1998).
The introduction of fluids would lower the solidus temperatures of the peridotites causing partial melting in hotter portions of the wedge. It is impossible to determine if the remelting process occurred beneath the Choiseul Island to generate typical arc basalts (Fig. 2-20B). The high degree of melting (15-25%) and the fact that the melting was initiated in the garnet facies indicate that the Choiseul peridotites might have first melted beneath the ridge center and then remelted in the SSZ setting. However the arc volcanism related to the Pacific Plate subducting beneath the Indo-Australian Plate (stage 1 volcanism) (Petterson et al., 1999) is fairly limited on Choiseul. The sequence related to that event is represented by the Mole Formation sediments, which are crystal- and lithic-rich turbidites during the Oligocene-Miocene times. This Formation seems to be quite thick (estimated between1000-2500m) indicating intense contemporaneous tectonic activity. But only small amounts of andesitic tuff were recovered from the Mole Formation meaning that the stage 1 volcanism beneath the basement of the Choiseul Island was restricted.
I suggest that the Choiseul peridotites derived from a two-stage origin of ocean-ridge-like residual harzburgites (Fig. 2-20A) that were subsequently infiltrated by a reactive hydrous melt released from the subducted slab underneath the pre-Miocene basement of Choiseul (Fig. 2-20B).

12.2 Exhumation and obduction

In response to the Ontong-Java Plateau collision with the Solomon arc, most subduction of the Pacific Plate underneath the Indo-Australia Plate ceases with perhaps the exception of the deeper parts of the Plateau (Mann et al., 2004) (Fig. 2-20C). As a result, the peridotites from the mantle wedge were exhumed rapidly along the down-slab dip (Fig. 2-20C). Continuously exposed to fluids released from the slab, clinopyroxene was hydrated in the amphibolite facies, spinel was altered into chlorite in the greenschist facies and serpentine occurred in a late retrogression stage.

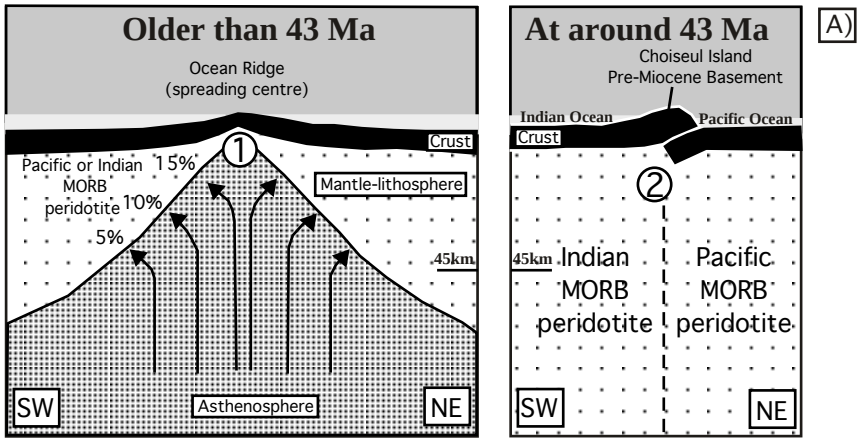

A) Pacific or Indian oceanic lithosphere was formed at the mid-ocean ridge. As a consequence, the mantle lithosphere is depleted during melting processes to generate MORB-type basalts (1). The residual mantle has an "abyssal peridotite" composition. Then the lithosphere drifted away from the spreading centre. At around 43 Ma, change of plate of motions triggered the subduction of the Pacific Plate underneath the Indo-Australian Plate (2). As a result, the Indo-Australian Plate is uplifted forming the pre-Miocene basement of the Choiseul Island.

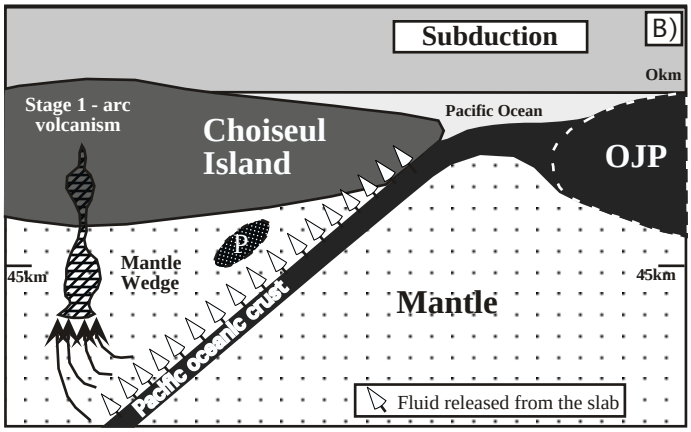

B) The Pacific oceanic lithosphere subducted beneath the Choiseul pre-Miocene basement. During that time, aqueous fluids or hydrous melts, released from the descending slab, interacted with the abyssal peridotites. The reaction between the abyssal peridotites and the metasomatising agents forms the Choiseul peridotites (annotated P).
As depth, the infiltration of metasomatising agents within the mantle wedge is the cause of stage 1 - arc volcanism represented by the Mole Formation turbidites on the Choiseul Island.

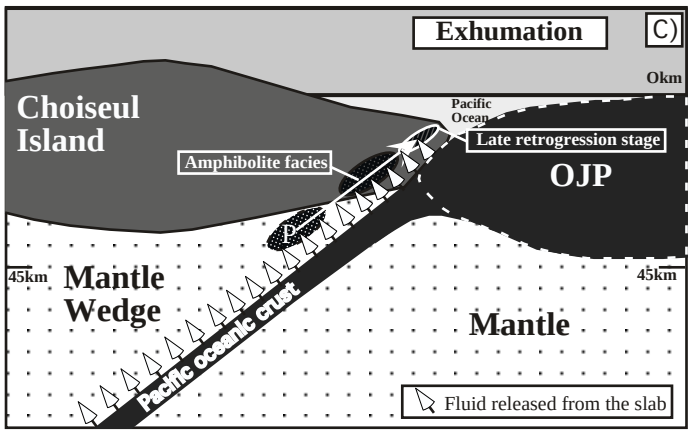

C) Ontong Java Plateau (OJP) collided with the Solomon arc (including Choiseul Island). The compressional régime initiated the exhumation of metasomatised upper mantle. During their exhumation, the Choiseul peridotites were still exposed to fluids from slab. As a result, hydration of clinopyroxene to amphibole occurred in the amphibolite facies. Continued interaction of aqueous fluids with the peridotites resulted in a late retrogression stage with occurrence of tremolite and serpentine.

Fig. 2-20 A, B and C: Tectonic Model of peridotites formation and exhumation.

13 CONCLUSION

The Siruka Ultramafics or Choiseul peridotites are largely exposed in Southeastern Choiseul (Eastern Solomons) as a coherent thrust sheet. The peridotites are relatively fresh harzburgites and their textures range coarse-grained through porphyroclastic to mylonitic and show variable degrees of deformation. Dominated by olivine and orthopyroxene, the harzburgites only contain a small modal proportion of clinopyroxene (< 7%) and hydrous phases such as amphibole (magnesiohorblende to tremolite) and chlorite occur only occasionally.

The harzburgites are characterised by olivine with high Fo (89-93), high magnesium (Mg#>90) pyroxenes depleted in Al_2O_3 (<4 wt%) and relatively high Cr# spinels all indicative of a refractory origin for the Choiseul peridotites. Low REE contents of both whole rock and clinopyroxene also indicate that the harzburgites have undergone a high degree of melting. Whole rock and clinopyroxene MREE-HREE data are consistent with melting in the garnet facies followed by melting in the spinel field. However LREE enrichment in whole rock cannot be explained by melting modeling. In addition, whole rock and clinopyroxene are also marked by variable LILE, Sr and Pb enrichment indicating that the metasomatising fluid enriched in these elements has reacted with the peridotites. Similar enrichments are described in SSZ-peridotites, which are formed by interaction of residual mantle with a slab-derived fluid.

The Choiseul peridotites represent typical depleted MORB-type peridotites that have interacted with a metasomatising agent (likely to be an aqueous fluid) released from the subducted slab in a SSZ tectonic setting. This two-stage origin for these residual harzburgites is attributed to the melting process at mid-ocean ridge that have generated Indian or Pacific MORB basalts prior to any subduction followed by the metasomatic interaction of these peridotites with the fluid released from the Pacific plate subducting underneath the pre-Miocene basement of Choiseul. Limited retrograde assemblages in these peridotites suggest that they were exhumed rapidly to the surface. This exhumation and obduction process is interpreted to result from the OJP-arc collision.

Chapter 3:
Supra-Subduction Zone pyroxenites from San Jorge and Santa Isabel (Solomon Islands): a metasomatic origin.

1 INTRODUCTION

Pyroxenites are enigmatic ultramafic rocks that generally occur in two distinct settings: 1) as veins/dykes that are generally sampled in various mantle peridotite lithologies (including xenoliths and ultramafic complexes) on a variety of scales and 2) as crustal accumulates that formed in crustal magma chambers.

Mantle-derived pyroxenites occur in relatively small volume (Fabriès et al., 1991), probably <5% of the upper mantle (Hirschman and Stolper, 1996), and consist of orthopyroxenite, websterite and clinopyroxenite. Crustal pyroxenites on the other hand consist dominantly of clinopyroxenite and are commonly found in arc environments (Schiano et al., 2000) where they may comprise relatively large volumes of cumulates from primitive island arc magmas in crustal magma chambers (DeBari and Coleman, 1989; Schiano et al., 2000). However, little is known about possible pyroxenites in the mantle wedge between the subducted slab and the base of the arc lithosphere. On the basis of peridotite xenoliths found in Lihir and Tubaf (volcanoes located to the rear of the New Britain-Bougainville arc of Papua New Guinea), McInnes et al. (2001) suggested that pyroxenites might be common in supra-subduction zone (SSZ) settings, but detailed studies of coherent bodies have not been reported.

Several processes have been proposed for the genesis of these different types of pyroxenite. Field, geochemical, and experimental studies have shown that clinopyroxene can be a liquidus phase in various basalt magma types, and high-pressure mineral segregation from primitive magmas can result in the formation of massif pyroxenite (DeBari and Coleman, 1989; Girardeau and Ibarguchi, 1991; Pearson et al., 1993; Müntener et al., 2001; Parlak et al., 2002; Santos et al., 2002). Alternatively, recycling of elongated slices of subducted oceanic lithosphere through the convective mantle may also result in pyroxenite formation (Polvé and Allègre, 1980; Allègre and Turcotte, 1986; Hamelin and Allègre, 1988; Kornprobst et al., 1990; Kerr et al., 1995). While these first two processes can explain a wide spectrum of occurrence, they are unable to explain crosscutting networks of pyroxenite veins in mantle peridotites. In such settings, many authors proposed that pyroxenite originates from melt/fluid-rock reaction in the upper mantle (Kelemen et al., 1992; Smith and Riter, 1997; Wilkinson and Stolz, 1997; Garrido and Bodinier, 1999; Smith et al., 1999; Zanetti et al., 1999; McInnes et al., 2001; Wang et al., 2001).

In this chapter, we combine a field study with petrological, mineralogical, and geochemical investigations in order to characterise pyroxenites exposed on the islands of San Jorge and Santa Isabel (Solomon Islands). The pyroxenites crop out in a boundary zone between the Ontong Java Plateau (OJP) and the Solomon Arc. Our aim is to demonstrate that these pyroxenites formed in a SSZ mantle setting rather than beneath an oceanic plateau. We document the mineralogical and chemical characteristics of this type of SSZ pyroxenite, which has not previously been described in detail, and compare it to typical mantle and crustal pyroxenite. We then discuss the processes responsible for the formation and the exhumation of SSZ pyroxenite in the Solomon Islands specifically.

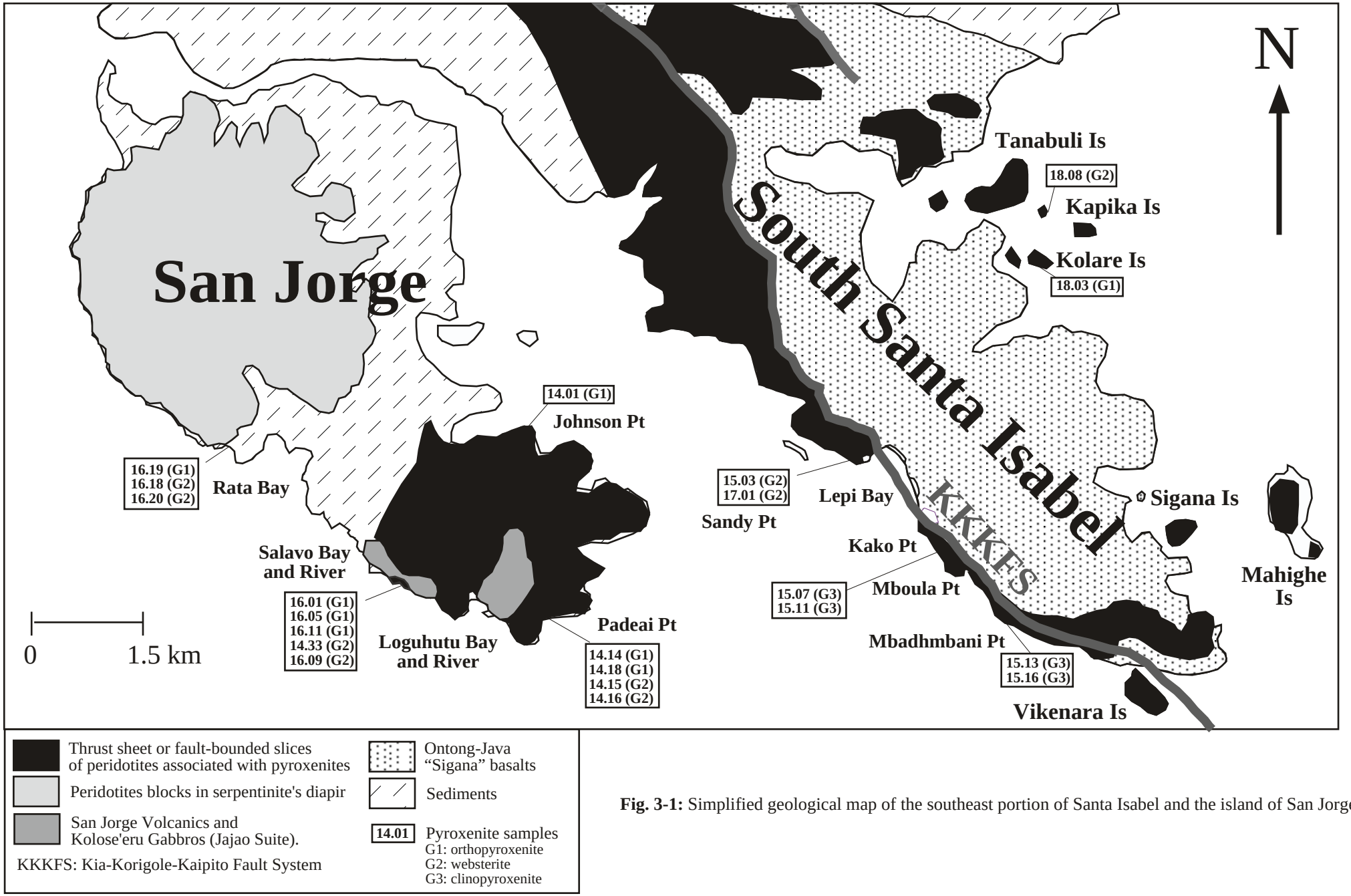

Fig. 3-1: Simplified geological map of the southeast portion of Santa Isabel and the island of San Jorge.

2 GEOLOGICAL SETTING

The Solomon Islands are not products of a simple arc system but rather were formed through a complicated geological history (Petterson et al., 1999). A collage of crustal terranes forms the Solomons (Coleman, 1965) that are bounded by two trench systems: the Vitiaz Trench to the northeast and to the southwest is the South Solomon Trench System (SSTS) (*Chapter 1*). The juxtaposition of terranes is mainly caused by the collision between the OJP and Solomon Arc (Petterson et al., 1997).
In response to the OJP-arc collision, the leading edge of the OJP began to be exhumed and portions are now exposed in the islands of Santa Isabel, Malaita, Ulawa and Makira (Petterson et al., 1997). These uplifted, overthrusted, largely unmetamorphosed portions of the OJP are termed the Pacific Province (Coleman, 1965). Together with OJP-related terranes, thin fault-bounded slices of peridotite associated with pyroxenite occur on the islands of San Jorge and the southern part of Santa Isabel.

3 SAMPLING AND PERIDOTITE-PYROXENITE FIELD RELATIONS

The detail of the geology of San Jorge and Santa Isabel is given in *Chapter 1*. A simplified geological map is also presented in Figure 3-1 where the location of the samples is shown. The San Jorge and Santa Isabel pyroxenites generally occur as layers and veins/dykes with sharp contacts in host harzburgites and dunites (Fig. 3-2A). No lherzolites have been found. The harzburgites and dunites are variably serpentinised and some are deformed. But the pyroxenite veins remain surprisingly fresh varying from orthopyroxene- to clinopyroxene-rich in composition. The pyroxenite layers are generally subparallel to the foliation of their host ultramafic rocks. Conversely, the veins/dykes are organised in a multi-generational network crosscutting the host peridotites (Fig. 3-2B). The thickness of these pyroxenites is variable ranging from ~1cm to ~30cm. Veins or dykes are occasionally folded and sheared.
On Santa Isabel, the pyroxenites are exposed on both sides of the KKKFS. The clinopyroxene-rich rocks including websterites and clinopyroxenites seem to be more abundant than the orthopyroxene-rich samples. On San Jorge, the pyroxenites occur in two locations: at the southern end of the island, they are incorporated into an ultramafic massif whereas in northern San Jorge, they crop out in a serpentine diapir. At Johnson Point (Fig. 3-1), the orthopyroxenite outcrops over an area of about 100 m^2 without any clear relation with neighbouring peridotite. Websterite is abundant as beach cobbles and pebbles, particularly in the vicinity of the southern ultramafic massif.

4 ANALYTICAL METHODS

4.1 Whole rock analysis

Whole rock analyses of 21 representative pyroxenites, sampled from different locations on Santa Isabel and San Jorge Islands, were carried out using X-ray fluorescence (XRF) (Department of Earth and Marine Sciences, ANU) to determine their major element compositions.
Trace element concentrations in the pyroxenites were measured with two types of inductively coupled plasma spectrometry (ICP-MS) techniques: 1) The solution ICP-MS (University of Montpellier, France) and 2) The Laser Ablation (LA) ICP-MS system (Australian National University, Australia). Further details of the analytical methods can be found in Appendix 1.

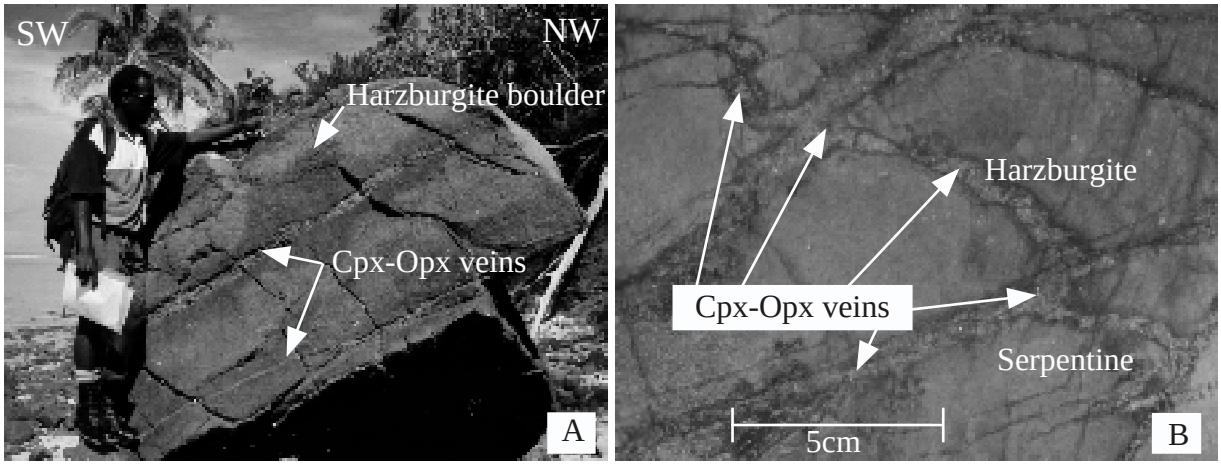

Fig. 3-2: Photos showing the relationship between pyroxenite veins and host peridotites. (a) Harzburgite boulder crosscut by two parallel veins of websterites at Padei Point (San Jorge). (b) Outcrop of a dunite exposed on the South side of the KKKFS (Sandy Point, Santa Isabel), showing different generations of Cpx-Opx veins crosscutting each other.

4.2 Mineral analysis

Major element compositions for minerals (including all silicate and oxide phases) were determined using a Cameca Microbeam Electron MicroProbe Analyser (EMPA) housed at Research School of Earth Sciences (RSES, ANU) and a JEOL 6400 Scanning Electron Microscope (SEM) housed at Research School of Biological Sciences (RSBS, ANU). Details of the analytical procedures are given in Appendix 1.

5 PETROGRAPHY

The pyroxenite samples from San Jorge and Santa Isabel have variable mineralogy and have been classified into three groups with respect to the proportions of orthopyroxene:clinopyroxene as follows:

- Group 1 (G1): orthopyroxenites (orthopyroxene>80%)
- Group 2 (G2): websterites (60%<clinopyroxene<80% and orthopyroxene>10%)
- Group 3 (G3): clinopyroxenites (clinopyroxene>80%)

Tables 3-1 and 3-2 summarise the modes and petrographic features of these pyroxenites.

5.1 Primary assemblages

The major phase assemblages are dominated by clinopyroxene and orthopyroxene with minor amounts of olivine and spinel. The pyroxenites are usually fresh rocks exhibiting a small degree of serpentinisation and a low degree of loss on ignition (LOI: monitor of alteration) (LOI < 6 wt %) (Fig. 3-3). The G3-clinopyroxenites are the most altered (particularly samples 15.11 and 15.13) whereas the G2-websterites are practically unaltered (LOI < 1 wt%). The G1-orthopyroxenites have a variable degree of alteration (0.2 < LOI < 4.1 wt%) (Fig. 3-3).

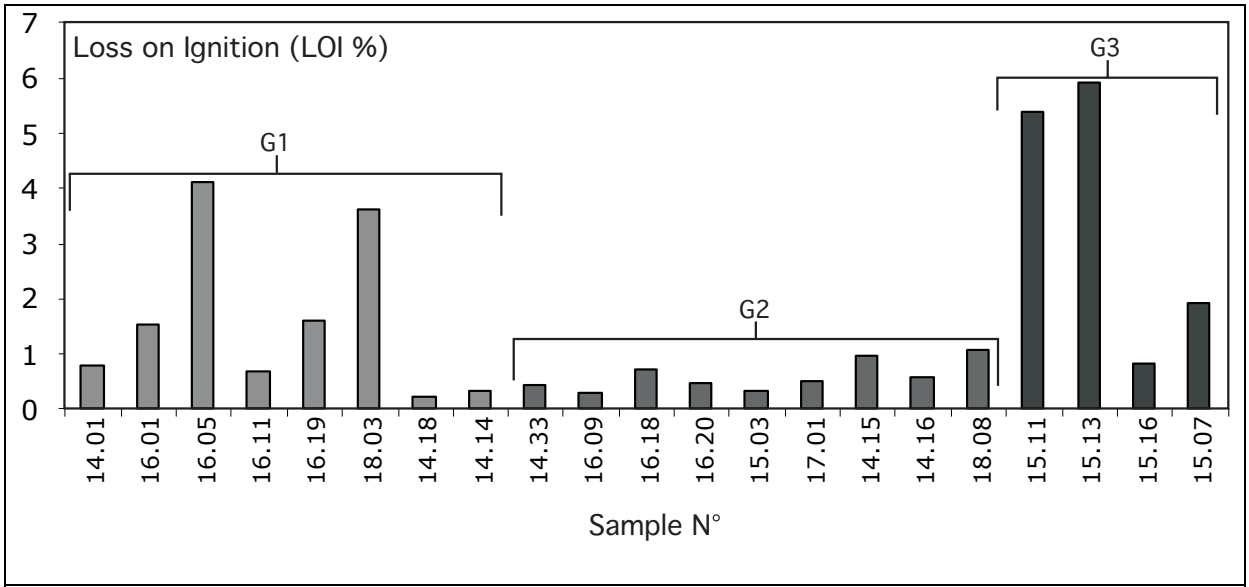

Fig. 3-3: Loss on ignition (LOI) contents (wt %) for the three groups (G1-orthopyroxenites, G2-websterites and G3-clinopyroxenites) of the San Jorge / Santa Isabel pyroxenites

The fabric of the pyroxenites varies from large grains of approximately equal size in a fine-grained matrix (inequigranular) to complete gradation of fine- to coarse-grained fabric (seriate) (Moore, 1970). The grain boundaries range between straight and lobate. Lobate grain

Table 3-1: Petrological and mineralogical characteristics of the San Jorge / Santa Isabel pyroxenites (The Solomon Islands).

					Description			Primary Assemblage				Secondary Assemblage			
Group	Sample	Island	Location	Sampling	Rock Description	Fabric/Texture	Deformation	Opx	Cpx	Ol	Sp	Amphibole		Serp	Others
Type	Number	Name	Name	Type		Type	Degree	(%)	(%)	(%)	(%)	Hb	Trem	(%)	Type
Orthopyroxenite (G1)	14.01	San Jorge	Johnson Pt	outcrop	Ol-Sp Orthopyroxenite	Porphyroclastic	moderate to high	89	3	6	1	Yes	Yes	0.5	-
	16.01	San Jorge	Salavo Bay	pebble	Sp Orthopyroxenite	Porphyroclastic	low to moderate	82	15	-	1	Yes	No	0.5	Fe_2O_3
	16.05	San Jorge	Salavo Bay	outcrop	Sp Orthopyroxenite	Porphyroclastic	moderate to high	80	13	-	2	Yes	No	1	Fe_2O_3, CpxII, Pectolite
	16.11	San Jorge	Salavo Bay	pebble	Cpx-Sp Orthopyroxenite	Porphyroclastic	low to moderate	79	2	-	1	Yes	Yes	2	-
	16.19	San Jorge	North Jorge	pebble	Ol-Sp Orthopyroxenite	Porphyroclastic	high	82	7	9	2	Yes	No	4	Wo
	18.03	St Isabel	Kolare Is	pebble	Ol-Sp Orthopyroxenite	Porphyroclastic	high	59	5	20	1	Yes	No	5	-
	14.18	San Jorge	Padeai Pt	pebble	Composite Ol bearing Ortho-Clino-pyroxenite	Inequigranular - Interlobate	no deformation	86	6	6	-	Yes	No	2	-
	14.14	San Jorge		pebble	Composite Ol bearing Ortho-Clino-pyroxenite	Inequigranular - Interlobate	low	83	9	6		Yes	Yes	2	-
Websterite (G2)	14.33	San Jorge	Salavo Bay	pebble	Cpx Websterite	Inequigranular - Interlobate/Polygonal	no deformation	20	78	-	-	Yes	No	-	FeS_2, Fe_2O_3
	16.09	San Jorge	Salavo Bay	pebble	Cpx Websterite	Replacing Inequigranular - Interlobate	no deformation	23	74	-	-	Yes	No	1	FeS_2
	16.18	San Jorge	North Jorge	pebble	Cpx Websterite	Inequigranular - Interlobate/Polygonal	no deformation	25	73	-	-	Yes	No	0.2	Fe_2O_3
	16.20	San Jorge	North Jorge	pebble	Cpx Websterite	Inequigranular - Interlobate	no deformation	20	80	-	-	Yes	No	2	-
	15.03	St Isabel	Lepi Bay	outcrop	Ol-Cpx-Websterite	Inequigranular - Interlobate	low	36	70	2	-	Yes	Yes	4	FeS_2, Fe_2O_2
	17.01	St Isabel	Lepi Bay	outcrop	Websterite	Inequigranular - Interlobate	low	40	58	-	-	Yes	Yes	1	FeS_2, Fe_2O_3
	14.15	St Isabel	Padeai Pt	pebble	Websterite	Seriate - interlobate	no deformation	46	54			Yes	No	0.1	-
	14.16	San Jorge	Padeai Pt	pebble	Websterite	Seriate - interlobate	no deformation	47	53	-	-	Yes	No	0.1	-
	18.08	St Isabel	Kapika Is	outcrop	Cpx Websterite	Seriate - interlobate	no deformation	22	68	-	-	Yes	Yes	3	Pectolite, Fe_2O_3
Clinopyroxenite (G3)	15.11	St Isabel	Kako Pt	pebble	Clinopyroxenite	Mosaic seriate - interlobate	high	-	90	Trace	Exsol	Yes	No	10	FeS_2, Chl
	15.13	St Isabel	Mbadhmbani Pt	pebble	Clinopyroxenite	Mosaic seriate - interlobate	high	-	96	-	Exsol	Yes	No	2	FeS_2, NiFeS, Fe_2O_3
	15.16	St Isabel	Mbadhmbani Pt	pebble	Clinopyroxenite	Seriate - interlobate	low	7	80	10	Exsol	Yes	No	3	FeS_2
	15.07	St Isabel	Kako Pt	pebble	Clinopyroxenite with abundant amphibole	Seriate - interlobate	low	2	45	10		35%	No	10	-

Table 3-2: Mineral assemblages in the San Jorge/Santa Isabel pyroxenites

	Mantle Stage	Pyroxenite crystallisation	Pyroxenite re-equilibration	Amphibolite	Late Retrogression
Cpx		**Cpx I**	**Cpx exsolution in Opx**		**Cpx II**
Opx	**Opx relict**	**Opx**	**Opx exsolution in Cpx**		
Olivine					
Spinel		**Cr-Al Spinel**			**Magnetite**
Fl Inc		**I**	**I**	**II**	
Amphibole				**MgHb→Trem Hb**	**Trem**
Sulphide				**Grains**	**Veins**
Magnetite					
Serpentine					
Pectolite					
Wollastonite					
Chlorite					

Abbreviations: Opx: orthopyroxene; Cpx: clinopyroxene; Fl Inc: Fluid Inclusions; MgHb: magnesio-hornblende; TremHb: tremolitic hornblende; Trem: tremolite.
Numbers (I, II) refer to different generations of fluid inclusions or clinopyroxenes.

boundaries are consistent with dynamic recrystallisation that is indicative of relatively high temperature conditions (Passchier and Trouw, 1996).

The G1-pyroxenites mainly have porphyroclastic microstructures accompanied by a variable degree of deformation. Some samples have no deformation (Fig. 3-4A) whereas others show evidence of high deformation illustrated by kinked orthopyroxene crystals (Fig. 3-4B). The most deformed orthopyroxenites (samples 16.05 and 18.03) generally have the highest degree of alteration (Fig. 3-3). In contrast, samples 14.18 and 14.14 have undeformed coarse-grained textures. These two samples are composite orthopyroxenites with locally clinopyroxene-enriched zones (Fig. 3-4D). G1-orthopyroxene generally occurs either as large subhedral grains with lobate grain boundaries or as small grains. Large orthopyroxene grains exhibit abundant exsolution lamellae of clinopyroxene (Fig. 3-5A), whereas small orthopyroxene crystals show more restricted exsolution features. Clinopyroxene is not a very abundant phase in the G1-orthopyroxenites with a modal proportion not exceeding 15%. Clinopyroxene occurs as relatively small sized (10μm to 400μm across) grains with anhedral crystal shapes (Fig. 3-5C). Orthopyroxene exsolution lamellae within clinopyroxene are restricted. Spinel is a common minor phase of the orthopyroxenites but with a limited modal abundance (< 2%). Spinel forms discrete subhedral rhombs at grain boundaries (Fig. 3-5D) or is included in large orthopyroxene grains. Olivine occurs relatively frequently as interstitial anhedral grains between pyroxene crystals but in the small proportion (< 10 modal %). Sample18.03 is an exception as the olivine constitutes 20 % modal proportion (Table. 3-1).

The G2-websterites are distinct from the G1-orthopyroxenites by having clinopyroxene: orthopyroxene > 1. In contrast to the deformed porphyroclastic textures of the G1-orthopyroxenites, the G2-websterites are characterised by inequigranular fabric with no to low deformation (Fig. 3-4D, 3-4E). In addition, the size of the grains is also generally more homogeneous than in G1 (1 to 2mm across). Exsolution lamellae of orthopyroxene only occur in clinopyroxene biggest grains (Fig. 3-5B) while no exsolution exists in small clinopyroxene grains. No exsolution of clinopyroxene has been observed in any orthopyroxene grain. The G2-websterites are devoid of spinel. Olivine appears rarely except in sample 15.03, which contains approximately 2 %.

The texture of the G3 clinopyroxenites is typically seriate with large subhedral grains (1-5mm in size) of clinopyroxene enclosed in a mosaic of fine-grained clinopyroxene (200μm across) (Fig. 3-4F). Many of the clinopyroxene grains have exsolution of spinel; these form aligned needles characterised by small size (<10μm) and some are accompanied by orthopyroxene exsolution blebs (Fig. 3-5E, 3-5F). However, only small amounts (<10 modal %) of orthopyroxene and/or olivine occur as small grains interstitially or as inclusions in clinopyroxene. Although sample 15.07 is texturally similar to the other G3-clinopyroxenites, its mineralogy is radically different by containing a large amount of amphibole (35 modal %) for only 45 modal % clinopyroxene (instead of >80 modal % for G3-clinopyroxenites). In this sample, amphibole and clinopyroxene are texturally in equilibrium. Serpentine appears frequently in this sample while orthopyroxene remains very discreet. Because of its distinct mineralogy, the sample 15.07 belongs to the sub-group G3b whereas the other clinopyroxenites (15.11, 15.13 and 15.16) are part of the G3a Group (Table 3-1).

Exsolution textures in the San Jorge and Santa Isabel pyroxenites attest that after crystallisation, the pyroxenes re-equilibrated. Intragranular clusters of fluid inclusions are found trapped in clinopyroxene crystals remote from grain boundaries (Fig. 3-5G). They are interpreted to represent primary fluid inclusions (Fig. 3-5G) and are consistent with the presence of fluid during clinopyroxene growth (Van Den Kerkhof and Hein, 2001). Although the mineralogy of the three petrographic groups of pyroxenites seem to be relatively simple, it is nevertheless possible to discern a complex polystage history of pyroxene growth and equilibration. For example, within G2 and G3, small (<0.2mm) relics of optically-continuous

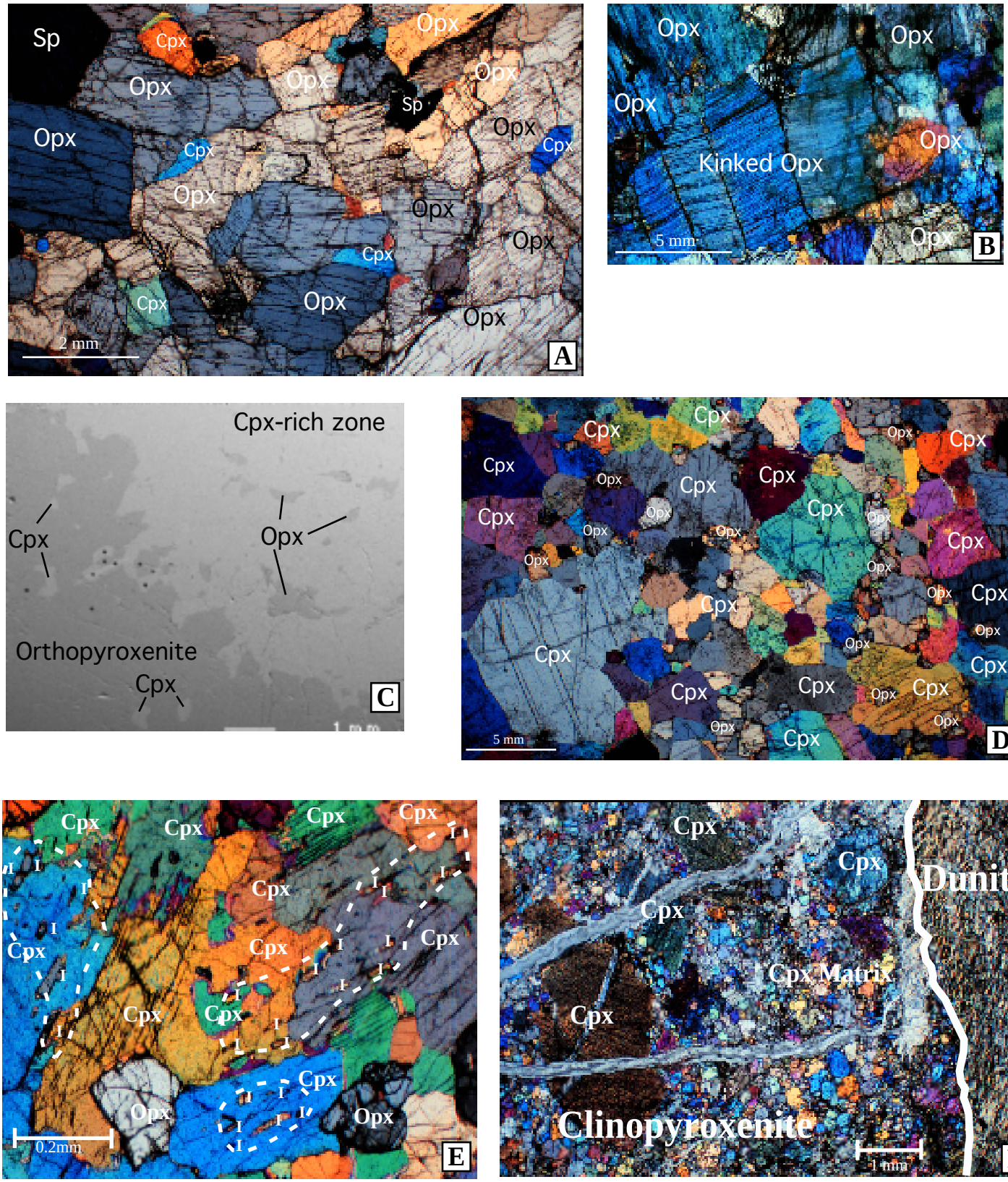

Fig. 3-4: Textural characteristics of the pyroxenites from San Jorge and Isabel.
List of Abbreviations: Opx=orthopyroxene; Cpx: clinopyroxene; Sp=spinel.
A) Cross-polar images of the undeformed porphyroclastic G1-orthopyroxenite (sample 16.11).
B) Cross-polar images of the G1-orthopyroxenite 14.01 featuring the highly deformed kinked orthopyroxene porphyroclast (at the centre of the picture) surrounded by small orthopyroxene neoblasts.
C) Back-scattered SEM image of a composite orthopyroxenite (sample 14.18). In the bottom left corner of the image, the orthopyroxene crystals (dark color) are dominant whereas in the top right corner, the orthopyroxene crystals become scattered in a clinopyroxene-dominated zone.
D) Cross-polar images of typical inequigranular G2-websterite (14.15) containing small to large pyroxene crystals. In this sample, the orthopyroxene grains are smaller than the clinopyroxene crystals.
E) Cross-polar images of the replacing texture of a websterite (16.09) I: relict of mantle opx.
F) Cross-polar images of the contact between clinopyroxenite (vein) and a dunite (sample 15.13).

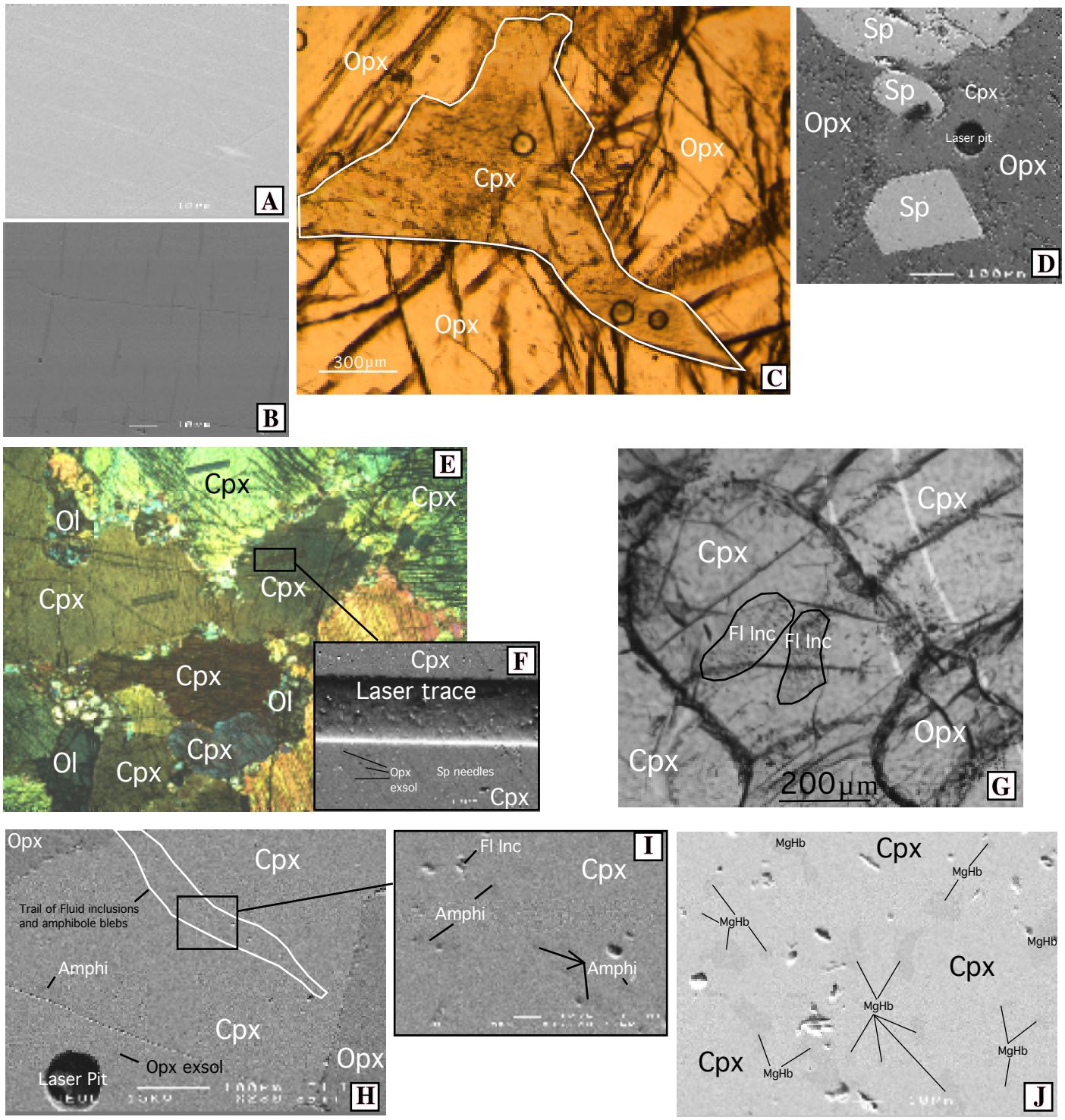

Fig. 3-5: Petrological characteristics of the pyroxenites from San Jorge and Isabel.
A) Back scattered SEM image of clinopyroxene exsolutions (bright lines) within an orthopyroxene grain (dark background) from the sample 14.01 (G1-orthopyroxenite).
B) Back scattered SEM image of orthopyroxene exsolutions (dark lines) within an orthopyroxene grain (bright background) from the sample 16.09 (G2-websterite).
C) Microscopic image of an anhedral clinopyroxene (Cpx) interlocked between orthopyroxene porphyroclasts (Opx) in the G1-orthopyroxenite (sample 14.01).
D) Back scattered SEM image of spinel subhedral rhombs between pyroxene crytals (sample 14.01: G1-orthopyroxenite).
E) Cross-polar image of inequigranular G3-clinopyroxenite (sample 15.16) containing variable-sized large clinopyroxene (Cpx) and small interstitial olivine grains (Ol).
F) Back scattered SEM image of needle-shaped spinel exsolutions (Sp) within large clinopyroxene crystals (Cpx) from sample 15.16 (b).
G) Back scattered SEM image of primary fluid inclusions wihtin a clinopyroxene crystal from a G2-websterite (sample 18.08)
H) Back scattered SEM image of a trail of secondary fluid inclusions accompanied by amphibole. The trail of fluid inclusions and amphibole crosscuts a clinopyroxene crystal in the G1-orthopyroxenite (sample 16.01).
I) Zoom in (Back scattered SEM image) on the amphibole blebs (Amphi) associated with the fluid inclusions (Fl Inc).
J) Back scattered SEM image of magnesiohornblende (MgHb) blebs scattered within a clinopyroxene crystal in a G2-websterite (sample 18.08).

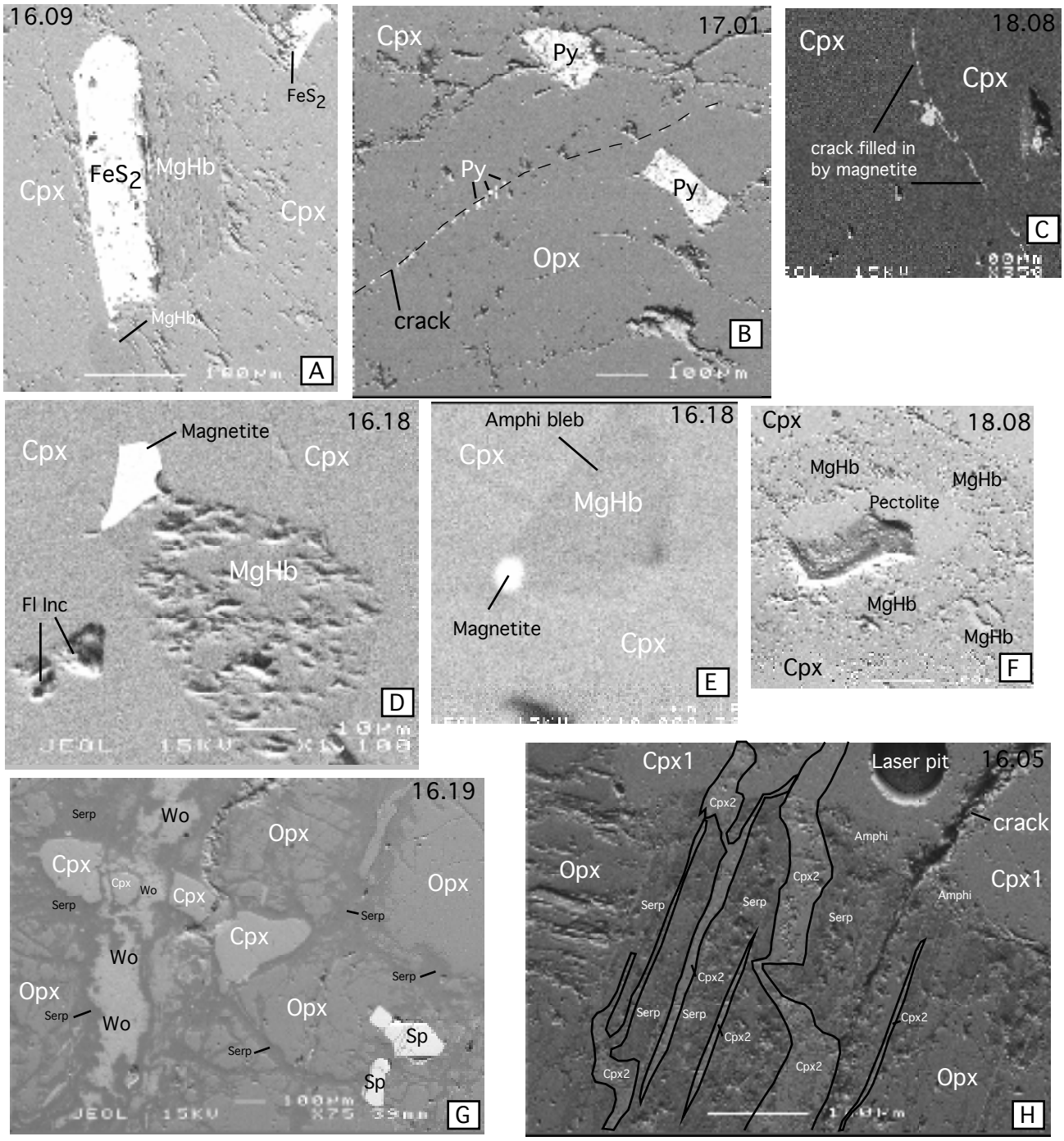

Fig. 3-6: Back-scattered SEM images of the secondary assemblages of the San Jorge and Santa Isabel pyroxenites.

List of Abbreviations: Opx=orthopyroxene; Cpx=clinopyroxene; Sp=spinel; Amphi=amphibole; MgHb=magnesiohornblende; FeS_2=Fe-sulfide; Py=pyrite; Serp=serpentine; Wo=wollastonite; Chl=chlorite.

A) Fe-sulfide associated with grain of magnesiohorblende in a G2-websterite (sample 16.09).
B) Anhedral Pyrite in a late-stage crack (G2-websterite: sample 17.01).
C) Magnetite formed in the late-stage crack crossing a clinopyroxene crystal (G2-websterite: sample 18.08).
D) Magnetite grain associated with amphibole (magnesiohorblende) (G2-websterite: sample 16.18).
E) Tiny anhedral magnetite grain crystallised at the periphery of an amphibole bleb within a clinopyroxene crystal of the sample 16.18 (G2-websterite).
F) Pectolite within a magnesiohornblende-rich area (G2-websterite: sample 18.08).
G) Anhedral Wollastonite in a late-stage vein of serpentine crossing the G1-orthopyroxenite (sample 16.19).
H) Complex multistage alteration process in the sample 16.05 (G1-orthopyroxenite). Multi veins of secondary clinopyroxenes (Cpx2) crosscutting an anhedral-shaped clinopyroxene (Cpx1) and highly serpentinised orthopyroxene porphyroclast. Interstitial amphibole grains also rim of the Cpx1-clinopyroxene.
I) Rare chlorite amongst a serpentine vein in the sample 15.11 (G3-clinopyroxenite).

orthopyroxene occur surrounded by modally predominant clinopyroxene (Fig. 3-4E). At a macroscopic level, the invasion of a pre-existing peridotitic mantle assemblage by pyroxene veins is clear (Fig. 3-4F). Figure 3-4F illustrates some microscopic effects of the contact between a dunite and invasive clinopyroxenite.

5.2 Retrograde assemblages

With the exception of sample 15.07, amphibole is a common retrograde phase in all pyroxenites, but rarely exceeds 2% of the mode. In these samples, amphibole occurs as an interstitial phase between interlocking pyroxene crystals, and can appear as blebs, mainly within clinopyroxene. Amphibole streaks or flames are generally very small (10μm in length), but can be highly concentrated within clinopyroxene, giving a poikilitic aspect to the pyroxene crystals (Fig. 3-5J). Amphibole in pyroxene is typically accompanied by secondary fluid inclusions (Fig. 3-6I). These fluid inclusions form trails crosscutting grain boundaries (Fig. 3-5H, 3-5I), consistent with entrapment after the growth of the host clinopyroxene, and possibly contemporaneous with growth of amphibole. Interstitial amphibole is often associated with grains of Fe-sulfide (pyrite and pyrrhotite) (Fig. 3-6A) and Ni-sulfide; the sulfide appears to be in textural equilibrium with the amphibole (Fig. 3-6A). Anhedral Fe-sulfide is also present in late-stage cracks (Fig. 3-6B).
Magnetite only appears in trace amounts, and is often closely associated with amphibole (Fig. 3-6D). Tiny anhedral magnetite grains, as small as 1 μm in maximum dimension, are crystallised at the periphery of amphibole blebs and grains (Fig. 3-6E). Magnetite also formed in late cracks crossing all of the minerals (Fig. 3-6C). Thin rims of serpentine surround many orthopyroxene and olivine grains, but the majority of the pyroxenites have < 1% serpentine. In some samples of G1 orthopyroxenite (16.05, 16.19, and 18.03), serpentine forms veins crosscutting all the phases and is presumably related to late alteration (Fig. 3-6H). Wollastonite ($CaSiO_3$) is present in the most altered orthopyroxenite (16.19), and accompanies late-stage vein serpentinisation (Fig. 3-6G). Chlorite is very limited and only occurs, amongst the serpentine matrix in one G3 clinopyroxenite (15.11) (Fig. 3-6I). Pectolite [$Ca_2NaH(SiO_3)_3$] is present in samples 16.05 (G1) and 18.08 (G2) in association with serpentine veins (16.05) and late amphibole (18.08) (Fig. 3-6F), indicating a late stage alteration paragenesis. Secondary clinopyroxene is also present in orthopyroxenite 16.05, occurring in veins developed syn- to post-serpentinisation (Fig. 3-6H).

6 BULK ROCK COMPOSITION

6.1 Major Elements

The major element compositions of the pyroxenites are strongly controlled by their abundances (Table 3-1 and Table 3-3). The pyroxenites are characterised by high $Mg^{2+}/(Mg^{2+}+Fe \text{ as } Fe^{2+})$ (Mg#) ranging from 0.83 to 0.92 (Fig. 3-7). The orthopyroxenites (G1) and clinopyroxenites (G3) tend to have higher Mg#s than the websterites (G2). As might be anticipated, in a plot of CaO versus Mg# (Fig. 3-7A), the orthopyroxenites (G1) are clearly distinctive compared with the G2 and G3 pyroxenites. The G2-websterites differ from the G3-clinopyroxenites by having a wider range in Mg# over a similar range of CaO contents. In details, the composite orthopyroxenites plot together with close the other orthopyroxenites despite having clinopyroxene-rich patches. This indicates that these clinopyroxene-rich zones are not too frequent in the analysed sample.

Table 3-3: Whole rock major compositions.

Sample	14.01	16.01	16.05	16.11	16.19	18.03	14.18	14.14	14.33	16.09	16.18	16.20	15.03	17.01	14.15	14.16	18.08	15.11	15.13a	15.16	15.07
Group	G1-orthopyroxenite								G2-websterite									G3-clinopyroxenite			
SiO_2	55.37	54.05	50.57	54.57	53.14	49.06	56.61	55.87	53.07	53.52	53.35	53.31	53.01	53.05	54.75	54.89	52.56	47.89	46.49	51.69	51.46
Al_2O_3	1.16	1.90	2.07	2.69	1.59	1.26	0.67	0.79	2.01	1.85	1.23	1.65	1.63	1.77	0.66	0.74	2.24	1.77	2.15	2.62	3.57
Fe_2O_3	6.88	7.60	6.74	8.17	7.39	8.39	6.69	6.65	4.96	5.22	5.99	5.43	8.51	8.69	4.70	4.89	6.39	5.04	4.64	3.99	4.87
MnO	0.15	0.16	0.14	0.17	0.15	0.15	0.15	0.15	0.13	0.13	0.16	0.15	0.20	0.19	0.13	0.13	0.14	0.10	0.10	0.09	0.10
MgO	33.80	32.47	31.34	31.29	32.72	35.05	32.85	31.26	19.85	20.30	20.95	19.40	20.90	21.44	24.97	25.03	20.02	23.65	24.55	18.87	20.90
CaO	1.53	1.67	3.85	2.29	2.24	1.55	2.63	4.76	18.79	17.91	17.26	19.27	15.31	14.25	13.51	13.17	17.44	15.43	15.12	21.07	15.92
Na_2O	0.02	0.02	0.10	0.06	0.02	0.02	0.03	0.05	0.22	0.20	0.15	0.21	0.13	0.13	0.21	0.17	0.19	0.39	0.11	0.20	0.71
TiO_2	0.02	0.04	0.05	0.07	0.04	0.03	0.02	0.03	0.07	0.07	0.06	0.07	0.08	0.07	0.03	0.03	0.10	0.13	0.15	0.18	0.17
Cr_2O_3	0.75	0.74	1.44	0.65	1.24	1.20	0.41	0.43	0.58	0.56	0.32	0.46	0.06	0.15	0.64	0.65	0.26	0.56	0.86	0.77	0.34
NiO	0.10	0.09	0.09	0.09	0.10	0.16	0.10	0.10	0.07	0.08	0.04	0.05	0.02	0.05	0.08	0.08	0.04	0.07	0.08	0.04	0.06
LOI	0.78	1.52	4.10	0.67	1.59	3.60	0.20	0.32	0.43	0.29	0.70	0.46	0.33	0.50	0.94	0.55	1.08	5.38	5.89	0.82	1.89
Total	100.6	100.3	100.5	100.7	100.2	100.5	100.4	100.4	100.2	100.2	100.2	100.4	100.2	100.3	100.6	100.3	100.5	100.4	100.2	100.4	100.1
FeO	6.19	6.83	6.07	7.35	6.65	7.54	6.02	5.98	4.46	4.70	5.39	4.88	7.66	7.82	4.23	4.40	5.75	4.53	4.17	3.59	4.39
Mg#	0.91	0.89	0.90	0.88	0.90	0.89	0.91	0.90	0.89	0.89	0.87	0.88	0.83	0.83	0.91	0.91	0.86	0.90	0.91	0.90	0.89

All major elements are in wt %
Samples 14.14 & 14.18 are the composite orthopyroxenites and sample 15.07 is the amphibole-rich clinopyroxenite.

Table 3-4: Whole rock trace element compositions.

Sample	14.01*	16.01*	16.05*	16.11*	16.19*	18.03**	14.18**	14.14*	14.33*	16.09**	16.18**	16.20*	15.03*	17.01*	14.15*	14.16*	18.08*	15.11**	15.13*	15.16**	15.07**
Group	G1-orthopyroxenite								G2-websterite									G3-clinopyroxenite			
Rb	0.127	0.138	0.783	bdl	0.050	0.438	0.755	0.088	0.059	0.132	0.121	0.065	0.041	0.010	0.170	0.073	0.057	0.082	0.039	0.065	0.203
Sr	2.312	2.111	16.119	1.852	6.503	24.453	2.206	3.593	14.612	9.926	16.505	11.885	10.567	6.461	17.111	12.154	15.007	12.986	9.341	12.593	21.458
Y	0.175	0.312	0.506	0.741	0.378	0.313	0.348	0.446	2.720	3.223	2.283	1.930	2.461	1.911	0.977	0.800	1.654	3.000	2.853	4.466	4.042
Zr	0.028	0.209	0.327	0.324	0.202	0.262	0.310	0.201	0.809	1.137	0.985	1.029	1.550	0.795	0.472	0.549	2.048	3.225	2.282	2.944	21.651
Nb	0.008	0.005	0.007	bdl	0.012	0.013	0.013	0.004	0.013	0.032	0.019	0.006	0.016	0.007	0.001	0.007	bdl	0.042	0.012	0.035	0.346
Cs	1.153	1.224	5.544	0.076	0.238	0.013	0.199	0.154	0.161	0.883	1.530	0.160	bdl	bdl	1.507	0.106	bdl	0.010	bdl	0.008	0.012
Ba	2.673	3.219	33.457	5.355	308.480	0.512	1.625	1.160	2.503	5.537	20.325	9.526	0.570	0.109	2.651	2.238	0.138	1.777	0.852	0.225	4.667
La	bdl	0.147	bdl	0.013	0.017	0.016	0.033	0.008	0.058	0.089	0.101	0.053	0.061	0.023	0.032	0.033	0.085	0.329	0.124	0.179	2.137
Ce	bdl	0.418	bdl	0.014	0.016	0.010	0.016	0.029	0.210	0.216	0.211	0.122	0.253	0.101	0.133	0.149	0.364	0.678	0.435	0.520	4.752
Pr	bdl	0.049	bdl	bdl	bdl	bdl	bdl	0.007	0.055	0.052	0.047	0.027	0.060	0.024	0.034	0.033	0.079	0.111	0.107	0.120	0.566
Nd	bdl	0.194	0.025	0.031	0.018	0.012	0.017	0.054	0.385	0.382	0.311	0.190	0.416	0.175	0.254	0.219	0.522	0.654	0.740	0.842	2.102
Sm	bdl	0.033	0.022	0.022	0.018	0.009	0.018	0.032	0.213	0.233	0.169	0.124	0.222	0.113	0.133	0.103	0.231	0.311	0.343	0.448	0.542
Eu	bdl	0.009	0.009	0.010	0.014	0.006	0.006	0.012	0.086	0.088	0.067	0.055	0.085	0.050	0.040	0.038	0.100	0.113	0.138	0.166	0.180
Gd	0.009	0.032	0.046	0.064	0.031	0.024	0.023	0.058	0.380	0.414	0.296	0.264	0.376	0.249	0.181	0.161	0.353	0.457	0.527	0.660	0.650
Tb	bdl	bdl	bdl	bdl	bdl	bdl	bdl	0.011	0.073	bdl	bdl	0.052	0.070	0.051	0.028	0.026	0.058	bdl	0.096	bdl	
Dy	0.029	0.050	0.084	0.115	0.071	0.044	0.049	0.085	0.544	0.353	0.380	0.394	0.502	0.376	0.171	0.169	0.376	0.540	0.689	0.812	0.700
Ho	0.009	0.014	0.022	0.031	0.018	0.012	0.011	0.020	0.121	bdl	bdl	0.089	0.110	0.085	0.036	0.035	0.076	bdl	0.141	bdl	
Er	0.032	0.052	0.077	0.107	0.063	0.033	0.042	0.061	0.344	0.309	0.256	0.258	0.326	0.250	0.096	0.096	0.206	0.308	0.360	0.467	0.419
Tm	0.007	0.010	0.013	0.018	0.012	bdl	bdl	0.010	0.049	bdl	bdl	0.038	0.047	0.038	2.347	0.014	0.029	bdl	0.051	bdl	
Yb	0.055	0.081	0.095	0.129	0.094	0.066	0.054	0.067	0.309	0.330	0.248	0.237	0.310	0.249	0.094	0.090	0.184	0.266	0.307	0.378	0.375
Lu	0.011	0.016	0.017	0.023	0.018	0.008	0.009	0.011	0.049	0.052	0.039	0.038	0.050	0.040	0.016	0.015	0.029	0.040	0.048	0.055	0.060
Hf	bdl	0.010	0.020	0.023	0.010	0.010	0.012	0.015	0.049	0.062	0.046	0.055	0.079	0.053	0.021	0.032	0.123	0.115	0.116	0.140	0.565
Pb	0.122	0.161	0.056	0.057	0.266	1.066	1.055	bdl	0.227	0.626	0.424	0.105	0.243	0.157	0.750	0.065	0.129	0.572	0.228	0.444	0.558
Ti	147	220	281	369	212	180	134	156	440	452	326	390	470	395	165	162	589	754	941	1079	972

All trace elements are in ppm. Measured by ICP-MS; * = solution ICP-MS, ** = Laser ablation ICP-MS (LA-ICP-MS)
bdl: below detection limit
Samples 14.14 & 14.18 are the composite orthopyroxenites and sample 15.07 is the amphibole-rich clinopyroxenite.

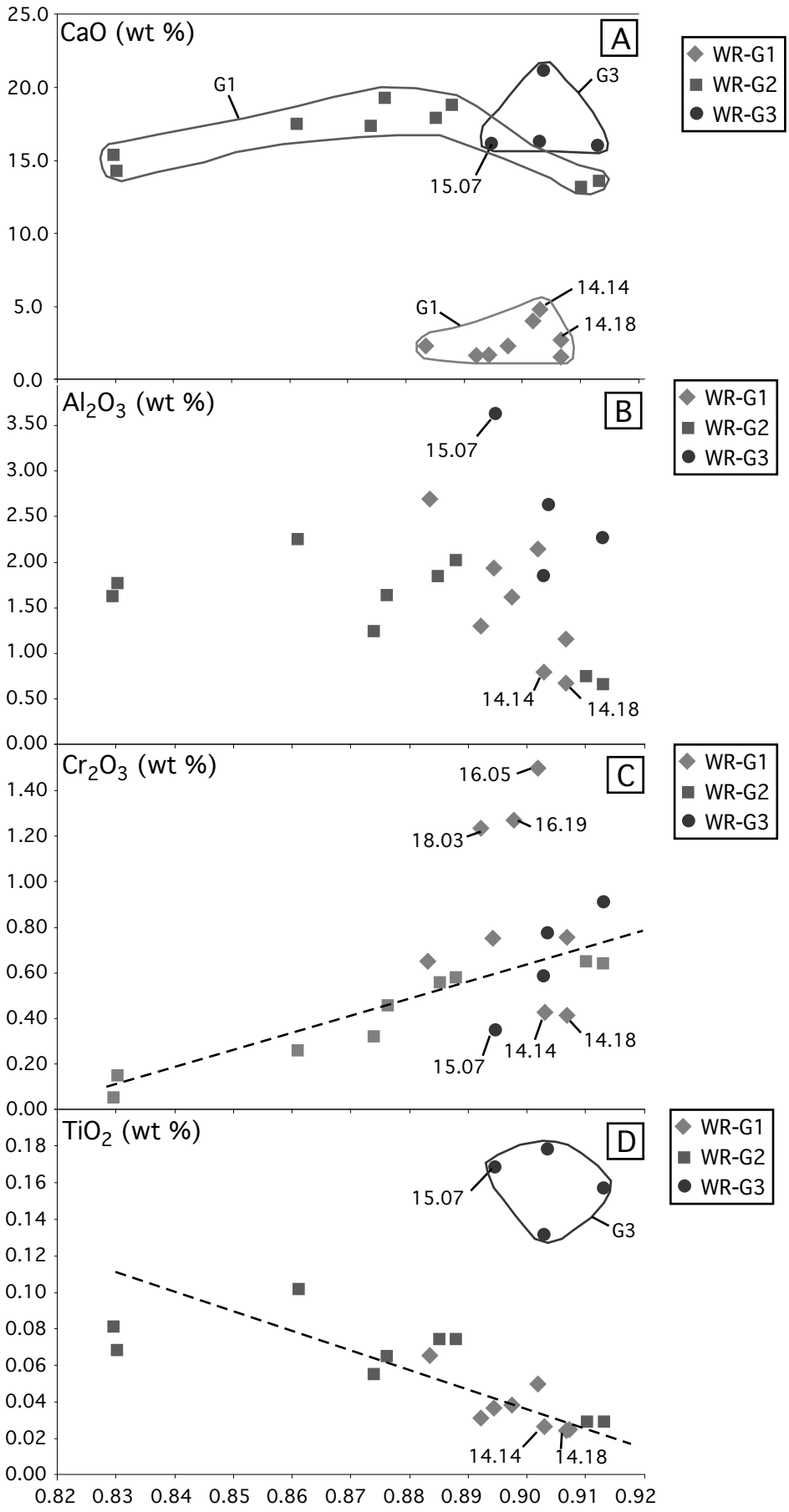

Fig. 3-7: Variation diagrams of wt % CaO (A), Al_2O_3 (B), Cr_2O_3 (C) and TiO_2 (D) vs. Mg-number (Mg#) for the whole rock (WR) pyroxenites.
Samples 14.14 & 14.18 are the composite orthopyroxenites and sample 15.07 is the amphibole-rich clinopyroxenite.

All of the pyroxenites are characterised by restricted but low Al_2O_3 contents (0.6-2.7%) regardless of Mg# with the exception of the sample 15.07 which has the highest Al_2O_3 (3.6 wt %). Excluding this sample, the orthopyroxenite 16.11 has a high Al_2O_3contents (2.7 wt%) compared to the other pyroxenites which average 1.5 wt % Al_2O_3. No correlation exists within any Group between the Mg# and Al_2O_3 (Fig. 3-7B). In contrast, a positive correlation does exist between Mg# and Cr_2O_3 contents, particularly for the G2-websterites (Fig. 3-7C). Orthopyroxenites with high modal spinel proportions (16.05, 16.19 and 18.03) (Table. 3-1) are clearly offset from the grouping of other samples in terms of higher Cr_2O_3 contents at equivalent Mg#. The TiO_2 contents are negatively correlated with Mg# for G1- and G2-pyroxenites, ranging from 0.02 wt % (Mg# = 0.91) to 0.08 (Mg# = 0.83) (Fig. 3-7D). By contrast, the TiO_2 contents (~0.18 wt %) of the G3-samples (including sample 15.07) are much higher than for the other groups.

6.2 Trace elements

Whole rock concentrations of trace elements in the pyroxenites are listed in Table 3-4. Trace elements concentrations were obtained using two types of ICPMS techniques (Solution- and LA- ICP-MS). Figure 3-8 illustrates the concentrations of trace element measured by LA ICP-MS and Solution ICP-MS for the sample 16.20 (G2-websterite), which is quite representative of the samples both analysed by the two methods. Overall, the comparison between the two methods used on the same samples, has proven that the concentrations of trace element were very similar (Fig. 3-8) except for Pb and Nb. Pb is systematically found more concentrated in the samples analysed by LA ICP-MS than it is by Solution ICP-MS, indicating a Pb contamination during sample preparation of fused disks. However the fact that high Pb concentration is variably observed in the samples measured by Solution ICP-MS suggests that contamination during sample preparation is not entirely responsible for the Pb enrichment. Unlike Lead, Nb is slightly more concentrated in the sample analysed by LA ICP-MS than by Solution ICP-MS for the same sample. This might suggest that Nb-bearing phases (i.e. spinel) are hard to dissolve into the solution when attacked by acids during sample preparation.

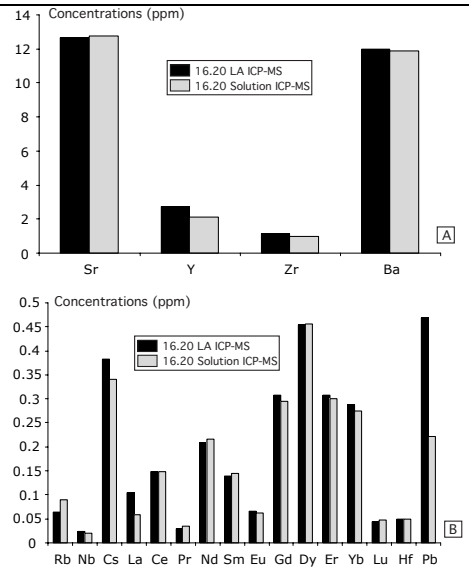

Fig. 3-8: Variations in trace element concentrations (ppm)
A) moderately concentrated (Sr, Y, Zr & Ba)
B) with low concentrations (REE, Rb, Cs, Pb, Nb, Lu & Hf) measured by LA ICP-MS and Solution ICP-MS for the whole-rock (WR) G2-websterite (sample 16.20) from San Jorge. Details of the analytical methods are given in the text.

6.2.1 Rare Earth Elements

Although the various pyroxenite groups show distinctive chondrite-normalised ($_N$) REE abundance patterns (Fig. 3-9), most of the pyroxenites from San Jorge and Santa Isabel are characterised by a consistent light (L)REE depletion together with relative low REE abundances.

The orthopyroxenites (G1) have very low heavy (H)REE contents (Yb_N= 0.2-0.8) and a steady decrease from the HREE to middle (M) atomic weight REE (Gd_N=0.04-0.16) (Fig. 3-9A). The light (L) atomic weight REE (LREE) (La-Eu) contents typically proved difficult to analyse because their concentrations are below the ICP-MS detection limits. By extrapolation, most of the orthopyroxenites seems to be LREE depleted with the exception of sample 16.01, which clearly displays a strong enrichment in LREE (La-Eu) (Fig. 3-9A). The composite orthopyroxenite samples (14.18 and 14.14) have similar HREE contents to the other pyroxenites but are distinct from them by having flatter HREE-MREE gradients and being more enriched in LREE, given them a convex-upward REE shape (Fig. 3-9A).

Some of the G2-websterites show similar convex-upward REE_N patterns with depleted LREE relative to MREE, and relatively flat HREE-MREE gradients [$(Gd/Yb)_N$~1]. However, three websterites (14.15, 14.16 and 18.08) are distinct from the G2a-websterites by having unusual bell-shaped REE_N patterns, characterised by enrichment in the MREE relative to both L- and HREE [$(Gd/Yb)_N$=1.4 - 1.6] (Fig. 3-9B). Overall all of the G2-websterites and the G1-orthopyroxenites have striking low HREE abundances (Yb_N between 0.4 and 2) even for samples with high modal proportions of clinopyroxene (Fig. 3-9B).

The REE_N patterns of the G3a-clinopyroxenites are comparable to those of the G2b-websterites (Fig. 3-9C) with characteristic bell shapes. However, the clinopyroxenites are slightly more enriched in REE than the G2-websterites with Ce_N = 0.7-1.1, Gd_N = 2.3-3.3 and Yb_N = 1.6-2.3 (Fig. 3-9C). Unlike the other clinopyroxenites, the clinopyroxenite 15.07 exhibits a LREE-enriched pattern with a strong negative La-Gd slope [$(La/Gd)_N$=2.8] (Fig. 3-9C). Despite its LREE enrichment, the sample 15.07 has similar HREE abundances to the G2a-clinopyroxenites.

6.2.2 Other trace elements

Primitive mantle-normalised, multi-element diagrams of the three pyroxenite groups are characterised overall by large ion lithophile element (LILE) enrichments relative to REE (except for G3 pyroxenites), and in particular, positive Pb and Sr anomalies relative to neighbouring REE (Ce and Nd, respectively) (Fig. 3-10). There is no correlation between the LOI and LILE (e.g., Cs, Rb and Ba) abundances (Fig. 3-11A), indicating that the general increase in LILE concentrations relative to the REE is not due to low temperature alteration. As serpentinisation is limited in the pyroxenites, the large positive Sr spikes seem to reflect a primary origin. Furthermore, the positive Sr anomalies relative to neighbouring REE elements are not correlated with positive Eu anomalies (Fig. 3-11B).

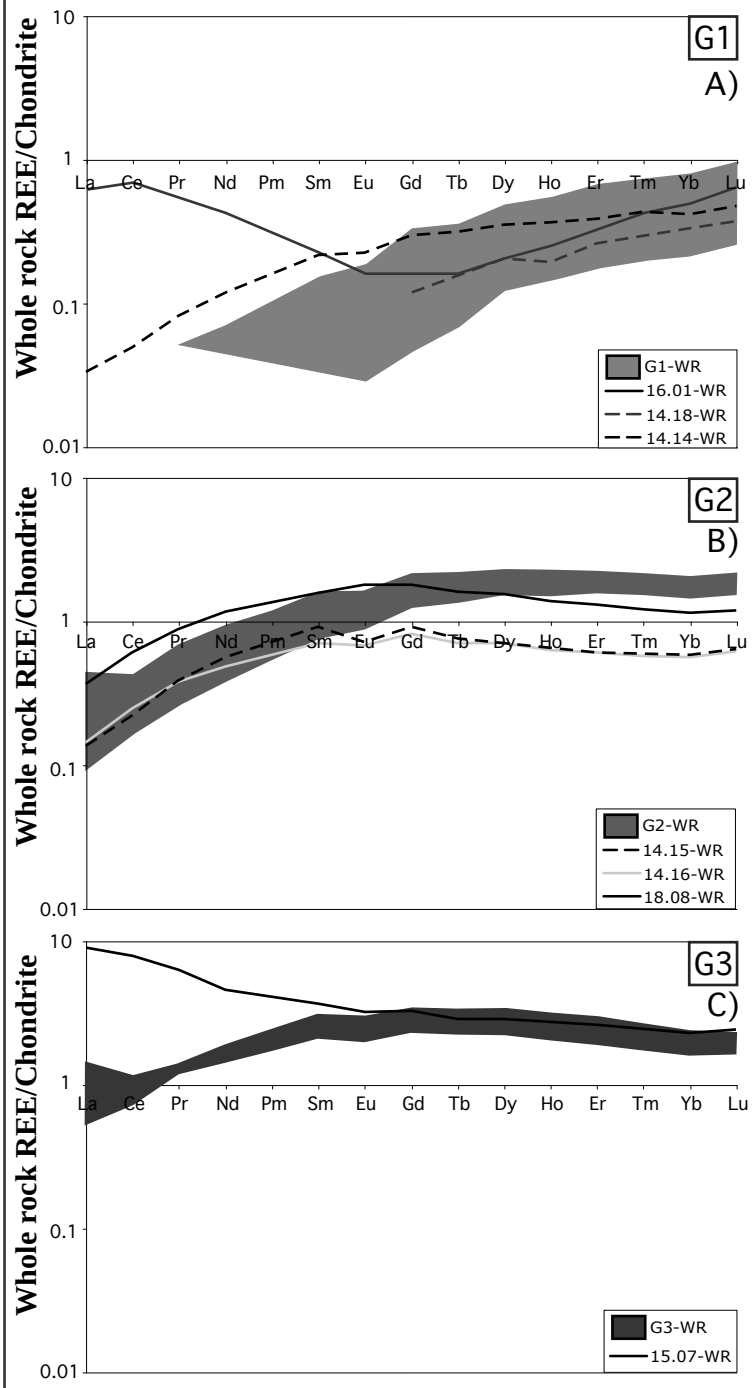

Fig. 3-9: Chondrite-normalised whole rock (WR) REE patterns for representative pyroxenites from San Jorge and Santa Isabel A) G1-orthopyroxenites; B) G2-websterites; C) G3-clinopyroxenites. Chondrite values from Sun & McDonough (1989).

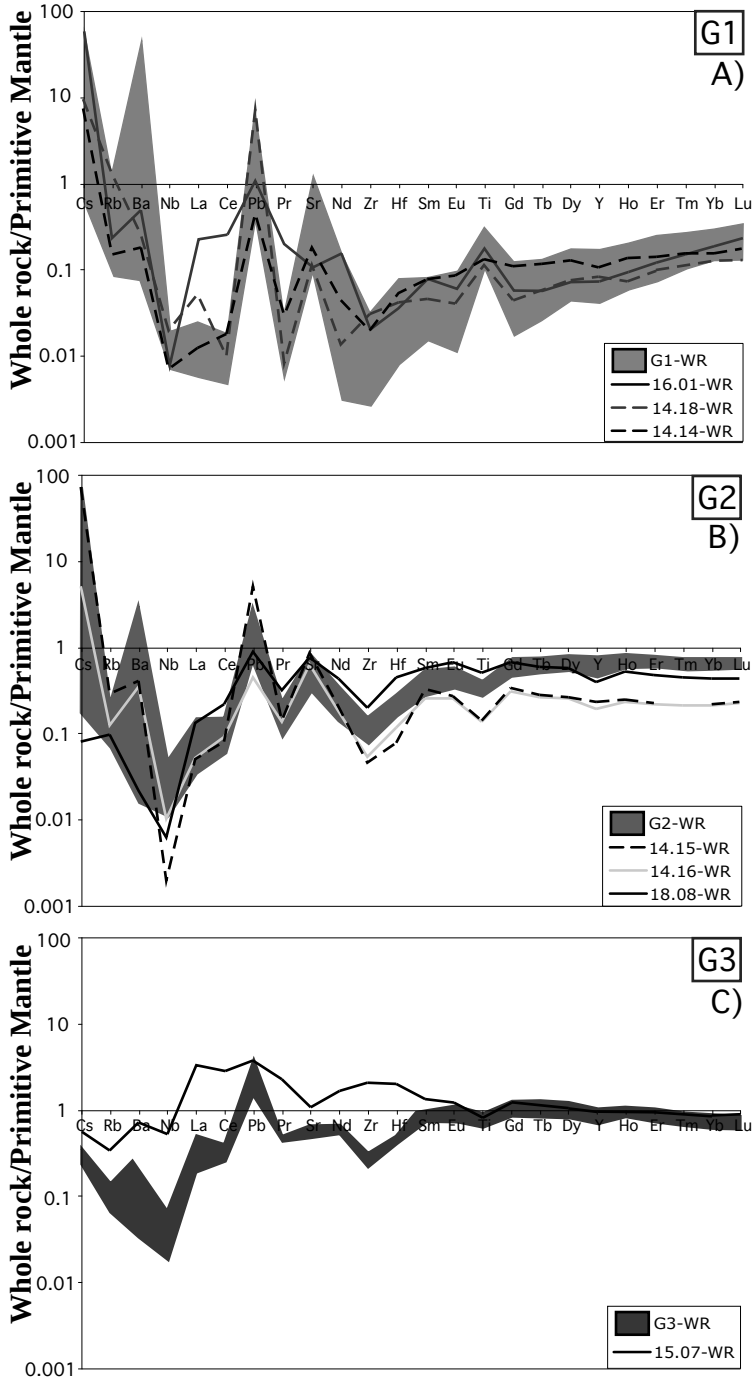

Fig. 3-10: Primitive Mantle-normalised whole rock (WR) multi-element patterns for representative pyroxenites from San Jorge and Santa Isabel A) G1-orthopyroxenites; B) G2-websterites; C) G3-clinopyroxenites. Primitive Mantle values from Sun & McDonough (1989).

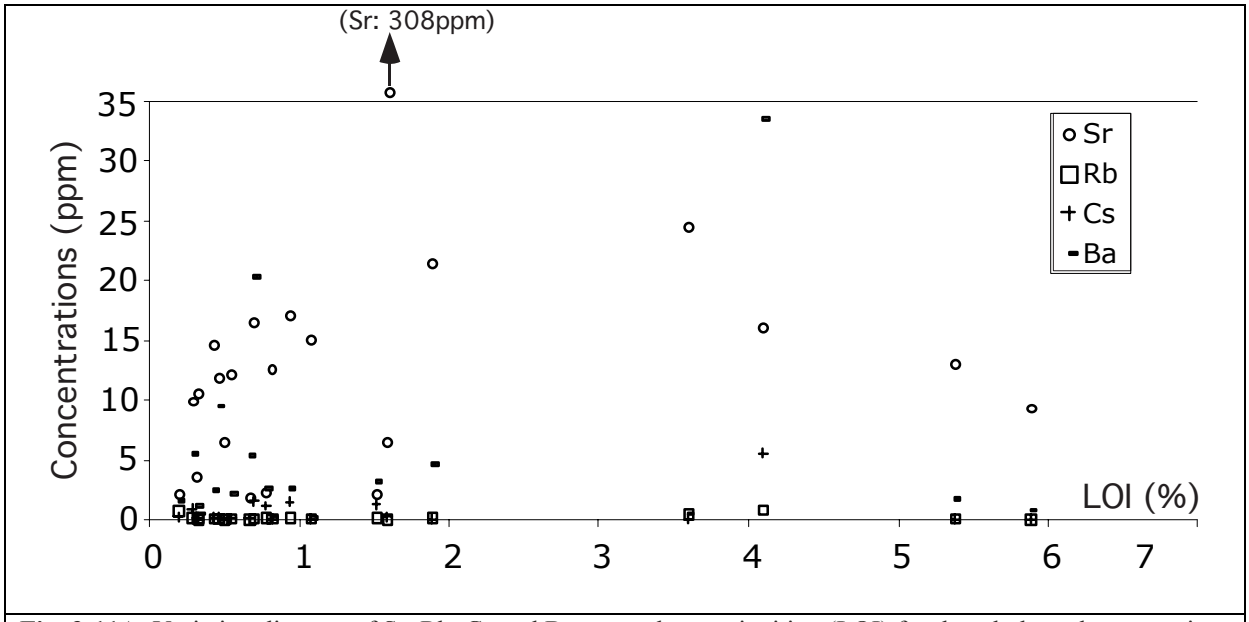

Fig. 3-11A: Variation diagram of Sr, Rb, Cs and Ba versus loss on ignition (LOI) for the whole rock pyroxenites. Sr, Rb, Cs and Ba are in ppm whereas LOI is expressed in %.

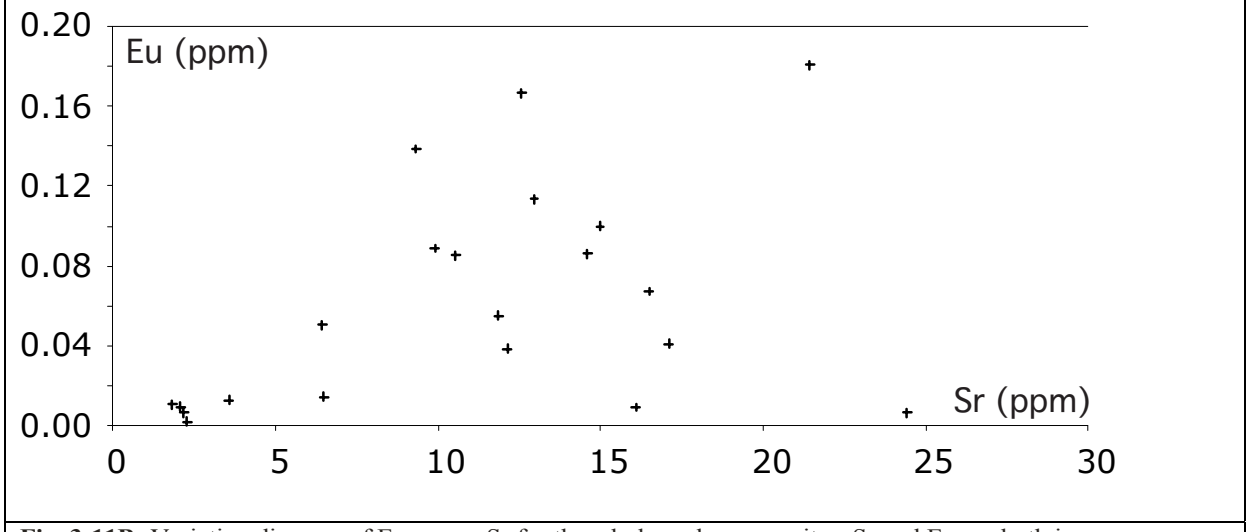

Fig. 3-11B: Variation diagram of Eu versus Sr for the whole rock pyroxenites. Sr and Eu are both in ppm.

Despite some overall similarities, the three-pyroxenite groups also differ from each other in terms of specific LILE and high field strength element (HFSE) abundance systematics. For example, the G1-orthopyroxenites are distinctive from the clinopyroxene-rich groups in terms of: 1) marked enrichments of Cs and Ba relative to Rb; 2) strikingly positive Pb and Sr spikes relative to Ce and Nd; 3) positive Ti spikes relative to Eu and Gd and; 4) absence of negative Zr and Hf anomalies relative to Nd and Sm. It is also noteworthy that the absolute abundances of Cs, Ba, Pb, and Sr are highest in the orthopyroxenites (Table 3-4, Fig. 3-10). No difference exists between the two subgroups of orthopyroxenites (G1a and G1b) in term of LILE, Pb, Sr and HFSE elements (Fig. 3-10A).

Like the G1-orthopyroxenites, the G2-websterites have striking enrichments in LILE, Pb and Sr relative to REE including for the samples with the REE bell-shaped patterns (Fig. 3-10B). The only differences in the primitive mantle-normalised multi-element patterns of the G1-orthopyroxenites and the G2-websterites are that the websterites exhibit variable negative anomalies in Nb relative to La [$(Nb/La)_N<1$] and negative Ti anomalies relative to Eu and Gd.

These Nb and Ti anomalies also feature in the primitive mantle-normalised multi-element patterns of the G3-clinopyroxenites. However, the G3-clinopyroxenites differ from the G2-websterites by only exhibiting moderate enrichments in Cs, Rb, Ba (LILE elements). Unlike the G2-websterites, there are no Sr spikes for the G3-clinopyroxenites while positive Pb anomalies still persist in these rocks (Fig. 3-10C). In addition to the LREE enrichment, the primitive mantle-normalised multi-element pattern for the sample 15.07 is distinct to the patterns for other clinopyroxenites (G3a). Sample 15.07 has no Nb negative anomaly, only a slight enrichment in Pb relative to the neighbouring elements (Ce and Pr) and a negative Sr anomaly compared to neighbouring REE (Pr and Nd) (Fig. 3-10C). Furthermore, it is the only sample amongst all the pyroxenites that Zr and Hf are enriched relative to Nd.

7 MINERAL COMPOSITION

7.1 Orthopyroxene

Representative orthopyroxene compositions are given in Table 3-5. Their CaO contents are relatively low (< 1 wt %). The Mg# of G1-orthopyroxene and G3-orthopyroxene are restricted and comparable to accepted mantle values ranging from 0.88 to 0.91. In contrast, the Mg# values for orthopyroxene in G2 range between 0.78 and 0.90 (Fig. 3-12). The Al_2O_3 contents of all of the orthopyroxene are all low, averaging 1.37 wt % in a range from 0.45-2.35wt %; the highest concentration is in orthopyroxene from sample G1-16.11 (Fig. 3-12A). Overall, a positive correlation between Cr_2O_3 content and Mg# is observed in orthopyroxene, although within groups this is not obvious, except possibly in G2. The Cr_2O_3 contents reach 0.64 wt % (for Mg# = 0.91) in the G1-orthopyroxenite, and decreases to 0.04 wt % (Mg# = 0.79) in the G2-websterites (Fig. 3-12B).
Figure 3-14A shows that no variation in major elements (SiO_2, MgO, FeO, Al_2O_3, Cr_2O_3 and Na_2O) was detected in the orthopyroxene grains from the sample 14.01 (G1-orthopyroxenite) using the Scanning Electron Microscope. This feature was also observed in orthopyroxene crystals from the other pyroxenites.

7.2 Clinopyroxene

7.2.1 Primary clinopyroxene

Clinopyroxene has limited compositional variation (Table 3-6). The Mg# decreases in the same sequence as for orthopyroxene (G1>G3>G2), consistent with equilibrium between the respective pyroxenes (Fig. 3-15A). As is the case with orthopyroxene, the Al_2O_3 contents of clinopyroxene remain unchanged with decreasing Mg# (Fig. 3-13A). Consistent with the coexisting orthopyroxene, the highest Al_2O_3 content (2.6 wt%) is present in clinopyroxene of orthopyroxenite 16.11; Al_2O_3 contents of the other clinopyroxene average 1.5 wt %. The Cr_2O_3 correlates positively with Mg# (Fig. 3-13B). While the Cr_2O_3 contents of clinopyroxene from G1 and G3 (except the sample 15.07) are relatively high ($Cr_2O_3 > 0.3$) for a given Mg# (~0.92), those of G2 have both lower Cr_2O_3 and Mg# (Fig. 3-13B). The Cr_2O_3 contents of the orthopyroxene from the sample 15.07 are low (~0.1 wt%) despite the high Mg# (~0.92).
Like in the orthopyroxene crystals, no zoning (rim-core) was observed in the clinopyroxene grains of the G1-orthopyroxenite 14.01 (Fig. 3-15B) as well as in the clinopyroxene crystals of the other pyroxenites.

Table 3-5: Representative analyses of orthopyroxene and calculated endmembers compositions.

Sample	14.01	16.01	16.05	16.11	16.19	18.03	14.18	14.14	14.33	16.09	16.18	16.20	15.03	17.01	14.15	14.16	18.08	15.16	15.07
Group	G1-orthopyroxenite								G2-websterite									G3-clinopyroxenite	
SiO_2	57.22	56.49	56.17	55.69	56.81	57.18	57.31	56.85	55.52	56.01	55.55	55.76	54.92	54.75	57.72	57.41	55.61	57.27	56.81
TiO_2	0.02	bdl	0.11	0.12	0.12	bdl	0.04	bdl	0.04	0.04	bdl	0.06	0.04	0.14	bdl	0.07	0.05	0.04	0.04
Al_2O_3	1.09	1.74	1.59	2.34	1.16	0.96	1.24	1.08	1.69	1.57	0.95	1.22	1.37	1.48	0.43	0.45	1.46	1.56	0.74
Cr_2O_3	0.51	0.56	0.63	0.54	0.44	0.37	0.46	0.26	0.41	0.38	0.20	0.14	0.04	0.15	0.21	0.35	0.15	0.25	0.15
FeO*	6.30	7.49	6.17	7.72	6.49	6.87	7.84	8.99	9.42	9.73	10.90	10.81	14.20	12.55	6.78	6.83	11.63	7.79	7.69
MnO	0.08	0.16	0.14	0.04	0.12	0.07	0.10	0.16	0.12	0.07	0.19	0.10	0.17	0.16	0.10	0.12	0.26	n.d.	0.23
MgO	34.54	33.10	33.00	32.05	33.18	33.66	33.06	32.41	31.17	31.18	30.70	30.42	28.53	29.04	34.12	33.65	30.70	33.40	33.28
CaO	0.70	0.66	0.91	0.93	1.02	0.61	0.68	0.82	0.85	0.67	0.77	0.73	0.80	0.97	0.95	0.94	0.58	0.52	0.55
Na_2O	n.d	0.22	0.22	0.21	0.25	0.25	0.23	0.13	0.26	0.27	n.d.	0.26	0.01	0.22	bdl	0.26	0.01	0.21	bdl
Σ	100.46	100.16	98.57	99.46	99.24	99.79	100.82	100.64	99.19	99.77	99.27	99.32	100.08	99.11	100.32	99.75	100.44	101.05	100.12
% En	90	88	89	86	88	89	87	85	84	84	82	82	77	79	88	88	83	88	88
% Fs	9	11	9	12	10	10	11	13	14	15	16	16	21	19	10	10	16	11	11
% Wo	1	1	2	2	2	1	2	2	2	1	1	1	2	2	2	2	1	1	1
Mg#	0.91	0.89	0.91	0.88	0.90	0.90	0.88	0.87	0.86	0.85	0.83	0.83	0.78	0.80	0.90	0.90	0.84	0.88	0.89

*Total iron as FeO
n.d: not determined
bdl: below detection limit
Samples 14.14 & 14.18 are the composite orthopyroxenites and sample 15.07 is the amphibole-rich clinopyroxenite.

Table 3.6: Representative analyses of clinopyroxene and calculated endmembers composition.

Sample	14.01	16.01	16.05 (1)	16.05 (2)	16.11	16.19	18.03	14.18	14.14	14.33	16.09	16.18	16.20	15.03	17.01	14.15	14.16	18.08	15.11	15.13	15.16	15.07
Sub-group	G1-orthopyroxenite									G2-websterite									G3-clinopyroxenite			
SiO_2	55.15	53.81	54.02	54.59	52.46	54.06	54.07	54.73	53.58	52.71	53.00	53.98	53.08	52.73	52.85	54.29	54.25	54.59	54.03	54.04	52.50	54.31
TiO_2	bdl	bdl	0.16	0.22	0.13	0.07	0.14	0.16	bdl	0.11	0.08	0.10	0.17	0.08	0.18	bdl	0.15	bdl	0.08	0.09	0.15	0.07
Al_2O_3	1.15	1.60	1.23	0.23	2.61	1.52	1.25	1.35	1.07	1.88	1.69	1.14	1.40	1.56	1.70	0.66	0.63	1.84	0.62	1.82	2.12	0.68
Cr_2O_3	0.74	0.66	0.83	0.18	0.80	0.77	0.74	0.74	0.37	0.59	0.58	0.29	0.22	bdl	0.13	0.83	0.75	0.16	0.34	0.76	0.49	0.13
FeO*	2.17	2.52	2.78	4.76	2.89	2.15	2.47	2.72	3.14	3.45	3.27	4.01	3.81	4.95	4.90	2.14	2.30	4.21	2.41	2.59	2.88	2.82
MnO	0.08	0.08	0.09	bdl	0.08	0.10	bdl	bdl	bdl	0.09	bdl	0.07	bdl	0.09	0.08	bdl	0.08	0.05	bdl	bdl	0.11	bdl
MgO	17.94	17.42	16.94	16.66	16.60	17.43	17.25	17.36	17.15	16.57	16.32	17.11	16.29	16.19	16.22	17.17	17.35	16.87	17.14	17.55	16.94	17.34
CaO	24.78	23.81	24.11	24.54	23.53	23.80	24.14	24.45	23.47	23.06	23.57	23.22	23.56	23.74	23.00	24.05	23.84	24.17	24.78	24.74	23.49	24.55
Na_2O	0.12	0.27	0.34	0.17	0.21	0.35	0.29	0.33	bdl	0.34	0.37	0.26	0.31	bdl	0.38	0.00	0.41	0.07	bdl	bdl	0.26	bdl
Σ	102.17	99.94	100.26	101.34	99.10	100.40	100.13	101.85	98.81	98.32	98.52	99.87	98.46	99.28	98.84	99.28	99.22	102.01	99.15	101.58	98.61	99.90
% En	49	48	47	45	47	49	48	48	48	47	46	47	46	45	46	48	48	46	47	48	48	47
% Fs	3	4	4	7	5	3	4	4	5	6	5	6	6	8	8	3	4	6	4	4	5	4
% Wo	48	48	48	48	48	48	48	48	47	47	48	46	48	47	47	48	48	47	49	48	48	48
Mg#	0.94	0.92	0.92	0.86	0.91	0.94	0.93	0.92	0.91	0.90	0.90	0.88	0.88	0.85	0.86	0.93	0.93	0.88	0.93	0.92	0.91	0.92

*Total iron as FeO
(1): Primary clinopyroxene; (2) Secondary clinopyroxene (CpxII)
bdl: below detection limit
Samples 14.14 & 14.18 are the composite orthopyroxenites and sample 15.07 is the amphibole-rich clinopyroxenite.

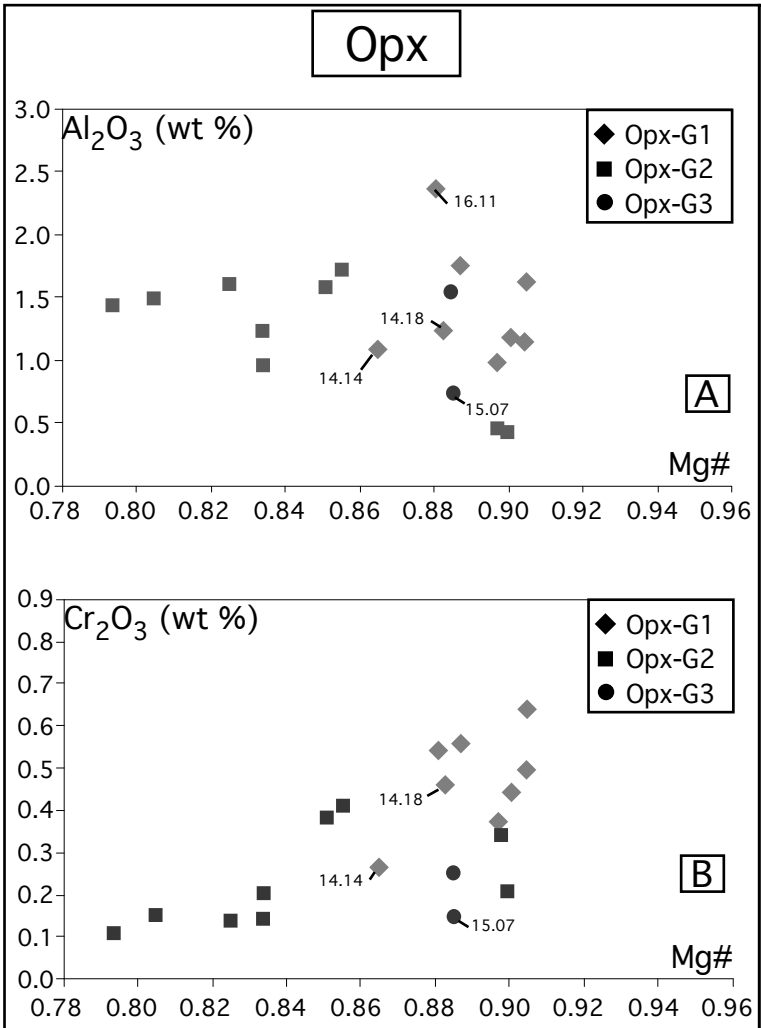

Fig. 3-12: Variation diagram of wt % Al_2O_3 (A) and Cr_2O_3 (B) versus Mg# for the orthopyroxene in the different pyroxenites (G1, G2, G3). Samples 14.14 & 14.18 are the composite orthopyroxenites and sample 15.07 is the amphibole-rich clinopyroxenite.

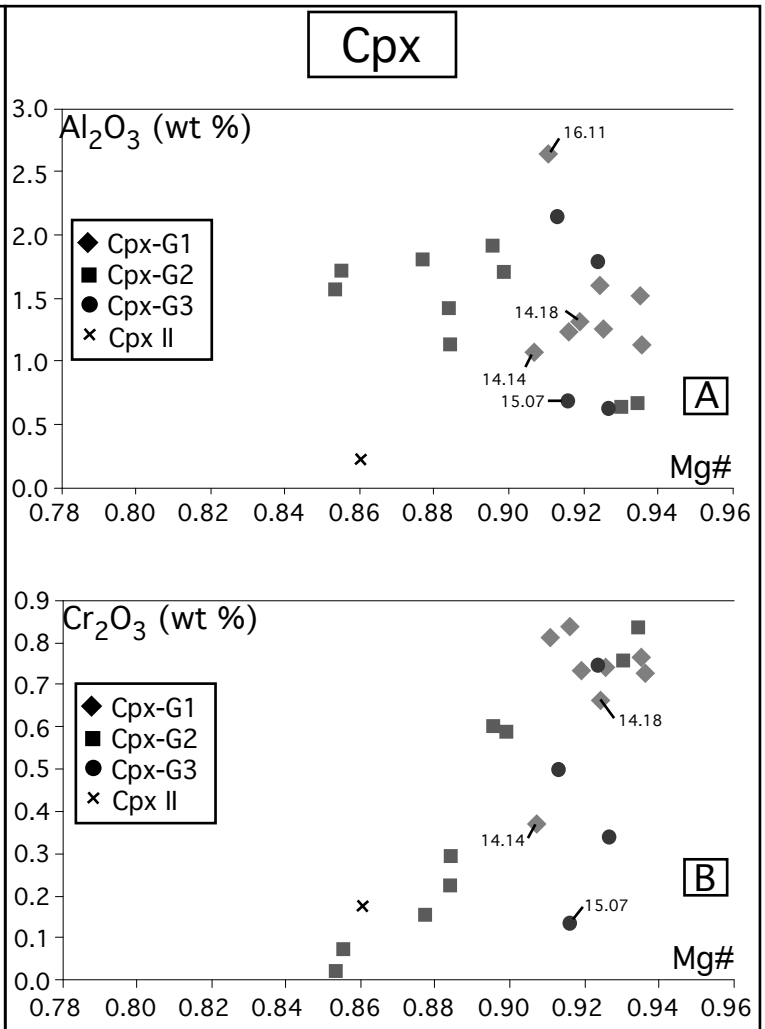

Fig. 3-13: Variation diagram of wt % Al_2O_3 (A) and Cr_2O_3 (B) versus Mg# for the clinopyroxene in the different pyroxenites (G1, G2, G3). Samples 14.14 & 14.18 are the composite orthopyroxenites and sample 15.07 is the amphibole-rich clinopyroxenite.

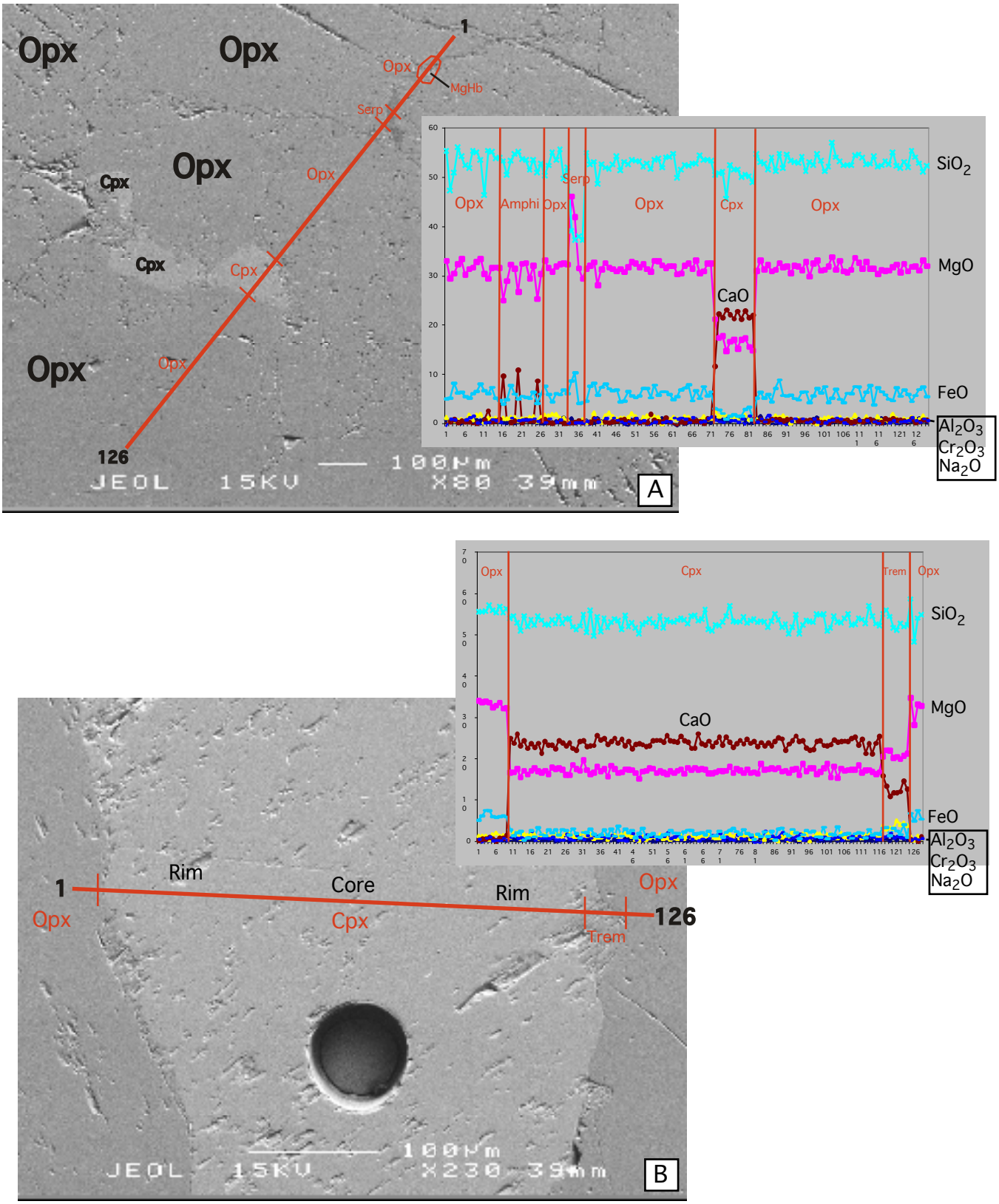

Fig. 3-14: Chemical variations in major elements (SiO_2, MgO, FeO, Al_2O_3, Cr_2O_3 and Na_2O) across orthopyroxene crystals (A) and within one clinopyroxene grain (B) from the orthopyroxenite 14.01. Major elements cross section compositions were determined using the scanning electron microscope (SEM) and shown above in the time versus major elements graphs. The SEM was used to obtain the back scattered images of the programmed traverses.
Abbreviations: Opx: Orthopyroxene; Cpx: Clinopyroxene; Amphi: Amphibole; Trem: Tremolite; Serp: Serpentine.

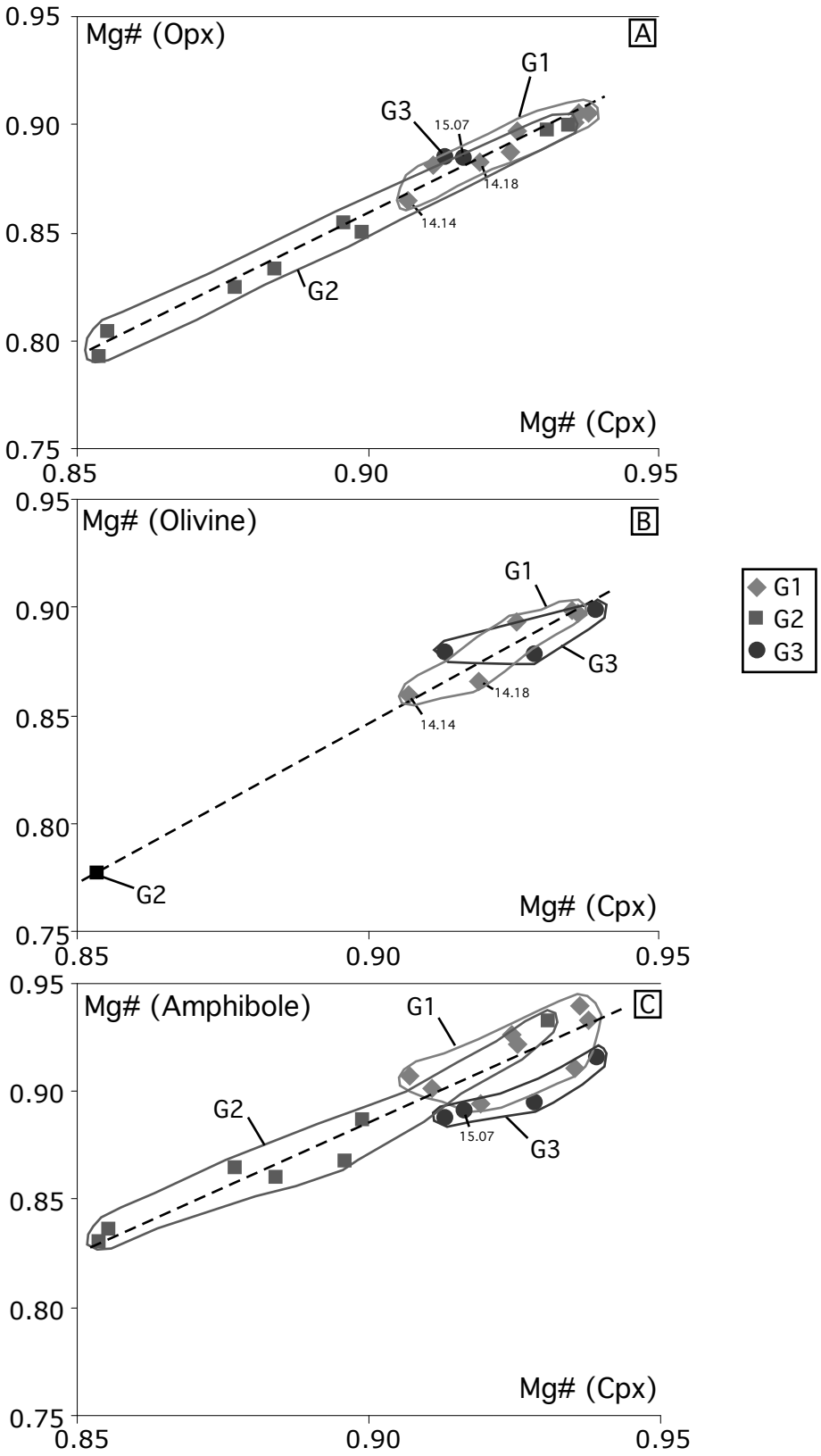

Fig. 3-15: Plot of Mg# of clinopyroxene versus Mg# of orthopyroxene (A), Mg# of olivine (B) and Mg# of amphibole (C) for the San Jorge / Santa Isabel pyroxenites.
G1: Orthopyroxenite; G2: Websterite; G3: Clinopyroxenite.
Note the perfect positive correlation between Mg# (Cpx) and Mg# Opx, olivine and amphibole.
Samples 14.14 & 14.18 are the composite orthopyroxenites and sample 15.07 is the amphibole-rich clinopyroxenite.

7.2.2 Secondary clinopyroxene

The secondary clinopyroxene (Cpx II) (Table 3-6) is chemically distinct from the primary clinopyroxene in having lower Al_2O_3 (0.23 wt %), and lower Cr_2O_3 (0.18 wt %) contents compared to primary clinopyroxene with similar Mg# (Fig. 3-13B).

7.3 Olivine

Olivine grains are compositionally unzoned and homogeneous within individual samples. Representative olivine compositions are given in Table 3-7. Within all pyroxenites, the forsterite (Fo) contents range from 76.5 – 90.3 mole%, with a high Fo average of 87.4%. The plot of NiO versus Mg# shows that the G1-olivine has high Fo (~89) and high NiO content (0.42 wt %) (Fig. 3-16) comparable to olivine from upper mantle peridotites (Girardeau and Ibarguchi, 1991). In contrast, the olivine from the composite orthopyroxenites has significantly lower Fo (~86) with slightly lower NiO concentrations. Sample 15.03 is the only websterite (G2), which contains olivine. Olivine from this sample has markedly low Fo (~76.8) content as well as a very low NiO content (0.15 wt %). G3-olivine is generally similar in terms of major elements (Fo_{88}) to G1-olivine, but has lower NiO (0.22 wt %). No olivine was found in the sample 15.07. Note that olivine seems to be in equilibrium with clinopyroxene and orthopyroxene, as the Fo correlates positively with the Mg# of clinopyroxene and orthopyroxene (Fig. 3-15B).

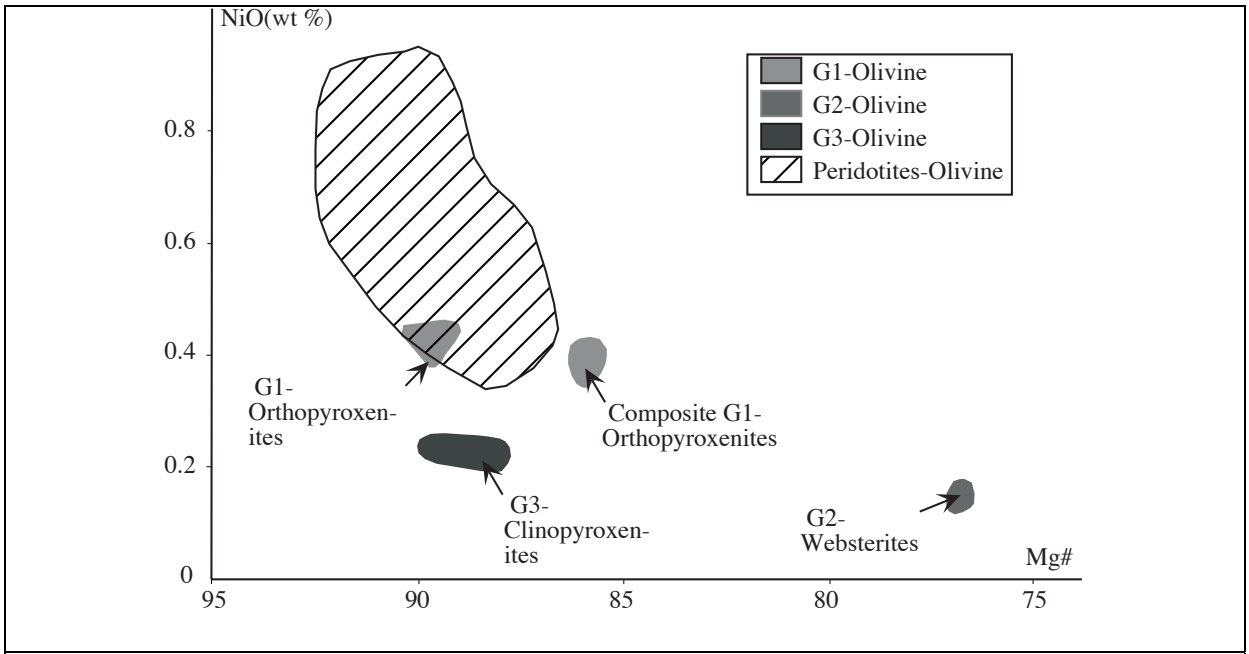

Fig. 3-16: NiO versus Mg# of olivine. Field of the Cabo Ortegal peridotites is from Girardeau & Ibarguchi, 1991.
Composite G1-orthopyroxenites are represented by samples 14.14 & 14.18. The G2-olivine was only found in the sample 15.03. No olivine occurs in the sample 15.07 (amphibole-rich clinopyroxenite).

7.4 Spinel

Representative chromian spinel compositions are presented in Table 3-8. Only spinel from G1 and G3 pyroxenites are plotted as no spinel was found in the websterites (G2). The G1 and G3

Table 3-7: Representative analyses of olivine.

Sample	14.01	14.32	16.19	18.03	14.18	14.14	15.03	15.11	15.13	15.16
Group	G1-orthopyroxenite						G2	G3-clinopyroxenite		
SiO_2	40.85	41.42	40.46	41.26	40.72	40.39	39.23	41.34	41.25	40.92
FeO	10.21	10.12	9.88	10.16	12.90	13.42	21.11	11.79	9.81	11.62
MgO	49.05	49.12	48.58	48.11	46.57	46.71	39.41	47.80	48.79	47.78
NiO	0.44	n.a.	0.41	n.a.	0.41	0.42	0.13	n.a.	0.24	0.24
Total	100.7	100.7	99.6	99.9	101.0	101.1	100.2	101.5	100.4	100.8
Fo	90	90	90	89	87	86	77	88	90	88
Fa	11	10	10	11	13	14	23	12	10	12

Single representative point analyses of olivine are given. Ions are calculated on the basis of four oxygens
*Total iron as FeO
n.a., not analysed
Samples 14.14 & 14.18 are the composite orthopyroxenites.

Table 3-8: Representative spinel analyses.

Sample	14.01	16.01	16.05	16.05	16.05	16.11	16.19	18.03	15.13	15.16
Group	G1-orthopyroxenite								G3-clinopyroxenite	
TiO_2	0.18	0.18	0.25	0.32	0.21	0.20	0.16	0.17	0.27	0.28
Al_2O_3	14.56	20.83	19.41	19.28	18.16	27.09	16.60	16.37	25.47	34.10
Cr_2O_3	50.60	42.04	49.63	49.68	49.12	36.35	48.16	49.03	36.21	26.67
MgO	9.63	10.86	12.18	12.49	11.67	11.88	10.47	9.53	10.65	11.55
Fe_2O_3	5.05	6.55	2.36	2.31	3.01	5.10	4.72	3.56	6.72	5.90
FeO	18.83	18.46	16.94	16.42	16.94	17.75	18.21	19.63	19.59	19.20
Total	99.62	98.26	98.38	98.70	98.81	97.86	97.84	97.93	98.24	97.11
Ti^{4+}	0.004	0.004	0.006	0.007	0.005	0.005	0.004	0.004	0.006	0.006
Al^{3+}	0.560	0.780	0.712	0.708	0.681	0.985	0.637	0.633	0.936	1.215
Cr^{3+}	1.307	1.055	1.221	1.223	1.236	0.887	1.240	1.271	0.893	0.638
Mg^{2+}	0.469	0.514	0.565	0.580	0.554	0.547	0.508	0.466	0.495	0.521
Fe^{3+}	0.124	0.156	0.055	0.054	0.072	0.119	0.116	0.088	0.158	0.134
Fe^{2+}	0.514	0.490	0.441	0.428	0.451	0.458	0.496	0.538	0.511	0.486
Mg#	0.477	0.512	0.562	0.576	0.551	0.544	0.506	0.464	0.492	0.517
Cr#	0.700	0.674	0.731	0.737	0.728	0.474	0.661	0.697	0.488	0.344
$Fe^{3+}/3+$	0.062	0.079	0.028	0.027	0.036	0.060	0.058	0.044	0.079	0.068
$Fe^{3+}/Fetot$	0.194	0.242	0.111	0.112	0.138	0.206	0.189	0.140	0.236	0.217

Single representative point analyses of spinel are given.
*Fe_2O_3 calculated on the basis of 3 cations and 4 oxygens

Table 3-9: Representative analyses of amphibole.

Sample	16.05	16.11	18.03	16.09	16.18	14.18	15.03	17.01	18.08	15.13	15.16	15.07
Group	G1-orthopyroxenite						G2-websterite			G3-clinopyroxenite		
Type	2	1	2	1	1	1	1	3	2	1	1	1
SiO_2	52.61	49.33	53.06	51.31	51.62	51.26	49.67	55.64	53.68	50.58	47.53	50.06
TiO_2	0.29	0.39	0.20	0.48	0.13	0.20	0.63	0.13	0.13	0.57	0.90	0.40
Al_2O_3	5.71	9.80	5.42	7.38	6.29	7.27	9.03	2.38	4.77	8.41	10.37	6.87
Cr_2O_3	1.80	1.63	1.43	1.42	0.69	0.68	0.15	0.17	0.11	1.28	1.08	0.86
FeO	2.35	3.89	2.95	4.62	5.92	4.39	7.12	5.37	5.27	3.32	4.43	4.30
MgO	20.96	19.12	21.53	19.44	19.63	20.12	17.86	21.19	20.57	19.93	19.11	20.23
CaO	13.30	12.69	12.30	12.57	12.99	12.67	12.65	12.75	12.60	13.06	12.77	12.53
Na_2O	1.29	1.49	0.97	1.32	1.30	1.80	1.43	0.45	0.89	1.45	2.14	1.60
total	98.31	98.34	97.86	98.54	98.74	98.39	98.54	98.08	98.02	98.60	98.33	96.85
Si	7.26	6.81	7.28	7.07	7.14	7.08	6.91	7.63	7.38	6.96	6.61	7.00
Al iv	0.74	1.19	0.72	0.93	0.86	0.92	1.09	0.37	0.62	1.04	1.39	1.00
Al vi	0.19	0.40	0.16	0.27	0.16	0.26	0.39	0.02	0.15	0.33	0.31	0.13
Ti	0.03	0.04	0.02	0.05	0.01	0.02	0.07	0.01	0.01	0.06	0.09	0.04
Cr	0.20	0.18	0.16	0.15	0.08	0.07	0.02	0.02	0.01	0.14	0.12	0.10
Fe^{3+}	0.01	0.38	0.34	0.34	0.40	0.32	0.40	0.44	0.48	0.21	0.39	0.46
Fe^{2+}	0.26	0.06	0.00	0.19	0.28	0.19	0.43	0.18	0.13	0.17	0.12	0.04
Mg	4.31	3.93	4.40	3.99	4.05	4.14	3.70	4.33	4.22	4.09	3.96	4.22
Ca	1.97	1.88	1.81	1.86	1.92	1.87	1.88	1.87	1.86	1.93	1.90	1.88
Na	0.35	0.40	0.26	0.35	0.35	0.48	0.39	0.12	0.24	0.39	0.58	0.43
(Na+K)(A)	0.31	0.27	0.14	0.21	0.27	0.36	0.27	0.00	0.09	0.31	0.48	0.35
Mg#	0.94	0.90	0.93	0.88	0.86	0.89	0.82	0.88	0.87	0.91	0.88	0.89

Single representative point analyses of amphibole grains are given.
Cations are calculated on the basis of Sum(cations)-(Na+Ca+K)-13
Types of amphibole: 1: magnesio-hornblende; 2: tremolitic hornblende; 3: tremolite
bdl: below detection limit
K_2O was below detection limit (< 0.05 wt %)
Sample 14.18 is the composite orthopyroxenite and sample 15.07 is the amphibole-rich clinopyroxenite.

spinels are characterised by high molar Cr/(Cr+Al) (Cr#) (Fig. 3-17). In the G3-clinopyroxenite, individual spinel grains and exsolution blebs have similar compositions. On a plot of Cr# versus Mg# shown in Figure 3-18, the G1 and G3 spinel plot at higher Cr# and lower Mg# than the peridotite abyssal array (Dick and Bullen, 1984). The G1 and G3 spinel overlap in terms of Cr# but also extend to lower Mg# than spinel from the SSZ peridotite suite of the Izu-Bonin forearc peridotites (Parkinson and Pearce, 1998).

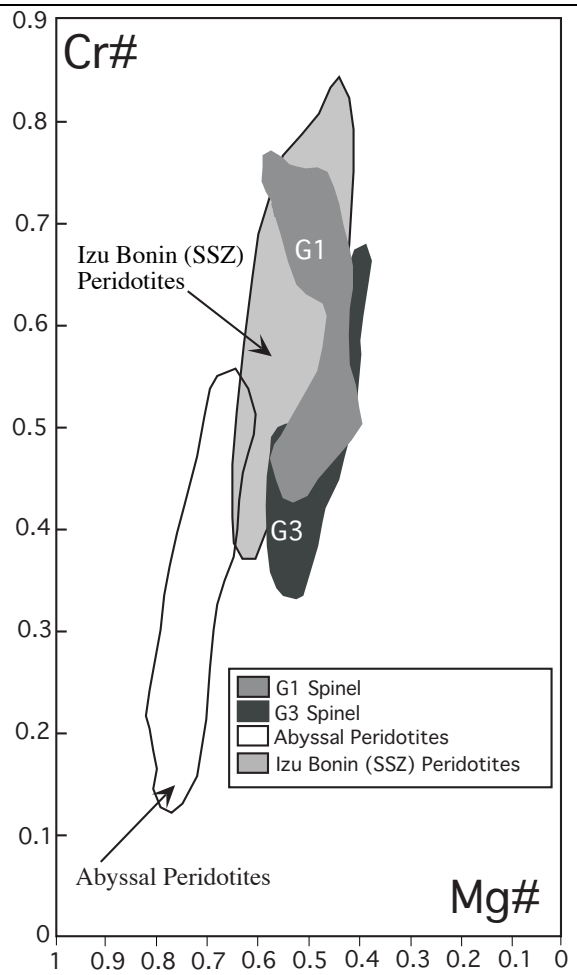

Fig. 3-17: Cr# versus Mg# for spinel of the pyroxenites. The field for the abyssal peridotites is from Dick and Bullen (1984). Field of Izu Bonin (SSZ) peridotites is from Parkinson & Pearce (1998).
No spinel was found in the composite orthopyroxenites (G1) and G3-spinel represented spinel from the clinopyroxenites with the exception of the amphibole-rich clinopyroxenite (sample 15.07) in which no spinel was to be found.

7.5 Amphibole

The composition of amphibole ranges from calcic hornblende to tremolite (Table 3-9, Fig. 3-18). The three groups of pyroxenites all contain magnesiohornblende, tremolitic-hornblende and tremolite. No distinction is made between the amphibole of different sub-groups and only the 3 major groups (G1, G2 and G3) are considered to classify the amphibole (see Fig. 3-18).

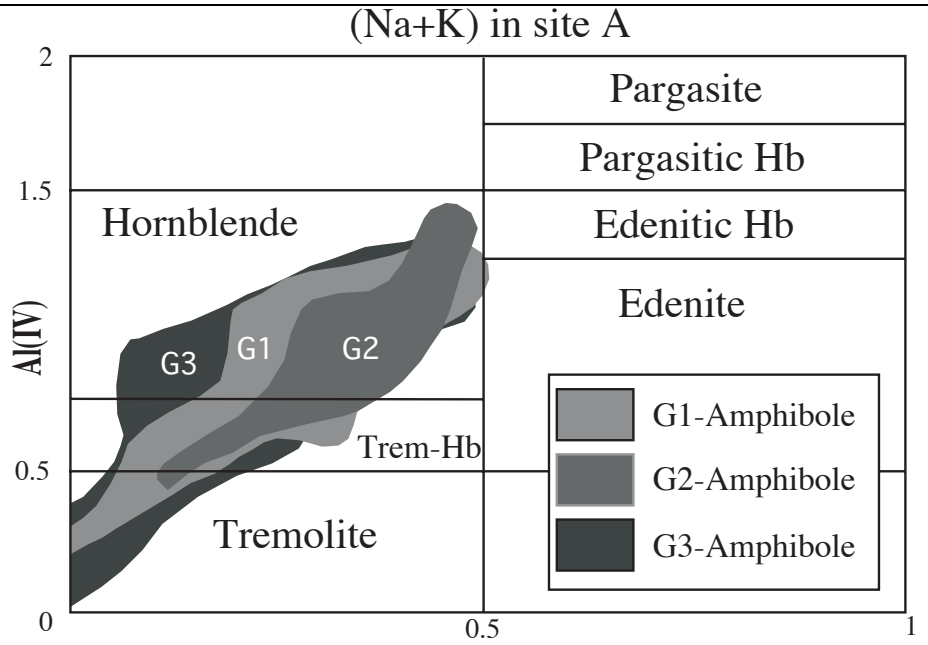

Fig. 3-18: Plot of (Na+K) in site A versus Al (IV) for amphibole after the classification of amphibole by Leake et al. (1978).

In all the groups, the hornblende has low TiO_2 (<0.2 wt %), K_2O (<0.2 wt %), intermediate Cr_2O_3 (0.84 – 0.99 wt %), and Na_2O (0.87 – 1.5 wt %), (Table. 3-9). The Al_2O_3 content is relatively high ranging from 5.66 to 11.44 wt % for the magnesiohornblende and between 1.49 and 6.06 wt % for the tremolitic-hornblende. Some magnesiohornblende from spinel-bearing orthopyroxenite is enriched in Cr_2O_3 (2.38 – 3.12 wt %). Tremolite has low Al_2O_3 content (2.2 – 4.3 wt %) as well as low Na_2O (0.37 wt % on average), but relatively high Cr_2O_3 contents (0.93 wt % in average). In a plot of Mg# (clinopyroxene versus amphibole), scatter of the data suggest only partial equilibrium between amphibole and pyroxene has been achieved, consistent with a retrograde origin for the amphibole (Fig. 3-15C).

8 CONDITIONS OF FORMATION OF THE PYROXENITES

8.1 Temperature

The equilibrium coexistence of clino- and orthopyroxene permits estimation of the temperatures of equilibration of the pyroxenites, with the conventional two-pyroxene thermometer of Wells (1969). The three groups (G1, G2, G3) of pyroxenite are estimated to have equilibrated at temperatures between 808°C and 935°C (Fig. 3-19A). The average temperatures calculated for G1 (879°C), G2 (884°C), and G3 (839°C) (Fig. 3-19B) are within error, probably not distinguishable, and provide evidence for recrystallisation at 850-900°C. These recrystallisation temperatures are consistent with the occurrence of lobate grain boundaries, indicating deformation has occurred at relatively high temperatures. Note that the clinopyroxenite 15.07 has a distinct temperature of equilibration (808°C) compared to the other pyroxenites (Fig. 3-19B), indicating that this amphibole-rich sample has equilibrated at lower temperatures.

There is evidence of previous higher-temperature histories preserved within some of the pyroxenites, given the presence of exsolution textures. Two methods were used to integrate the exsolution lamellae into the pyroxene analyses to estimate original temperatures of

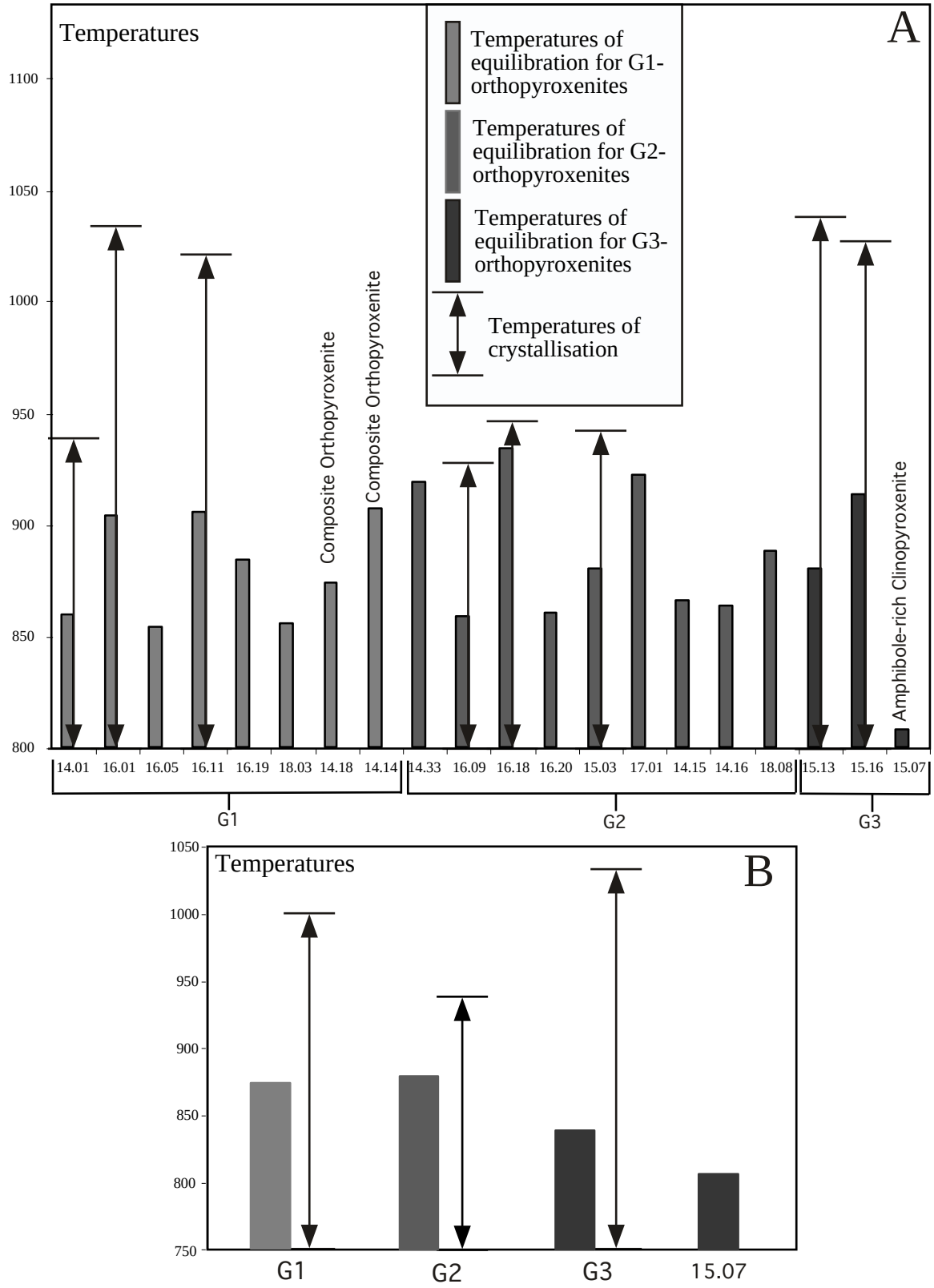

Fig. 3-19: Two pyroxene thermometer (Wells, 1977). A) Calculation of equilibration and crystallisation temperatures. B) Average calculated temperatures of equilibration and crystallisation.
Shaded bars represent the temperatures calculated directly from coexisting pyroxenes whereas the double-headed arrows provide an estimate of the original crystallisation temperatures. The latter have been determined using compositions recalculated from grains displaying exsolution lamellae (see text for details).

crystallisation. The first method consisted of analysing large host-lamellae areas by scanning the beam over a $10^3 \mu m^2$ area in order to restore the bulk composition of the pyroxenes prior to exsolution. In the second method, an image corresponding to the area analysed by the first method was taken and treated by Geological Information System (GIS) technique, using ER Mapper software, to quantify the area that the exsolutions represent relative to the host pyroxene. Then the relative areas were combined with spot analyses of the single phases to recalculate the original pyroxene composition. Both methods indicated that in G1-orthopyroxenite up to 8% of exsolution lamellae is present. Consequently the recalculated temperature of crystallisation is significantly higher, and reaches an average of 998°C (Fig. 3-19B). A very similar temperature of 940°C is obtained from restored pyroxene analyses from G2-pyroxenites. G2 pyroxene generally has lesser exsolution than G1 pyroxene, and thus the temperature of formation is closer to the temperature of recrystallisation. No exsolution features were observed in the 15.07 clinopyroxenite meaning that they were formed and recrystallised at low temperatures (800°C). However, the G3-clinopyroxenites (excluding sample 15.07) yield a higher average temperature of 1033°C. A higher temperature of formation for these G3-clinopyroxenites is in agreement with the observation that clinopyroxene contains abundant spinel exsolution, a feature that has not been found in G1 and G2.

8.2 Pressure

The absence of plagioclase and garnet together with the presence of spinel in both pyroxenites and surrounding peridotites constrains the origin of the pyroxenites to be within the stability field of spinel peridotite. Rough estimates of pressure for the pyroxenites can be assessed by the absence of garnet. As garnet is stable to lower pressure in pyroxenite than in peridotite (Ho et al., 2000), these pyroxenites must have equilibrated at pressures < 1.7 GPa. Experiments on natural pyroxenites (Hirschman and Stolper, 1996; Irving, 1974) estimate 1.3 to 1.7 GPa corresponds to the low-pressure stability limit for garnet on the solidus.

9 DISCUSSION

9.1 Arc- or plume-related pyroxenites?

The occurrence of peridotites associated with pyroxenites on Santa Isabel and San Jorge, at the boundary zone between clear arc- and OJP-related rock suites, gives no clear evidence as to the provenance(s) of these ultramafic rocks. Based on geochemical and geophysical arguments, it has been speculated that "hidden" cumulates in the crust of the OJP constitute the major part of its huge thickness (Neal et al., 1997). Until now, the cumulate assemblages of oceanic plateaus remain unknown. As the OJP supposedly represents the products of a mantle plume head (Coffin and Eldholm, 1994), its lower cumulative part should be generated from hot primitive magma.

Estimates of temperatures of crystallisation indicate that the Santa Isabel and San Jorge pyroxenites were formed at temperatures of about 1000°C (and not exceeding 1050°C) before being partially re-equilibrated at 850-900°C on average. This range of temperatures indicates the pyroxenites originated in a relatively cold environment that is incompatible with the high temperatures expected for OJP-related pyroxenite cumulates. While the OJP is supposed to be generated in a relatively H_2O-poor environment, the presence of primary fluid inclusions in the Santa Isabel and San Jorge pyroxenites may indicate involvement of a H_2O–rich fluid at

some stage in their development. Together, these features are more consistent with an arc-related origin of the pyroxenites in Santa Isabel and San Jorge.
A subduction-related origin for the pyroxenite is further supported by mineral and bulk rock compositions. The high Cr# in spinel is suggested by many authors (Bonatti and Michael, 1989; Kausar, 1998; Wang et al., 2001), to be characteristic of spinel from a subduction setting. Spinel from the G1- and G3-pyroxenites is similar in terms of Mg# and Cr# to spinel formed in SSZ mantle rocks (Fig. 3-17). Bulk rocks compositions moreover are relatively enriched in LILE, Sr, and Pb (Fig. 3-10). These elements are well known to be mobile in subduction zone environments (Tatsumi et al., 1986; McCulloch and Gamble, 1991; Brenan et al., 1995; Keppler, 1996; Ayers et al., 1997). The San Jorge and Santa Isabel pyroxenites exhibit similar trace element characteristics as the SSZ-related Izu-Bonin peridotites (Fig. 3-10) (Parkinson and Pearce, 1998).
All these arguments provide strong evidence that the formation of the San Jorge and Santa Isabel pyroxenites was related to subduction zone processes and not to the genesis of the OJP. The field observation that the pyroxenites occur mainly as vein and dykes within peridotites suggests that they formed in a SSZ mantle wedge rather than as cumulates formed at the base of an island arc crust. This hypothesis is supported by the finding of rare, relic orthopyroxene of mantle affinity within the pyroxenites. Therefore, we postulate the San Jorge and Santa Isabel rocks represent a new type of pyroxenite that has not been recognised previously.

9.2 Mantle versus crustal arc pyroxenites

We turn now to a comparison of "mantle" vs. "crustal" pyroxenite characteristics as outlined in the opening paragraph, with those of the SSZ pyroxenites documented here. It is appropriate to note that distinguishing between crust and mantle on the basis of seismic compressional wave velocities becomes somewhat arbitrary given velocities now acquired in the depth range 20 to 40 km beneath the Izu-Bonin and Aleutian arcs of ~ 7.6 to 8.0 kms^{-1} (Suyehiro et al., 1996; Fliedner and Klemperer, 1999). It is possible that these velocities correspond to clinopyroxenite and wehrlite lithologies formed through accumulation from primitive arc magmas, and adjacent to the crust-mantle boundary.
Pyroxenites have been described from a number of arc environments such as the Alaskan complexes (Irving, 1974; Debari et al., 1987, 1989), North America/Canada ultramafic rocks (Findlay, 1969; James, 1971; Quick, 1981; Snoke et al., 1981), intra-oceanic arc-related cumulates in southern New Zealand (Spandler et al., 2003), the deep crustal cumulates (in part, garnet-bearing) of the Jijal complex (Pakistan) (Jan and Howie, 1981; Kausar, 1998), the pyroxenite-rich peridotites from Cabo Ortegal (Spain) (Girardeau and Ibarguchi, 1991; Santos et al., 2002) and the Beni Bousera massif (Morocco) (Pearson et al., 1993). These are interpreted as medium to high-pressure, ultramafic cumulates formed in mid- to lower crustal magma chambers, some spanning the crust-mantle boundary at the base of an arc (DeBari and Coleman, 1989).
Given the predominance of olivine and clinopyroxene as early-formed minerals in arc magmas, it follows that arc-related pyroxenites are likely to be dominated by these phases leading to high CaO at relatively low SiO_2 contents in typical cumulate assemblages (Fig. 3-20A). Mantle-derived pyroxenites differ from arc crustal pyroxenites in having a wider range of CaO (18.5 to <5 wt % (Hirschmann and Stolper, 1996). Mantle pyroxenites generally include a large variety of rock types ranging from orthopyroxenite through websterite to clinopyroxenite. The Santa Isabel and San Jorge pyroxenites are characterised by mineralogical diversity similar to that of mantle-derived pyroxenites. In a CaO versus SiO_2 diagram (Fig. 3-20A), the G1-orthopyroxenite field overlaps that of mantle pyroxenite

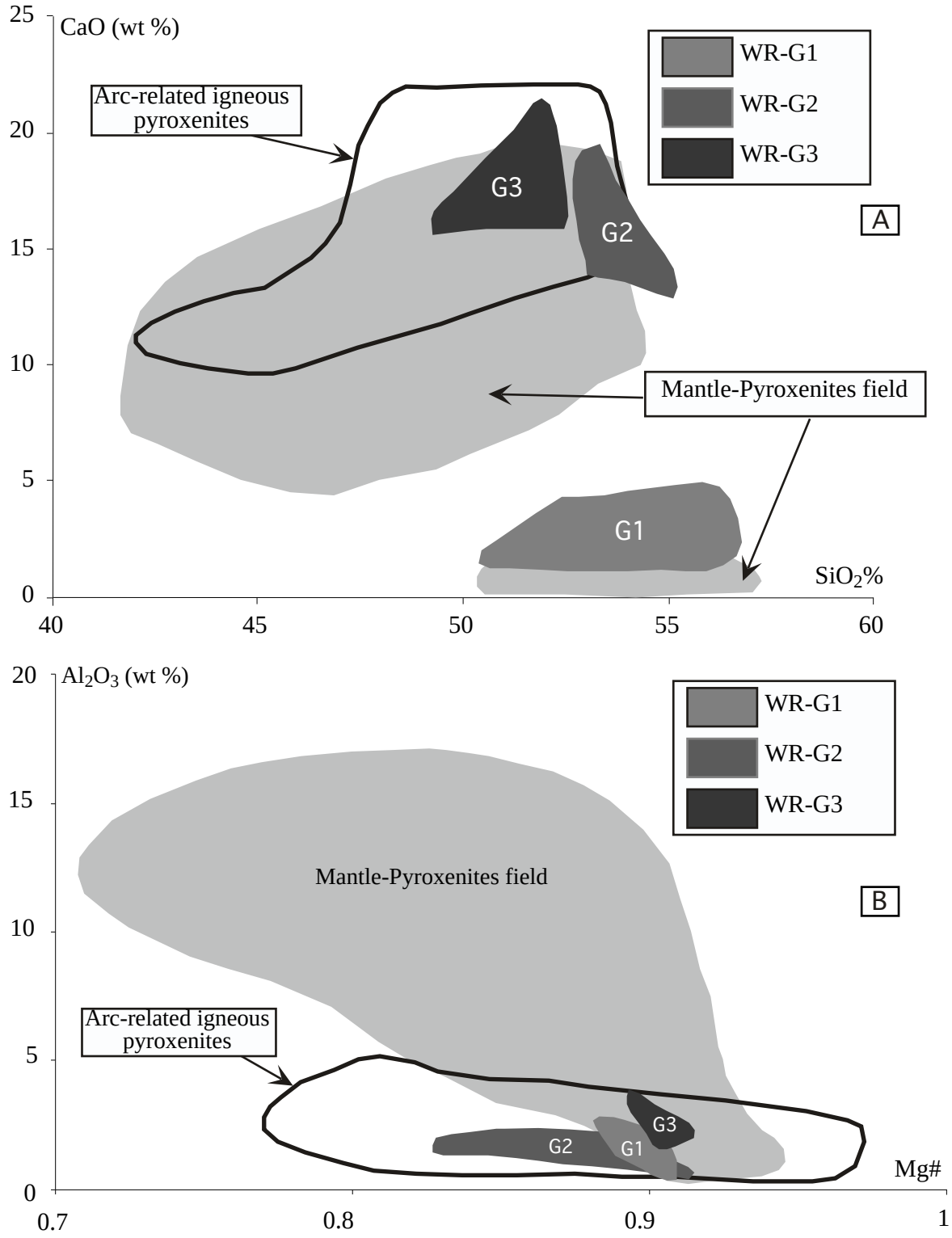

Fig. 3-20: A) SiO_2 versus CaO (wt %) for the whole rock pyroxenites; B) Mg# versus Al_2O_3 (wt %) for the whole rock pyroxenites.
References are from arc-related peridotites (Parkinson and Pearce, 1998), mantle pyroxenites (Kornprobst, 1969; Irving, 1974, 1980; Frey et al., 1978; Sinigoi et al., 1980; Bodinier et al., 1987, 1988; Seyler et al., 1989, 1993; Griffin et al., 1988; Piccardo et al., 1988, Shervais, 1990; Pearson et al., 1993; Rivalenti et al., 1995; Vaselli et al., 1995; Kumar et al., 1996; Wilkinson and Stolz, 1997; Garrido et al., 1999; Zanetti et al., 1999; McInnes et al., 2001) and arc-related igneous pyroxenites (Findlay, 1969; James, 1971; Jan and Howie, 1981; Quick, 1981; Snoke et al., 1981; DeBari and Coleman, 1989; Girardeau and Ibarguchi, 1991; Kausar, 1998; Smith et al., 1999; Parlak et al., 2002; Santos et al., 2002; Spandler et al., 2003; Worden, 2002).

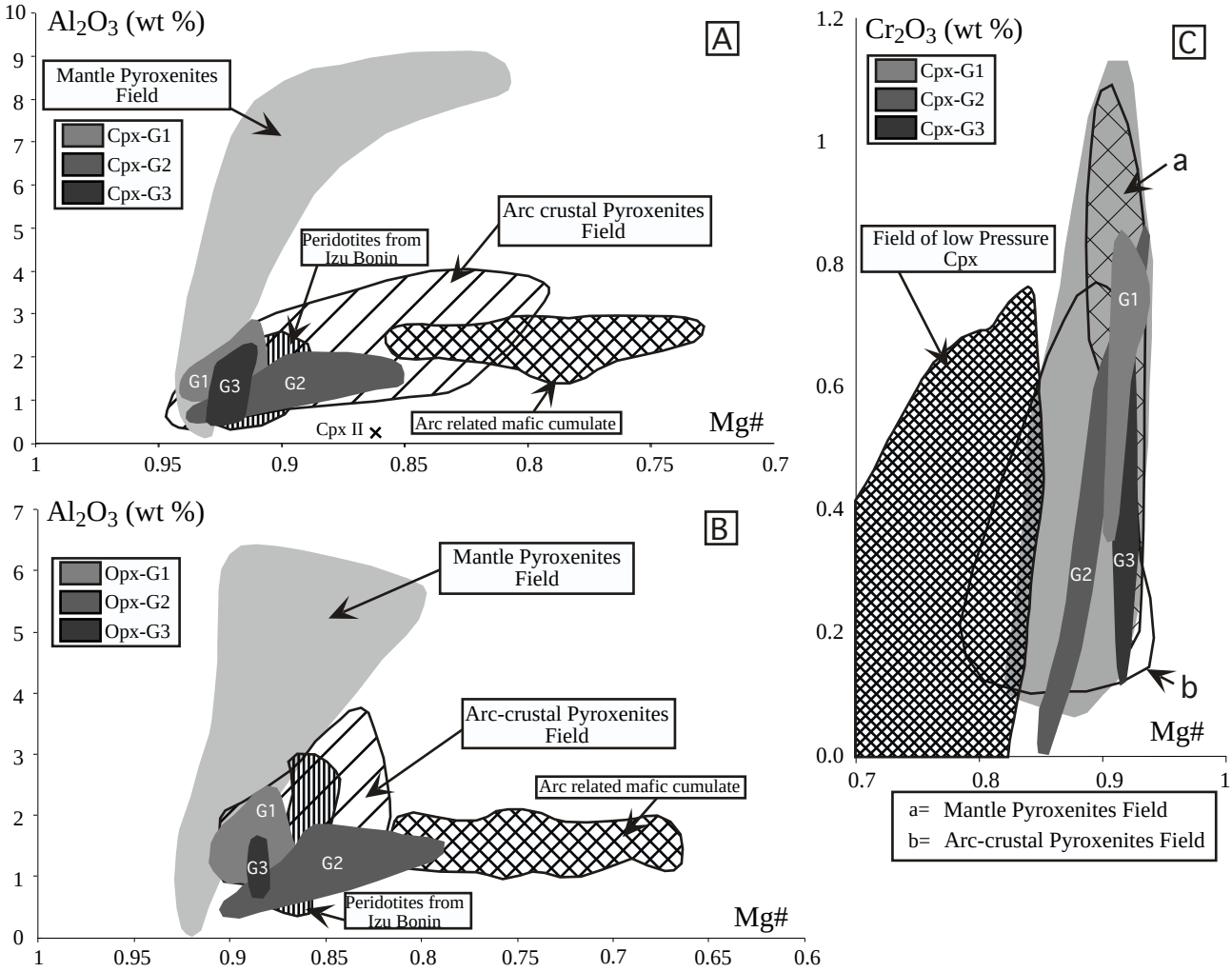

Fig. 3-21: A) Plots of Al_2O_3 versus Mg# for the clinopyroxene (A) and orthopyroxene (B) and plot of Cr_2O_3 versus Mg# (C) for the clinopyroxene.
References are from arc-related peridotites (Parkinson and Pearce, 1998), mantle pyroxenites (Kornprobst, 1969; Irving, 1974, 1980; Frey et al., 1978; Sinigoi et al., 1980; Bodinier et al., 1987, 1988; Seyler et al., 1989, 1993; Griffin et al., 1988; Piccardo et al., 1988, Shervais, 1990; Pearson et al., 1993; Rivalenti et al., 1995; Vaselli et al., 1995; Kumar et al., 1996; Wilkinson and Stolz, 1997; Garrido et al., 1999; Zanetti et al., 1999; McInnes et al., 2001) and arc-related igneous pyroxenites (Findlay, 1969; James, 1971; Jan and Howie, 1981; Quick, 1981; Snoke et al., 1981; DeBari and Coleman, 1989; Girardeau and Ibarguchi, 1991; Kausar, 1998; Smith et al., 1999; Parlak et al., 2002; Santos et al., 2002; Spandler et al., 2003; Worden, 2002).

whereas G2 and G3 pyroxenites span both the mantle and crustal arc fields. Crustal arc pyroxenite is characterised by a narrow range of Al_2O_3 contents compared to mantle pyroxenite (Fig. 3-20B). The Santa Isabel and San Jorge pyroxenites have low Al_2O_3 contents, and are all coincident with the arc-related field. G1-orthopyroxenites and G3-clinopyroxenites overlap the field of low-Al_2O_3 mantle pyroxenite whereas G2-websterites do not overlap that field (Fig. 3-20B).
A comparison of Al_2O_3 content vs. Mg# is shown in Figures 3-21A & 3-21B between ortho- and clinopyroxene compositions in the Solomons' occurrences with peridotites from Izu-Bonin and the respective fields for mantle pyroxenites. G1 and G3 pyroxenes have strong affinities with mantle-derived pyroxenes whereas the field of G2-pyroxenes overlaps the arc crustal pyroxenite field, and trends towards arc-related mafic cumulates. More generally, there is close compositional similarity between G1 pyroxenes and those from the SSZ Izu-Bonin peridotites.
In a plot of Cr_2O_3 content versus Mg# of clinopyroxene (Fig. 3-21C), the more primitive, mantle-like character of the G1-clinopyroxene is apparent, and distinct from that of the G2-clinopyroxene which has a closer affinity to arc crustal pyroxenites. The nominal mantle signature is also documented in the NiO contents of G1-olivine whereas G2- and G3- olivine has both lower Mg# and NiO content than those from peridotite (Fig. 3-16). While comparison of Santa Isabel and San Jorge pyroxenites with literature data shows the G1-pyroxenites have a strong affinity with mantle pyroxenites, there are several features, especially the low Al_2O_3 contents, that are similar to arc-related cumulates. In fact, the chemical characteristics of the Santa Isabel and San Jorge pyroxenites are best described by the intersection of the two established pyroxenite fields (Fig. 3-20A, 3-20B). The observation that G2 pyroxenites, which clearly have a mantle origin, are situated within the field of crustal pyroxenites indicates that the existing distinctions on chemical arguments are not robust. Some low-Al_2O_3 mantle pyroxenites described in the literature might have formed in a similar way to the rocks described here.

9.3 Metasomatic formation of SSZ mantle pyroxenites

Three main processes have been proposed for the formation of pyroxenites. They can form as cumulates in lower crustal magma chambers (DeBari and Coleman, 1989; Schiano et al., 2000), from recycled elongated slices of oceanic crust (Polvé and Allègre, 1980; Allègre and Turcotte, 1986) or from melt/fluid – peridotite interaction (Kelemen et al., 1992; Smith and Riter, 1997; Wilkinson and Stolz, 1997; Garrido and Bodinier, 1999; Smith et al., 1999; Zanetti et al., 1999; McInnes et al., 2001; Wang et al., 2001). The multi-generational network of veins crosscutting massive harzburgites (Fig. 3-2) and the replacement textures, wherein mantle orthopyroxene relics occur amongst an orthopyroxene-clinopyroxene assemblage (Fig. 3-4E), exclude an origin as arc cumulates. These features underline a reaction between a peridotite and a metasomatic agent (aqueous fluid and/or melt). On the basis of the very low REE contents and the presence of mantle relics, the recycling of crustal material alone is an unlikely process to explain the formation of the pyroxenites.
A metasomatic origin of both orthopyroxenites and websterites with similar major element compositions has also been proposed for the Group D-Ronda pyroxenites (Betic Cordillera, Southern Spain) (Garrido and Bodinier, 1999). Based on trace element compositions, the authors suggested that some pyroxenites were formed by metasomatic replacement of mafic layers via melt-rock reactions. The REE_N patterns for the San Jorge and Santa Isabel pyroxenites (Fig. 3-9) are similar to those of Ronda-pyroxenites. In a primitive mantle-normalised multi-element diagram (Fig. 3-10), additional similarities between pyroxenites from San Jorge, Santa Isabel, and Ronda are clear. For example, positive Ti anomalies are

characteristic of G1 and D2 orthopyroxenites, and negative Ti anomalies in G2 and D3 websterites. Pyroxenites from both Ronda and Solomons are characterised by positive Sr and Pb anomalies relative to neighbouring REE. Based on similar petrological, mineralogical and geochemical characteristics, we propose that the G1-orthopyroxenites and the G2-websterites were the products of reaction between peridotite and a metasomatising agent (fluid or melt). While we can clearly infer that the Solomon Islands pyroxenite formed in a supra-subduction zone mantle wedge, this has not been possible to conclude for the Ronda pyroxenite. We suggest that the Ronda Group D - pyroxenite formed in a similar setting.
On the basis of the petrology, the mineralogy and the whole-rock geochemistry of the G3-clinopyroxenites, it is difficult to determine precisely their origin. What is clear is that they are totally distinct from the G1 and G2 pyroxenites in features such as higher temperature of formation (except for sample 15.07). We suggest that the G3-pyroxenites probably originate from interaction with a high temperature primitive hydrous melt. But the mineral trace element chemistry of the G3-clinopyroxenites would certainly help to unravel their mechanism of formation and maybe allow to understand the genesis of the amphibole-rich clinopyroxenite (sample 15.07).

10 TECTONIC MODEL OF PYROXENITES FORMATION AND EXHUMATION

10.1 Genesis of the pyroxenites

While the Pacific Plate subducted underneath the Solomon arc, dehydration of the descending slab presumably occurred continuously down-slab dip (Schmidt and Poli, 1998), and large quantities of oxidised hydrous fluids were expelled into the mantle at different depths (Stern, 2002) (Fig. 3-22A). At deep levels, the slab-derived fluids were responsible for lowering the solidus temperatures of the overlying mantle wedge, and caused partial melting in hotter portions of the wedge, generating the Solomon arc lavas.
At shallower levels (~45km depth), some slab-derived fluids from the subducted Pacific oceanic crust migrated via channelised pathways through the mantle wedge, locally changing its bulk composition and mineralogy. The interaction between fluid and peridotite resulted in vein and dyke formation of pyroxenite characterised by enrichments in fluid-mobile elements (Fig. 3-22A). The chemical characteristics of these pyroxenites share similarities with both upper mantle pyroxenites and arc-related deep crustal cumulates.

10.2 Exhumation of the pyroxenites

The exhumation of the pyroxenite is documented in minor retrograde assemblages (Table 3-2). As the temperatures and pressures decreased during exhumation, some hydrous metasomatism of the pyroxenites led to local formation of amphibole (Fig. 3-22B). The hydration of clinopyroxene to magnesio-hornblende and tremolitic hornblende occurs in the upper amphibolite facies with pyroxene breakdown (~<825°C) and above the hornblende solvus (T>600°C) (Kimball, 1985). Sulfide grains are texturally in equilibrium with the hornblende, and probably formed from the reaction between a hydrous fluid with high SO_2/H_2S and the pyroxenites. Such S-rich fluid arguably originates from the uppermost portion of the oceanic crust (McInnes et al., 2001). As the exhumation continued (Fig. 3-22B), the pyroxenites partially re-equilibrated with a late retrograde fluid under greenschist facies conditions. Below 400°C, hornblende became unstable relative to tremolite (Kimball, 1985) and continued interaction of aqueous fluid with the pyroxenites (and associated peridotite) resulted in minor serpentinisation of olivine, orthopyroxene, and clinopyroxene (Mevel,

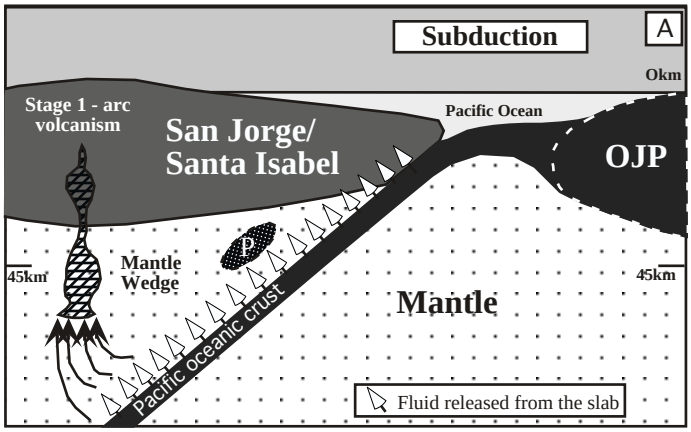

A) The Pacific oceanic lithosphere subducted beneath the San Jorge/Santa Isabel (Solomon arc). During that time, hydrous melts, released from the descending slab, interacted with the SSZ-peridotites. The reaction between the peridotites and the metasomatising agents forms the pyroxenites (annotated P).

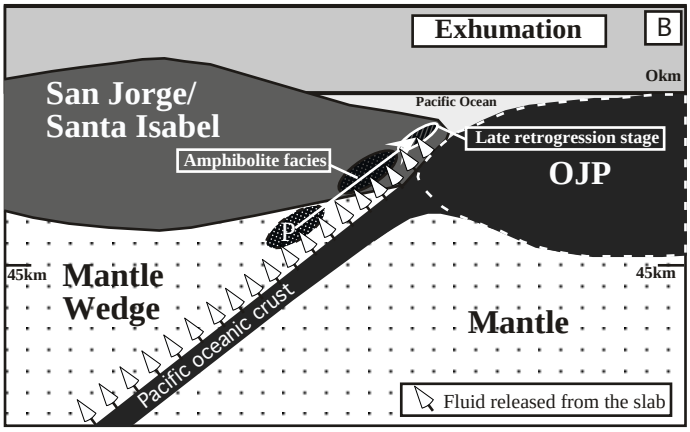

B) Ontong Java Plateau (OJP) collided with the Solomon arc (including San Jorge/Santa Isabel). The compressional régime initiated the exhumation of metasomatised upper mantle. During their exhumation, the pyroxenites were still exposed to fluids from slab. As a result, hydration of clinopyroxene to amphibole occurred in the amphibolite facies. Continued interaction of aqueous fluids with the peridotites resulted in a late retrogression stage.

Fig. 3-22 A and B: Tectonic model of peridotites formation and exhumation.

1988). The observed retrogression suggests that the pyroxenites were continually exposed to fluids released from the slab that underwent continuous dehydration process (Schmidt and Poli, 1998) (Fig. 3-22B).

11 CONCLUSION

It is proposed that the petrology, mineralogy, and geochemistry of the Santa Isabel and San Jorge pyroxenites indicate that they are related to subduction zone processes, and do not represent deep lithologies of the OJP. The pyroxenites are characterised by low temperature of formation (950-1000°C) consistent with a genesis resulting from interaction between an aqueous fluid and a harzburgitic upper mantle. These processes produced a chemical signature in mantle-derived pyroxenites, which is similar in some respects to arc-related cumulates.
In an arc setting, deep fluids (>120 km) released from the subducted slab are responsible for the partial melting of peridotites in the mantle wedge, generating arc magmas. We suggest that the Santa Isabel and San Jorge pyroxenites represent the products of subduction-related aqueous fluid and melt interaction with the mantle wedge at much shallower depths, corresponding to a deep crust-mantle level (~ 45km). As such, the pyroxenites exposed on the Islands of San Jorge and Santa Isabel constitute a new type of pyroxenite and provide an important opportunity to investigate the nature of fluids released at relatively shallow depths from the subducted slab. However, further studies (specifically the trace element compositions of minerals) need to be carried out to unravel the origin and nature of the different types of metasomatic agents involved to generate these pyroxenites.

Chapter 4:
Mineral trace element compositions, study of fluid inclusions and whole rock Re/Os system: indications of a complex slab-derived metasomatic origin for the San Jorge/Santa Isabel pyroxenites (Solomon Islands).

1 INTRODUCTION

The origin of a variety of layered pyroxenites found in ultramafic rocks and xenoliths from arc settings is still a matter of debate (Downes, 2001). Enrichment of orthopyroxene in sub-arc mantle xenoliths has been interpreted as a product of reaction between peridotites and fluids released from the subducted slab (Arai and Kida, 2000; Blatter and Carmichael, 1998; McInnes et al., 2001; Morishita et al., 2003; Smith et al., 1999; Yaxley et al., 1991; Zanetti et al., 1999). In contrast, clinopyroxene-rich pyroxenites from supra-subduction zone (SSZ) environments are interpreted to represent 1) cumulative rocks which are part of high pressure magma chamber that crystallised at the mantle/lower crust transition (DeBari and Coleman, 1989; Müntener et al., 2001; Parlak et al., 2002) or 2) products of metasomatic events resulting from infiltration of fluids or melts from the subducted slab into the mantle (Garrido and Bodinier, 1999; Parlak et al., 2002; Santos et al., 2002). The complex processes of interaction of fluids or melts with the surrounding peridotite (Zanetti et al., 1999) that operated to produce geochemical characteristics of opx-rich to cpx-rich pyroxenites are not well established.

Various SSZ-related pyroxenites have left open the question of the origin, the nature and the composition of the fluids or melts. For example, it is widely accepted that, worldwide subduction zone linked magmas characterised by enrichment of large-ion lithophile elements (LILE) over high field strength elements (HFSE) (Hawkesworth et al., 1993; McCulloch and Gamble, 1991) are attributed to processes within the subducted slab whereby slab-derived fluids transfer these incompatible elements into the overlying peridotitic mantle wedge (Parkinson and Arculus, 1999; Tatsumi and Eggins, 1995). These fluids released from the slab are responsible for lowering the peridotite solidus (Saunders et al., 1991) to instigate melting that generates explosive arc volcanism (Hawkesworth et al., 1993; Peacock, 1990; Stolper and Newman, 1994). Paradoxically, although study of genesis and evolution of the magmas are well understood, little is known about the metasomatising agents that begin the process of material transfer in subduction zones to generate these arc-basalts (Manning, 2004). In addition, continuous reactions consuming hydrous phases are reported to release gradually fluids or melts into the mantle wedge during prograde subduction of the slab (Schmidt and Poli, 1998) and therefore important mass transfer of elements also occurs at shallow depths in the forearc (Bebout et al., 1999). Hence the fate of these fluids or melts infiltrating the peridotites remains uncertain.

As suggested in *Chapter 3* and in Berly et al. (2006), petrological, textural and geochemical evidence of veins/dykes of San Jorge and Santa Isabel pyroxenites including orthopyroxenites, websterites and clinopyroxenites suggest that they result from the metasomatism of peridotites by metasomatising agents probably released from the subducting slab. In this chapter, I endeavour to define the characteristics of the metasomatism by examining the mineral trace element composition in order to unravel

the process of fluid-rock interaction responsible for the formation of the different types of pyroxenites. In addition to the trace element chemistry of the pyroxene, the study of fluid inclusions combined with the Re/Os data gives the opportunity to determine the nature and composition of the metasomatising agents. I will then discuss the different possible models of fluid interacting with the mantle wedge to constrain the metasomatic formation of these pyroxenites.

2 PRINCIPLES AND ANALYTICAL METHODS

2.1 Mineral trace element chemistry

2.1.1 Principles

Laser ablation inductively-coupled plasma mass spectrometry (LA ICP-MS) is used to in-situ analyse the trace element compositions of the minerals contained in the pyroxenites.

2.1.2 Analytical methods

Trace element concentrations were acquired by laser ablation inductively coupled-plasma mass spectrometry (LA ICP-MS) at RSES (ANU). The systems in use employed an ArF (193mm) EXCIMER laser together with 1) a Fisons PQ2 STE ICP-MS (from 1999-2002) or 2) a Hewlett Packard Agilent 7500 LA ICP-MS (from year 2002 onwards). The analytical procedure of LA ICP-MS is described in Appendix 1.

2.2 Study of Fluid Inclusions

2.2.1 Principles

The fluid inclusions represent trapped samples of fluid phases in the various events of the pyroxenites history. The complete study of the fluid inclusions including their petrology and geochemistry gives a great insight of the fluid-rock interaction mechanism which occurred at some stages of the history of the pyroxenites from their genesis to their exhumation at the surface of the earth. These fluid inclusions represent a unique source of data to determine the nature and the composition of the fluids.

2.2.2 Analytical methods

2.2.2.1 Raman Spectroscopy

The analysis of the fluid inclusions was carried out in the Mineral and Fluid inclusion laboratories of Geoscience Australia using the laser Raman microprobe. Laser Raman spectra of fluid inclusions were recorded on a Dilor® SuperLabram spectrometer equipped with a holographic notch filter, 600 and 1800 g/mm gratings, and a liquid N_2 cooled, 2000 x 450 pixel CCD detector. The inclusions were illuminated with 514.5 nm laser excitation from a Spectra Physics model 2017 argon ion laser, using 5 mW power at the samples, and a single 30 second accumulation. A 100X Olympus microscope

objective was used to focus the laser beam and collect the scattered light. The focused laser spot on the samples was approximately 1 μm in diameter. Wavenumbers are accurate to ± 1 cm^{-1} as determined by plasma and neon emission lines. For the analysis of CO_2, O_2, N_2, H_2S and CH_4 in the vapour phase, spectra were recorded from 1000 to 3800 cm^{-1} using a single 20 second integration time per spectrum. The detection limits are dependent upon the instrumental sensitivity, the partial pressure of each gas, and the optical quality of each fluid inclusion. Raman detection limits (Wopenka and Pasteris, 1987) are estimated to be around 0.1 mole % for CO_2, O_2 and N_2, and 0.03 mole percent for H_2S and CH_4 and errors in the calculated gas ratios are generally less than 1 mole %. Later advances in the study of fluid geochemistry by micro-Raman spectrometry were taken in account during the analysis of the fluid inclusions in accordance with the analytical methods of Dubessy et al., 1989.

2.2.2.2 LA ICP-MS

The analytical methods have been described above. The LA ICP-MS is used here to analyse the fluid inclusions contained in the host minerals (mainly the pyroxene). An example of the analytical procedure is illustrated in Figure 4-1. The clean pyroxene areas were distinguished from the pyroxene areas containing the fluid inclusions with the help of back-scattered images obtained by Scanning Electron Microscope (SEM) prior to LA ICP-MS analysis. During the LA ICP-MS sessions, "clean areas" were double-checked employing an optical microscope integrated to the laser ablation micro-sampler system. Once the area to analyse was clearly defined, the laser was activated ablating the mineral. I obtain a data report on the full sweep of analysed masses about every 0.6 seconds. Fluctuation of selected masses such as Ba, Cs, Rb, Sr and Pb, which were monitored constantly for each mineral analysis, was an indication of the presence of fluid inclusions (Fig. 4-1).

2.3 The Re/Os system

2.3.1 Principles

Re and Os form a long-lived isotope system based on β decay of ^{187}Re to ^{187}Os (Shirey and Walker, 1998). Unlike the other isotopic systems (Rb-Sr, Sm-Nd and Lu-Hf), Re and Os, which are siderophile and chalcophile, have differing chemical behaviour during melting (Shirey and Walker, 1998). Re behaves as a mildly incompatible element and fractionate into the melt whereas Os is highly compatible with a solid mantle residue (Allègre and Luck, 1980; Morgan and Lovering, 1967). In contrast to Sm, Nd, Rb and Sr, which are all more soluble in volcanic magmas than in the mantle residues, most of daughter product Os remains in the mantle during basalt genesis (Burton et al., 1998). The particularity of the Re-Os system provides a unique insight into old partial melting events in the residues after melt extraction. Besides, the different behaviour of compatibility between the parent Re and the daughter Os makes the Re-Os system interesting to study the metasomatism of mantle peridotites by fluids or melts (Becker et al., 2001; Brandon et al., 1996).

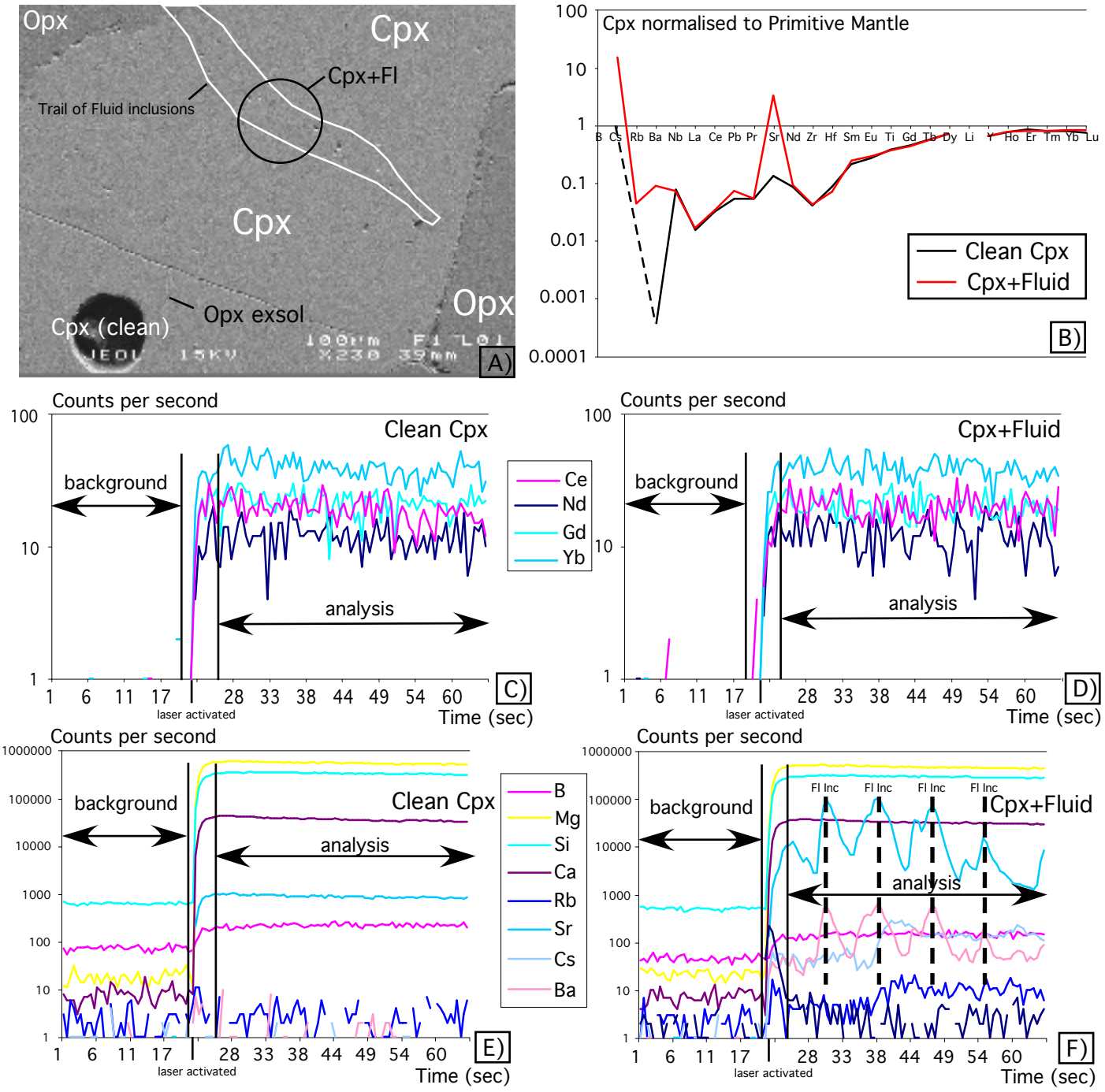

Fig. 4-1: Analytical procedure to measure the concentrations of the fluid inclusions.
A): Back-scattered image of a pseudosecondary trail of fluid inclusions cutting a crystal of clinopyroxene. In this image, the traces of the laser ablation are located in an area deprived of fluid inclusions ("clean" Cpx) and in the area of the trail of fluid inclusions.
B): Primitive mantle-normalised multi-element plots of the "clean" clinopyroxene compared to the clinopyroxene including the fluid inclusions (Cpx+Fl).
C): Counts per second analysed by the ICP-MS for Ce, Nd, Gd and Yb in the case of the "clean" Cpx.
D): Counts per second analysed by the ICP-MS for Ce, Nd, Gd and Yb in the case of the Cpx+Fluid.
E): Counts per second analysed by the ICP-MS for B, Mg, Si, Ca, Rb, Sr, Cs and Ba in the case of the "clean" Cpx.
F): Counts per second analysed by the ICP-MS for B, Mg, Si, Ca, Rb, Sr, Cs and Ba in the case of the Cpx+Fluid.
In the event of the analysis of the fluid inclusions, several variations in counts per second occur for elements such as Ba, Rb, Cs and Sr indicative of the contents of the fluid. Note that these variations are not accompanied by variations in major elements such Si, Ca and Mg indicating that the mineral analysed is still the clinopyroxene. In addition, the variations in Ba, Rb, Cs and Sr do not correlate with any variations in REE (Ce, Nd, Gd and Yb) indicating that the fluid does not contain significant amounts of REE.

2.3.2 Analytical methods

Briefly, 2-2.5 g of powder was spiked with ^{185}Re and ^{190}Os and digested with inverse aqua regia in a Carius tube for 7 days following a modified version of the method described in Shirey and Walker (1995). Os and Re are separated using a solvent extraction scheme described in Cohen and Waters (1996) or more recently using the method described in Birck et al (1997). Os is then purified using a micro-distillation method and Re is purified using small anion columns. Os and Re concentrations and $^{187}Os/^{188}Os$ ratios were measured as negative ions on a Finnigan 261 mass spectrometer using a secondary electron multiplier (SEM). Some of the Re concentrations were measured on a ThermoFinnigan Triton. Precision of the $^{187}Os/^{188}Os$ ratios based on counting statistics ranges from 0.05 to 0.3% (2 standard errors). A DTM standard run routinely in our laboratory over the last three years yields a $^{187}Os/^{188}Os$ ratio of 0.173962 ± 0.000171 (n=140 from 10/2/97–19/10/00) with $^{187}Os/^{188}Os$ normalised to $^{192}Os/^{188}Os$ = 3.08262, which equates to an external precision of <0.2% (2 standard deviations). Two total procedural blanks (TPB) are run with each batch of Carius tube dissolutions. During the course of this study the Os TPB was 0.5 pg with a $^{187}Os/^{188}Os$ ratio of 0.17. The Re TPB had a value of 10 pg. More details about the Re/Os analytical methods are given in Appendix 1.

3 RESULTS

3.1 Mineral trace element chemistry

Major element mineral compositions have been studied in the *Chapter 3* of this thesis and are also in Berly et al. (2006).

3.1.1 Clinopyroxene

In situ average trace element compositions of clinopyroxene from each pyroxenite are provided in Table 4-1.

3.1.1.1 Rare Earth Elements (REE)

Figure 4-2 illustrates the average chondrite-normalised rare earth elements (REE) compositions of the clinopyroxene for each of the three groups of pyroxenites. The clinopyroxene all exhibits great variations in shape depending on the samples and the rock types. Despite that, their REE concentrations remain remarkably homogeneous for every grain of clinopyroxene analysed in each sample. No zoning in REE composition was observed between cores and rims of each clinopyroxene.

The chondrite-normalised REE patterns for the G1-clinopyroxene (Fig. 4-2A) vary from a shallow downward slope middle (M)REE – high (H)REE (for the samples 14.01 and 16.01) to a relatively flat MREE-HREE gradient (for the other samples) with both a concave down-trend to light (L)REE. The G1-clinopyroxene has remarkably low HREE abundances ($1.35<Yb_N<3.62$) and even lower LREE plummeting down between 0.001 times and 0.1 the chondrite values. LREE fractionation relative to the MREE is highly

Table 4-1: Average trace element compositions of clinopyroxene from the pyroxenites.

Sample	14.01	16.01	16.05	16.19	18.03	14.18	14.14	14.33	15.03	16.09	16.18	17.01	14.15	14.16	18.08	15.11	15.13	15.16	15.07
Rock Type	G1a	G1a	G1a	G1a	G1a	G1b	G1b	G2a	G2a	G2a	G2a	G2a	G2b	G2b	G2b	G3a	G3a	G3a	G3b
Ti	323	425	479	414	295	272	258	466	546	494	308	475	188	167	615	681	1043	1086	284
Rb	0.026	0.015	0.014	0.013	0.009	0.015	0.011	0.041	0.016	0.041	0.011	0.021	0.019	0.020	0.059	0.051	0.031	0.049	0.028
Sr	1.558	7.751	3.986	7.561	1.225	6.822	11.625	25.813	15.256	12.028	15.823	11.096	25.629	20.157	20.185	13.242	11.588	13.198	21.834
Y	1.830	2.922	4.417	3.153	2.748	2.121	2.251	3.467	3.841	3.610	2.507	3.464	1.688	1.592	2.401	3.158	4.215	4.406	2.326
Zr	0.250	0.426	2.281	0.944	1.236	0.568	0.634	0.890	1.876	1.137	0.947	1.017	0.833	0.811	2.256	1.802	2.833	2.847	8.115
Nb	0.048	0.046	0.055	0.045	0.048	0.035	0.022	0.028	0.004	0.033	0.014	0.008	0.044	0.042	0.012	0.030	0.045	0.043	0.014
Cs	0.193	0.179	0.064	0.011	bdl	0.016	0.038	0.073	0.001	0.112	0.053	0.004	0.221	0.006	0.004	0.002	0.001	0.020	n.a.
Ba	0.300	0.069	0.529	687	0.022	0.142	1.627	1.096	0.033	0.576	2.214	0.023	0.338	0.176	0.212	0.261	0.233	0.128	0.139
La	0.003	0.010	0.013	0.021	0.001	0.024	0.032	0.049	0.072	0.061	0.052	0.035	0.065	0.049	0.094	0.180	0.108	0.104	1.113
Ce	0.017	0.049	0.108	0.078	0.015	0.115	0.151	0.250	0.331	0.267	0.242	0.160	0.308	0.229	0.475	0.482	0.493	0.502	2.730
Pr	0.005	0.012	0.035	0.020	0.009	0.025	0.033	0.061	0.076	0.061	0.053	0.037	0.067	0.049	0.103	0.091	0.113	0.119	0.325
Nd	0.051	0.103	0.341	0.172	0.123	0.180	0.245	0.464	0.559	0.465	0.372	0.278	0.471	0.342	0.666	0.666	0.844	0.891	1.342
Sm	0.050	0.089	0.264	0.141	0.139	0.113	0.140	0.259	0.318	0.278	0.199	0.192	0.229	0.164	0.318	0.310	0.414	0.438	0.342
Eu	0.025	0.041	0.110	0.068	0.063	0.044	0.056	0.103	0.122	0.108	0.077	0.081	0.081	0.063	0.133	0.125	0.160	0.170	0.115
Gd	0.145	0.232	0.502	0.338	0.332	0.217	0.256	0.439	0.531	0.475	0.332	0.387	0.319	0.250	0.448	0.474	0.638	0.656	0.375
Dy	0.302	0.467	0.732	0.548	0.489	0.349	0.366	0.591	0.668	0.633	0.420	0.585	0.313	0.274	0.479	0.572	0.778	0.789	0.410
Ho	0.072	0.113	0.159	0.120	0.105	0.079	0.080	0.129	0.142	0.136	0.091	0.130	0.061	0.056	0.096	0.117	0.159	0.162	0.081
Er	0.228	0.360	0.458	0.355	0.306	0.249	0.243	0.381	0.421	0.401	0.277	0.392	0.175	0.165	0.274	0.328	0.455	0.455	0.238
Tm	0.033	0.053	0.062	0.048	0.042	0.037	0.035	0.053	0.062	0.056	0.039	0.057	0.023	0.023	0.037	0.046	0.063	0.062	0.033
Yb	0.217	0.354	0.377	0.303	0.264	0.247	0.228	0.349	0.388	0.362	0.260	0.369	0.149	0.151	0.241	0.279	0.407	0.390	0.223
Lu	0.031	0.052	0.053	0.043	0.037	0.036	0.034	0.052	0.056	0.053	0.039	0.054	0.022	0.022	0.035	0.043	0.059	0.056	0.035
Hf	0.014	0.025	0.099	0.051	0.051	0.023	0.031	0.049	0.097	0.056	0.044	0.055	0.038	0.036	0.110	0.080	0.142	0.136	0.218
Pb	0.015	0.010	0.018	0.104	0.173	0.106	0.017	0.048	0.195	0.094	0.028	0.147	0.020	0.028	0.118	0.426	0.396	0.275	0.250

All trace elements are in ppm (analysed by LA ICP-MS)
List of Abbreviations:
G1: orthopyroxenites; G2: websterites; G3: clinopyroxenites
a, b: indicate the subgroups of pyroxenites (refer to text for explanation)

See Appendix 2 for representative trace element compositions of clinopyroxene.

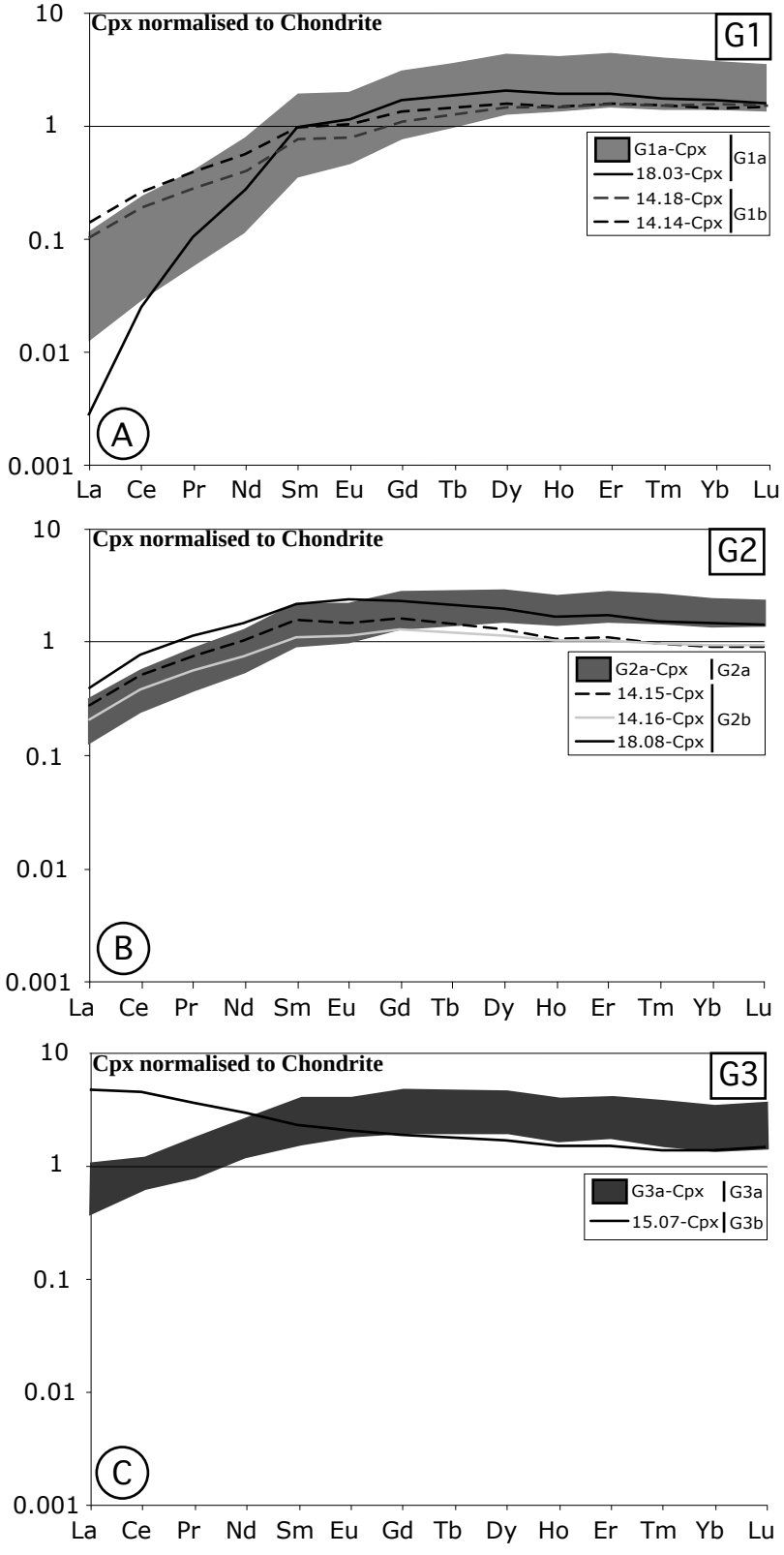

Fig. 4-2: Chondrite-normalised REE average compositions for the clinopyroxene from each of the three groups of pyroxenites.
Fig. 4-2A represents the chondrite-normalised REE average compositions for the clinopyroxene from the G1-orthopyroxenites. In this diagram, G1b-orthopyroxenites are the composite orthopyroxenites whereas the other samples are labelled G1a-orthopyroxenites.
Fig. 4-2B represents the chondrite-normalised REE average compositions for the clinopyroxene from the G2-websterites. In this diagram, the G2b-websterites have the bell shaped clinopyroxene REE patterns whereas the other samples (G2a-websterites) exhibit convex-upward clinopyroxene REE patterns with flat MREE-HREE gradients.
Fig. 4-2C represents the chondrite-normalised REE average compositions for the clinopyroxene from the G3-clinopyroxenites. In this diagram, the G3b-clinopyroxenite is the amphibole-rich clinopyroxenite whereas the other clinopyroxenites are referred as G3a-clinopyroxenites.
Chondrite normalising values are from Sun and McDonough (1989).

variable with $(Ce/Yb)_N$ ranging between 0.02 and 0.19 for the G1-clinopyroxene. For example, the clinopyroxene from the sample 18.03 has, by far, the most fractionated LREE relative to MREE with $(Ce/Yb)_N$ below 0.02 the chondrite. Apart from this sample, the La_N values for the G1-orthopyroxene range approximately between 0.01 and 0.14 times chondrite. The clinopyroxene is more LREE-depleted in the orthopyroxenites that contain the less proportion of clinopyroxene relative to orthopyroxene. Likewise, the composite orthopyroxenites (14.14 and 14.18) have the less LREE/MREE fractionated clinopyroxene.

The chondrite-normalised REE patterns for the G2-clinopyroxene are represented in the Figure 4-2B. Based on their REE patterns, the G2-clinopyroxene can be divided into two subgroups: G2a-cpx and G2b-cpx. Flat MREE-HREE gradients characterise the G2a-clinopyroxene whereas the REE patterns of the G2b-clinopyroxene are bell-shaped with MREE enrichment relative to HREE. For instance, the $(Gd/Yb)_N$ ratios range between 1.37 and 1.77 for the G2b-clinopyroxene whereas $(Gd/Yb)_N$ ratios are lower for the G2a-clinopyroxene averaging approximately 1. Clinopyroxene from these two subgroups is LREE-depleted and their HREE concentrations are within the same range. Compared to the G1-clinopyroxene, the LREE of both G2a and G2b-clinopyroxene are less depleted (La_N=0.15-0.31 for G1-cpx against La_N=0.01-0.14 for G2-cpx). The LREE fractionation over to MREE for the G2-clinopyroxene is also less important than it is for the G1-clinopyroxene [$(Ce/Yb)_N$=0.13-0.27 for G2a instead of $(Ce/Yb)_N$=0.01-0.19 for G1].

The Figure 4-2C outlines that the G3a-clinopyroxene is also marked by bell-shaped REE patterns comparable to ones described for the G2b-clinopyroxene. Like the G2b-clinopyroxene (Figure 2B), the G3a-clinopyroxene has high $(Gd/Yb)_N$ ratios (1.3-1.4) showing a MREE enrichment relative to HREE. HREE abundances of the G3a-clinopyroxene are low (Yb_N=1.7-2.5), similar to those of the clinopyroxene from the other pyroxenites. Similarly to the G1 and G2-clinopyroxene, the G3-clinopyroxene displays LREE-depleted REE patterns with Ce/Gd_N comprised between 0.25 and 0.33 (Ce/Gd_N (G1-cpx)= 0.01-0.1 and Ce/Gd_N (G2a-cpx)= 0.1-0.25). The G3-clinopyroxene overall has the highest abundances in LREE with La_N=0.45-0.77 compared to the clinopyroxene from other pyroxenites. The chondrite-normalised clinopyroxene REE patterns for the G3b-clinopyroxenites (Fig. 4-2C) change drastically from the ones of the G3a-clinopyroxene. The G3b-clinopyroxene is marked by LREE-enriched patterns (Ce/Gd_N>1) reaching nearly 5 times the chondrite values (La_N=4.7) followed by a steady decrease from LREE to MREE and a relatively flat MREE-HREE gradient. Concentrations in HREE remain very low identically to the HREE abundances of the clinopyroxene from the other pyroxenites.

3.1.1.2 Other trace elements

The primitive mantle-normalised multi-element average compositions of the G1-, G2- and G3-clinopyroxene are summarised in Figure 4-3. This clinopyroxene features Li enrichments relative to Dy and Y (when analysed), variable enrichments in LILE relative to REE, variable positive Pb and Sr spikes relative to Ce and Nd and negative Ti anomalies relative to Eu and Gd.

The G1-clinopyroxene (Fig. 4-3A) is enriched in Nb relative to La [$(Nb/La)_N$>1] whereas Nb is slightly to highly depleted relative La for the G2- and G3-clinopyroxene with [$(Nb/La)_N$] ratios remaining inferior to 1 (Fig. 4-3B and 4-3C). Although the

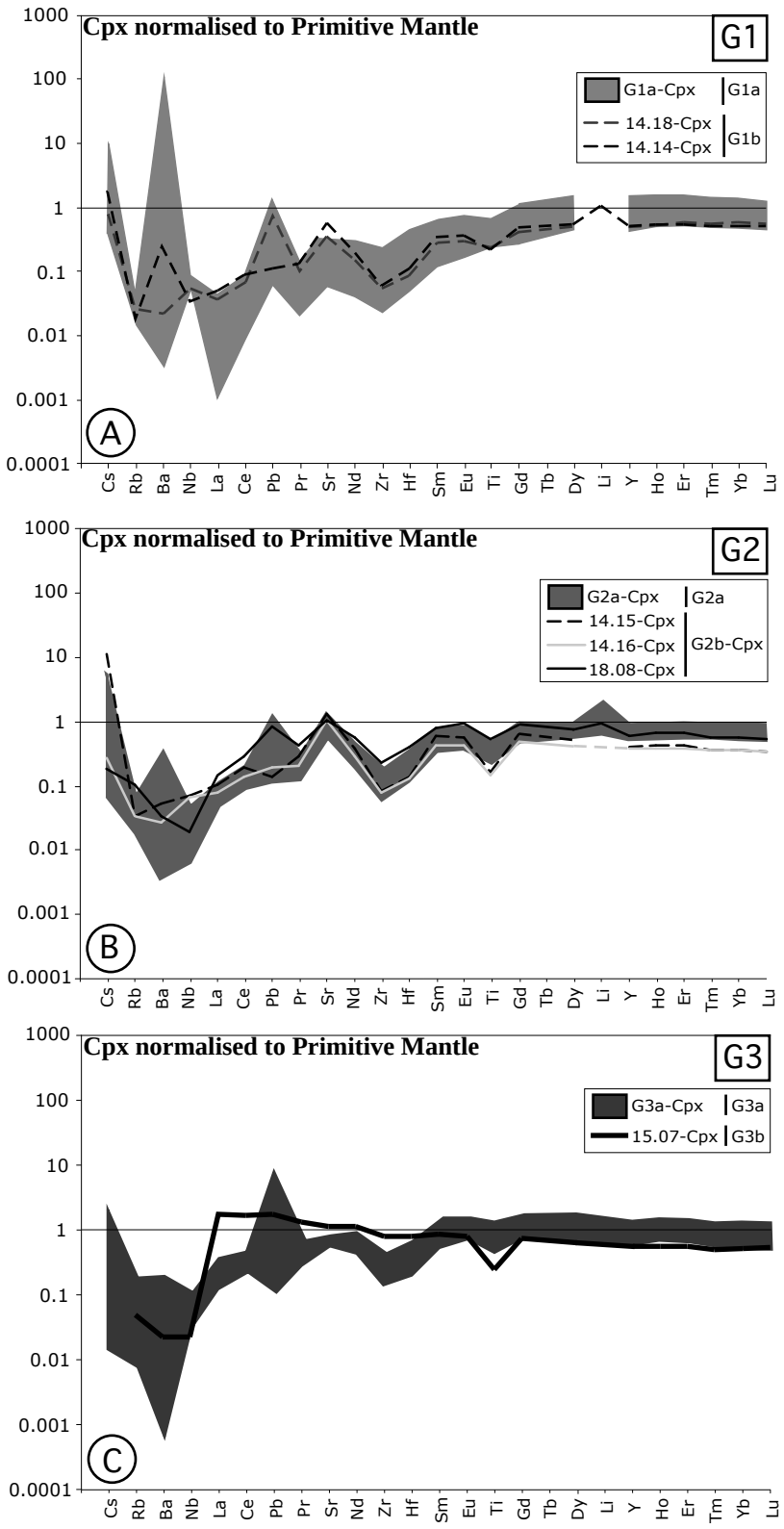

Fig. 4-3: Primitive mantle-normalised multi-element average compositions for the clinopyroxene from each of the three groups of pyroxenites.
Fig. 4-3A represents the primitive mantle-normalised multi-element average compositions for the clinopyroxene from the G1-orthopyroxenites. In this diagram, G1b-orthopyroxenites are the composite orthopyroxenites whereas the other samples are labelled G1a-orthopyroxenites (including the sample 18.03).
Fig. 4-3B represents the primitive mantle-normalised multi-element average compositions for the clinopyroxene from the G2-websterites. In this diagram, the G2b-websterites have the bell shaped clinopyroxene REE patterns whereas the other samples (G2a-websterites) exhibit convex-upward clinopyroxene REE patterns with flat MREE-HREE gradients.
Fig. 4-3C represents the primitive mantle-normalised multi-element average compositions for the clinopyroxene from the G3-clinopyroxenites. In this diagram, the G3b-clinopyroxenite is the amphibole-rich clinopyroxenite whereas the other clinopyroxenites are referred as G3a-clinopyroxenites.
Primitive mantle normalising values are from Sun and McDonough (1989).

clinopyroxene analysed from the different G1-orthopyroxenites shows similar but variable positive Sr anomalies relative to Pr and Nd, clinopyroxene from the sample 18.03 exhibits absolutely no Sr spikes (Fig. 4-3A). In this sample, Nd is consistently depleted relative to Zr whereas the $(Nd/Zr)_N$ ratios for the other G1-clinopyroxene are always superior to 1. No major difference exists between G1a- and G1b-orthopyroxenites in regards to the trace element compositions of the clinopyroxene (Fig. 4-3A).
The primitive mantle-normalised multi-element diagrams for the G2-clinopyroxene (Fig. 4-3B) resemble the ones for the G1-clinopyroxene. The G2-clinopyroxene also features the LILE enrichments and the Sr and Pb positive spikes relative to neighbouring elements. The only chemical distinction between G1- and G2- clinopyroxene resides in the systematic Nb depletion relative to La [$(Nb/La)_N<1$]. In addition, the G2-clinopyroxene shows huge variations in Ba concentrations (from 10 times to 0.0001 times the chondrite values).
The main characteristic of the primitive mantle-normalised multi-element diagrams for the G3-clinopyroxene (Fig. 4-3C) is the near-absence of Sr positive anomalies relative to Pr despite showing Pb positive spikes. The G3-clinopyroxene also shows limited enrichments in Cs, Rb and particularly Ba. The G3-clinopyroxene has $(Nb/La)_N<1$ typical of the G2-clinopyroxene. But unlike the G3a-clinopyroxene, the G3b-clinopyroxene is LREE-enriched and does not have Pb positive spikes relative to Ce and Pr. Nb is also depleted relative to La and Zr does not show any negative anomalies relative to Nd.

3.1.2 Orthopyroxene

In situ average trace element compositions of orthopyroxene from each pyroxenite are provided in Table 4-2.

3.1.2.1 Rare Earth Elements (REE)

LA ICP-MS analyses were conducted on the orthopyroxene from the San Jorge and Santa Isabel pyroxenites. Figure 4-4 shows the average REE compositions normalised to chondrite of orthopyroxene for each of the three groups of pyroxenites. The orthopyroxene compositions in REE are remarkably low (below 0.001 times the chondrite values < REE < 1 time the chondrite values). LREE concentrations are often below the detection limit whilst the MREE to HREE concentrations are well above the detection limit.
Due to the limited presence of the orthopyroxene crystals and their small size, no trace element concentrations were obtained for the G3-orthopyroxene. Only the orthopyroxene minerals from the G1-orthopyroxenites and G2-websterites were analysed (Fig. 4-4). Their REE patterns have very similar steep and positive HREE-LREE gradients with a shallow convex-upward slope from HREE to MREE. They are remarkably low in HREE abundances approximating the concentration of the chondrite. The constant depletion in REE from Lu to La leads to a very low concentration in LREE plummeting down to 0.001 times the chondrite values for Ce. The orthopyroxenite 16.19 is the only sample, which shows orthopyroxene with variable La-Sm enrichments (Table 4-2).
The G2b-orthopyroxene (Fig. 4-4) is distinct from the other orthopyroxene by not having such steep positive HREE-LREE gradients. While Ce/Yb_N ratios range from 0.002 to

Table 4-2: Average trace element compositions of orthopyroxene from the pyroxenites.

Sample	14.01	16.01	16.05	16.19	18.03	14.18	14.14	14.33	15.03	16.09	16.18	17.01	14.15	14.16	18.08
Rock Type	G1a	G1a	G1a	G1a	G1a	G1b	G1b	G2a	G2a	G2a	G2a	G2a	G2b	G2b	G2b
Ti	186	171	167	205	93	154	183	199	274	285	232	282	125	112	304
Rb	0.130	0.037	0.224	0.029	0.023	0.034	0.017	0.072	0.019	0.097	0.077	0.056	0.053	0.009	0.026
Sr	0.530	0.153	2.329	0.328	0.165	0.182	0.235	1.655	0.117	0.409	0.708	0.283	0.338	0.246	0.285
Y	0.213	0.230	0.318	0.351	0.183	0.218	0.234	0.268	0.397	0.349	0.323	0.442	0.100	0.119	0.247
Zr	0.045	0.054	0.158	0.186	0.080	0.067	0.066	0.080	0.171	0.128	0.106	0.137	0.054	0.056	0.249
Nb	0.030	0.023	0.022	0.022	0.017	0.022	0.016	0.018	0.004	0.021	0.012	0.006	0.019	0.018	0.011
Cs	0.936	0.974	1.761	0.059	0.001	0.069	0.030	0.069	0.000	0.404	0.425	0.013	0.588	0.009	0.004
Ba	0.137	0.139	0.529	3.706	0.057	0.090	0.203	0.178	0.027	0.890	2.503	0.017	0.343	0.043	0.082
La	bdl	0.001	bdl	0.002	bdl	bdl	bdl	0.001	0.001	0.001	0.001	bdl	0.001	0.001	0.002
Ce	0.000	0.001	0.002	0.004	0.001	0.001	0.001	0.003	0.003	0.002	0.001	0.001	0.002	0.002	0.008
Pr	bdl	bdl	0.001	0.001	bdl	0.001	bdl	0.001	0.001	0.001	0.001	bdl	0.001	bdl	0.002
Nd	0.002	0.002	0.005	0.003	0.001	0.002	0.002	0.006	0.004	0.005	0.002	0.003	0.004	0.003	0.009
Sm	0.003	0.002	0.005	0.003	0.002	0.002	0.003	0.005	0.006	0.006	0.005	0.004	0.002	0.002	0.006
Eu	0.001	0.001	0.002	0.002	0.001	0.001	0.001	0.002	0.003	0.003	0.001	0.002	0.001	0.001	0.004
Gd	0.006	0.005	0.014	0.011	0.006	0.007	0.007	0.011	0.015	0.015	0.012	0.014	0.005	0.005	0.013
Dy	0.021	0.022	0.038	0.037	0.020	0.023	0.025	0.028	0.045	0.045	0.032	0.049	0.013	0.013	0.031
Ho	0.007	0.008	0.011	0.011	0.006	0.007	0.007	0.009	0.014	0.012	0.011	0.016	0.004	0.004	0.009
Er	0.033	0.036	0.042	0.047	0.026	0.033	0.035	0.038	0.059	0.053	0.048	0.069	0.014	0.016	0.037
Tm	0.007	0.008	0.008	0.009	0.005	0.006	0.007	0.007	0.012	0.010	0.009	0.014	0.003	0.003	0.007
Yb	0.062	0.074	0.064	0.079	0.043	0.063	0.066	0.070	0.113	0.092	0.095	0.128	0.026	0.030	0.068
Lu	0.011	0.015	0.011	0.015	0.008	0.012	0.013	0.014	0.022	0.017	0.018	0.024	0.005	0.006	0.014
Hf	0.002	0.003	0.006	0.006	0.003	0.003	0.003	0.004	0.009	0.005	0.004	0.007	0.002	0.002	0.011
Pb	0.006	0.002	0.018	1.375	0.038	0.212	0.003	0.011	0.194	0.052	0.025	0.027	0.038	0.003	0.088

All trace elements are in ppm (analysed by LA ICP-MS)
List of Abbreviations:
G1: orthopyroxenites; G2: websterites; G3: clinopyroxenites
a, b: indicate the subgroups of pyroxenites (refer to text for explanation)

See Appendix 2 for representative trace element compositions of orthopyroxene.

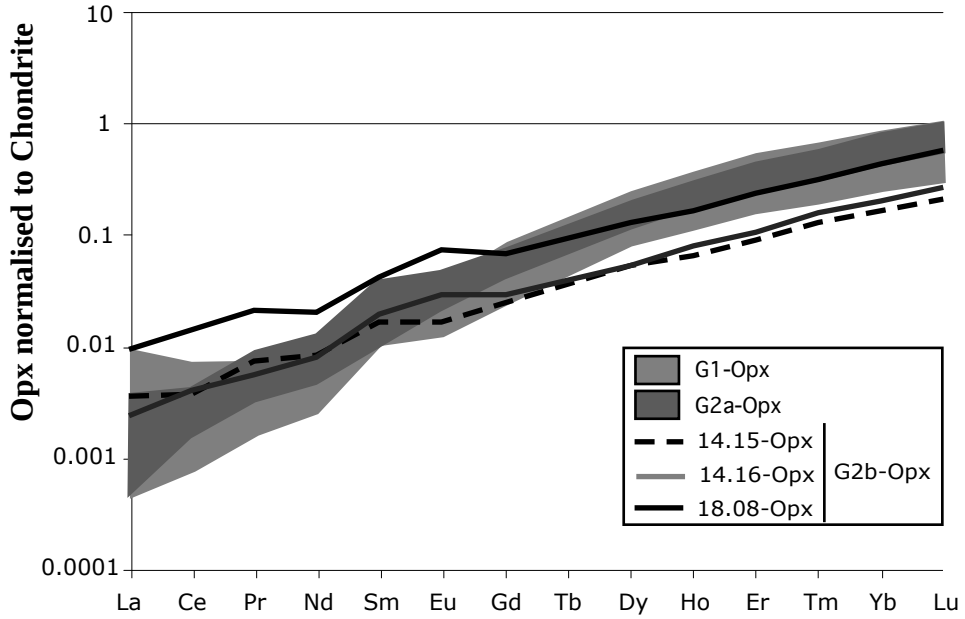

Fig. 4-4: Chondrite-normalised REE average compositions for the orthopyroxene from G1- and G2- pyroxenites.
Note that no distinction was made between the G1a- and the G2b-orthopyroxene.
Chondrite normalising values are from Sun and McDonough (1989).

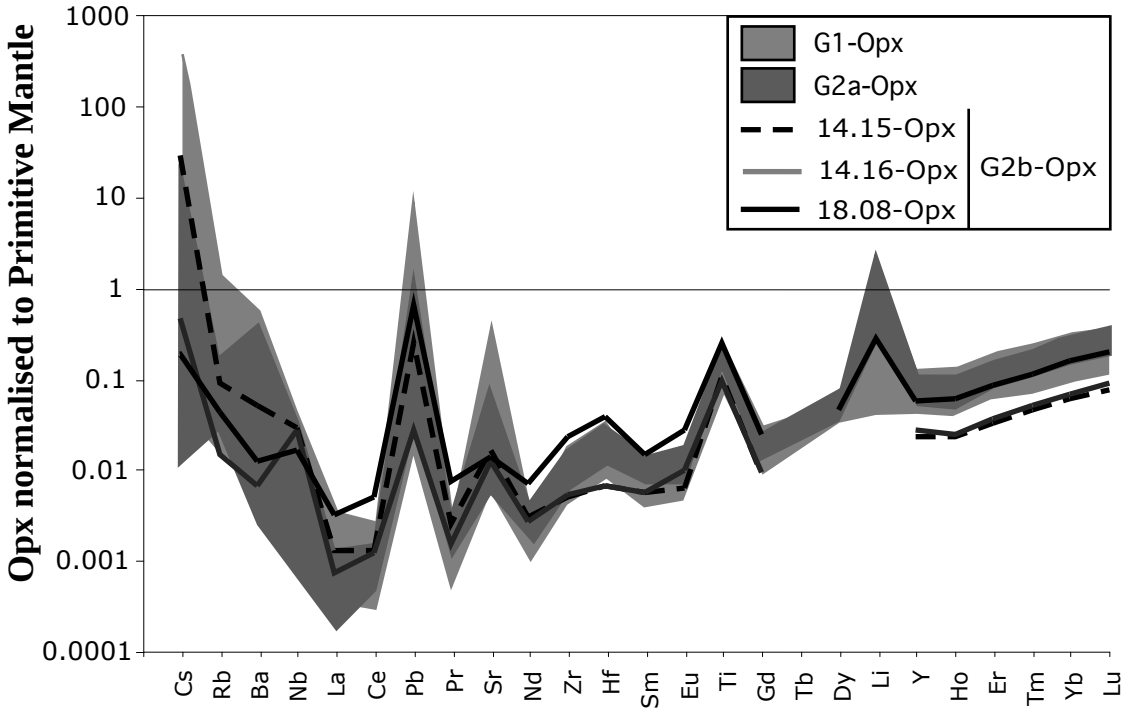

Fig. 4-5: Primitive mantle-normalised multi-element average compositions for orthopyroxene from the G1- and G2- pyroxenites.
Note that no distinction was made between the G1a- and the G2b-orthopyroxene.
Primitive mantle normalising values are from Sun and McDonough (1989).

0.01 for G1- and G2a-orthopyroxene, these ratios increase to around 0.02 for the G2b-orthopyroxene. Another particularity was observed for two orthopyroxene crystals from the sample 18.08, which are distinct from the others with remarkable flat HREE-LREE gradients (Ce/Yb_N=0.14 & 0.26).

3.1.2.2 Other trace elements

The primitive mantle-normalised multi-element average compositions for the orthopyroxene (Fig. 4-5) have the same spoon-shaped patterns caused by enrichments in incompatible elements such LILE (Cs, Rb, Ba) at the left hand of the multi-element diagrams. Nb contents are elevated ranging from 0.001 to 0.1 times chondrite, which are reflecting in $(Nb/La)_N$ ratios exceeding 1. Orthopyroxene has remarkably large Sr and Pb spikes. Li is enriched relative to Dy and Y, forming a large positive anomaly when measured or/and above the detection limit of the LA ICP-MS. The orthopyroxene is also characterised by strong positive Ti spikes and variable Zr and Hf positive anomalies respectively relative to Nd and Sm. No major difference is noticeable in regards to the primitive mantle-normalised multi-element diagrams between the orthopyroxene from the different groups.

3.1.3 Amphibole

In situ LA ICP-MS analyses of amphibole were possible only on five different pyroxenites because of the general small size of the interstitial amphibole grains. No amphibole was analysed from any samples that belong to either the G1b-orthopyroxenites or the G3a-clinopyroxenites. The trace element contents of the amphibole are shown in Table 4-3.

3.1.3.1 Rare Earth Elements (REE)

All the amphibole (except the ones from the sample 15.07) has convex-upward REE patterns with depleted LREE relative to MREE (Fig. 4-6A). Overall, the amphibole exhibits relatively low REE concentrations with HREE and MREE concentrations ranging from 1 to 6 times chondrite and LREE concentrations between 0.1 and 1 times chondrite. The G2-amphibole is distinct from the G1-amphibole by having relatively flat [$(Gd/Yb)_N$~1] to MREE-HREE gradients whereas the G1-amphibole displays steep but convex MREE-HREE profiles [$(Gd/Yb)_N$<1]. Due to this steep MREE-HREE aspect, the LREE depletions of the G1-amphibole [$(Ce/Gd)_N$=0.06] are less apparent than for the G2-amphibole [$(Ce/Gd)_N$=0.2-0.4]. The chondrite-normalised REE patterns for the G2b-amphibole have characteristic downward-inflected (G2b) MREE-HREE patterns [$(Gd/Yb)_N$>1] whilst the G2a-amphibole is marked by flat MREE-HREE gradients [$(Gd/Yb)_N$=1]. With only three amphibole crystals analysed, the sample 16.09 shows a wide range of REE concentrations (Yb_N= 1.1-6.1) whilst keeping the same REE profiles.
Amphibole from sample 15.07 (G3b-clinopyroxenite) has a distinct LREE-enriched pattern compared to the other amphibole (Fig. 4-6A). The La to Gd enrichments reach nearly 20 times chondrite for La while the MREE and HREE are similar to the values of some of the other amphibole (Gd_N=6 and Yb_N=4.5).

Table 4-3: Average trace element compositions of amphibole from the pyroxenites.

Sample	16.01	14.33	16.09	18.08	15.07
Rock Type	G1a	G2a	G2a	G2b	G3b
Ti	1259	734	298	1365	2240
Rb	0.140	7.646	0.212	1068.739	0.651
Sr	4.486	11.536	8.867	18.987	36.011
Y	7.267	3.775	1.703	22.198	7.799
Zr	0.955	0.825	0.617	5.796	52.507
Nb	0.162	0.035	0.022	2.418	0.978
Cs	2.340	1.575	0.899	0.015	0.004
Ba	0.231	1.079	2.462	0.806	11.217
La	0.021	0.133	0.032	0.933	4.123
Ce	0.087	0.286	0.147	0.763	9.695
Pr	0.022	0.209	0.034	0.767	1.165
Nd	0.181	0.538	0.236	0.997	4.925
Sm	0.167	0.296	0.138	1.273	1.159
Eu	0.072	0.251	0.052	0.585	0.338
Gd	0.470	0.659	0.240	0.769	1.250
Dy	1.086	0.680	0.339	1.243	1.304
Ho	0.279	0.265	0.070	0.782	0.265
Er	0.936	0.436	0.205	0.509	0.762
Tm	0.154	0.178	0.031	0.429	0.107
Yb	0.997	0.393	0.190	0.385	0.715
Lu	0.145	0.071	0.027	0.380	0.107
Hf	0.049	0.056	0.034	0.167	1.512
Pb	0.024	0.062	0.134	0.173	0.350

All trace elements are in ppm (analysed by LA ICP-MS)
List of Abbreviations:
G1: orthopyroxenites; G2: websterites; G3: clinopyroxenites
a, b: indicate the subgroups of pyroxenites (refer to text for explanation)

Table 4-4: Average trace element compositions of olivine, spinel and pectolite from the pyroxenites.

Sample	16.19	18.03	14.14	15.16	G1	18.08
Mineral	Ol	Ol	Ol	Ol	Sp	Pect
Rock Type	G1a	G1a	G1b	G3a	G1	G2b
Ti	4	14	7	15	9569	547
Rb	0.005	bdl	0.052	0.264	0.139	0.069
Sr	0.309	0.002	0.904	1.259	0.654	21.240
Y	0.004	0.014	0.003	0.023	0.122	1.266
Zr	0.010	0.021	0.003	0.014	15.909	1.333
Nb	0.001	bdl	0.001	0.003	15.725	0.013
Cs	0.022	bdl	0.159	0.082	bdl	0.002
Ba	0.979	bdl	0.532	0.526	0.001	0.354
La	bdl	bdl	bdl	0.004	0.016	0.061
Ce	bdl	bdl	bdl	0.010	0.005	0.315
Pr	bdl	bdl	bdl	0.002	bdl	0.068
Nd	bdl	0.004	0.001	0.015	bdl	0.391
Sm	bdl	bdl	bdl	0.006	bdl	0.195
Eu	bdl	bdl	bdl	0.001	bdl	0.080
Gd	bdl	bdl	bdl	0.007	bdl	0.252
Dy	0.002	bdl	bdl	0.002	bdl	0.285
Ho	0.000	bdl	bdl	0.002	bdl	0.058
Er	0.001	bdl	bdl	0.004	bdl	0.151
Tm	0.000	0.002	bdl	0.000	0.010	0.024
Yb	0.002	bdl	0.002	0.005	0.028	0.145
Lu	0.001	0.003	bdl	0.002	0.003	0.019
Hf	bdl	bdl	bdl	0.002	0.039	0.072
Pb	0.021	0.035	0.009	0.313	0.300	0.100

All trace elements are in ppm (analysed by LA ICP-MS)
List of Abbreviations:
G1: orthopyroxenites; G2: websterites; G3: clinopyroxenites
a, b: indicate the subgroups of pyroxenites (refer to text for explanation)
Ol: Olivine; Sp: Spinel; Pect: Pectolite
bdl: below detection limit

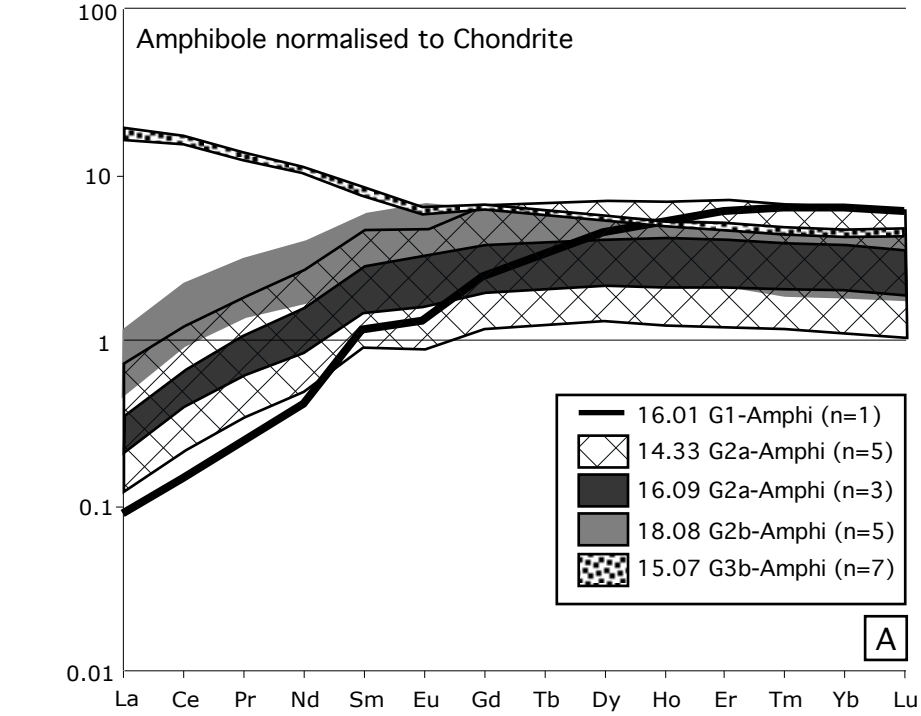

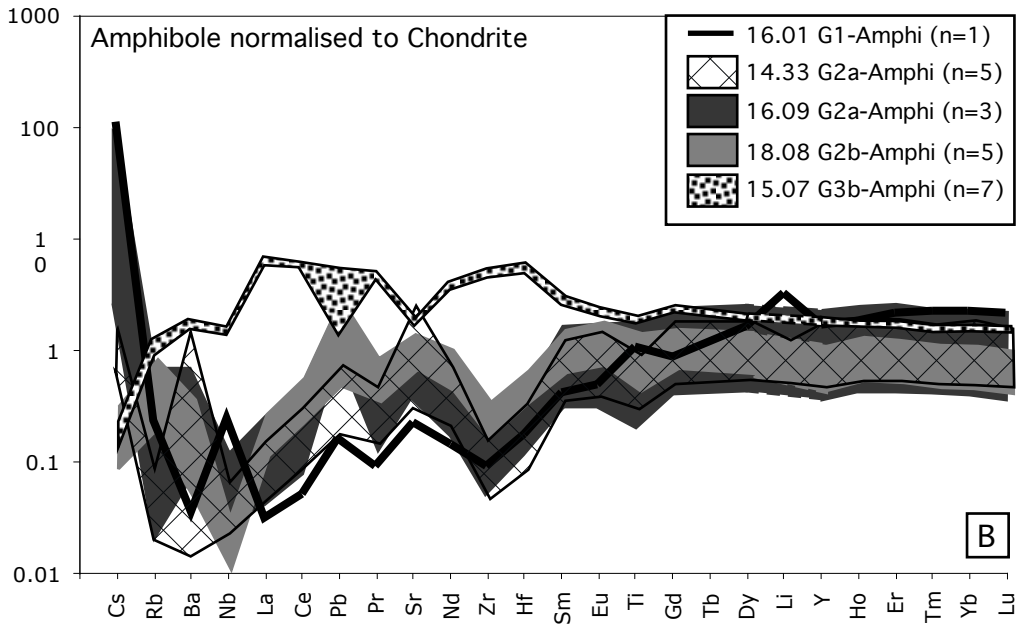

Fig. 4-6*:* Chondrite-normalised REE (A) and primitive mantle-normalised multi-element (B) diagrams for the amphibole from some of the pyroxenites.
n: indicates the number of analyses undertaken per sample.
Primitive mantle normalising values are from Sun and McDonough (1989).

3.1.3.2 Other trace elements

Amphibole shows LILE enrichments and large positive Pb and Sr spikes except for the amphibole from the G3b-clinopyroxenite (Fig. 4-6B). In this sample, the amphibole is characterised by depletions in LILE elements relative to LREE and large Sr and Pb negative anomalies. Zr and Hf also have positive anomalies relative to Nd and Sm, which contrast with the Zr-Hf negative anomalies for the other amphibole. Apart from their typical REE signatures, the G1-amphibole differs from the G2-amphibole by exhibiting positive Ti anomalies while the G2-amphibole have negative Ti anomalies.

3.1.4 Other minerals

3.1.4.1 Olivine

Average trace element compositions are listed in Table 4-4 and represented in Figure 4-7. Olivine has extremely low REE contents ($0.01<REE_N<0.1$) (Fig. 4-7A). Most of the REE concentrations are actually below the detection limit. However the G3-olivine is more enriched in REE than the other olivine and shows relatively flat LREE-HREE patterns (Fig. 4-7A).

Olivine exhibits enrichments in incompatible elements such as LILE (Cs, Rb and Ba) as well as Pb and Sr (Fig. 4-7B), which are probably attributed to the presence of inclusions within the olivine.

3.1.4.2 Spinel

Large spinel grains are only found in the G1-orthopyroxenites. The average spinel composition (Table 4-4) for the G1-spinel is shown in the primitive mantle-normalised multi-element plot (Fig. 4-8). As expected, Ti and Nb are strongly partitioned in the spinel phase. High Pb concentrations are also found in the spinel likely to be caused by presence of inclusions.

3.1.4.3 Pectolite

Trace element compositions of a pectolite are provided in Table 4-4. Figure 4-9 details the primitive mantle-normalised multi-element diagram for one grain of pectolite that was found in the sample 18.08 (G2b-websterite). The pattern mimics exactly the average clinopyroxene composition for this sample with similar LILE enrichments, positive Pb and Sr spikes and MREE enrichment relative to HREE. The only distinction between the patterns of the pectolite and the clinopyroxene for the sample 18.08 is the negative Ti anomaly, which is very small for pectolite compared to the clinopyroxene.

3.2 Study of the fluid inclusions

3.2.1 Petrography

3.2.1.1 Criteria

Spatial relationships of fluid inclusions provide information about the timing of formation with regard to host mineral. Roeder (1979, 1984) proposed the diagnostic criteria for classifying fluid inclusions as primary, pseudosecondary or secondary inclusions. Primary fluid inclusions are trapped during growth of their host crystal whereas

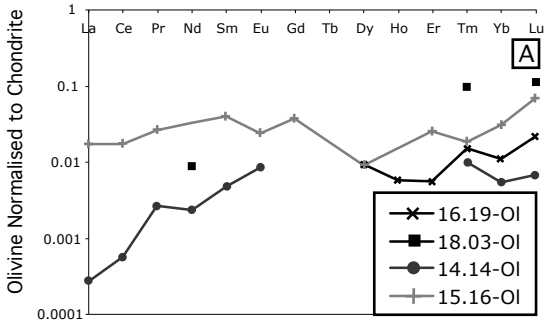

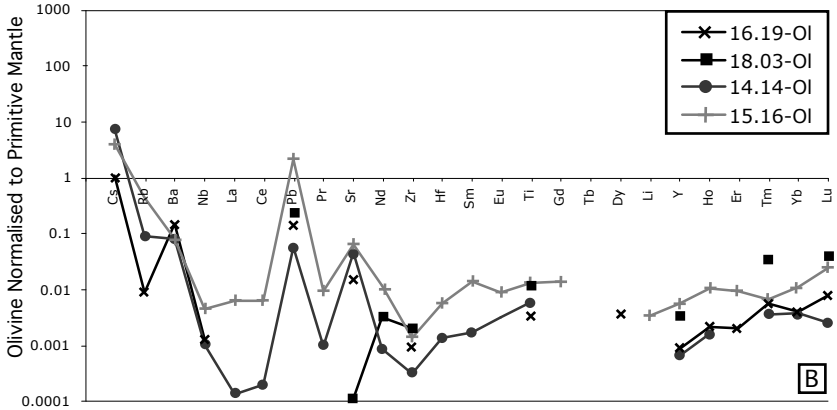

Fig. 4-7: Chondrite-normalised REE (A) and primitive mantle-normalised multi-element (B) average compositions for the olivine from the orthopyroxenites.
Chondrite and primitive mantle normalising values are from Sun and McDonough (1989).

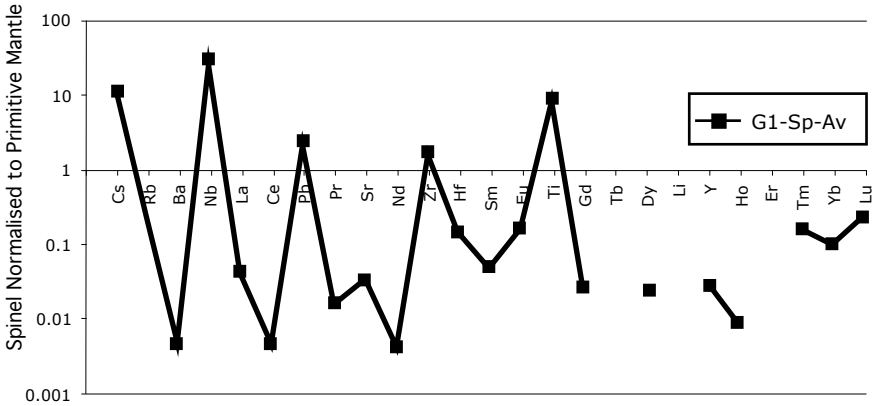

Fig. 4-8: Primitive mantle-normalised multi-element average compositions for the G1-spinel.
Primitive mantle normalising values are from Sun and McDonough (1989).

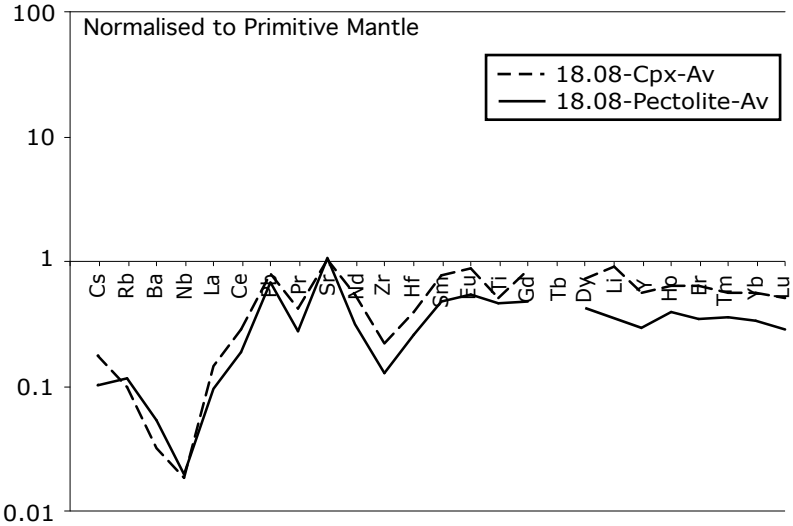

Fig. 4-9: Primitive mantle-normalised multi-element diagram for average pectolite compositions (sample 18.08) compared to average trace element compositions (18.08-Cpx-Av) for the clinopyroxene from this sample.
Primitive mantle normalising values are from Sun and McDonough (1989).

secondary fluid inclusions are trapped at any time after the crystal growth. Pseudo-secondary fluid inclusions characterise fluids in microcracks during crystal growth.

3.2.1.2 Fluid inclusions occurrence

The main host minerals for the fluid inclusions in the San Jorge/Santa Isabel pyroxenites are the clinopyroxene and the orthopyroxene. Because of its deformed and altered aspect in most of the samples, it is difficult to evaluate if the olivine contains or not fluid inclusions. On the other hand, it seems that fluid inclusions are rare in spinel. Despite the presence of cleavage, it is easy to observe the fluid inclusions in the pyroxene. Overall, the fluid inclusions seem to be more apparent in the clinopyroxene than in the orthopyroxene. The reason is that most of the clinopyroxene crystals are riddled with numerous amphibole blebs strongly associated with the inclusions giving a poikilitic aspect to the clinopyroxene grains. Although the fluid inclusions are well preserved in both clinopyroxene and orthopyroxene from the G1-orthopyroxenites, the small size of the orthopyroxene grains in the G2-websterites renders difficult to assess if they contain or not fluid inclusions. Nonetheless, fluid inclusions were observed in one orthopyroxene crystal from the sample 17.01 (not shown) indicating that fluid inclusions are rare but exist in the orthopyroxene minerals from the G2-websterites. Due to the scarcity and the small size of orthopyroxene in the G3-websterites, it is impossible to determine whether or not fluid inclusions are trapped in the G3-orthopyroxene. Despite their abundance, the fluid inclusions, within clinopyroxene or/and orthopyroxene, are usually small ranging between 5 and 15μm (Fig. 4-10). They are generally dark in thin sections but frequently appear heterogeneous in colour indicating that they contain solid phases as well as liquid and gas (or vapor) (Andersen and Neumann, 2001).

The distribution and textural characteristics of the fluid inclusions show evidence that the three classical criteria of classification (primary, pseudosecondary and secondary) are present in the pyroxenites. In these rocks, the fluid inclusions occur rarely in well-defined clusters likely to be primary fluid inclusions (Fig. 4-10B) but the vast majority of fluid inclusions forms trails representing healed microcracks or fractures. This does not necessarily imply that such fluid inclusions are secondary. According to the terminology by Krantz (1983) and Simmons and Ritchter (1976), the trails of the fluid inclusions, identified in the pyroxenites, are either transgranular cross-cutting grain boundaries (Fig. 4-10A) or intragranular occurring within single grains (Fig. 4-10D). The latter is likely to represent primary inclusions whereas the transgranular trails of fluid inclusions indicate that fluids were trapped after initial growth of the host mineral along healed fractures or microcracks (Van den Kerkhof and Hein, 2001). Some fluid inclusions form trails crosscutting only two mineral phases and are akin to be pseudosecondary (Fig. 4-10C).

3.2.2 Geochemical study of the fluid inclusions

3.2.2.1 By the Raman spectroscopy

Only one orthopyroxenite (14.01) and one websterite (16.18) were selected for the study of inclusions based on the quality, abundance and diversity of the fluid inclusions preserved in these two samples. Figure 4-11 shows the example of two representative fluid inclusions, which contain solid phases including calcite and amphibole and a gaseous phase represented by methane (CH_4). More generally, the fluid inclusions

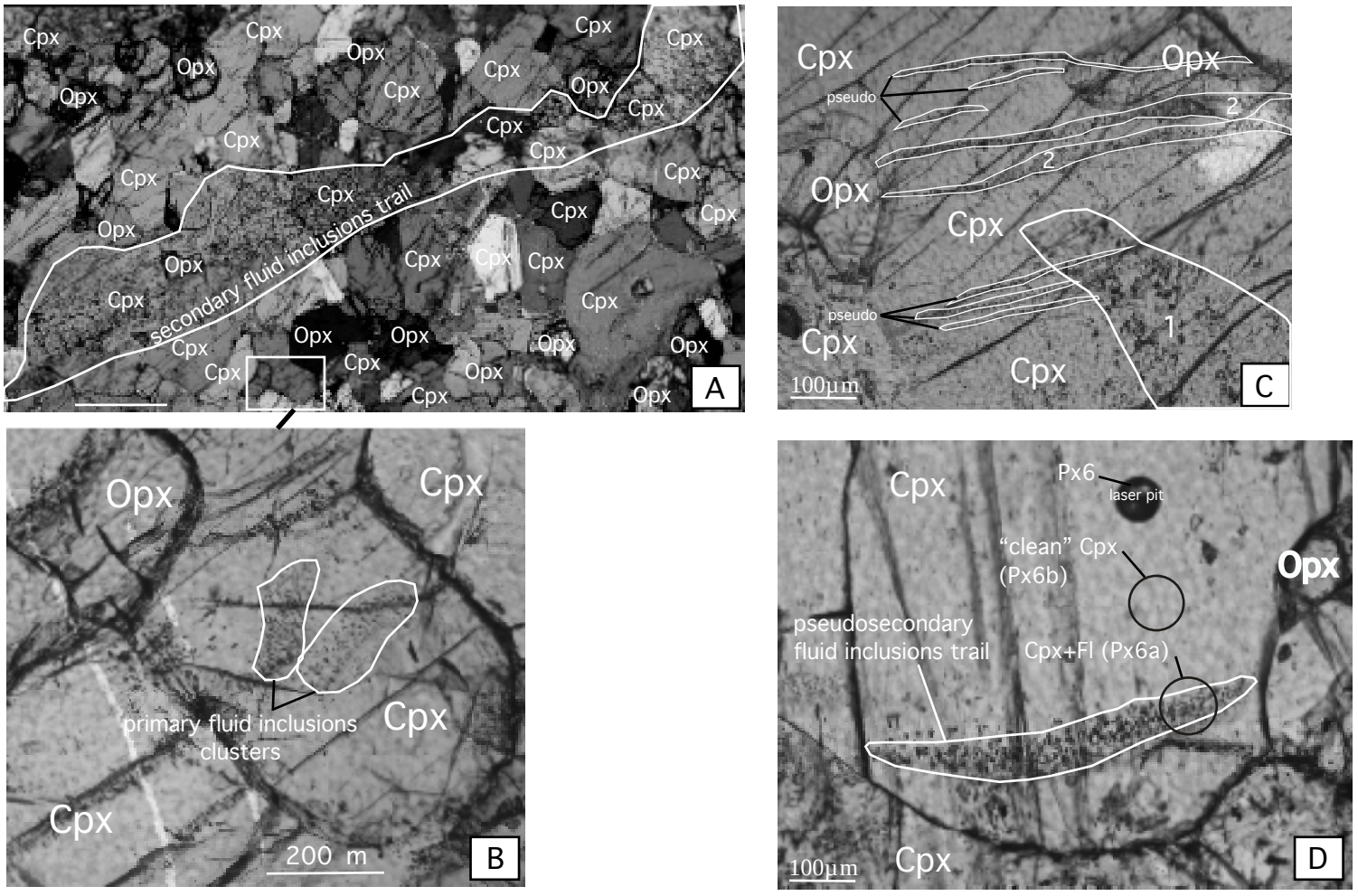

Fig. 4-10: Plane-polarized transmitted light photomicrograph of thin sections illustrating the pyroxene hosting different types of fluid inclusions.
A): Extensive transgranular trail of secondary fluid inclusions cross-cutting grain boundaries (websterite 18.08).
B): Well-defined clusters of primary fluid inclusions enclosed within one clinopyroxene crystal from the websterite 18.08.
C): Pseudosecondary trails of fluid inclusions (2) cross-cutting only two mineral phases (opx-cpx or cpx-cpx) together with primary fluid inclusions (1) (sample 16.18).
D): Pseudosecondary intragranular trail of fluid of inclusions within one clinopyroxene grain (websterite 17.01). The two drawn circles mark the areas where the laser ablated the "clean" cpx (without any inclusions) and the cpx with the fluid inclusions (Cpx+Fl: Px6a).

analysed consistently contain the same daughter minerals (calcite and amphibole) and a gaseous phase (methane) regardless of the fluid inclusion types (primary and secondary), the host minerals (orthopyroxene and clinopyroxene) and the rock type (orthopyroxenite and websterite).

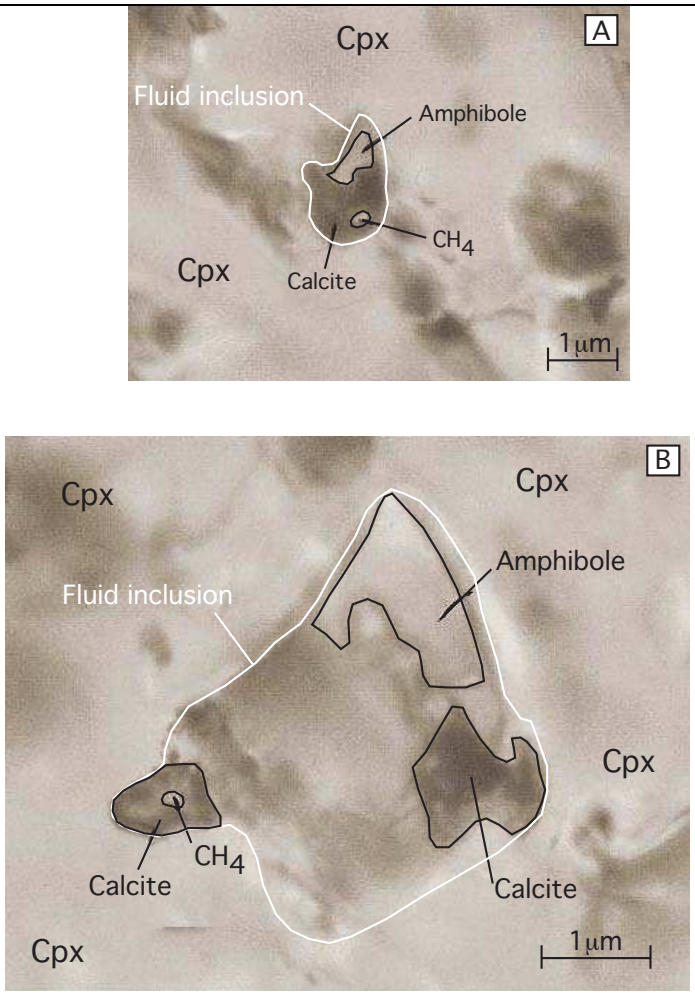

Fig. 4-11:Photomicrograph of secondary fluid inclusions A) from the 14.01-orthopyroxenite and B) from the 16.18 websterite (Raman Spectroscopy).
Both examples of fluid inclusions are hosted within a clinopyroxene crystal (Cpx) and include methane (CH4) and daughter minerals such as amphibole and calcite.

3.2.2.2 By the LA ICP-MS

It is important to clarify that using the LA ICP-MS technique to measure the composition of the fluid inclusions leads to purely qualitative trace element concentrations. Absolute concentrations of trace elements in the fluid inclusions are impossible to determine as no internal standardisation could be applied to these data. Because of their small size, it is also impossible to laser-ablate only the fluid inclusions without partially pulverizing the host mineral (Fig. 4-1).

The qualitative results are shown in the multi-element normalised to primitive mantle diagrams (Fig. 4-12), which graphically outline the relative difference in trace elements

Table 4-5: Average trace element compositions of pyroxene with fluid inclusions compared to pyroxene without fluid inclusions.

Sample	14.01	14.01	16.01	16.19	14.14	14.33	16.18	17.01	18.08
Mineral	Cpx	Opx	Cpx	Cpx	Cpx	Cpx	Cpx	Opx	Cpx
Rock Type	G1a	G1a	G1a	G1a	G1b	G2a	G2a	G2a	G2b
Rb	bdl	0.003	bdl	bdl	0.001	0.017	0.003	0.105	0.065
Sr	1.008	0.018	2.573	4.914	10.748	11.236	15.015	0.286	20.063
Y	1.751	0.202	2.793	3.256	2.289	3.307	2.368	0.407	2.238
Zr	0.233	0.043	0.433	1.116	0.646	0.867	0.890	0.149	2.127
Nb	0.046	0.029	0.045	0.059	0.020	0.029	0.011	0.006	0.010
Cs	0.002	0.006	0.005	0.001	0.000	0.012	0.001	0.013	0.002
Ba	0.033	0.007	0.004	0.051	0.005	0.065	0.002	0.014	0.191
La	0.003	0.000	0.010	0.029	0.035	0.049	0.051	0.000	0.089
Ce	0.018	0.000	0.051	0.110	0.160	0.249	0.246	0.002	0.459
Pr	0.005	0.001	0.013	0.024	0.035	0.062	0.052	0.001	0.100
Nd	0.050	0.004	0.104	0.217	0.251	0.456	0.367	0.003	0.631
Sm	0.049	0.003	0.088	0.165	0.148	0.252	0.193	0.005	0.301
Eu	0.026	0.002	0.041	0.083	0.057	0.102	0.074	0.003	0.127
Gd	0.143	0.005	0.239	0.403	0.259	0.430	0.323	0.014	0.430
Dy	0.292	0.019	0.480	0.620	0.371	0.582	0.396	0.048	0.456
Ho	0.070	0.007	0.115	0.128	0.081	0.128	0.086	0.016	0.091
Er	0.220	0.030	0.365	0.386	0.246	0.372	0.265	0.067	0.262
Tm	0.033	0.006	0.054	0.052	0.035	0.053	0.037	0.014	0.036
Yb	0.211	0.063	0.354	0.347	0.221	0.340	0.248	0.124	0.228
Lu	0.030	0.011	0.051	0.044	0.036	0.051	0.036	0.024	0.033
Hf	0.014	0.003	0.024	0.058	0.033	0.048	0.039	0.007	0.103
Pb	0.012	0.011	0.009	0.015	0.013	0.058	0.019	0.052	0.064

Sample	14.01	14.01	16.01	16.19	14.14	14.33	16.18	17.01	18.08
Mineral	Cpx+Fl	Opx+Fl	Cpx+Fl	Cpx+Fl	Cpx+Fl	Cpx+Fl	Cpx+Fl	Opx+Fl	Cpx+Fl
Rock Type	G1a	G1a	G1a	G1a	G1b	G2a	G2a	G2a	G2b
Rb	0.030	0.266	0.028	0.005	0.036	0.080	0.017	0.081	0.120
Sr	1.908	1.087	19.378	8.998	16.186	31.807	15.240	0.628	21.104
Y	1.856	0.232	2.809	3.032	2.250	3.409	2.333	0.465	2.527
Zr	0.263	0.050	0.426	0.848	0.640	0.865	0.882	0.157	2.400
Nb	0.050	0.032	0.047	0.039	0.019	0.024	0.012	0.007	0.012
Cs	0.286	1.825	0.438	0.012	0.080	0.122	0.085	0.009	0.006
Ba	0.449	0.261	0.194	1143	8.516	2.155	4.593	0.034	0.466
La	0.003	0.000	0.010	0.019	0.034	0.049	0.051	-0.001	0.102
Ce	0.017	0.000	0.051	0.065	0.159	0.251	0.235	0.002	0.529
Pr	0.005	0.000	0.013	0.018	0.035	0.061	0.051	0.001	0.114
Nd	0.052	0.002	0.108	0.155	0.250	0.458	0.355	0.005	0.714
Sm	0.052	0.003	0.087	0.130	0.143	0.257	0.190	0.004	0.343
Eu	0.025	0.001	0.040	0.062	0.056	0.103	0.074	0.002	0.143
Gd	0.148	0.007	0.229	0.312	0.257	0.436	0.313	0.015	0.480
Dy	0.314	0.025	0.471	0.523	0.370	0.587	0.394	0.052	0.520
Ho	0.075	0.009	0.114	0.118	0.080	0.127	0.086	0.017	0.104
Er	0.238	0.037	0.364	0.343	0.241	0.379	0.260	0.076	0.296
Tm	0.034	0.008	0.053	0.047	0.036	0.053	0.037	0.015	0.040
Yb	0.226	0.068	0.355	0.287	0.223	0.349	0.241	0.145	0.262
Lu	0.033	0.012	0.053	0.042	0.034	0.051	0.037	0.028	0.037
Hf	0.014	0.003	0.025	0.048	0.031	0.048	0.041	0.007	0.118
Pb	0.022	0.010	0.013	0.054	0.024	0.052	0.035	0.042	0.248

All trace elements are in ppm (analysed by LA ICP-MS)
List of Abbreviations:
G1: orthopyroxenites; G2: websterites; G3: clinopyroxenites
a, b: indicate the subgroups of pyroxenites (refer to text for explanation)
Cpx: Clinopyroxene; Cpx+Fl: Clinopyroxene + Fluid inclusions; Opx: Orthopyroxene; Opx+Fl: Orthopyroxene + Fluid inclusions
bdl: below detection limit

See Appendix 2 for representative trace element compositions of clinopyroxene.

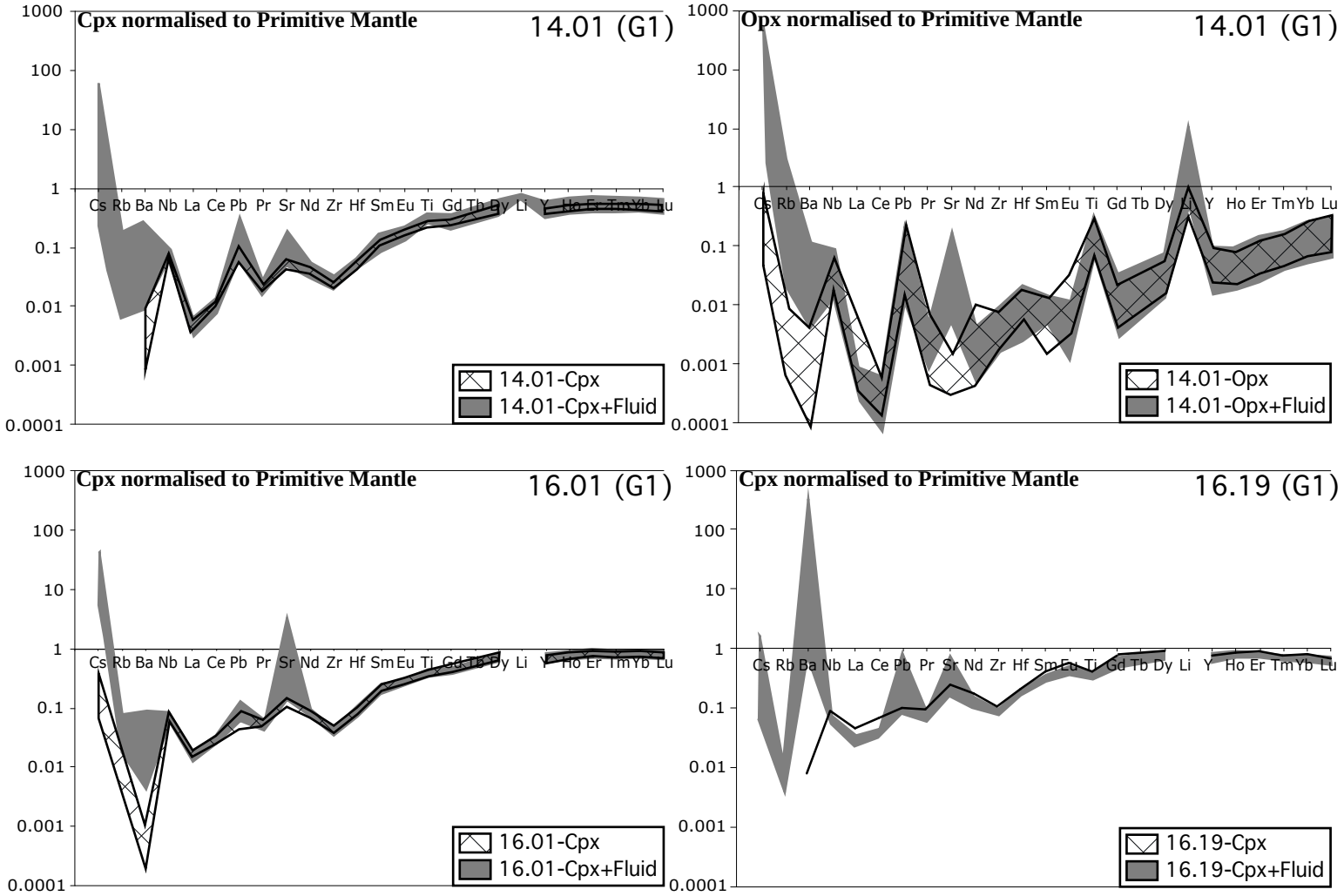

Fig. 4-12: Primitive mantle-normalised multi-element plots of "clean" pyroxene (Cpx or Opx) (without any fluid inclusions) compared to clinopyroxene containing fluid inclusions (Cpx+Fluid or Opx+Fluid) for each of the G1-orthopyroxenites analysed. Primitive mantle normalising values are from Sun and McDonough (1989).

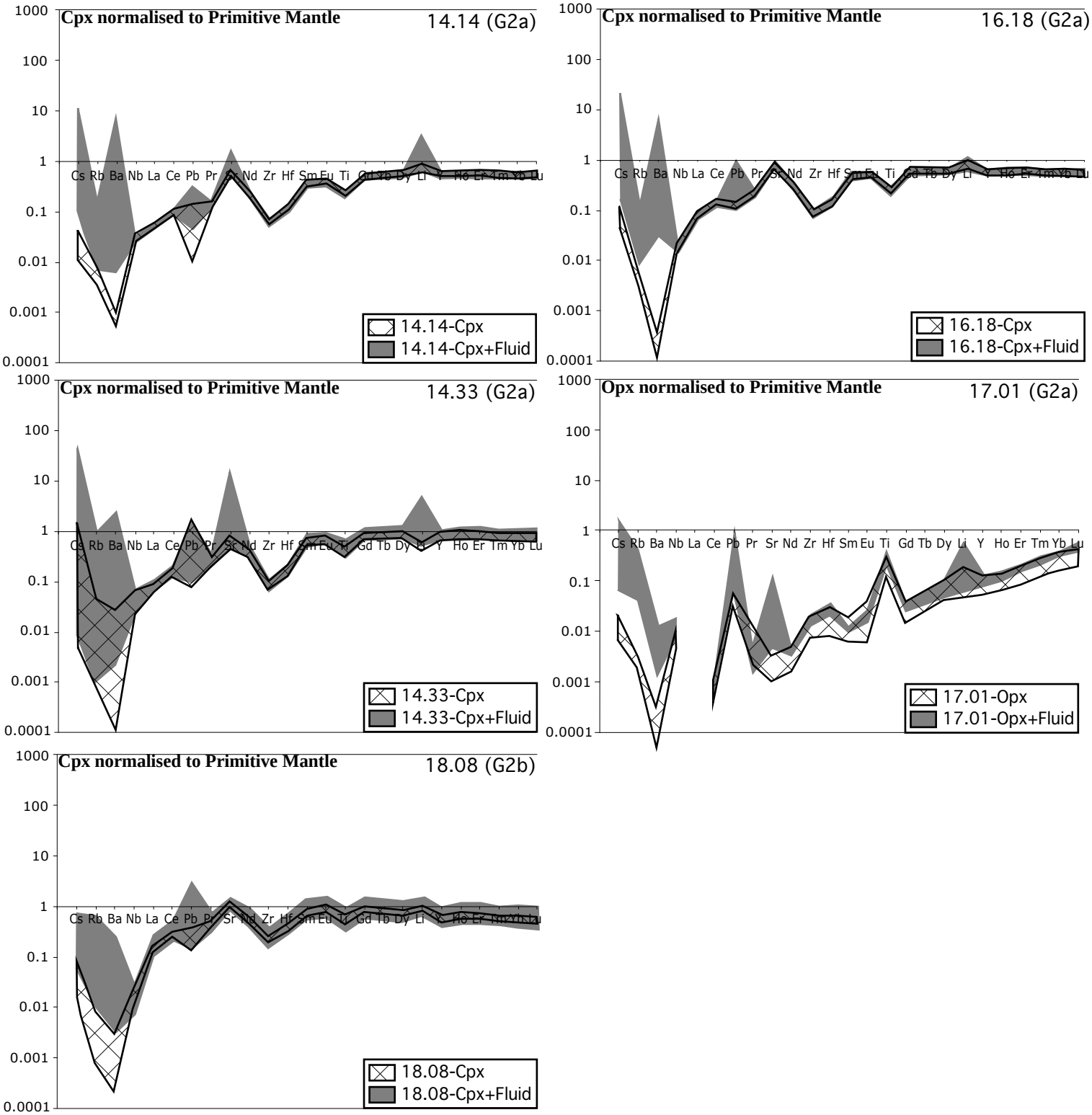

Fig. 4-12 (continued): Primitive mantle-normalised multi-element plots of "clean" pyroxene (Cpx or Opx) (without any fluid inclusions) compared to pyroxene containing fluid inclusions (Cpx+Fluid or Opx+Fluid) for each of the G2-websterites analysed. Primitive mantle normalising values are from Sun and McDonough (1989).

between the pyroxene containing fluid inclusions (Px+Fl) and the clean pyroxene (Clean Px). At this stage, it is noteworthy to say that no geochemical differences in trace elements compositions were identified between the primary and secondary fluid inclusions. Consequently both types of fluid inclusions are referred to a common fluid Phase (Fl). This implies that fluids trapped during or after the growth of the host pyroxene have the same overall compositions.

Both clinopyroxene (Cpx) and orthopyroxene (Opx) were analysed by LA ICP-MS. By comparing the concentrations of the pyroxene (opx and cpx) with inclusions against the "clean" pyroxene (clean cpx and clean opx), I can indirectly determine the solute contents of the fluid. Normalisation of pyroxene with inclusions to "clean" pyroxene (Fig. 4-13) reveals that the fluid is highly enriched in Ba and Cs and a lesser extent Rb, Pb and Sr. Although Pb and Sr are enriched relative to Pr in the "clean pyroxene", the fluid inclusions contain even more Sr and Pb. Additionally, the primitive mantle-normalised multi-element diagrams for the pyroxene with inclusions are very similar to the ones for the clean pyroxene. They both have identical concentrations in REE and HFSE (Zr, Hf and Ti) and show similar features with substantial Pb and Sr spikes. Hence, pyroxene containing fluid inclusions differs from the clean "pyroxene" by being more enriched in LILE and sometimes Pb, Sr and Li.

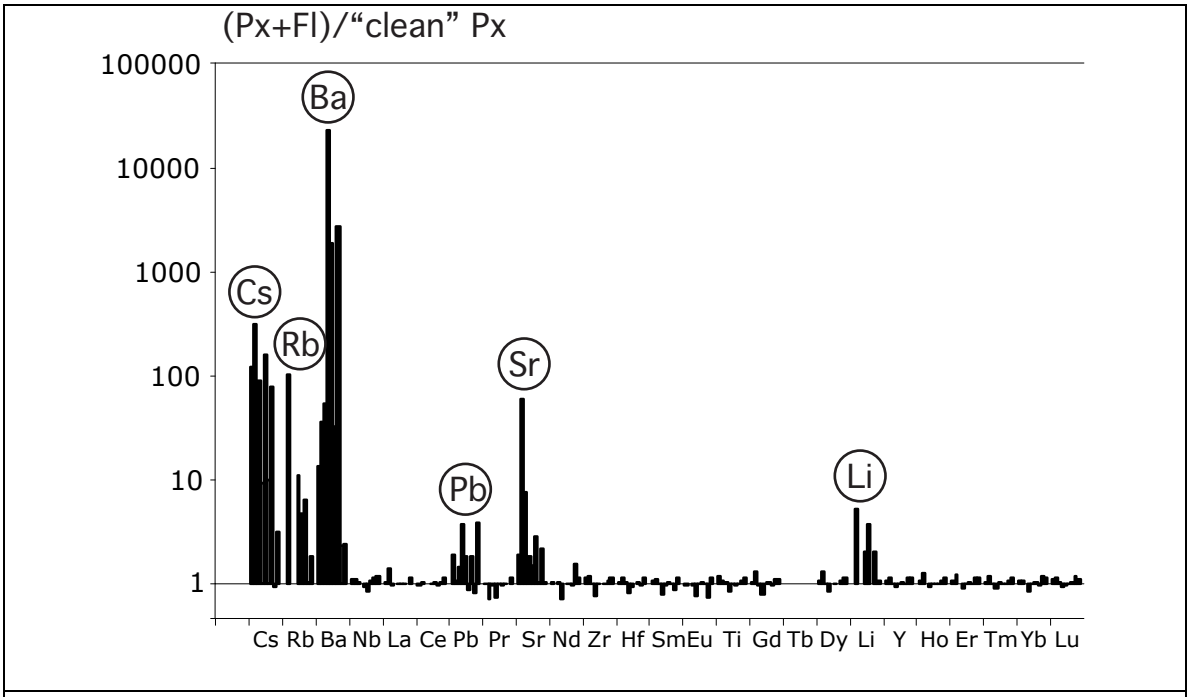

Fig. 4-13: Normalisation of pyroxene with fluid inclusions (Px+Fl) to pyroxene without fluid inclusions ("clean" Px).
This plot indicates that the fluid inclusions are highly enriched in Cs, Rb, Ba and Sr but moderately in B, Li, and Pb compared to the pyroxene.

3.3 The Re/Os geochemistry

The Re and Os data are given in the Table 4-6. Os isotopic compositions were only analysed for a few samples from the G1-orthopyroxenites and the G2-websterites but no G3-clinopyroxenites. The G1- and G2-pyroxenites are characterised by low Os contents (0.05-0.6ppb) with the exception of one sample. Orthopyroxenite 16.05, which displays the lowest $^{187}Os/^{188}Os$ ratio, is the most enriched sample in Os with the Os concentration reaching 3.4ppb. The Re contents are low ranging from 0.02 to 1.1 ppb.

Table 4-6: Re-Os isotopic data for San Jorge pyroxenites and Choiseul peridotites.

Sample	Rock Type	Location	Re (ppt)	Os (ppt)	$^{188}Re / ^{188}Os$	$^{187}Os / ^{188}Os$
16.01	G1a-orthopyroxenite	San Jorge	17.7	267.2	0.319	0.1430
16.05	G1a-orthopyroxenite	San Jorge	46.5	3398.3	0.066	0.1275
16.11	G1a-orthopyroxenite	San Jorge	63.7	274.7	1.117	0.1302
14.32	G1a-orthopyroxenite	San Jorge	15.9	638.9	0.120	0.1275
18.03	G1a-orthopyroxenite	San Jorge	n.a.	103.1	n.a.	0.1355
14.14	G1b-orthopyroxenite	San Jorge	77.8	50.6	7.415	0.1358
14.33	G2a-websterite	San Jorge	1084.7	111.3	47.191	0.1673
16.03	G2a-websterite	San Jorge	33.4	220.3	0.731	0.1288
14.15	G2a-websterite	San Jorge	135.8	353.6	1.848	0.1228
21.08	Choiseul peridotite	Choiseul	183.7	4460.2	0.198	0.1277
21.10	Choiseul peridotite	Choiseul	232.2	4217.6	0.265	0.1266

In the Re vs. Os diagram (Fig. 4-14A), the samples clearly plot apart from MORB field and define a negative trend the left of the OIB field. The same trend is observed in the logarithmic $^{187}Re/^{188}Os$ vs. Os diagram (Fig. 4-14B) where the pyroxenites plot within the OIB field with low $^{187}Re/^{188}Os$ ratio and high Os concentrations.

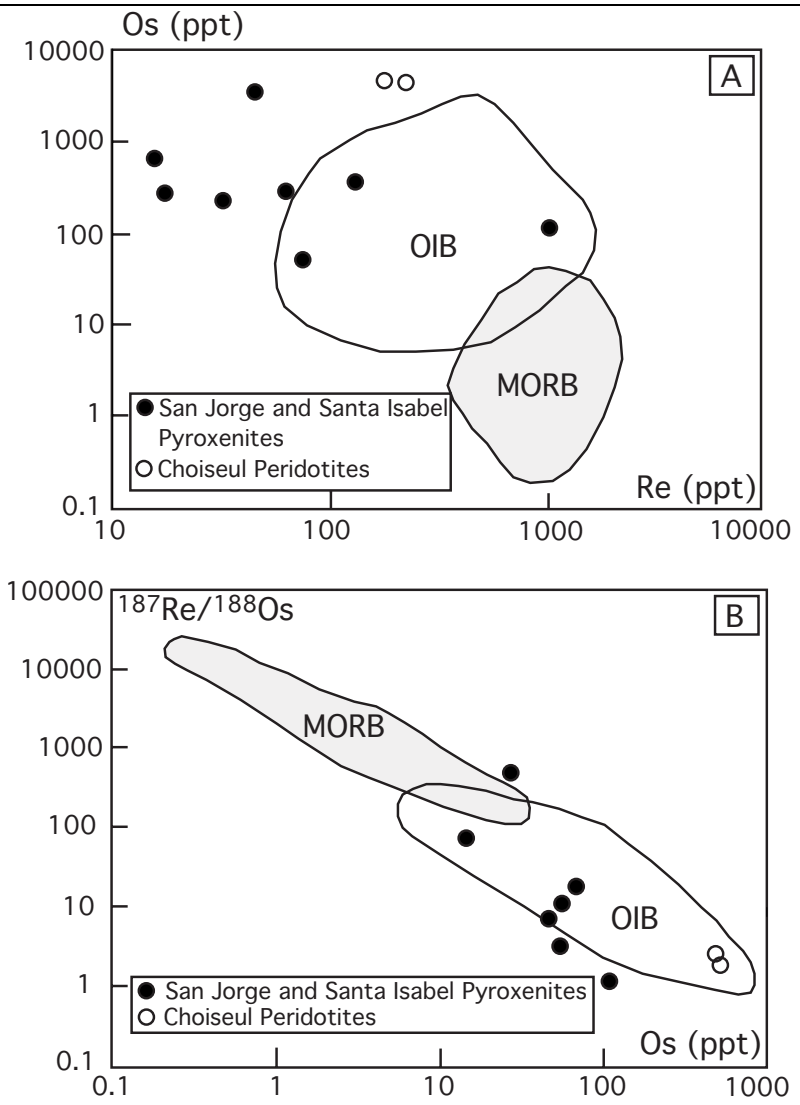

Fig. 4-14*:* Os concentrations vs. Re concentrations (A) and $^{187}Re/^{188}Os$ vs. Os concentrations on a logarithmic scale for the San Jorge and Santa Isabel Pyroxenites and the Choiseul Peridotites.
MORB and OIB data are from the compilation made by Alvès et al. (1999).

The $^{187}Os/^{188}Os$ ratios of the G1- and G2-pyroxenites range from 0.1228 to 0.1673. Most of the pyroxenites are more radiogenic than the Choiseul peridotites (average of 0.1272) except for the websterite 14.15, which has slightly lower $^{187}Os/^{188}Os$ ratio (0.1228). The $^{187}Os/^{188}Os$ ratios of the orthopyroxenite 16.01 (0.1430) and the websterite 14.33 (0.1673) are much higher compared to the other pyroxenites, which the $^{187}Os/^{188}Os$ ratios only average 0.1299 (Table 4-6).

4 INTERPRETATIONS

4.1 Mineral Partition Coefficients

4.1.1 Opx/Cpx

Knowledge of the equilibrium partitioning of elements among co-existing phases such as orthopyroxene (Opx) and clinopyroxene (Cpx) is useful for recording the true crystallographic partitioning between minerals and predicting the distribution of trace element in these pyroxenites. Average inter-mineral distribution coefficients $D^{opx/cpx}$ for trace elements obtained from in situ analyses of orthopyroxene and clinopyroxene are given in Table 4-8 and are respectively illustrated in Figure 4-15.

Our results show that the partition coefficients for REE between orthopyroxene and clinopyroxene from the pyroxenites (Fig. 4-15A) are similar except for LREE, which show higher values in the G1-orthopyroxenites. The REE values obtained for the G2-websterites are comparable to those obtained for the websterites and peridotites from Ronda (Garrido et al., 2000) indicating that the orthopyroxene and the clinopyroxene from the G2-websterites are in equilibrium. On the other hand, the G1-orthopyroxenites have slightly higher $D^{opx/cpx}$ values for LREE than those reported from Ronda (Garrido et al., 2000). Two samples (18.03 and 14.01) respectively show discrepancies for LREE and MREE compared to the Ronda websterites and peridotites. For example, the $D^{opx/cpx}$ LREE values for the sample 18.03 are much higher than any of the other pyroxenites from San Jorge/ Santa Isabel and Ronda. This upward inflection from La to Sm of $D^{opx/cpx}$ is related to the extremely LREE-depleted pattern of the clinopyroxene for the sample 18.03 when the orthopyroxene from this sample has similar chondrite-normalised REE patterns to the orthopyroxene from the other pyroxenites. The same applies to the sample 14.01.

Despite that, the $D^{opx/cpx}$ for most of the other trace elements are comparable to published values for separated pyroxene measured by Garrido et al., 2000 (Fig. 4-14B). The $D^{opx/cpx}$ for Zr and Hf is an order of magnitude higher than Nd and Eu attesting the potential of orthopyroxene to fractionate Zr and Hf from REE. Incompatible elements such as LILE, Sr and Pb show high to very high $D^{opx/cpx}$ for all pyroxenites including the two samples 18.03 and 14.01. Similar high $D^{opx/cpx}$ values for Rb, Ba and Sr has been reported also in spinel peridotite xenoliths (Bedini and Bodinier, 1999; Garrido et al., 2000) and in Ronda websterites (Garrido et al., 2000) and ascribed as incompatible elements-enriched fluid inclusions trapped in clinopyroxene and other minerals. $D^{opx/cpx}$ for Ti are identical to around 1 for all of the orthopyroxenites and websterites indicating that Ti is incorporated similarly in both pyroxenes.

Overall, the $D^{opx/cpx}$ values between the G1-orthopyroxenites and the G2-websterites are very similar for immobile elements such as MREE, HREE, Zr, Hf and Ti but slightly differ for LILE, Pb and Sr, which are supposed to be mobile in fluids. Only some orthopyroxenites (18.03 and 14.01) show noticeable discrepancies in their $D^{opx/cpx}$ values for LREE compared to $D^{opx/cpx}$ mantle values for LREE indicating that the clinopyroxene in these samples represents a relict from the mantle.

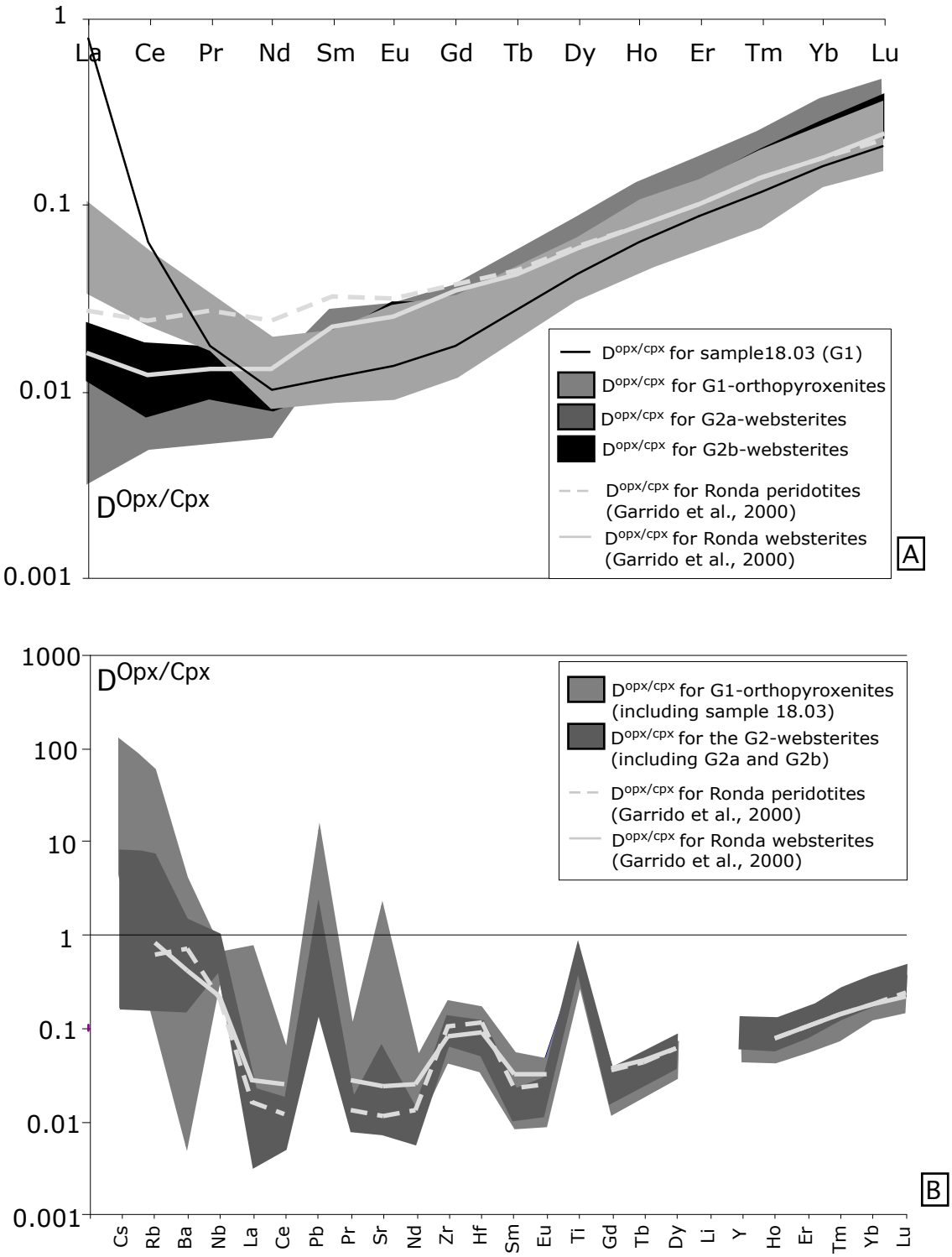

Fig. 4-15: Average $D^{opx/cpx}$ for REE (A) and extended trace elements (B) of the G1-orthopyroxenites and the G2-websterites.

The $D^{opx/cpx}$ for the San Jorge and Santa Isabel pyroxenites are compared to those of Garrido et al. (2000) calculated for peridotites and websterites from Ronda (Spain).

4.1.2 Amphi/Cpx

Comparing the primitive mantle-normalised multi-element diagrams for the amphibole (Amphi) and the clinopyroxene (Cpx) (Fig. 4-16) reveals that, for most of the samples (except 15.07), the amphibole and clinopyroxene have similar REE patterns and are both characterised by variable enrichments in LILE, striking Pb and Sr spikes, and depletions of Zr and Hf relative to Nd and Sm.

The resulting partition coefficients, calculated from in situ analyses of trace elements in coexisting amphibole and clinopyroxene pairs (Table 4-9), are plotted in Figure 4-17. As a whole, D_{REE} are consistent across all the pyroxenites with a same range of 0.5-3.7 for LREE, MREE and HREE (Fig. 4-17A). While the REE are more partitioned into the amphibole than into the clinopyroxene ($D^{amphi/cpx}$ >1), the websterite 16.09 is the only sample with $D^{amphi/cpx}$ <1 for REE (Figure 11A). This indicates that the amphibole and clinopyroxene are in equilibrium with each other in the pyroxenites except for the sample 16.09. Even if the amphibole is considered to be the product of retrograde hydration of clinopyroxene, most of the amphibole has re-equilibrated with the clinopyroxene probably because the fluid responsible for this hydration percolated the pyroxenites just after their formation. Only the amphibole from the sample 16.09 is in disequilibrium with the clinopyroxene, which indicates the fluid involved into the clinopyroxene hydration came after the pyroxenites were re-equilibrated.

Figure 4-17B shows that the average amphibole/clinopyroxene partition coefficients for LILE are higher (close to 10) relative to the other elements. This reflects that the amphibole is systematically more enriched than the clinopyroxene for the LILE elements (Fig. 4-16). The D values for Sr are lower to the ones for Nd suggesting that Sr fractionates more in the clinopyroxene than in the amphibole (Fig. 4-17B). However, D_{Ti} indicates a strong preference for amphibole. Partitioning in amphibole-clinopyroxene for the sample 15.07 is different to the D values for the other samples. For sample 15.07, D_{Zr} and D_{Hf} indicate a strong selectivity for amphibole whereas Pb and Sr have a strong preference for the clinopyroxene. Like for the other samples, D_{Ti} indicates a strong preference for amphibole in the sample 15.07. In this sample, Nb is strongly partitioned into the amphibole with D_{Nb} values similar to D_{Ba} (D=100).

In situ analyses of trace elements in coexisting amphibole and clinopyroxene pairs are still scarce. Vanucci et al. (1995) have compiled data of amphibole/clinopyroxene partition coefficients for REE, Sr, Zr and Ti for spinel lherzolites representative of the subcontinental mantle. The authors also determined similar D values to those mantle rocks for spinel websterite dykes. The observed partitioning of REE in amphibole-clinopyroxene pairs does not differ from those for spinel lherzolites and websterites described by Vanucci et al. (1995) (Fig. 4-17). Alike the $D^{amphi/cpx}$ for the San Jorge and Santa Isabel pyroxenites, their D_{REE} are still in the same range (0.5-3.7) for all REE (Fig. 4-17A). The D_{Ti} values determined by Vanucci et al. (1995) also closely match our values with Ti/Ti* values higher than unity, indicating that Ti has a strong preference for amphibole in all of the samples (Fig. 4-17B). In contrast to the San Jorge and Santa Isabel pyroxenites, Sr is more partitioned in amphibole than it is in the clinopyroxene resulting from Sr/Sr* superior to 1 (instead of Sr/Sr*<1 for the pyroxenites) (Fig. 4-17B).

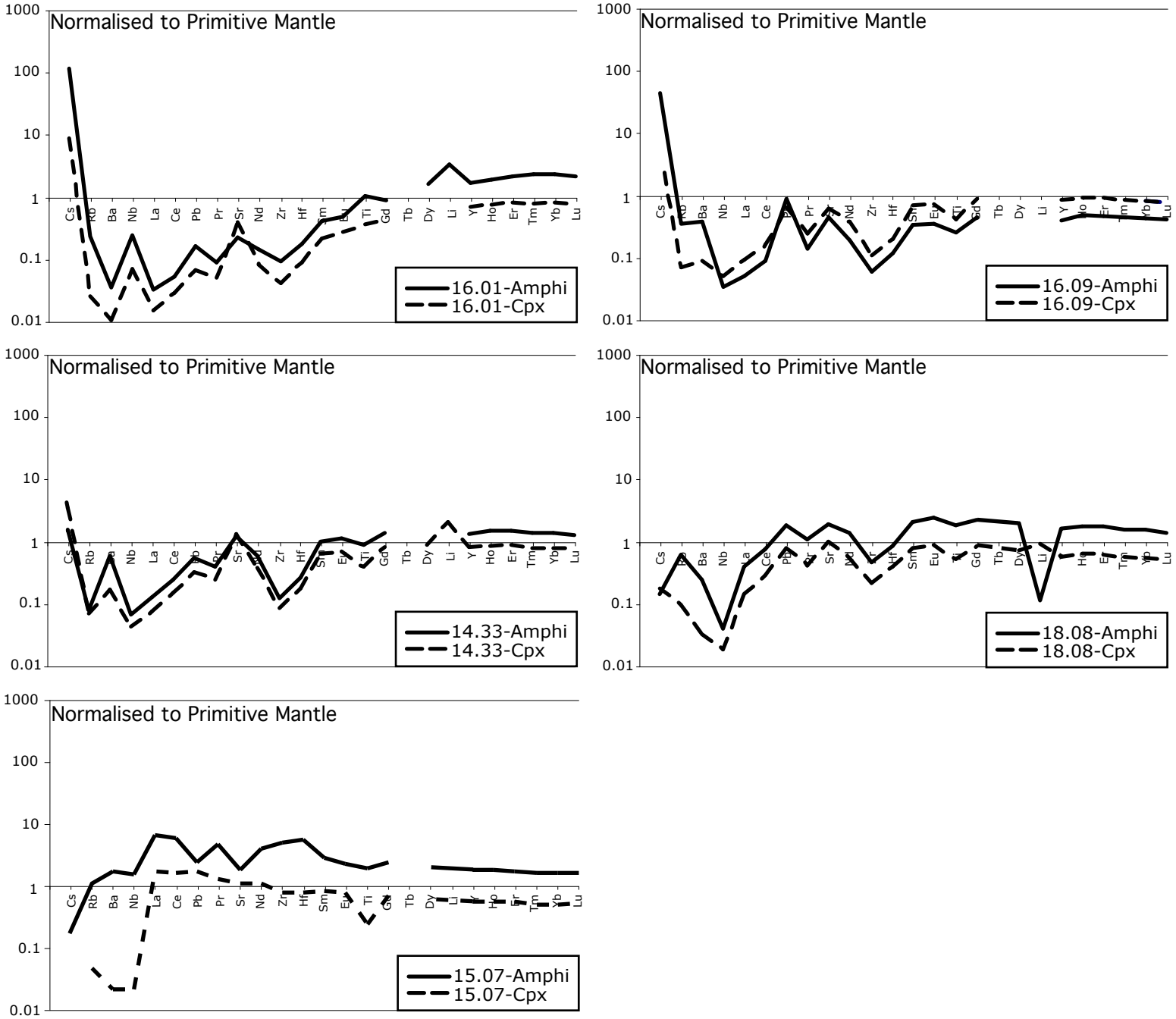

Fig. 4-16: Comparison between the primitive mantle-normalised multi-element average compositions for clinopyroxene and for the amphibole from some of the pyroxenites.
Primitive mantle normalising values are from Sun and McDonough (1989).

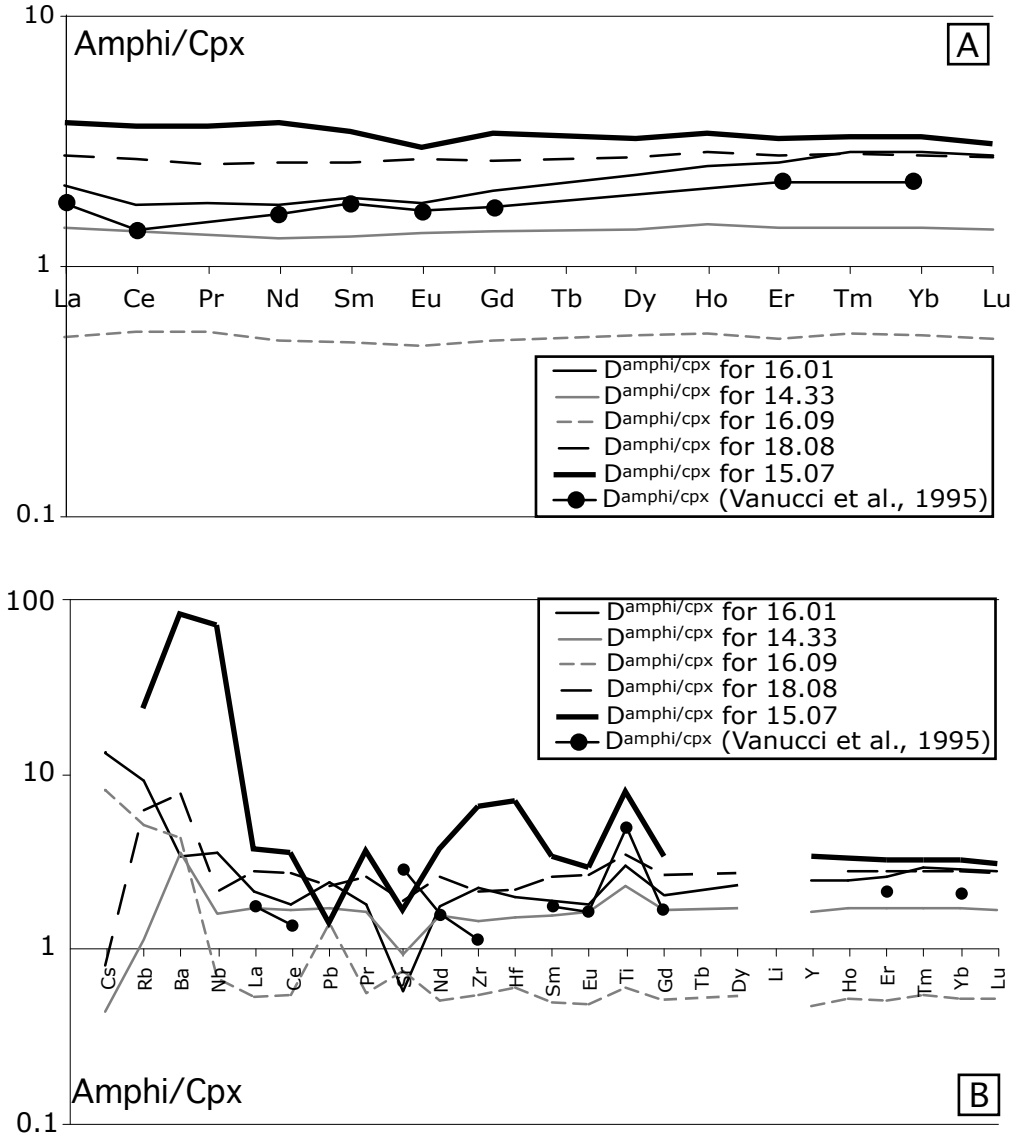

Fig. 4-17: Average $D^{amphi/cpx}$ for REE (A) and extended trace elements (B) of some of the pyroxenites.
The $D^{amphi/cpx}$ for the San Jorge and Santa Isabel pyroxenites are compared to those of Vanucci et al. (1999) calculated for lherzolites from subcontinental mantle.

4.2 Whole rock elemental budgets

4.2.1 Mass balance: comparison between whole rock and mineral trace element chemistry

Average trace element abundances of in-situ analyses of clinopyroxene and orthopyroxene determined by LA ICP-MS are compared to the whole rock compositions in trace elements for each sample from the three different groups of pyroxenites. The results are shown in the primitive mantle-normalised multi-element diagrams (Fig. 4-18). One important observation is that the data for clinopyroxene, orthopyroxene and whole rock from all of the pyroxenites show the same geochemical characteristics including striking LILE enrichments, Pb and Sr spikes relative to Pr coupled with low REE abundances and LREE depletion. That is to say that LILE, Pb and Sr are enriched in both bulk rock and minerals trace element data, which indicate that these enrichments are partly primary (Fig. 4-18).

The trace element compositions of the whole rock are strongly dictated by the mineral proportion of the samples. The G1-orthopyroxenites are dominated by the large number of orthopyroxene contained in these samples (Fig. 4-18A). Representing more than 80% of the modal proportion, the orthopyroxene trace element "signature" is apparent in the primitive mantle-normalised bulk rock multi-element diagrams with the positive Ti anomalies and similar HREE abundances. Although the G1-orthopyroxenites contain a small amount of interstitial spinel and olivine, the trace element compositions of the whole rock are not affected by these minerals as spinel and olivine are poor in trace elements. Only Nb and Ti are enriched in the spinel. But considering their limited amount in the pyroxenites (1-2% modal proportion), spinel does not change the budget of these elements for the G1-whole rocks. Despite being in small proportion, the clinopyroxene phase plays an important role in the whole rock trace element budget and particularly for the REE. A small increase in the modal proportion of clinopyroxene causes a significant ascent in the REE budgets of the whole rock. This feature is obvious with all of orthopyroxenites containing more than 5% modal proportion of clinopyroxene. In these samples but 16.01, the primitive mantle-normalised bulk rock multi-element diagrams for the whole rock plot exactly between the ones for the orthopyroxene and the clinopyroxene. Sample 16.01 is the only orthopyroxenite that the whole rock chemistry shows a LREE enrichment, which contrast with the LREE-depleted patterns for other G1-clinopyroxene and G1-orthopyroxene.

The whole rock chemistry of the G2-websterites is totally dominated by the trace element compositions of the clinopyroxene (Fig. 4-18B). As revealed by the primitive mantle-normalised multi-element diagrams, the profiles for the clinopyroxene and the whole rock are practically similar with the exception of the LILE. Negative Ti and positive Sr spikes are typical to the G2-whole rock and G2-clinopyroxene data. Same concentrations and patterns in the trace elements of the clinopyroxene and the whole rock means that even if the orthopyroxene phase accounts for a significant amount of the G2-websterites, this mineral plays a minor role in the trace element budget of the G2-whole rock. The G2b-websterites are distinct from the G2a-websterites by having the bell-shaped REE profiles for the whole rock composition, which is also characteristic to the G2b-clinopyroxene.

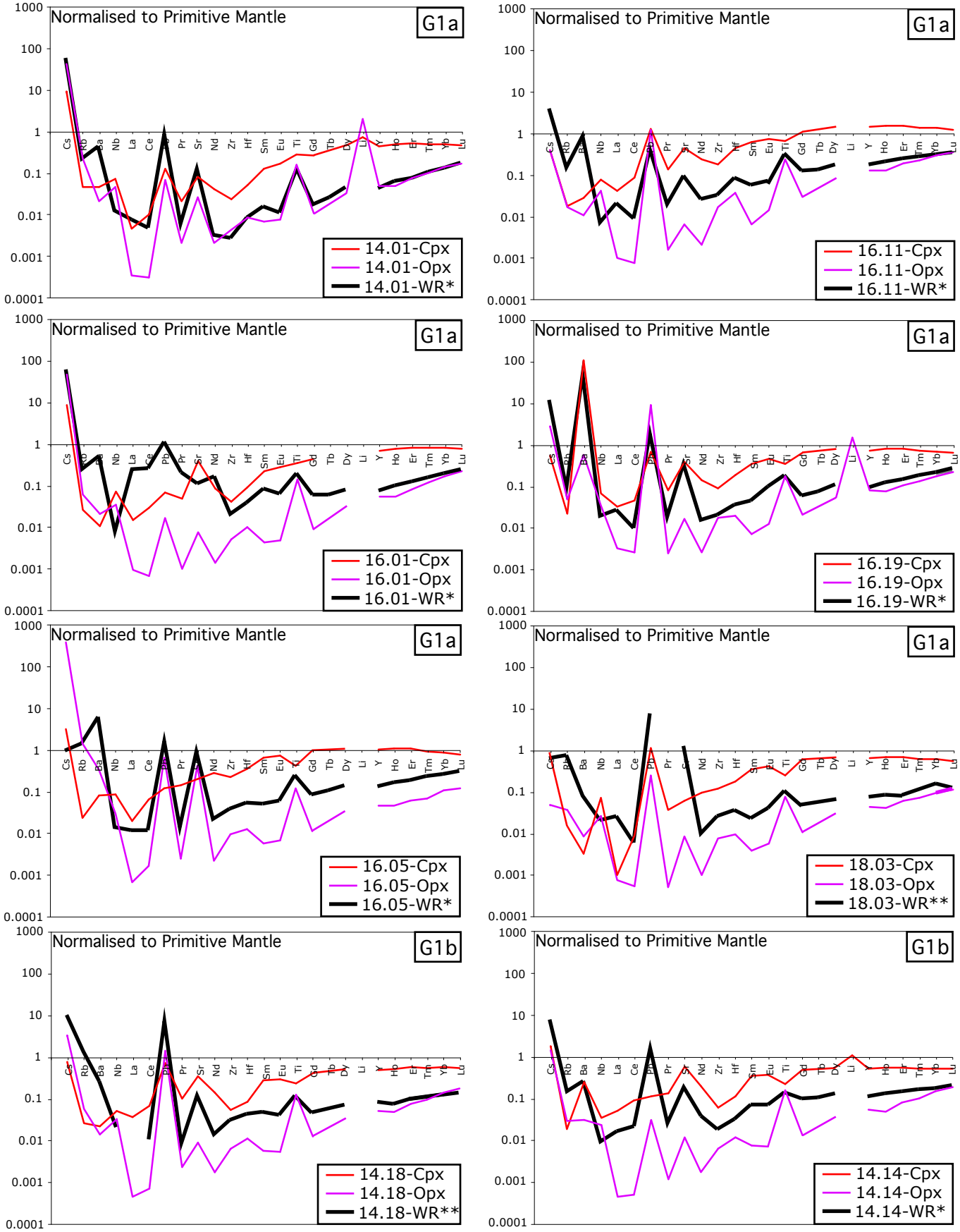

Fig. 4-18A: Primitive mantle-normalised multi-element average compositions for clinopyroxene (Cpx), orthopyroxene (Opx) and whole rock (WR) from the G1-orthopyroxenites.
Primitive mantle normalising values are from Sun and McDonough (1989).
* indicates that the whole rock trace element compositions were determined by Solution ICP-MS
** indicates that the whole rock trace element compositions were determined by LA ICP-MS

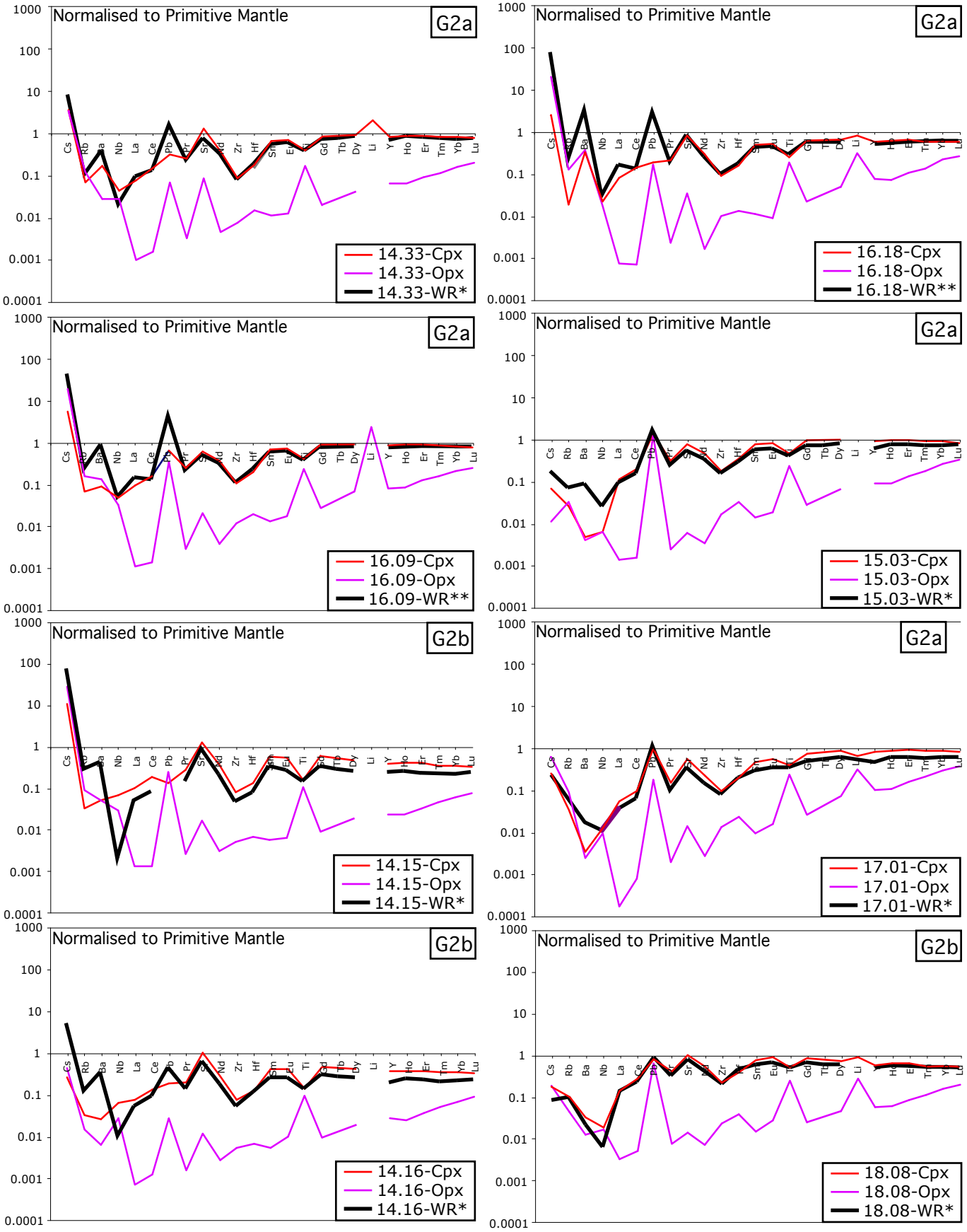

Figure 4-18B: Primitive mantle-normalised multi-element average compositions for clinopyroxene (Cpx), orthopyroxene (Opx) and whole rock (WR) from the G2-websterites.
Primitive mantle normalising values are from Sun and McDonough (1989).
* indicates that the whole rock trace element compositions were determined by Solution ICP-MS
** indicates that the whole rock trace element compositions were determined by LA ICP-MS

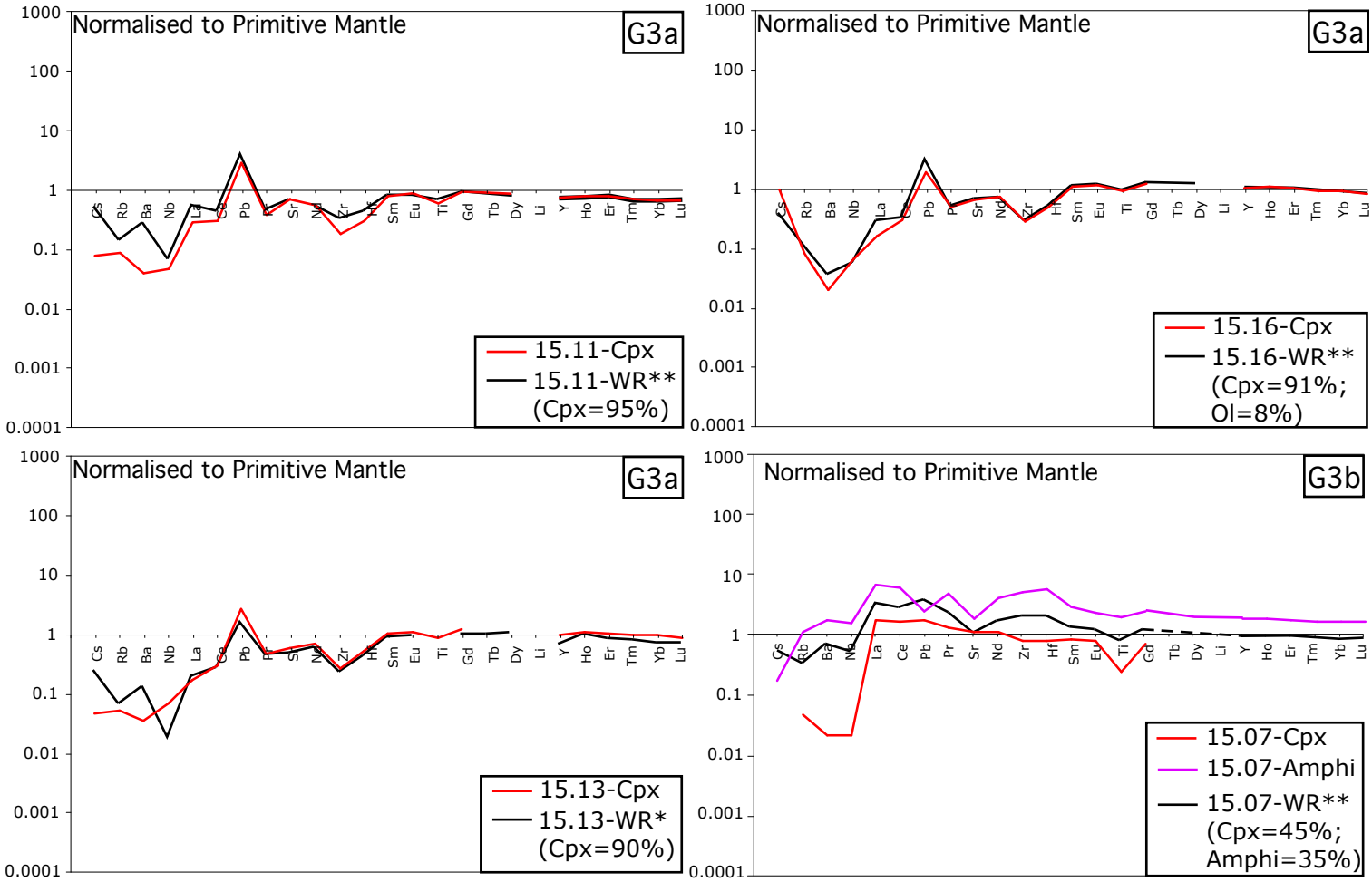

Fig. 4-18C: Primitive mantle-normalised multi-element average compositions for clinopyroxene (Cpx) and whole rock (WR) from the G3-clinopyroxenites.
Primitive mantle normalising values are from Sun and McDonough (1989).
No orthopyroxene was analysed for this type of pyroxenites. Average amphibole composition is represented for the sample 15.07 (G3b-clinopyroxenite).
* indicates that the whole rock trace element compositions were determined by Solution ICP-MS
** indicates that the whole rock trace element compositions were determined by LA ICP-MS

The G3a-whole rock and G3a-clinopyroxene have identical trace element compositions (Fig. 4-18C). They both exhibit exactly the same multi-element diagrams normalised to primitive mantle with LILE depletion relative to LREE, positive Pb spikes, negative Zr-Hf anomalies relative to Nd and Sm and slight Ti negative anomalies relative to Eu and Gd. This attests that the clinopyroxene controls totally the trace element budget of the G3-clinopyroxenites. The G3b-clinopyroxenite differs from the other pyroxenites (G3a) in having a large amount of amphibole (35% modal proportion). This mineralogical change is accompanied with a difference of compositions for the clinopyroxene, the amphibole and the whole rock compared to the other pyroxenites (Fig. 4-18C). For instance, multi-element normalised to primitive mantle diagrams for the G3b-clinopyroxenite are radically different to other pyroxenites (Fig. 4-18C). However the G3b-whole rock chemistry is consistent with the compositions of the amphibole and clinopyroxene that are contained in this sample with similar common features (i.e. LREE –enriched patterns and negative Sr anomalies). This means that amphibole and clinopyroxene are both important in the trace element budget of the G3b-clinopyroxenite.

4.2.2 Trace element distribution for the pyroxenites

The trace element budget among the mineral inventory of the pyroxenites was calculated using the relative proportions of minerals and the average trace element composition of each mineral. Mineral modes were determined by mass balance using the bulk-rock major element chemistry (measured by XRF) and the total major-element mineral chemistry (measured by Microprobe). The calculated trace element concentrations are compared to the whole rock compositions in the primitive mantle-normalised multi-element diagrams presented in Figures 4-19A and 4-19B. To calculate a precise budgeting of the trace elements in the pyroxenites, not only the clinopyroxene and orthopyroxene were included but also olivine and spinel (especially for the G1-orthopyroxenites) and amphibole were taken in account.

The first observation is that the trace element budgets calculated from the various minerals completely match the whole rock compositions in most of the pyroxenites. Nonetheless, trace element compositions calculated from the mineral inventory can exceed 100% percent of the whole rock for some samples. This poor budgeting arises for one of the following reasons; (1) analytical problem to measure accurately the whole rock and mineral trace element compositions due to their low trace element chemistry; (2) the fact that some samples are heterogeneous in petrology (i.e.G1b-orthopyroxenites) and mineralogy causes fluctuation in the whole rock composition and makes it difficult to determine precisely their mineral propositions; (3) the use of average compositions of minerals when individual minerals display compositional variations in volatile elements for each sample probably due to fluid inclusions; (4) the lack of data for minor phases at grain boundaries or inside primary minerals (alteration phases).

For instance, systematic discrepancy between the whole rock and calculated trace element budgets is obvious for Nb contents in the primitive mantle-normalised multi-element diagrams for all of the pyroxenites. This Nb deficit in the whole rock trace element contents is most likely related to a problem of sample preparation. Comparing the whole rock concentrations determined by Solution ICP-MS and LA ICP-MS reveals that the Nb deficit between whole rock and calculated compositions is more important for

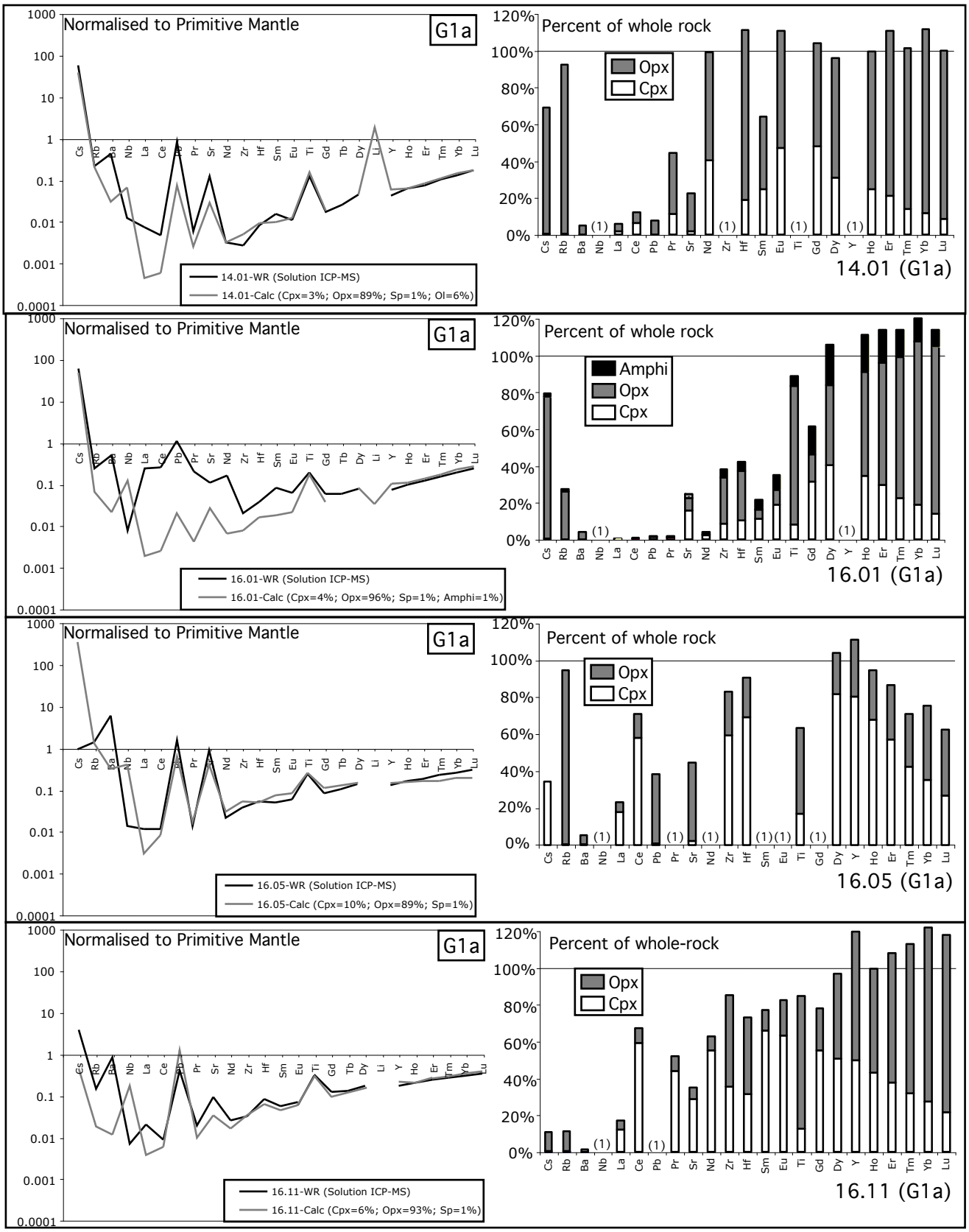

Fig. 4-19A: Primitive mantle-normalised multi-element plots of calculated and analysed whole rock combined with the trace element distribution between orthopyroxene and clinopyroxene for each orthopyroxenite.
Primitive mantle normalising values are from Sun and McDonough (1989).
Mineral proportions (in brackets) were determined by mass balance to calculate the trace element budgets
List of abbreviations: Cpx: clinopyroxene; Opx: orthopyroxene; Ol: olivine; Sp: spinel; Amphi: amphibole
(1): signifies that the percent of the whole-rock exceeds 120% for the element in question. This indicates that the calculated concentration is higher than the measured content for this element (see text for details).
(na): not applicable as 1) the element was not be measured during the ICP-MS or 2) the analysis of the element was below the limit of detection of the ICP-MS.

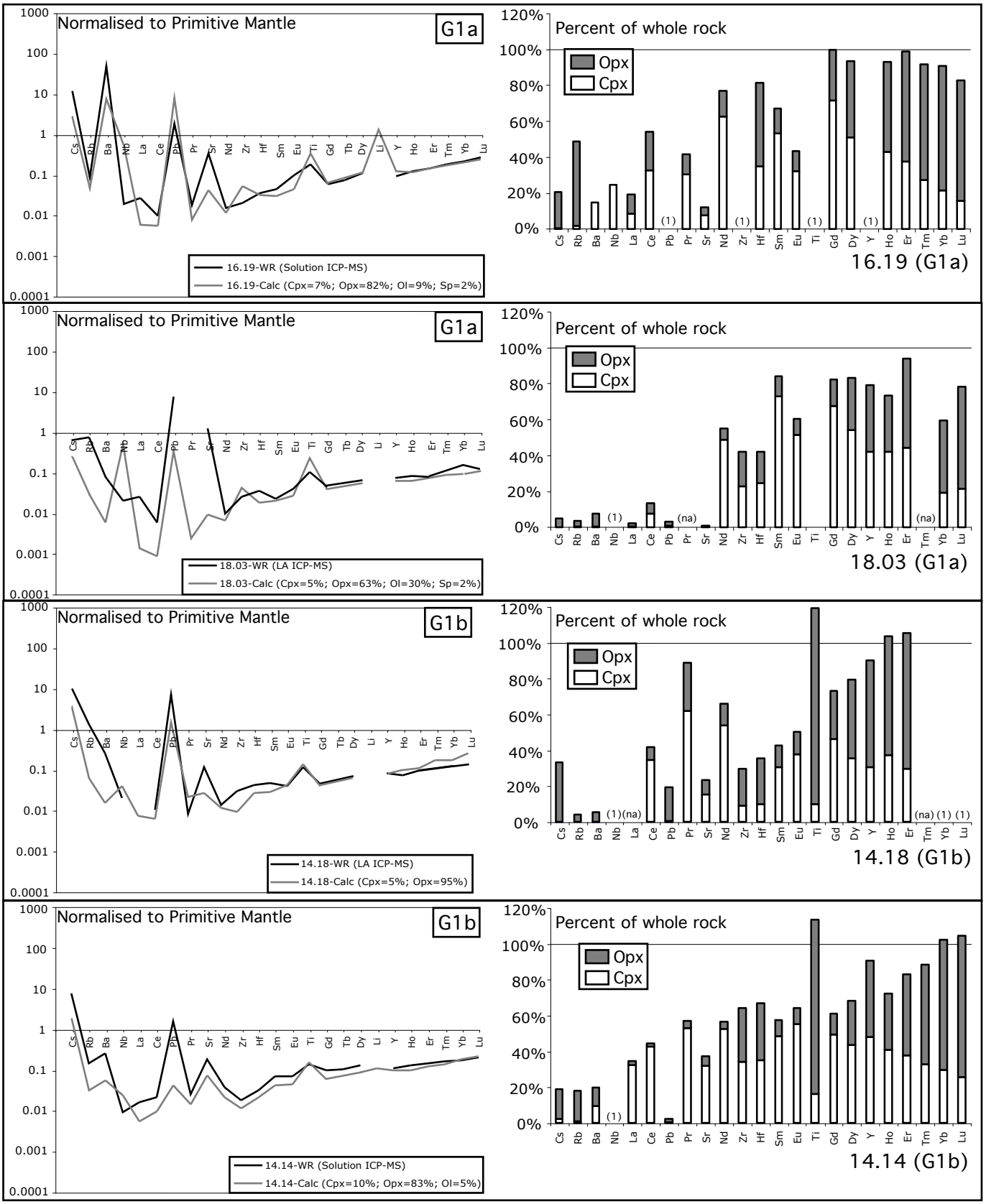

Fig. 4-19A (continued): Primitive mantle-normalised multi-element plots of calculated and analysed whole rock combined with the trace element distribution between orthopyroxene and clinopyroxene for each orthopyroxenite.
Primitive mantle normalising values are from Sun and McDonough (1989).
Mineral proportions (in brackets) were determined by mass balance to calculate the trace element budgets
List of abbreviations: Cpx: clinopyroxene; Opx: orthopyroxene; Ol: olivine; Sp: spinel; Amphi: amphibole
(1): signifies that the percent of the whole-rock exceeds 120% for the element in question. This indicates that the calculated concentration is higher than the measured content for this element (see text for details).
(na): not applicable as 1) the element was not be measured during the ICP-MS or 2) the analysis of the element was below the limit of detection of the ICP-MS.

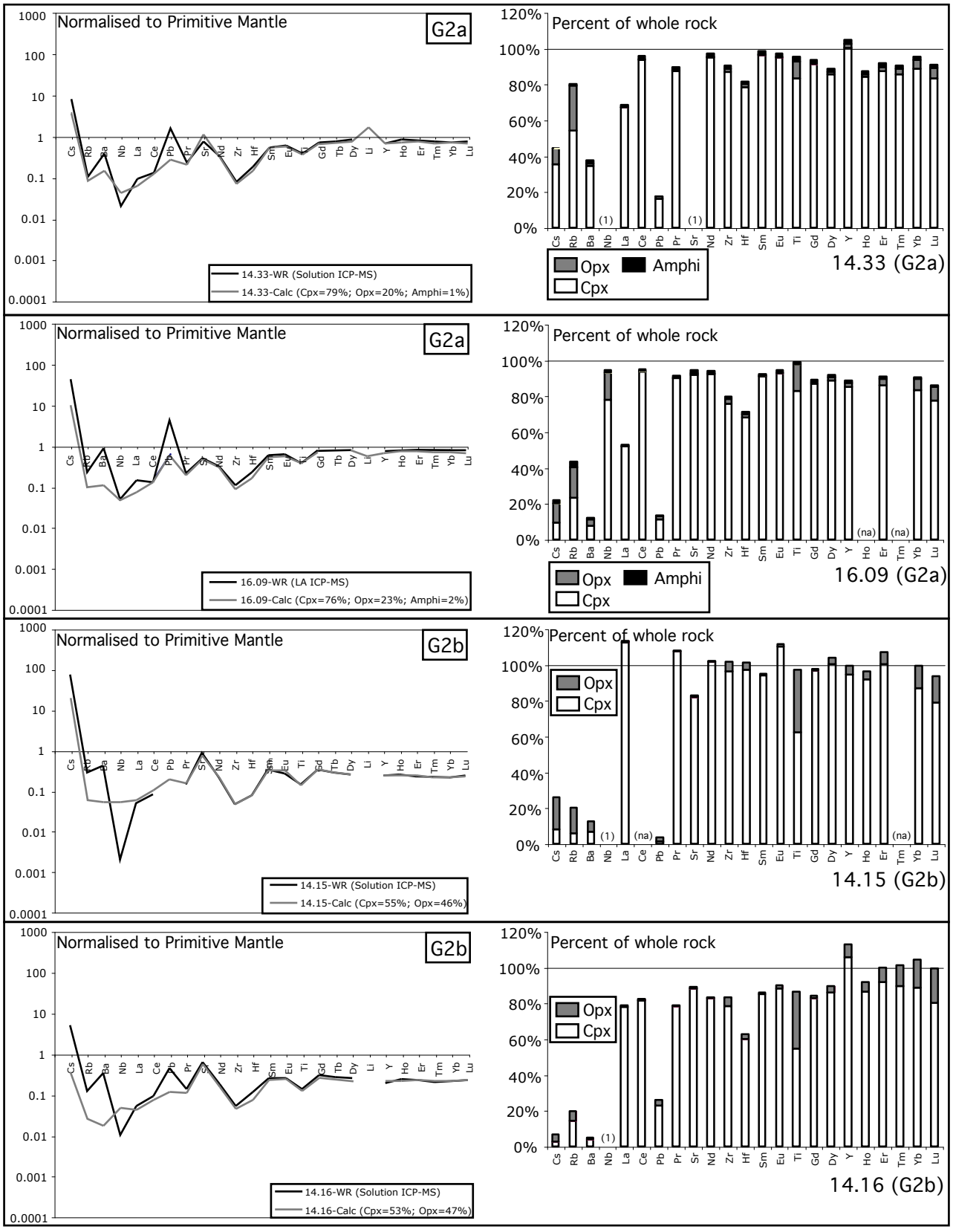

Fig. 4-19B: Primitive mantle-normalised multi-element plots of calculated and analysed whole rock combined with the trace element distribution between orthopyroxene and clinopyroxene for each websterite.
Primitive mantle normalising values are from Sun and McDonough (1989).
Mineral proportions (in brackets) were determined by mass balance to calculate the trace element budgets
List of abbreviations: Cpx: clinopyroxene; Opx: orthopyroxene; Ol: olivine; Sp: spinel; Amphi: amphibole
(1): signifies that the percent of the whole-rock exceeds 120% for the element in question. This indicates that the calculated concentration is higher than the measured content for this element (see text for details).
(na): not applicable as 1) the element was not be measured during the ICP-MS or 2) the analysis of the element was below the limit of detection of the ICP-MS.

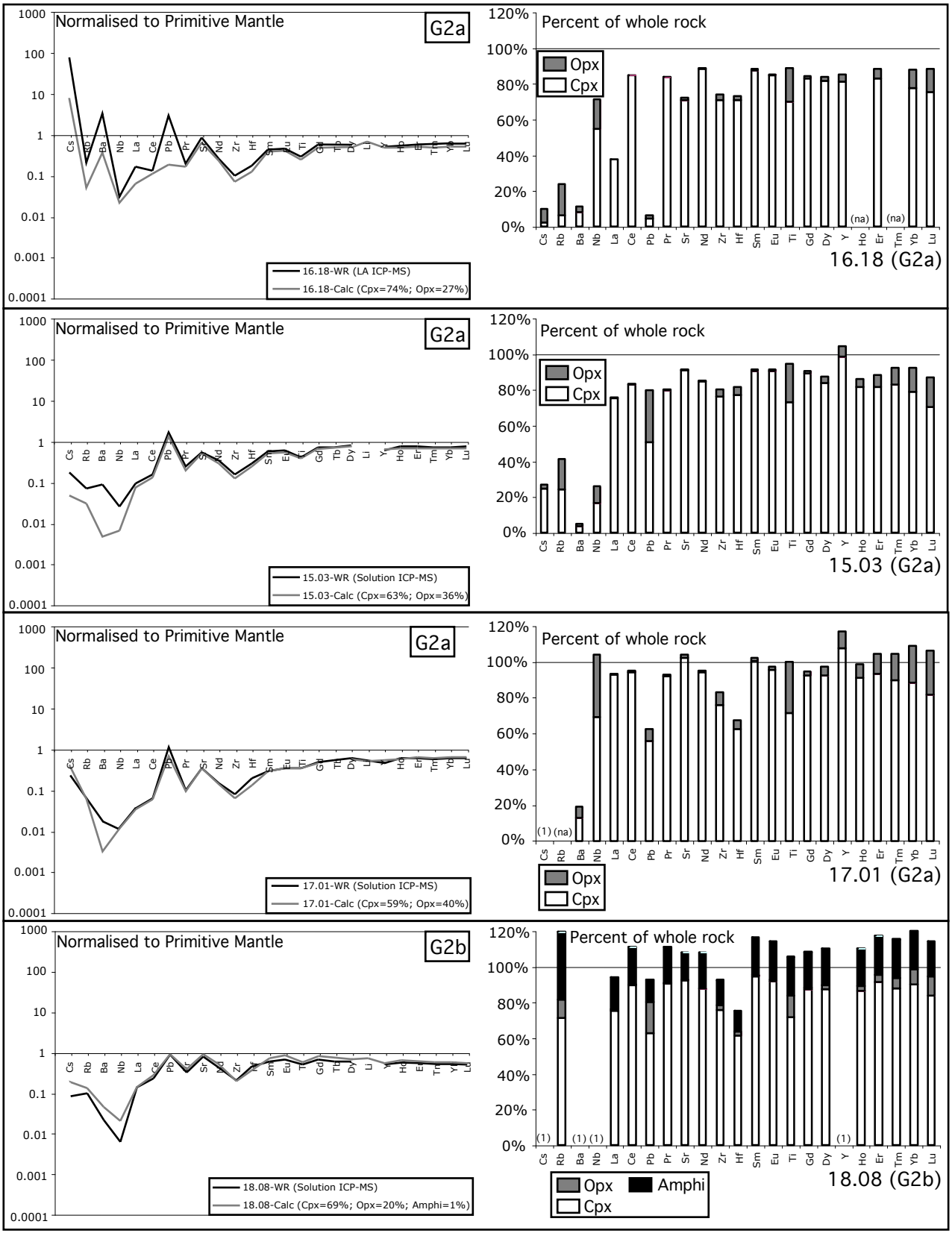

Fig. 4-19B (continued): Primitive mantle-normalised multi-element plots of calculated and analysed whole rock combined with the trace element distribution between orthopyroxene and clinopyroxene for each websterite.
Primitive mantle normalising values are from Sun and McDonough (1989).
Mineral proportions (in brackets) were determined by mass balance to calculate the trace element budgets
List of abbreviations: Cpx: clinopyroxene; Opx: orthopyroxene; Ol: olivine; Sp: spinel; Amphi: amphibole
(1): signifies that the percent of the whole-rock exceeds 120% for the element in question. This indicates that the calculated concentration is higher than the measured content for this element (see text for details).
(na): not applicable as 1) the element was not be measured during the ICP-MS or 2) the analysis of the element was below the limit of detection of the ICP-MS.

the samples analysed by Solution ICP-MS. Spinel, which is the main repository mineral for Nb, is probably not entirely dissolved by acids during the sample preparation involved in the Solution ICP-MS analysis. This problem is avoided in the sample preparation of the fused whole rock disks, which explain their values in Nb close to the Nb concentrations assessed from the calculated mineral budgets. In addition, the Nb discrepancy between the whole rock and the calculated trace element budgets seems to be reduced for the G2-websterites even for the whole rock chemistry obtained by Solution ICP-MS. The fact that G2-websterites are the only pyroxenites devoid of any spinel phase further indicates the problem of spinel dissolution during the sample preparation for Solution ICP-MS is the main explanation for the Nb deficit. Similarly to Nb, Zr and Ti (and sometimes Y) could be undervalued in the whole rock compositions especially for certain samples of G1-orthopyroxenites. This could reflect analytical problems. However Zr, Ti and Y could also be overvalued in the calculated compositions from the mineral inventory due to inaccurate estimation of mineral proportion.
The REE budget for whole rock clinopyroxene-rich samples (G2 and G3) is identical to the trace element budget calculated from the mineral inventory. However, this is not the case for the G1-orthopyroxenites. Despite having good similarities in regards to HREE, the G1-orthopyroxenites exhibit clear discrepancies in LREE between the whole rock and the calculated trace element compositions. The G1-orthopyroxenites being the most affected by alteration and deformation, the LREE deficit could be partially explained by the lack of data for recrystallised secondary phases. However, the sample 16.01, which has a limited degree of alteration, shows extreme LREE deficit indicating the probable occurrence of LREE-rich minor phases at grain boundaries.
Figure 4-18 (A, B and C) revealed that the pyroxene and the whole rock data have striking LILE enrichments relative to LREE. The whole rock trace element compositions are consistently more enriched in LILE (particularly Ba) than the trace element contents calculated from the mineral inventory across all of the pyroxenites. This clear LILE discrepancy is illustrated in the Figures 4-19A and 4-19B where clinopyroxene, orthopyroxene and amphibole collectively account for 20% in average of the total Ba contents in the whole rock budget. In some samples, Sr and Pb bear the same discrepancies despite being both strongly enriched in both the minerals and the whole rocks. The methods (Solution ICP-MS versus LA ICP-MS) used to analyse the samples do not affect those discrepancies indicating that LILE, Sr and Pb deficits in the calculated budget are independent to analytical issues. It is important to note that this LILE and to a certain extent Sr and Pb deficits persist for the freshest pyroxenites suggesting that LILE deficit is not entirely correlated to unmeasured alteration phases rich in LILE elements. One prognosis is that these elements are concentrated in the fluid inclusions, which are not taken in account so far in the calculated trace element distribution.

4.3 Fluid inclusions

The study of the fluid inclusions outlines that the primary and secondary fluid inclusions contain amphibole and calcite as daughter solid phases and CH_4 as gaseous phase (Fig. 4-11).
According to the mineral reaction (Anhydrous host mineral + H_2O + CO_2 = amphibole + carbonate), the presence of amphibole and calcite in the fluid inclusions is an indirect

evidence that the fluid was originally enriched in CO_2 and H_2O (Andersen and Neumann, 2001). During exhumation, the fluid inclusions have stretched and decrepitated on their way to surface (Van den Kerkhof and Hein, 2001). This partial leakage considerably changes the fluid of composition. Because of its elusive behaviour, water preferentially escapes from the trapped fluids. Water can be partitioned into hydrous minerals such as the amphibole described as a daughter phase in the fluid inclusions (Andersen and Neumann, 2001). Alternatively water can be removed from trapped fluids by in-situ hydration reactions. The amphibole blebs found in the close vicinity of the fluid inclusions are in fact the evidence of the reaction of the water removed from the decrepitated fluid inclusions with the host minerals such as the pyroxene. As water is much more mobile due to high polarity of H_2O molecules compared to gas (Van den Kerkhof and Hein, 2001), the fluid inclusions lose water but are enriched in gas compounds (Bakker and Jansen, 1990, 1994; Hall and Sterner, 1993). Methane is therefore included in the fluid inclusions as this gaseous phase is stable in the COH system (Huizenga, 2001). No CO_2 was detected using the Raman spectroscopy. However, the dark color of the fluid inclusions might be related to their CO_2-rich composition or due to the difference of refractive index with the host minerals (Van den Kerkhof and Hein, 2001). Similar CO_2-H_2O fluid inclusions were reported by (Andersen and Neumann, 2001) in the mantle xenoliths from supra-subduction zones. Despite the water loss during the decrepitation process, fluid inclusions from Ichinomegata – Japan (Roedder, 1965; Trial et al., 1984) and the Batan-Philippine arc (Schiano et al., 1995) contain major amounts of water (vapor +liquid) sometimes accompanied to hydrous daughter minerals (amphibole).

Concentrations of the pyroxene with inclusions normalised to the "clean" pyroxene give an indication of the relative compositions of the fluid (Fig. 4-13). In this plot, the fluid is highly enriched in Ba and Cs and a lesser extent Rb, Pb and Sr. For instance, Ba is more than 10000 times enriched in the fluid inclusions than in the "clean pyroxene". Although Pb and Sr are enriched relative to Pr in the "clean pyroxene", the fluid inclusions contain even more Sr and Pb contents. Li is always more enriched in the pyroxene with inclusions than in the clean pyroxene indicating that the fluid is rich in Li. The variable LILE, Sr and Pb contents measured in both the clean pyroxene and the pyroxene with inclusions for each sample clearly explain the variations in composition for these elements in the primitive mantle normalised multi-element diagrams observed in Figures 4-3 and 4-5. The highest LILE (particularly Ba), Sr and Pb concentrations are probably due to a significant proportion of fluid inclusions incorporated in these analyses.

4.4 The Re-Os System

4.4.1 Evidence for Metasomatism

Both San Jorge/Santa Isabel pyroxenites have higher $^{187}Os/^{188}Os$ ratios than the abyssal peridotites.

In order to elevate the $^{187}Os/^{188}Os$ of the mantle, the mantle source can be enriched 1) directly slab-derived radiogenic Os from melts or fluids or; 2) indirectly through time-integrated two stage processes whereby the subduction component would have had a high Re/Os ratio for a long period of time. The former implies that Os is mobilized from the

subducted slab to the sub-arc mantle whereas the latter means that Os is not mobile in arc environments and only metasomatic minerals, which have been emplaced in the mantle at some time in the past, have grown more radiogenic through the ^{187}Re decay to ^{187}Os.

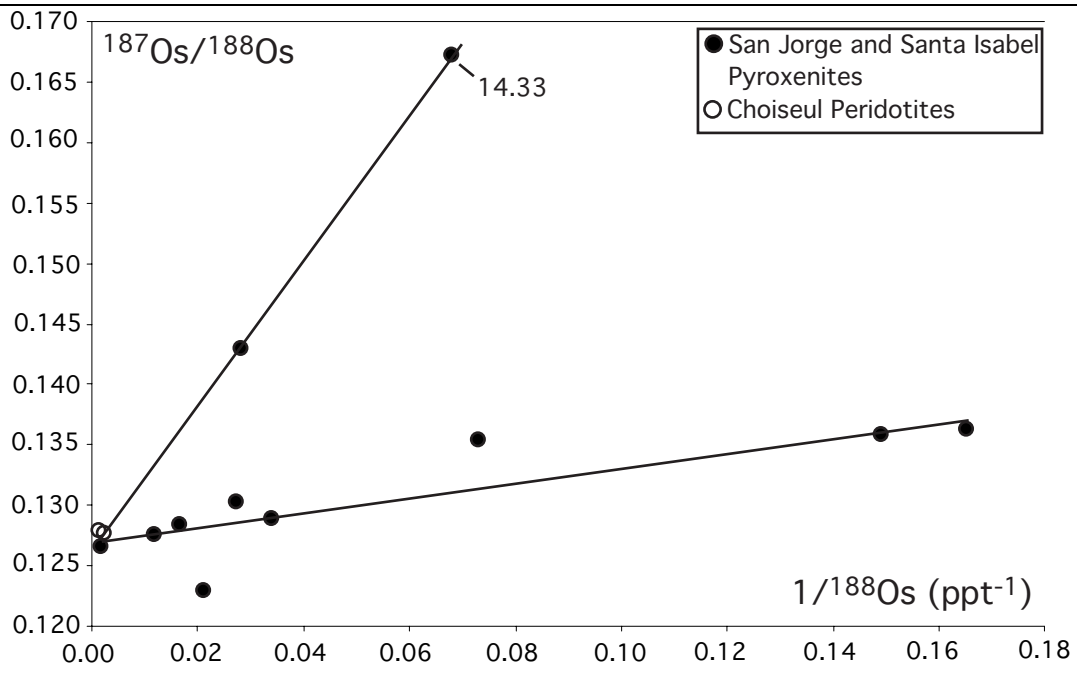

Fig. 4-20: Os isotopic composition vs. the inverse of ^{188}Os concentrations for the San Jorge/Santa Isabel pyroxenites.
See text for discussion.

In the $^{187}Os/^{188}Os$ vs. $1/^{188}Os$ diagram (Fig. 4-20), the pyroxenites display two-well defined positive linear correlations, which may represent simple binary mixtures between unradiogenic Os source and two different radiogenic Os components. The unradiogenic Os source is represented by the Choiseul peridotites, which have low $^{187}Os/^{188}Os$ and $1/^{188}Os$ ratios. Alvès et al. (1999) described the Java arc lavas with similar radiogenic components as different proportions of subducted oceanic crust and sediments. Recycling lithosphere (oceanic and sediments) leads to the increase of the Os isotopic ratios of the mantle sources contributing to their heterogeneity because 1) High $^{187}Os/^{188}Os$ is caused by subducting marine sediments with isotopic ratios as high as the seawater (1.023) (Koide et al., 1991) and 2) oceanic crust (MORB) has higher Re/Os ratios for a long period of time and therefore high $^{187}Os/^{188}Os$. In this scenario, recycling radiogenic Os in the mantle implies that Os becomes incompatible in the slab-derived fluids. For the Solomon Islands, the subduction of the old Pacific Plate (~120Ma) covered by a thick layer of pelagic sediments would release highly radiogenic materials into the overlying mantle wedge through fluids or melts during the dehydration of the slab to influence the $^{187}Os/^{188}Os$ ratios of the mantle.

Hence, there is a strong debate over the radiogenic Os mobilisation from the subducted slab to sub-mantle in the fluid. Addition of a subduction component with a high Re/Os ratio over a long period of time ago is for some authors (i.e. Chesley et al., 2004) the only process to influence the $^{187}Os/^{188}Os$. However, in the case of the Solomon Islands, this

scenario seems not to be plausible as the subduction of the Pacific Plate underneath only began approximately 43 Ma ago. One argument in favour of the enrichment of radiogenic Os by slab-derived fluids or melts to elevate the $^{187}Os/^{188}Os$ ratios is well supported by the 14.33websterite, which has the most radiogenic Os isotope composition at high Os concentrations (3.3ppb) comparable with values reported for the Choiseul peridotites (Table 4-6).

It is important to point out at this stage that a major fraction of Os in the upper mantle is controlled by minor unradiogenic Os-bearing phases such as sulfides, which can account for 80-96% of Os distribution of the peridotites (Shirey and Walker, 1998). The fact that Re can also reside in a sulfide component in the mantle renders very difficult to understand the mantle processes from the Re-Os system perspectives. However, Brandon et al. (1996) suggested that under oxidizing regimes, Os could be moderately incompatible resulting in low concentrations of Os in xenoliths. The authors added that metasomatism in oxidizing conditions can also destabilize the mantle sulfides. Under these conditions, the volability of Os and more largely is dependent of F_{H2O} and F_{HCL} indicating that the metasomatic fluids or melts are likely to be rich in Cl (Brandon et al., 1996). Becker et al. (2001) argue that metasomatism at low melt/rock ratios could refertilise depleted peridotites with respect of Re, only causing a minor influence on the $^{187}Os/^{188}Os$. However according to the authors, high melt/rock ratios are responsible for the replacement of mantle Os with slab-derived radiogenic from melts or fluids, precipitating pyroxene-rich rocks. Based on their elevated $^{187}Os/^{188}Os$ ratios relative to the Choiseul peridotites and their low Os contents, we assume that pyroxenites result from percolation of metasomatic slab-derived fluids into the mantle wedge at high fluid/rock ratios. In addition, the suprachondritic $^{187}Os/^{188}Os$ together with the mantle-like Os contents of the Choiseul peridotites indicate that low melt/rock ratios are only required to slightly elevate their $^{187}Os/^{188}Os$ ratios compared to the abyssal peridotites. On the Re-Os perspective, the Choiseul peridotites have SSZ affinity, similar to other SSZ peridotites.

Other pyroxenites formed by similar metasomatism processes have been studied to determine their Re-Os system. Beni Bousera (Pearson and Novell, 2004) and Ronda (Reisberg et al., 1991) pyroxenites have similar range of Os contents (0.03 and 2.2ppb) to the San Jorge and Santa Isabel pyroxenites. Like the 14.33 websterite from the Solomon Islands, several pyroxenites from Beni Bousera have relatively high radiogenic Os isotope compositions at high Os contents (2.2ppb). However the Ronda and Beni Bousera have very radiogenic$^{187}Os/^{188}Os$ ratios compared to the Solomon Islands pyroxenites. For example, the $^{187}Os/^{188}Os$ ratios for the Beni Bousera pyroxenites range widely between 0.1264 and 0.8337 whilst the San Jorge and Santa Isabel pyroxenites have much more limited and lower range of $^{187}Os/^{188}Os$ values between 0.1228 and 0.1673. This indicates that the enrichment of Os radiogenic is less prevalent for the Solomon Islands than for the other pyroxenites from Spain as the addition of radiogenic Os was probably caused by the contamination process related to the radiogenic overlying continental crustal material during the pyroxenites' exhumation in case of Beni Bousera and Ronda.

4.4.2 Re-Os isochron and possible age model

The $^{187}Os/^{188}Os$ vs. $^{187}Re/^{188}Os$ diagram (Fig. 4-21) illustrates that the whole rock Re-Os data for the San Jorge/San pyroxenites define a rough positive correlation with the exception of the sample 16.01, which has a high $^{187}Os/^{188}Os$ (0.142989) ratio for a low $^{187}Re/^{188}Os$ ratio (0.32) compared to the other pyroxenites. Two regressions are calculated (Fig. 4-21). Regression 1 includes the sample 16.01 and gives an apparent age of 48 Ma. Regression 2 omitting the sample 16.01 yields an age of 55 Ma.

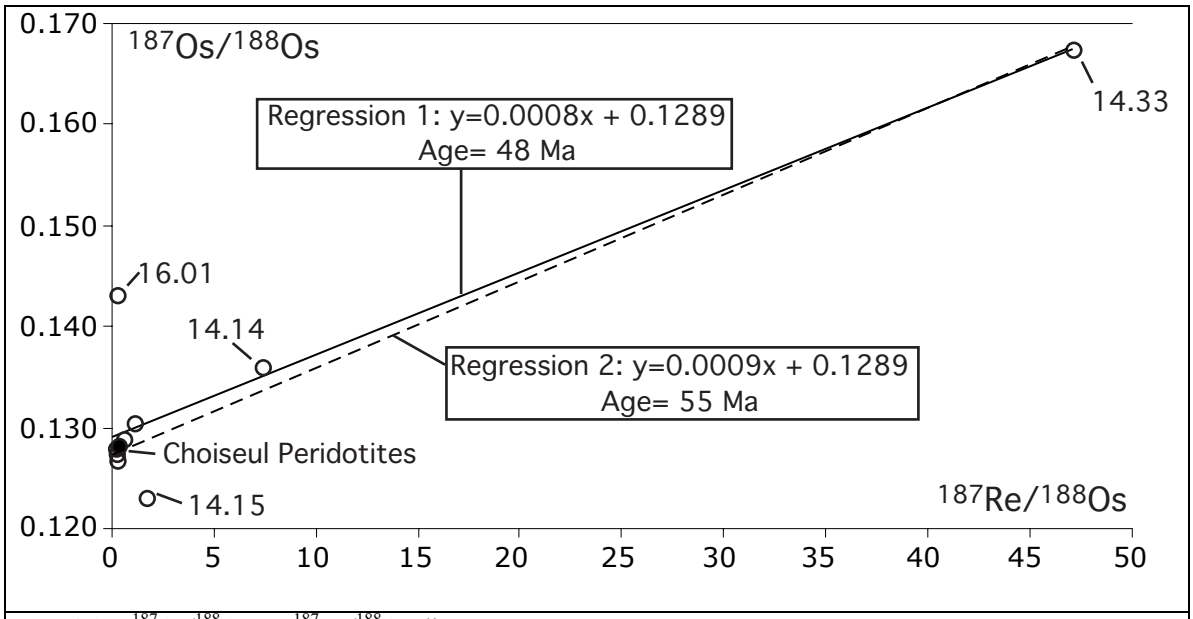

Fig. 4-21: $^{187}Os/^{188}Os$ vs. $^{187}Re/^{188}Os$ diagram.
Two isochrons were calculated: one including the sample 16.01 gives a regression of 0.0008x + 0.1289 (regression 1) and the other excluding the sample 16.01 yields a regression of 0.0009x + 0.1271 (regression 2). Using the equation $^{187}Os/^{188}Os = (^{187}Os/^{188}Os)_0 + [(^{187}Re/^{188}Os)*(e^{\lambda t}-1)]$, the regression 1 gives an age of 48 Ma with $(^{187}Os/^{188}Os)_0$ similar to the Primitive Upper Mantle (PUM) values (0.1287) (Meisel et al.,1996) whereas the regression 2 gives an age of 55 Ma with $(^{187}Os/^{188}Os)_0$ similar to chondrite values (0.1270) (Smoliar et al., 1996).

Taking in account their metasomatic origin, the young Re/Os age (~ 50 Ma) of these pyroxenites is interpreted to represent the age of the mixing event between an old mantle residue and a young metasomatic addition. No other geochronology evidence (Nd or Sr model ages) for these pyroxenites is available to compare with this Re/Os geochronology study.

5 DISCUSSION

5.1 Characteristics of the pyroxenites from the Solomon Islands

Petrological, whole rock chemistry in major and trace elements, mineral composition in major elements and geothermometry characteristics of the three groups (G1, G2 and G3) of pyroxenites are summarised in Table 4-7.

5.1.1 Similarities between the three groups of pyroxenites: a common SSZ affinity

The pyroxenites include a large variety of rock-type including the orthopyroxenites (G1), the websterites (G2) and the clinopyroxenites (G3). With the exception of some orthopyroxenites and clinopyroxenites that were serpentinised, the pyroxenites are relatively fresh rocks with minimal degree of alteration (LOI~ 1 wt%). Orthopyroxene and clinopyroxene represent the major primary phases accompanied rarely of olivine and spinel. Amphibole (hornblende to tremolite), serpentine, magnetite, Fe-Ni-sulfide constitutes the most common phases of retrograde assemblages whereas wollastonite, pectolite, Cpx II and chlorite can be found occasionally. Primary and secondary fluid inclusions are common features of these pyroxenites. They rarely occur in clusters but mostly form trails crosscutting from one to few minerals. Geochemically unzoned, the pyroxene has similar low Al_2O_3 contents (<3.6 wt%) and variable Mg# (Mg#=0.85-0.94 for Cpx and Mg#=0.83-0.91 for Opx). Clinopyroxene is characterised by high CaO contents (>23 wt%) whereas orthopyroxene has low CaO contents (<1 wt %). Using the two-pyroxene thermometers, the temperatures of re-equilibration are estimated between 808°C and 935°C but pyroxene exsolutions occurring in both clinopyroxene and orthopyroxene indicate that the temperatures of crystallisation are significantly higher (950-1050°C).
The whole rock chemistry of the pyroxenites is characterised by very low HREE abundances and variable enrichments in LILE (Cs, Rb and Ba) coupled with positive Sr and Pb anomalies relative to neighbouring elements. These features are also strongly recorded in the trace element compositions of the pyroxene indicating that 1) the pyroxene is the main repository of the trace elements and 2) the enrichments in incompatible elements such as Ba, Rb, Cs, Sr and Pb are not related to an alteration process. The primary origin of the LILE, Pb and Sr enrichments, which typical to the SSZ materials, is important to confirm that these pyroxenites have a strong supra-subduction zone signature.

5.1.2 Differences between the three groups of pyroxenites

5.1.2.1 G1-orthopyroxenites

The G1-orthopyroxenites were the only pyroxenites not to be found in veins or dykes. This does not necessarily mean that veins of orthopyroxenites do not exist but that they have not been recognised in the field. The G1-orthopyroxenites are also characterised by their abundance of orthopyroxene over the clinopyroxene. They generally contain a small proportion of olivine (<10% except for the sample 18.03) and the spinel phase is quite

Table 4-7: Summary of the three groups of pyroxenites.

		G1-orthopyroxenite	G2-websterite	G3-clinopyroxenite	
				G3a-clinopyroxenite	G3b-clinopyroxenite
Petrology	Primary Assemblage	Cpx (2-15%); Opx (>60%); Ol (0-10% except for the sample 18.03 (20%); Sp (1-2%)	Cpx (50-80%); Opx (20-50%); Ol (<5%); Sp (0%)	Cpx (>80%); Opx (<7%); Ol (10%); Sp (<0.5%)	Cpx (45%); Amphibole (35%)
	Texture	Porphyroclastic	Inequigranular	Seriate	Seriate
	Deformation	Low to high	No to low	Low to high	Low
	Mineral characteristics	Large and small Opx grains; Small anhedral-shaped Cpx grains; Interstitial lobate Sp; Intertitial Ol; Amphi (blebs)	Large and small Cpx grains; Small Opx grains; Rare interstitial Ol; No Sp; Amphi (interstitial & blebs)	Large and small Cpx grains; Rare and small Opx grains; Intertitial Ol; No Intertitial Sp; Amphi (interstitial & blebs)	Medium-sized Cpx and Amphi; Primary Amphi (Mg-Hb);No Sp & no Ol
	Zoning	No	No	No	No
	Fluid inclusions	Primary and Secondary	Primary and Secondary	Yes	Yes (less frequent)
	Pyroxene exsolutions	Cpx exsolutions in large Opx porphyroclasts;Opx exsolutions in Cpx grains	Opx exolutions only in Cpx biggest grains; No Cpx exsolutions in Opx grains	Opx and Sp exolutions in Cpx grains; No Cpx exsolutions in Opx grains	No exsolutions in pyroxene grains
	Secondary assemblage	Amphibole (Hb-Trem); Serpentine (quite frequent); Magnetite (rare); Wollastonite (rare); Cpx II (rare) Pectolite (rare)	Amphibole (Hb-Trem); Serpentine (rare); Magnetite (frequent); Sulfide (frequent); Pectolite (rare)	Amphibole (Hb); Serpentine (frequent); magnetite (frequent), sulfide (frequent); chlorite (rare)	Serpentine (frequent)
Whole rock chemistry	Major Elements	High Mg# (0.88-0.91), high (G1a) to moderate (G1b) Cr_2O_3 contents (0.4-1.5 wt%), low CaO contents (<5 wt%), low Al_2O_3 contents(<2.6 wt%), low TiO_2 contents (<0.08 wt%)	High to low Mg# (0.83-0.91), high to low Cr_2O_3 contents (0.03-0.70 wt%), high CaO contents (>13 wt%), low Al_2O_3 contents (<2.5 wt%) low TiO_2 contents (0.1 wt%)	High Mg# (0.90-0.92), high Cr_2O_3 contents (0.5-1.0 wt%), high CaO contents (>15 wt%), low Al_2O_3 contents (<2.6 wt%), high TiO_2 contents (0.12-0.18 wt%)	High Mg# (0.895), low Cr_2O_3 contents (0.4 wt%), high CaO contents (16 wt%), moderate Al_2O_3 contents (3.6 wt%), high TiO_2 contents 0.17 wt%)
	REE	REE depletion (except sample 16.01); steady increase from the MREE to HREE (G1b) or slight convex-upward REE patterns (G1b); low HREE abundances;	Convex-upward (G2a) to bell-shaped (G2b) REE patterns with depleted LREE relative to MREE; low HREE abundances	Bell-shaped REE patterns with depleted LREE relative to MREE and slightly depleted HREE relative to MREE; low HREE abundances	LREE-enriched REE patterns with relatively flat MREE-HREE gradients; low HREE abundances
	Other Trace elements	Strong enrichments in LILE (Cs, Ba and to lesser extent Rb); Strong Pb and Sr anomalies relative to their respective neighbouring elements; positive Ti anomalies relative to Eu and Gd; No Nb anomalies	Moderate enrichments in LILE (Cs, Ba and to lesser extent Rb); Moderate Pb and Sr anomalies relative to their respective neighbouring elements; negative Ti anomalies relative to Eu and Gd; Strong negative Nb anomalies relative to La	Slight enrichments in LILE (Cs, Ba and to lesser extent Rb); Moderate Pb relative to Ce and Pr; No to small Sr positive anomalies; small negative Ti anomalies relative to Eu and Gd; Strong negative Nb anomalies relative to La	Depletion of LILE elements compared to La; No Nb anomalies; No Pb anomalies; Moderate negative Sr anomalies; Small Ti negative anomalies
Mineral Composition (Major elements)	Cpx	High Mg# (0.91-0.94) , moderate to high Cr_2O_3 contents (0.37-0.84 wt %), low Al_2O_3 contents (1.08-2.64 wt %)	High to low Mg# (0.85-0.93), high to low Cr_2O_3 contents (0.02-0.84 wt %), low Al_2O_3 contents (0.64-1.91 wt %)	High Mg# (0.91-0.94), moderate to high Cr_2O_3 contents (0.34-0.74 wt%), low Al_2O_3 contents (0.63-2.15 wt%)	High Mg# (0.92), low Cr_2O_3 contents (0.13 wt%), low Al_2O_3 contents (0.68 wt %)
	Opx	High Mg# (0.86-0.91), high Cr_2O_3 contents (0.25-0.64 wt%), low Al_2O_3 contents (0.97-2.35 wt%)	High to low Mg# (0.79-0.90), high to low Cr_2O_3 contents (0.11-0.41 wt%), low Al_2O_3 contents (0.43-1.71 wt%)	High Mg# (0.88), moderate Cr_2O_3 contents (0.25 wt%), low Al_2O_3 contents (1.54 wt%)	High Mg# (0.88), low Cr_2O_3 contents (0.15 wt%), low Al_2O_3 contents (0.74 wt%)
	Olivine	High Fo (0.86-0.90) and high NiO contents (0.38-0.44 wt%)	Low Fo (0.78) and low NiO contents (0.1 wt%)	High Fo (0.88-0.90) and moderate NiO contents (0.1-0.34 wt%)	No Ol
	Spinel	High Cr# (0.43-0.74), Low Mg# (0.46-0.56)	No Sp	High to moderate Cr# (0.34-0.67), Low Mg# (0.41-0.52) (close to SSZ peridotites)	No Sp
	Amphibole	High Mg# (0.89-0.94)	High to low Mg# (0.83-0.94)	High Mg# (0.89-0.92)	High Mg# (0.89)
Mineral Composition (Trace elements)	Cpx	Low HREE abundances; strong to moderate LREE depletion with shallow downward (G1a-cpx) to relatively flat MREE-HREE gradients (G1b-cpx); Strong enrichments in LILE (Cs, Ba and to lesser extent Rb); Strong Pb and Sr spikes; Negative Zr and Hf anomalies relative to Sm	Low HREE abundances; moderate LREE depletion with flat (G2a-cpx) to bell-shaped (G2b-cpx) MREE-HREE gradients; Strong enrichments in LILE (Cs, Ba and to lesser extent Rb); Strong Pb and Sr spikes; Negative Zr and Hf anomalies relative to Sm	Low HREE abundances; moderate LREE depletion with bell-shaped MREE-HREE gradients; limited enrichments in LILE (essentially Cs); moderate Pb and no Sr spikes; Negative Zr and Hf anomalies relative to Sm	Low HREE abundances; LREE enrichment with flat MREE-HREE gradients; No enrichments in LILE; No Pb and Sr spikes; No Zr and Hf anomalies relative to Sm
	Opx	Low REE abundances; Steep and positive HREE-LREE gradients with a shallow convex-upward slope from HREE to MREE; Strong enrichments in LILE, Pb (and Li) and Sr; Ti positive anomalies	Low REE abundances; Very (G2a-opx) to moderately (G2b-opx) steep and positive HREE-LREE gradients with a shallow convex-upward slope from HREE to MREE; Strong enrichments in LILE, Pb (and Li) and Sr; Ti positive anomalies	Not analysed	Not analysed
	Olivine	REE below detection limit; Selective enrichments in LILE (alteration or inclusions)	Not analysed	Low REE abudances (flat LREE-HREE gradients)	No Ol
	Spinel	Poor in REE; Spikes of Nb, Zr, Ti; relative enrichments in LILE, Pb (inclusions)	No Sp	Not analysed (too small)	No Sp
	Amphibole	Same as Cpx	Same as Cpx	Not analysed	Same as Cpx except Zr and Hf positive anomalies relative to Sm
Fluid Inclusions	Relative Composition	Enrichments in Ba, Cs, Rb and a lesser extent Pb, Sr; rich in CO_2 and H_2O	Enrichments in Ba, Cs, Rb and a lesser extent Pb, Sr; rich in CO_2 and H_2O	Not analysed	Not analysed
Re/Os chemistry	Whole rock	Relatively high $^{187}Os/^{188}Os$	Relatively high $^{187}Os/^{188}Os$	Not analysed	Not analysed
Thermometry	Temperature of crystallisation	High (1000°c)	Moderate (950°c)	Very high (1050°c)	Low (800°c)

List of abbreviations for the minerals: Cpx: clinopyroxene; Opx: Orthopyroxene; Ol: Olivine; Sp: Spinel; Amphi: Amphibole; Hb: Hornblende; Trem: Tremolite
Other abbreviations: SSZ-peridotites: Supra-Subduction Zone peridotites; Mg#=$(Mg+Fe^{2+})/Mg$; Cr#=(Cr)/(Cr+Al); Fo= Forsterite number

common but does not exceed 2% modal proportion. Apart from common secondary minerals (amphibole, serpentine, magnetite and pectolite), wollastonite and Cpx II are the only retrograde minerals typically found in the G1-orthopyroxenites and not in the other pyroxenites. Unlike the G2-websterites, clinopyroxene and orthopyroxene include respectively frequent orthopyroxene and clinopyroxene exsolutions. As the result, the temperatures of equilibration (~880°C) are much lower than the temperatures of crystallisation (~1000°C). The G1-pyroxene is enriched in compatible elements such as Cr (Cr_2O_3 up to 1.5 wt%) and Mg (Mg#=0.91-0.94 for Cpx and Mg#=0.86-0.91 for Opx) similar to the pyroxene mantle values. Cogenetic olivine also has high Fo (86-90) and NiO contents (~0.42 wt%) comparable with the mantle values. The high Cr contents in the whole rock chemistry are attested by the presence of Cr-spinel, which only occurs as individual grains in the G1-orthopyroxenites and not in the cpx-rich groups.
The G1-orthopyroxenites exhibit the lowest HREE abundances and a steady increasing MREE-HREE gradient all reflecting the large proportion of orthopyroxene with low REE contents. Although in small amount, the clinopyroxene plays an important role in the REE budget of the G1-orthopyroxenites. Their whole rock REE patterns are typical to the clinopyroxene-like REE profiles with the LREE depletion relative to MREE. Though the whole rock REE profiles for the orthopyroxenites still record the strongest fractionation of LREE relative to MREE (except the sample 16.01). The G1-orthopyroxenites are marked by remarkable enrichments in LILE, Sr and Pb relative to other elements of similar incompatibility, which also feature in both chemistries of the clinopyroxene and the orthopyroxene. Once again, this attests that these enrichments are partly primary.

5.1.2.2 G2-websterites

The G2-websterites differ from the G1-orthopyroxenites by containing a large proportion of clinopyroxene. Only rare olivine occurs in these websterites but no spinel. Magnetite and sulfide are more commonly found in the G2-websterites than in the G1-orthopyroxenites. In contrast to the G1-orthopyroxenites, serpentine is less apparent. Orthopyroxene exsolutions only exist in large clinopyroxene grains and no clinopyroxene exsolutions were found in the orthopyroxene crystals. As a consequence, the temperatures of equilibration are relatively equivalent to the temperatures of crystallisation not exceeding 950°C. The G2-pyroxene exhibits a broad range of Mg# with Mg#=0.85-0.93 for Cpx and Mg#=0.79-0.90 for Opx usually exhibiting lower values compared to the G1-pyroxene. The same applies to the Cr_2O_3 contents of the G2-pyroxene (Cr_2O_3 0.11-0.43 wt %), which are lower than that of G1-pyroxene. In addition, the G2-Olivine has lower Fo and NiO contents than the G1-olivine. In summary, the G2-pyroxenites differ from the G1 websterites by being less enriched in compatible elements (Cr, Mg, Ni).
Overall the whole rock and pyroxene trace element compositions for the G2-websterites and the G1-orthopyroxenites are relatively similar. However the G2-websterites are slightly more enriched in trace elements than the G1-orthopyroxenites. This could be explained by the large amount of clinopyroxene in the G2-websterites compared to the G1-orthopyroxenites, as clinopyroxene dominates the trace element composition of the G2-websterites. The variation of the whole rock chemistry between the G2-websterites and the G1-orthopyroxenites is also caused by the difference in trace element composition between the G1- and G2-clinopyroxene. Comparison between the clinopyroxene of the two groups reveals that the G2-clinopyroxene is more enriched in

LREE than the G1-clinopyroxene whereas their compositions remain similar for most of the other trace elements. Briefly the difference in cpx/opx proportion and to a lesser extent variation in mineral chemical composition (mainly recorded in the clinopyroxene) accounts for the whole rock chemical difference between the two groups.

5.1.2.3 G3-clinopyroxenites (except sample 15.07)

The G3-clinopyroxenites only contain clinopyroxene with rare olivine and even rarer orthopyroxene. Like in the G2-websterites, amphibole, magnetite and sulfide represent a retrograde assemblage commonly found in the G3-clinopyroxenites, but chlorite only occurs in these clinopyroxenites. The G3-clinopyroxene forms subhedral grains, which reveal exsolutions of spinel as well as orthopyroxene. Spinel exsolutions only occur in the clinopyroxene from these clinopyroxenites revealing high temperatures of formation (approximating 1050°C) for these clinopyroxenites. This range of temperatures is well above the temperatures of crystallisation estimated for the G1-orthopyroxenites and the G2-websterites, indicating that the G3-clinopyroxenites were formed in hotter conditions and then equilibrated slowly exsolving spinel and orthopyroxene in the clinopyroxene grains. Whilst the G3-clinopyroxene has high Mg# and Cr_2O_3 contents similar to the G1-clinopyroxene, the G3-cpx reveals unusually high TiO_2 contents. Comparison between the trace element chemistry of the clinopyroxene and the whole rock for the G3-pyroxenites reveals that the clinopyroxene totally controls the trace element budget of these rocks with the clinopyroxene representing a large proportion (>90%). The whole rock and clinopyroxene REE patterns for the G3-clinopyroxenites resemble some of the G2-websterites by having high MREE relative to HREE giving them bell-shaped REE profiles. The G3-clinopyroxenites are also depleted in LREE relative to MREE but their LREE depletion is less marked than the one observed for the G2-websterites. The primitive mantle-normalised multi-element signatures of the G3-clinopyroxenites differ from the other pyroxenites (G1 and G2) with a limited enrichment in LILE elements. Even if Pb positive anomalies relative to Ce and Pr still persist, its magnitude is less important than it is for the G1-orthopyroxenites and the G2-websterites. In contrast to the other pyroxenites, there is no or small Sr positive anomaly.

5.1.3 Exceptions within the groups

5.1.3.1 In the G1- orthopyroxenites

Composite orthopyroxenites are predominantly opx-rich rocks but encompass zones/patches of clinopyroxene amongst orthopyroxene matrix. This composite origin is strongly reflected in their geochemistry. For instance, the pyroxene from these composite orthopyroxenites has an intermediate composition in Mg# and Cr_2O_3 between the G1-orthopyroxenites and the G2-websterites. This is also the case for olivine, which shows transitional composition in Mg# and NiO contents between the G1-olivine and the G2-olivine. The chondrite-normalised whole rock REE patterns for the composite orthopyroxenites have similar convex-upward REE profiles to the ones of the G2-websterites but show the same low REE abundances to the G1-orthopyroxenites. This is also reflected in their compositions of the clinopyroxene, which has similar trace element abundances to the G2-clinopyroxene.

Apart from these composite orthopyroxenites, the sample 16.01 shows unusual features compared to the other orthopyroxenites with LREE enrichment (La-Eu) while the others are LREE depleted. This LREE enrichment does not feature in the trace element chemistry of either the clinopyroxene or the orthopyroxene. Because the fluid inclusions do not contain any significant amount of LREE, this indicates that LREE-rich minor phases must occur at grain boundaries.
The sample 18.03 is marked by unusually high modal proportion of olivine (20%) compared to other orthopyroxenites. The clinopyroxene from this sample is extremely depleted in LREE and not in equilibrium with the coexisting orthopyroxene. This indicates that the clinopyroxene is likely to be a mantle relict whereas the clinopyroxene from the other G1-orthopyroxenites has totally recrystallised from the metasomatic reaction between a peridotite source and an infiltrating fluid.

5.1.3.2 In the G2-websterites

In the *Chapter 3*, I indicate that, despite being petrologically and mineralogically identical to the other websterites, three samples (14.15, 14.16 and 18.08) (G2b-websterites) differ from the others (G2a-websterites) by typical bell-shaped REE profiles instead of the upward-convex REE patterns with flat MREE-HREE gradients for the other websterites. The G2b-clinopyroxene also features the characteristic bell-shaped REE profiles. The examination of the REE patterns for the G2b-orthopyroxene reveals much shallower positive HREE-LREE compared to the other G2a-orthopyroxene. Similar $D^{opx/cpx}$ for the two subgroups is consistent with change of MREE-HREE gradients for the G2b-pyroxene. This suggests that the G2a-websterites and the G2b-websterites derive from the same process.

5.1.3.3 In the G3-clinopyroxenites

Mineralogically, the G3b-clinopyroxenite (sample 15.07) contains a large proportion of primary amphibole (35% of modal proportion), which seems to have co-crystallised with the clinopyroxene phase. Serpentine is the only recognisable retrograde phase and neither magnetite nor sulfide was identified. Unlike the other clinopyroxenites, absolutely no exsolutions in clinopyroxene grains were observed. As a result, their temperatures of crystallisation are estimated to be similar to the temperatures of re-equilibration, which are remarkably low (~800°C). The clinopyroxene of the sample 15.07 has lower Cr_2O_3 and higher Al_2O_3 contents for similar Mg# and TiO_2 contents compared to other G3-clinopyroxene.
Distribution of trace elements reveals that amphibole and clinopyroxene account for all the whole rock for the G3b-clinopyroxenite. Amphibole and clinopyroxene trace element compositions of the G3b-clinopyroxenite are completely different to those of the G3a-clinopyroxenites. G3b-amphibole and G3b-clinopyroxene are unusually LREE-enriched $[(La/Gd)_N>1]$ whereas the other clinopyroxenites display LREE-depleted patterns. They are also characterised by a lack of LILE enrichment, an absence of Sr positive anomaly relative to Ce and Pr and no or a negative Pb positive anomaly compared to the amphibole and clinopyroxene from the G3a-clinopyroxenites. Compared to amphibole from the other pyroxenites, the G3b-amphibole is also the only one to have Zr and Hf positive anomalies relative to Nd and Sm.

Overall, the petrology, mineralogy and geochemistry of the sample 15.07 show that this sample is radically different to the other clinopyroxenites

5.2 Characteristics of the metasomatism: evidence from the G1-orthopyroxenites and the G2-websterites

5.2.1 Types of metasomatism

Metasomatism is manifested in the mantle by different types of flow: 1) Porous flow (Zanetti et al., 1999) or/and 2) channelised flow (Manning, 2004). Clinopyroxene-rich veins or dykes were found on both Santa Isabel and San Jorge Islands. The veins of websterites occur in various sizes crosscutting the host peridotites. This metasomatism generally results from channeled fluid flow, which infiltrates and reacts with the peridotites (Gao and Klemd, 2001). The channel flow is initiated by hydraulic fractures of the sub-mantle (Yardley, 1985) locally producing zones with high fluid/rock (Manning, 2004), which latter precipitated the websterites during cooling. Conversely, the orthopyroxenites were never found in veins on either of the two islands. They rather occur in large outcrops. This probably indicates the orthopyroxenites were formed by porous fluid interaction with the rock matrix in a pervasive manner with a potential to metasomatise a large volume of peridotites. In summary, it seems that the websterites derive from channeled fluid flow whereas the orthopyroxenites are formed by more a porous flow.
Another way to characterise the metasomatism in the mantle is to determine if an added metasomatic agent interacts with the mantle via: 1) modal metasomatism when new phases are precipitated modifying the modal mineralogy and the bulk-rock chemistry of the mantle (Fabriès et al., 1989; Zanetti et al., 1999) or 2) cryptic metasomatism where the mantle is refertilised by the added component which change the bulk chemistry of the mantle rocks but not the mineralogy (Bizimis et al., 2000). Both types of metasomatism are common in sub-arc mantle (Rapp et al., 1999). Modification of the clinopyroxene minerals related to LILE and LREE enrichments is a classical evidence of cryptic metasomatism of the mantle peridotites (Garrido and Bodinier, 1999; O'Reilly and Griffin, 1987). There is no doubt that, in the case of the Solomon Islands, modal metasomatism by fluids or melts derived from the slab is responsible for crystallisation of anhydrous phases. However, modal metasomatism is often referred to recrystallisation of hydrated minerals such as amphibole and phlogopite (Downes, 2001; Zanetti et al., 1999). Due to infiltration of the pyroxene-saturated fluids or melts through the host peridotites, pyroxene ± olivine ± spinel are here formed primarily whereas amphibole (and other secondary minerals) crystallised as retrophase phases during the exhumation of the pyroxenites.

5.2.2 Composition of the fluid

There are different possibilities to directly or indirectly assess the composition of the fluid that infiltrated and reacted with the peridotites to form the G1- and G2-pyroxenites.
The first technique is to study of the fluid inclusions by LA ICP-MS. However, this method should be used with care as the inclusions have almost certainly undergone

passive enrichment through water loss during decrepitation. As the result, it is unlikely that the fluid trapped in the fluid inclusions was the initial one. But, despite significant element changes that have affected the analysed inclusions, their trace elements still reflect the characteristics of the fluid. As well, the fluid inclusions might not be automatically primary inclusions and therefore do not necessarily represent the fluid present at the time of the crystallisation. Having said that, it appears that there was no significant difference in composition between the studied secondary and primary inclusions. The results clearly show that the fluid was enriched in mobile elements such as LILE, Pb and Sr. In addition to be LILE-, Sr- and Pb-rich, the fluid was also originally enriched in CO_2-H_2O due to the presence of amphibole and calcite daughter phases in the fluid inclusions. All of these components are frequently described in fluid inclusions in mantle xenoliths especially in the SSZ-related peridotites (Rosenbaum et al., 1996).

As previously shown in the *Chapter 3* and in Berly et al., 2006, the San Jorge and Santa Isabel pyroxenites are inferred to result from the metasomatic reactions of a peridotite source with a metasomatic agent (fluid or melt). The newly crystallised pyroxene therefore represents the "fluid" cumulus phase (Rubatto and Hermann, 2003) from the infiltrating agent. Mineral/fluid partitioning calculated from experimental studies can be used to estimate the composition of the coexisting fluid from the "fluid" cumulus pyroxene. It is important to use the most appropriate partition coefficients for mineral/fluid at conditions (temperatures and pressures) close to those of formation of the pyroxenites. Unfortunately, the partition coefficients for mineral/fluid are too scarce to constrain the fluid composition from these pyroxenites. The only experimental studies for the determination of trace element behaviour in fluids or melts that are currently available either 1) do not account for the conditions of temperature (900°C or greater) and pressure (2.0-3.0 GPa) under which the San Jorge/Santa Isabel pyroxenites were formed (Green and Adam, 2003) or 2) only include a limited number of trace elements (Adam et al., 1997; Ayers et al., 1997; Brenan et al., 1995; Stalder et al., 1998). It is therefore hard to directly calculate a coexisting fluid using appropriate mineral/fluid partitioning. However I can assume that the fluid was enriched in mobile elements such as LILE, Pb and Sr on the basis of the compositions of the "clean" pyroxene, which are characterised by selective enrichments in these elements. This result corroborates the study of the fluid inclusions and gives further support to the LILE-, Pb- and Sr-rich composition of the fluid.

The content of the fluid can also be determined by comparing the G1- and G2-pyroxenites to their mantle sources before reacting with them. In this logic, the Choiseul peridotites, which represent metasomatised MORB-type, are good candidates of the mantle wedge before the intense metasomatism leading to the formation of the orthopyroxenites and websterites. The results show that the fluid was capable of carrying LREE and to a lesser extent MREE but not the HREE (Fig. 4-22A). The LREE-enriched characteristic of the fluid is further supported by the LREE-enrichment of the bulk-rock chemistry of the orthopyroxenite 16.01, which is likely to include LREE-hosting minerals at grain boundaries. Unfortunately, these grain boundaries components could not be detected in this sample but were reported by Garrido et al. (2000) in spinel peridotites associated with websterites. Both the Choiseul peridotites and the G1- and G2-pyroxenites both exhibit variable enrichments LILE, Pb and Sr relative to HFSE, which are both characteristic of the subduction-related metasomatism (Fig. 4-22B).

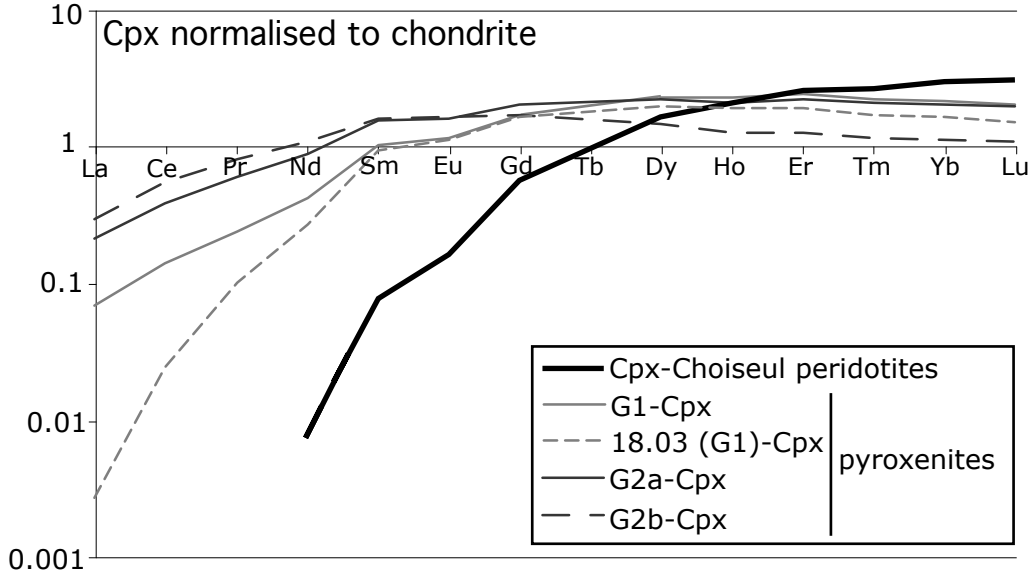

Fig. 4-22A: Average clinopyroxene REE compositions normalised to chondrite for the Choiseul peridotites and the San Jorge/Santa Isabel pyroxenites.
G1=orthopyroxenites; G2=websterites including the two subgroups (G2a and G2b).
The clinopyroxene from both the orthopyroxenites (G1) and the websterites (G2) is LREE-enriched relative to the Choiseul clinopyroxene indicating that the metasomatising fluid which react with the Choiseul peridotites was enriched in LREE.

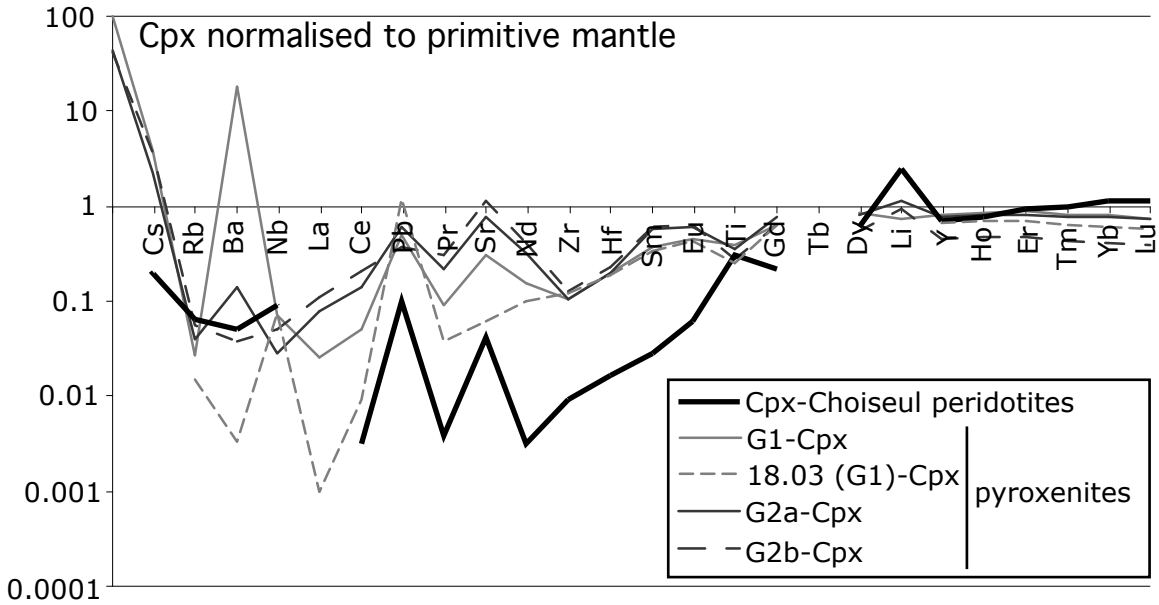

Fig. 4-22B: Average clinopyroxene multi-element compositions normalised to primitive mantle for the Choiseul peridotites and the San Jorge/Santa Isabel pyroxenites.
G1=orthopyroxenites; G2=websterites including the two subgroups (G2a and G2b).
The clinopyroxene from the Choiseul peridotites and the San Jorge/Santa Isabel pyroxenites both exhibit relative enrichments in LILE, Pb and Sr.

5.2.3 Provenance and nature of the fluid

Enrichments in LILE, Sr and Pb and to a lesser extent the LREE are characteristic to the subduction zone lavas (Tatsumi et al., 1986). These arc basalts are generated by melting of MORB-type mantle enriched in these elements, which were transported into the mantle wedge by a metasomatic agent released from the slab (Gill, 1981; Hawkesworth et al., 1993). Whole rock and mineral trace element chemistries of the G1- and G2-pyroxenites coupled with the study of the fluid inclusions all outline that the pyroxenites were formed by interaction of a peridotite source with a fluid enriched in these elements. Considering the fluid composition and the geological setting of the pyroxenites, it is evident that the pyroxenites represent the products of metasomatic reactions between the mantle wedge and the fluid released from the descending Pacific Plate. The slab origin of the fluid is further supported by the $CO_2 + H_2O$ composition of the fluid inclusions. These volatile components are considered to escape out of the subducting slab, reacting with the mantle wedge to form hydrated and carbonated phases. However, the G1- and G2-pyroxenites contain little amount of amphibole, which is considered to be a retrograde phase formed during the exhumation of the pyroxenites. The limited proportion of amphibole together with the non-crystallisation of phologopite and carbonate phases are indicative of low activities of both CO_2 and H_2O (Morishita et al., 2003; Zanetti et al., 1999). The H_2O and CO_2 activities are low only if the fluid contains a significant amount of solutes (Morishita et al., 2003). It is a fact that the formation of pyroxene in the mantle requires a solute-rich nature of the reacting fluid. For instance, to massively crystallise orthopyroxenites, the metasomatising fluid must carry significant amounts of Si. Recent studies of SSZ mantle xenoliths reveal the orthopyroxene-rich nature of the mantle wedge (McInnes et al., 2001; Morishita et al., 2003; Schneider and Eggler, 1986; Smith et al., 1999). These authors argue that these orthopyroxenites require the metasomatic agent (fluid or melt) to be Si-rich. Like the other SSZ orthopyroxenites, the San Jorge/Santa Isabel pyroxenites are enriched in LILE which is in agreement with the reaction and precipitation from SiO_2-rich aqueous fluid as high solubilities of LILE require for the fluid to contain the quantities of SiO_2 (McCulloch and Gamble, 1991). In the case of the websterites, the metasomatising fluid must carry significant amounts of elements such as Ca and Fe to be able to crystallise clinopyroxene in large proportion.

Even though it is clear that the fluid is enriched in solutes, the nature of the mobile metasomatic agents is yet uncertain (Scambelluri and Philippot, 2001) as they may consist of hydrous silicate melts (Green and Ringwood, 1968) or of aqueous fluids (Tatsumi et al., 1986) or of both referred as supercritical fluids (Bureau and Keppler, 1999). Lately, Hermann et al. (2006) have rather defined a metasomatic agent on its capacity to carry solutes: aqueous fluids include essentially water with only less than 30 wt% of solutes whereas the hydrous melts containing more than 65 wt% of solutes. Based on this assumption, It is here not possible to quantify the amount of solutes contained in the fluid and therefore to determine whether the slab-derived agent was an aqueous fluid or an hydrous melt.

5.2.4 Sediments: source of the metasomatising agents

Arc magmas are typically characterised by LILE enrichments relative to HFSE (Gill, 1981; Hawkesworth et al., 1993). These distinctive fingerprints known as the subduction component (Pearce et al., 1984) are assumed to result from the breakdown of trace element-rich minerals during prograde subduction as the main source of LILE-enriched fluids (Manning, 2004). However, the fluid sources and processes of mass transport during subduction, metamorphism and magma genesis are still matter of debate (Breeding et al., 2004; Scambelluri and Philippot, 2001). Recent studies (Chalot-Prat et al., 2003; Straub and Layne, 2003) comparing eclogitic mafic, ultramafic and metasedimentary rocks to low-grade or unmetamorphosed equivalent of rocks show that the breakdown of hydrous minerals associated with the eclogite facies does not result in significant loss of trace elements. For example, Pb and Sr are believed to be retained into the newly formed epidotite resulting from the decomposition of the lawsonite during prograde dehydration to eclogite-facies conditions (Busigny et al., 2003; Spandler et al., 2003, 2004). Hermann et al. (2006) also argue that the subducting slabs do not experience extensive loss of trace elements due to the breakdown of hydrous minerals and advocate for a decoupling of water and trace element released in the subducted oceanic crust. According to these authors, the subducting sediments, which constitute the main reservoir of LILE, Sr and Pb (Plank and Langmuir, 1998; Tenthorey and Hermann, 2004), are the only possible source for the slab-derived fluids enriched in these elements. Under these conditions, the fluids, which are equilibrated with metamorphosed mafic rocks, could either react with sedimentary rocks (Breeding et al., 2004) or cause partial melting of the sediments (Davies, 1999). The latter would produce a solute-rich fluid or hydrous granitic melt (Hermann and Green, 2001).
Making the analogy to the dehydration process and liberation of trace elements involved to generate the arc magmas, I suggest that the source of LILE, Sr and Pb enrichments of the pyroxene and the fluid inclusions from the G1- and G2-pyroxenites was also likely to the subducting sediments. The contribution of the sediments for the formation of the G1-orthopyroxenites and G2-websterites is also evidenced by their high $^{187}Os/^{188}Os$ ratios, which are interpreted to result from the simple mixture between unradiogenic Os peridotite source and a different radiogenic Os component represented by sediments.

6 IMPLICATIONS: GENESIS OF THE SAN JORGE AND SANTA ISABEL PYROXENITES

6.1.1 Formation of the G1-orthopyroxenites and the G2-websterites

Two models are proposed to explain the formation of the G1-orthopyroxenites and the G2-websterites.
The first model involves the aqueous fluid as the metasomatising agent to form both the websterites and the orthopyroxenites. In this model, the fluids released from continuous dehydration reactions may be capable of stripping the trace elements from the mafic rocks and the sediments producing hydrous Si-rich fluids enriched in LILE, Sr and Pb.

Once the fluids acquired the trace and major elements from the slab, they can migrate via porous flow, producing orthopyroxenites. Because of low fluid/rock ratio, the fluids get equilibrated rapidly with the host peridotites. Compatible elements (Mg, Cr and HREE) of the orthopyroxenites are directly controlled by the mantle and become comparable to the mantle values. Newly formed orthopyroxenites are variably enriched in incompatible elements such as LILE, Sr and Pb, which are saturated in the metasomatising fluids. In the same time, the same hydrous fluids could also locally ascend via permeable conduits exploiting fracture networks to crystallise mainly clinopyroxene. In this case, the Ca content necessary to precipitate the clinopyroxene could come from the large volume of fluid moderately enriched in Ca. Experimentally-determined Ca contents of quenched aqueous fluids at 30kbar, T=650-700°C were estimated to be less 1 wt % (Green and Adam, 2003; Hermann and Green, 2001). This implies that the fluid/rock ratio should be at least 12-20 to account for the formation of websterites. This estimation of fluid proportion relative to rock is not achievable in a context of a channeled fluid flow. Besides, Al being not soluble in the fluid, the interaction of peridotites with the aqueous fluids would account for low Al_2O_3 contents of the websterites. So there is an eventuality for the orthopyroxenites and the websterites to be formed from the aqueous fluids but respectively by porous flow and channeled flow. On the other hand, this model is struggling with the relatively high temperatures of crystallisation of the pyroxenites. The low temperature-aqueous fluids (~700°C) percolating the peridotites require an unusually hot mantle (probably in excess of 1000°C) to account for the relatively high temperatures of crystallisation (~950°C) of both the orthopyroxenites and the websterites. If the fluid to rock ratio is very small, the temperatures of crystallisation of the pyroxenites would be essentially restricted by the mantle. This is the case for the orthopyroxenites (low fluid/rock ratio). However, the websterites, which are likely to derive from high fluid/rock ratios, would have had much lower temperatures of crystallisation approaching the temperatures of the metasomatic agent if formed by interaction with an aqueous fluid. This is not the case as the temperatures of formation of the websterites are slightly lower than the ones of the orthopyroxenites. Apart from the temperature argument, recent study by Hermann et al. (2006) argues that even if a large volume of aqueous fluids can be released by dehydration reactions from the slab to the mantle, these hydrous fluids only contain 5 wt % solutes and are not good candidates to transport moderate amounts of LILE, Sr and Pb. Only slab-derived hydrous melts are more efficient in transferring trace elements such as LREE and LILE (Hermann et al., 2006).

A second model is therefore proposed whereby the hydrous melts escape out from the slab via channelways crystallising first the websterites and further migrate up through the inverted thermal gradients of the mantle wedge by pervasive flow until crystallising the orthopyroxenites. This model is outlined below and shown schematically in Figure 4-23. In this model, the fluid released from the dehydration reactions ❶ cause partial melting of sedimentary rocks producing hydrous granitic melts ❷. Estimating the composition of the resulting hydrous melts is very complicated because of 1) their signatures would inherit components of several types present in the subducted oceanic crust which could be very heterogeneous in composition; 2) the dehydration processes dictating the various metamorphic assemblages present at the time of the partial melting and 3) the characteristics of melting process (degree, type, etc…). However, experimental attempts (Hermann and Green, 2001) to assess the composition of these hydrous melts were

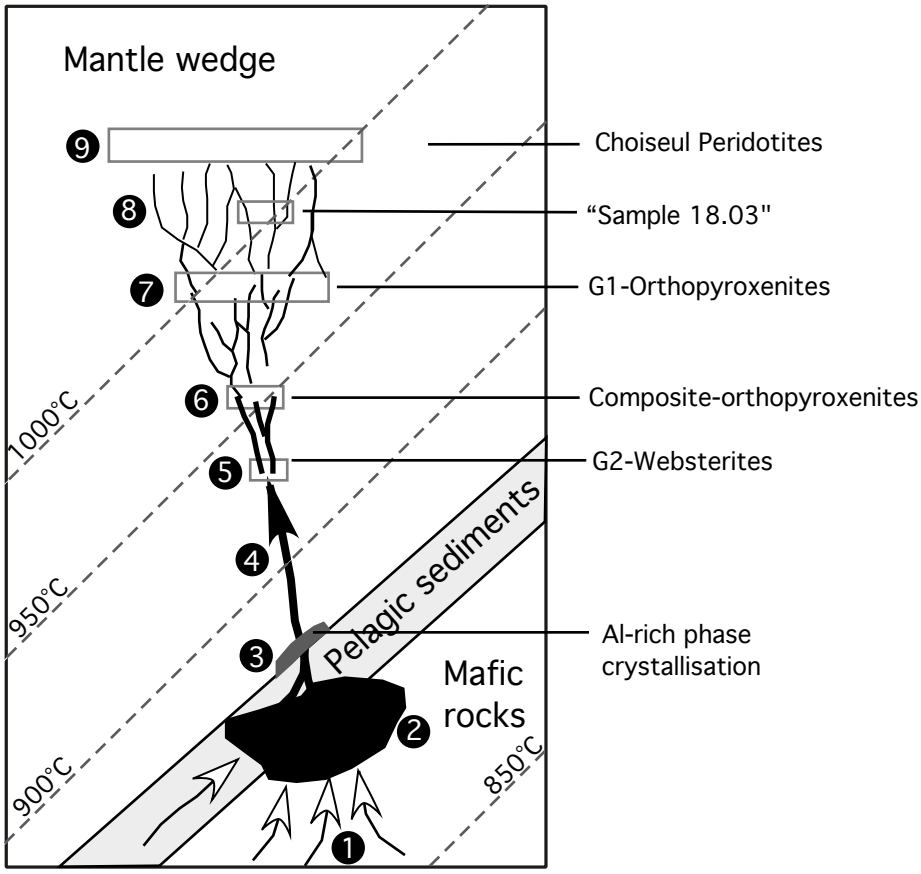

Fig. 4-23: Schematic cross section of the formation of the G2-websterites and the G1-orthopyroxenites by interaction of the mantle wedge with the hydrous melt released from the slab. The numbers refer to points discussed in the text.

undertaken with melting, at T=800-1050°C and P=20-45 kbar, of synthetic starting materials approaching the average compositions of an oceanic crust (sediments + MORB basalts). The results show that the hydrous melts have Si-rich granitic compositions with high Al, Na and K contents and relatively moderate MgO (6 wt%) and CaO contents (3-4 wt %) (Hermann and Green, 2001). This range of CaO contents implicate that only a realistic fluid/rock ratio of 4-5 is necessary to form the websterites (15-20 wt%). However, these experiments produce hydrous melts with high Al_2O_3 contents (12 wt %), which are hard to reconcile with low Al_2O_3 contents of the websterites (2-3 wt%). Only aqueous fluids result in having low Al_2O_3 (2-3 wt%) (Green and Adam, 2003) as Al is sparingly soluble in the fluids (Stolper and Newman, 1994). One alternative is that Al-rich phase is precipitated before the hydrous melts interact with the peridotite, perhaps at the contact mantle wedge-slab ❸ (J. Hermann, person. comm., 2005). The resulting low-Al hydrous melts exploit permeable conduits such as fracture networks (Yardley, 1985). Once released from the slab, channelised flow of hydrous melts produces high melt/rock ratio zones within the cold overlying mantle wedge ❹. At temperatures close or perhaps higher than the peridotite, the granitic hydrous melts react with silica-undersaturated mantle rocks and form Cpx-rich pyroxenites (Zanetti et al., 1999). Channeled flow of hydrous fluids produces zones in which fluid to rock ratios are much higher and so the hydrous melts interact with less rock per unit volume (Manning, 2004). Consequently, the newly fluid cumulates cpx and opx formed in the veins are not equilibrated with the mantle ❺. This relatively low temperature -pyroxene (950°C) is marked by low Mg# together with enrichments in LILE, Sr and Pb and LREE relative to HFSE, indicating that the newly crystallised pyroxene retains more the composition and the characteristic of their initial source. After the formation of the websterites, elements that are strongly partitioned into the fluid relative to the pyroxenites will remain in the metasomatising agents as they travel away through the mantle wedge. In contrast, relatively compatible elements such as Ca, Fe and maybe the REE are incorporated in the pyroxene. At this stage, because of their relatively low amounts of major elements (except Si), the hydrous melts are less dense becoming aqueous fluid-like (fluid phase). This transition is marked by the formation of the composite-orthopyroxenites ❻. As the fluid phases rise through the inverted thermal gradient of the mantle wedge, the temperatures increase and the fluid flow becomes more porous which favours infiltration of large mantle volumes. At this stage, the rock matrix (peridotite) controls largely the composition of the fluids. Consequently, the Si-saturated fluid phases become more and more equilibrated with the peridotites and precipitate mainly orthopyroxene ❼. Cr-rich spinel can also recrystallise as the result of the high Cr contents of the host peridotites. Only a small proportion of clinopyroxene has the potential to crystallise with the remaining Ca available in the fluid phases. Their HREE and MREE contents are constrained by the composition of neighbouring peridotites whereas LREE are slightly enriched compared to SSZ peridotites indicating that the fluid phases still carry a small amount of LREE. Enrichments in LILE, Sr and Pb relative to HFSE in the clinopyroxene reflect the composition of the fluid phase saturated in these incompatible elements. Eventually, away from the slab, the fluid phase would become more and more "consumed" through the mantle wedge. Large volume of peridotites would be affected by a diffuse metasomatism via porous fluid flow crystallising scarce orthopyroxene with mantle compositions amongst mantle relicts such as olivine and clinopyroxene (sample 18.03)

❽. Finally, the metasomatism becomes cryptic changing only the chemistry of mantle minerals. This cryptic metasomatism enriches the depleted MORB-type peridotites in the "subduction component" to form the typical SSZ-peridotites ❾ similar to the Choiseul peridotites.

6.1.2 Formation of the G3-clinopyroxenites

The formation of the G3-clinopyroxenites is illustrated in the Figure 4-24. Wet melting of mantle wedge metasomatism caused by fluid released from the slab would produce incompatible-element enriched hydrous melts (Manning, 2004) ①. After extraction, these primary melts ascend up through the mantle via channelised flow ② to crystallise cpx-rich cumulates in high-pressure magma chambers probably at the mantle-arc crust boundary (DeBari and Coleman, 1989; Müntener et al., 2001; Parlak et al., 2002) ③. When cooling in the channelways ②, the hydrous melts would react with the host peridotites to dissolve orthopyroxene and crystallise the G3-clinopyroxenites (Fig.4-23B) at relatively high temperatures (1050°C) (Bodinier et al., 1990; Fabriès et al., 1989). Under these conditions, olivine is expected to crystallise massively (Santos et al., 2002). However, the clinopyroxene has high Mg# indicating that they crystallise early relative to olivine otherwise olivine fractionation will rapidly deplete the derivative melt and resulting clinopyroxenites in Mg (Kushiro and Yoder, 1966). To reduce the interval of olivine crystallisation, the primitive magma has to be Si-rich and the cpx precipitation should occur at high pressure (Müntener et al., 2001; Parlak et al., 2002). In this process, the clinopyroxene represents the cumulative melt phase crystallised from the primitive melts saturated with a peridotite assemblage. Therefore, the clinopyroxene has high Mg#, high Cr_2O_3 contents together with relatively low REE abundances. Limited enrichments in LILE combined with the lack of Sr enrichments both relative to REE do not mean that the source of the melt is not enriched in these elements but instead that these elements partition into the melt and therefore are not incorporated in the clinopyroxene crystallising from primitive melts. Initial crystallisation of clinopyroxene as an anhydrous phase increase $P(H_2O)$ of the resulting melts which would intersect the amphibole stability fields (Zanetti et al., 1999). At lower temperatures (~800°C), clinopyroxene and amphibole can co-crystallise producing the amphibole-rich clinopyroxenite (sample 15.07). The amphibole and clinopyroxene have characteristic LREE-enrichments relative to HFSE indicating that the LREE remained in the fluid after primary crystallisation of the clinopyroxenites. Eventually, the resulting magma would form the arc basalts with typical LILE and LREE enrichments over HFSE ④.

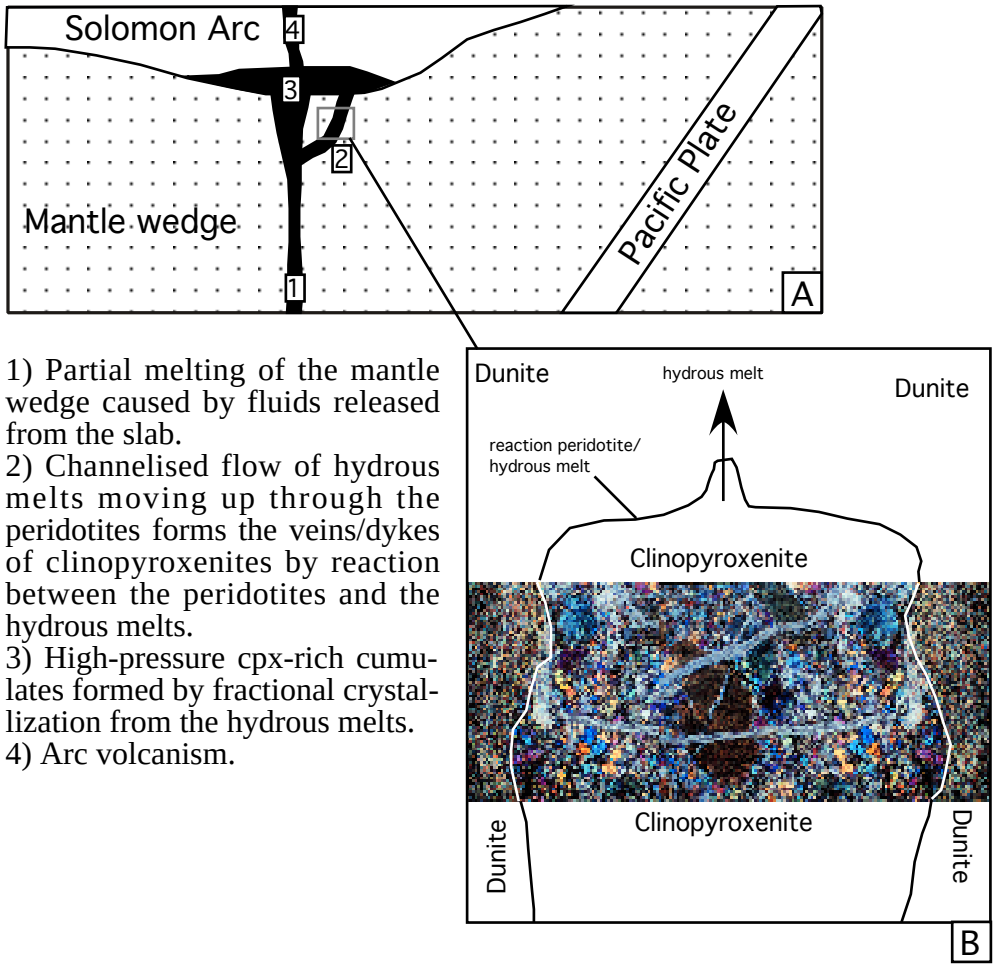

1) Partial melting of the mantle wedge caused by fluids released from the slab.
2) Channelised flow of hydrous melts moving up through the peridotites forms the veins/dykes of clinopyroxenites by reaction between the peridotites and the hydrous melts.
3) High-pressure cpx-rich cumulates formed by fractional crystallization from the hydrous melts.
4) Arc volcanism.

Fig. 4-24: Schematic cross section of the formation of the G3-clinopyroxenite (A) by interaction of the mantle wedge with the mantle hydrous melt (B). The numbers are also referred to points discussed in the text.

7 CONCLUSION

It was established (*Chapter 3* and Berly et al., 2006) that the San Jorge and Santa Isabel pyroxenites are the results of the interaction of a peridotite source with a metasomatising agent in the supra-subduction zone environment.
The combined study of the pyroxene trace element composition, the Re/Os system on the whole rock and the fluid inclusions from the San Jorge and Santa Isabel pyroxenites provide further evidence for the metasomatising agents to be enriched in elements such as LILE, Sr, Pb, ± LREE, and CO_2 + H_2O typical of the composition of fluids released from the slab. However mineralogical and geochemical differences between the pyroxenites indicate that the metasomatism is quite complex.
I propose that the G1-orthopyroxenites and the G2-websterites directly derive from the same metasomatic process involving hydrous melts released from the descending slab into the overlying mantle wedge at around 30 km. Large quantities of hydrous melts are expelled from the slab via channeled flow (high fluid/rock ratio) to react with the overlying mantle wedge producing the websterites (950°C). The resulting less dense agent still diffuses away from the slab through the inverted thermal gradients of the mantle wedge but via porous flow. At this stage the aqueous fluid-like agent equilibrated with the mantle reacts with host peridotites to form the G1-orthopyroxenites (1000°C).
Conversely, the G3-clinopyroxenites result from the high-pressure fractionation of the hydrous primitive melts generated by wet melting of the metasomatised mantle wedge and interacting with the host peridotites at relatively high temperatures (1050°C).
The formation of the pyroxenites provides therefore a unique opportunity to witness the process and the nature of interaction of the slab-derived fluids and the mantle wedge. This complexity of the metasomatism related to the subduction of the Pacific plate underneath the Solomon Islands is likely to be linked to the Ontong Java Plateau (OJP) entering in contact with the Solomon arc.

Chapter 5:
Origin and nature of the mafic complexes of the Santa Isabel, San Jorge and Choiseul Islands: evidence from mineralogical and geochemical characteristics

1 INTRODUCTION

The Ontong Java Plateau (OJP) is one of the few oceanic plateaus currently interacting with an active subduction zone (Mann and Taira, 2004). The present-day Solomon Islands provide the best opportunity to study the tectonic effects of the collision of OJP with the subduction zone. Santa Isabel is the only location in the Solomon Islands where a major terrane boundary between the OJP and Solomon island arc sequence is exposed (Tejada et al., 1996). In close proximity to the terrane boundary are a variety of gabbros and lavas which crop out in fault-bound slices together with mantle peridotites and pyroxenites (see *Chapter 3 and 4*). On Choiseul, the igneous rock sequence includes variably metamorphosed basalts and gabbros together with foliated schists (Choiseul Schists) in close tectonic association to harzburgites and dunites (the Siruka Ultramafics) (*Chapter 2*).

In this chapter, I focus on understanding the relevance of the variety of the igneous rocks on both islands in order to unravel the complex juxtaposition of the terranes caused by the OJP-arc collision. I present a combined petrological, mineralogical and geochemical (including isotopic) study of a new set of volcanic rocks, schists and gabbros to investigate the nature and the origin of these igneous rocks. In this study, I also investigate the geochemical criteria for discriminating between MORB-, arc- and OJP-rock types specifically for gabbros. The objective is to further characterise the geochemical characteristics of these igneous rocks in an attempt to best distinguish and recognise the different petrogenetic suites.

2 GEOLOGICAL BACKGROUND

The Solomon Islands are not the products of simple island arc environment but rather are a collage of crustal units (Petterson et al., 1997). This complicated geological history is principally caused by the active convergence of the world's largest and thickest oceanic plateau on Earth: the Ontong Java Plateau (OJP) (Mann and Taira, 2004).

A simplified geological map of Choiseul is presented in Figure 5-1. The igneous and metamorphic Pre-Miocene basement includes basalt lavas (the Voza Lavas) and basic schists (the Choiseul Schists), a gabbroic body (the Oaka Metamicrogabbro) and the ultramafic rocks (the Choiseul peridotites or Siruka Ultramafites). This basement sequence is considered to be typical to MORB sequence, which is part of the Central Province. Apart from this Cretaceous sequence, the Choiseul Island contains both stage 1- and stage 2-arc sequences. Stage 1-arc is represented by crystal and lithic-rich turbidites (the Mole Formation) whereas the Maetambe and Komboro Volcanics constitute the stage 2-arc sequence. The geology of Choiseul is better described in *Chapter 1*.

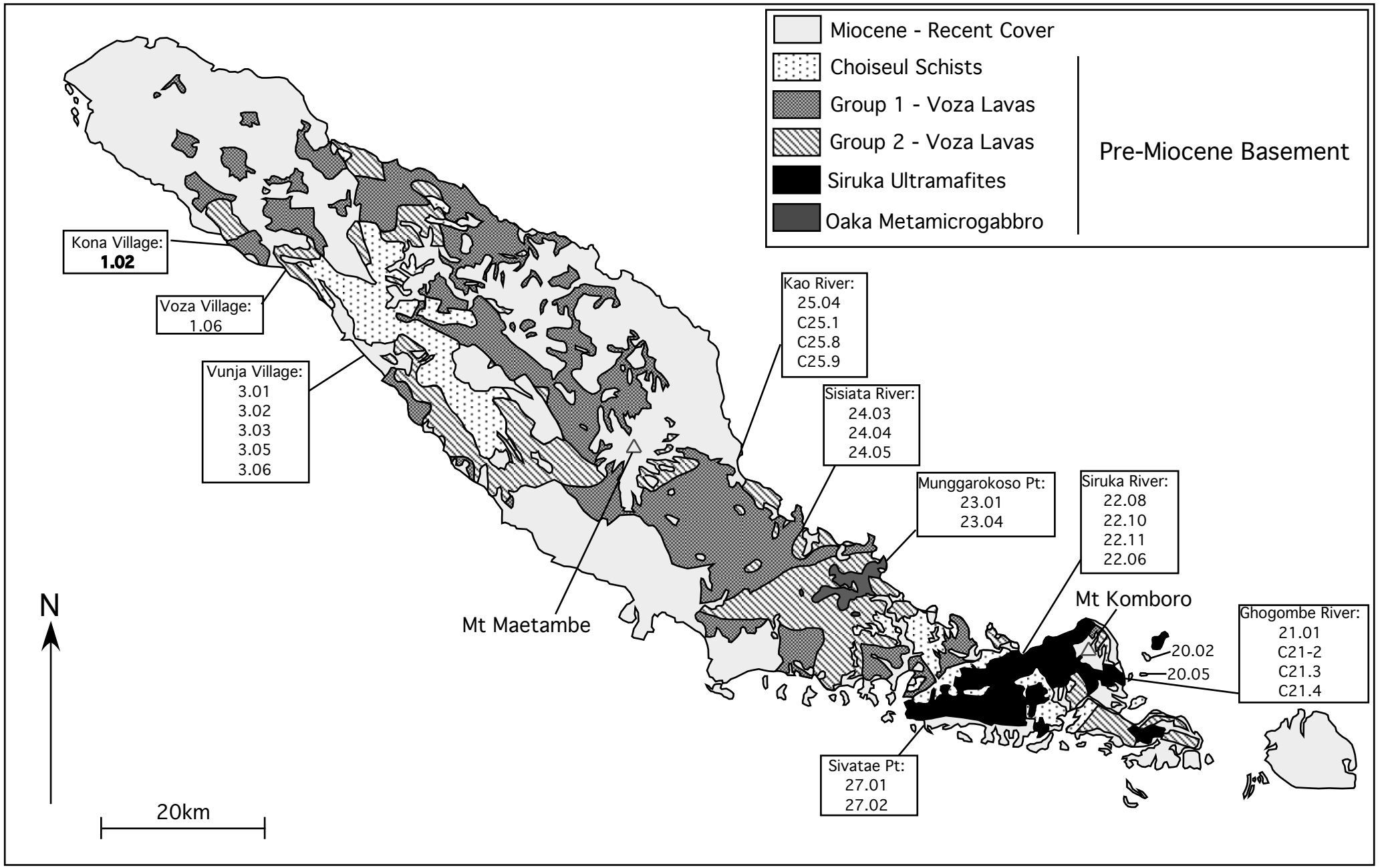

Fig. 5-1: Distribution of rock types in the Choiseul basement (after Ridgway and Coulson, 1987) and location of samples.

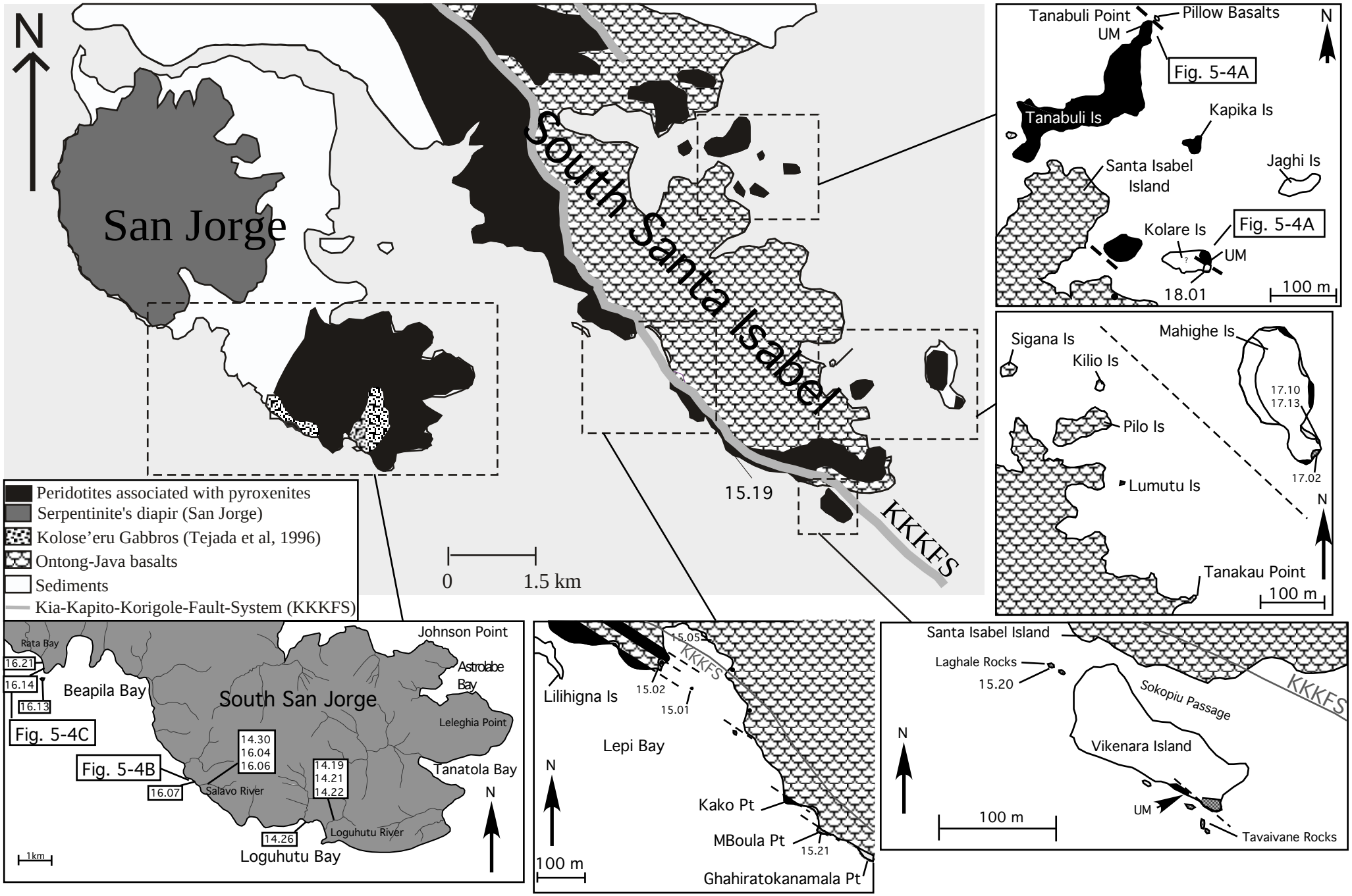

Fig. 5-2: Distribution of rock types in the Santa Isabel and San Jorge basements.

The geology of Santa Isabel (Fig. 5-2) is relatively complex with the Kia-Kaipito-Korighole Fault System (KKKFS) marking the boundary between the Pacific Province and the Central Province. A detailed description of the geology is also given in *Chapter 1*. At the north of KKKFS, faulted and folded lava sequences known as the Sigana Basalts, overlain by pelagic limestones and volcaniclastic sediments, represent the Pacific Province and are part of the OJPT terrane. South of the KKKFS, the mafic basement is dominated by the Jajao Igneous, which includes basalts (San Jorge Volcanics) and gabbros (Kolose'eru Gabbros). This mafic sequence is considered to represent the stage 1-arc basement (the Central Solomon Terrain-CST) (Petterson et al., 1999). As previously shown, ultramafic rocks including peridotites and pyroxenites are associated with the basaltic and gabbroic rocks on the both sides of the KKKFS (see *Chapters 3 and 4*).

3 SAMPLING AND FIELD RELATION

3.1 Choiseul Island

The location of the samples on the Choiseul Island is shown in Figure 5-1. The collection covers essentially the southeast coast of the island although few samples were collected by Cromwell Qopoto on the west and northwest of Choiseul. The majority of the samples for this study were pebbles recovered from riverbeds or beaches but few were collected from outcrops (20.02; 20.05; 21.01; 22.06 and 24.03) (Table 5-1).

Most of the samples were from the Voza Lavas formation (Table 5-1), which was first described by Coleman (1960). They occur either in pillowed (Fig. 5-3C) or massive lavas (Fig. 5-3D) with variable relative proportions from area to area. Brecciated flows were also identified in the northwest (Cromwell Qopoto, pers. comm.) but only pillowed and massive lavas were frequently found in close proximity in the southeast of the island.

The Choiseul Schists, which were first identified by Coleman (1960), constitute another widespread formation throughout Choiseul (Fig. 5-1). For this study, only three samples of the Choiseul Schists were collected from two different locations (Mbembelama Island and Vunja village) (Table 5-1). The Choiseul Schists are recognisable by their intense foliation (Fig. 5-3E). In the field, the Choiseul Schists are often found in close vicinity of the Voza Lavas.

The Oaka Metamicrogabbro formation (Fig. 5-3B) only outcrops in a relatively area compared to the other mafic rocks (Fig. 5-1) and only two samples were recovered from the coast (23.01 and 23.04) (Table 5-1). Ridgway and Coulson (1987) indicate that these altered gabbros intrude the Voza Lavas but no such field evidence were observed.

Another type of gabbros, never described before, were found at the Siruka River (Fig. 5-1) where three samples (22.08, 22.08 and 22.10) were taken (Table 5-1). They occur as variable-sized veins or dykes of coarse-grained to pegmatitic gabbros crosscutting blocks or outcrops of dunites and harzburgites (Fig. 5-3A).

Table 5-1: Textural and petrological characteristics of mafic rocks from Choiseul Island.

	Samples	Area	Location	Formation	Group	Texture
Gabbros	22.08	SE Choiseul	Siruka River	Pegmatic Gabbro	Pegmatic Gabbro	Pegmatic
	22.10	SE Choiseul	Siruka River	Pegmatic Gabbro	Pegmatic Gabbro	Pegmatic
	22.11	SE Choiseul	Siruka River	Pegmatic Gabbro	Pegmatic Gabbro	Pegmatic
	23.01	SE Choiseul	Munggarokoso Pt	Oaka metamicrogabbro	Microgabbro	Microgranular
	23.04	SE Choiseul	Munggarokoso Pt	Oaka metamicrogabbro	Microgabbro	Microgranular
	23.05	SE Choiseul	Munggarokoso Pt	Oaka metamicrogabbro	Microgabbro	Microgranular
Voza lavas and Choiseul Schists	20.02	SE Choiseul	Kagau Island	Voza Lavas	Group 2	Granular
	20.05	SE Choiseul	N Mbembelana Is	Choiseul Schists	Choiseul Schists	Heteroblastic
	21.01	SE Choiseul	Ghoghombe River	Voza Lavas	Group 2	Granular
	22.06	SE Choiseul	Siruka River	Voza Lavas	Group 1	Granular
	24.03	SE Choiseul	Sisiata River	Voza Lavas	Group 1	Microcrystalline
	24.04	SE Choiseul	Sisiata River	Voza Lavas	Group 1	Granular
	24.05	SE Choiseul	Sisiata River	Voza Lavas	Group 1	Granular
	25.04	SE Choiseul	Kao River	Voza Lavas	Group 1	Granular
	27.01	SW Choiseul	Sivatae Pt, E Keala Village	Voza Lavas	Group 1	Microcrystalline
	27.02	SW Choiseul	Sivatae Pt, E Keala Village	Voza Lavas	Group 1	Microcrystalline
	1.02	NW Choiseul	Kona village	Voza Lavas	Group 1	Micro-granular
	1.06	NW Choiseul	Kaqono River (Voza village)	Voza Lavas	Group 1	Micro-granular
	3.01	SE Choiseul	Vunja Village, Kolombangara R	Choiseul Schists	Choiseul Schists	Heteroblastic
	3.02	SE Choiseul	Vunja Village, Kolombangara R	Voza Lavas	Group 1	Granular
	3.03	SE Choiseul	Vunja Village, Kolombangara R	Voza Lavas	Group 2	Heteroblastic
	3.05	SE Choiseul	Vunja Village, Kolombangara R	Choiseul Schists	Choiseul Schists	Heteroblastic
	3.06	SE Choiseul	Vunja Village, Kolombangara R	Voza Lavas	Group 1	Granular

Table 5-2: Textural and petrological characteristics of mafic rocks from San Jorge and Santa Isabel.

		Samples	Area	Location	Rock and texture	Mineralogy
San Jorge	Gabbros	14.19	SW San Jorge	Loguhuto River	Microgabbro	
		14.21	SW San Jorge	Loguhuto River	Microgabbro	Cpx; Pl; Amphi
		14.22	SW San Jorge	Loguhuto River	Foliated-microgabbro	
		14.30	SW San Jorge	Salavo Beach	Granular to Coarse-grained Gabbro	
		16.04	SW San Jorge	Salavo River	Granular to Coarse-grained Gabbro	Opx; Cpx; Pl; Ol
		16.06	SW San Jorge	Salavo River	Granular to Coarse-grained Gabbro	Cpx; Pl; Ol
		14.25	SW San Jorge	Loguhuto Bay	Foliated-microgabbro	
		14.26	SW San Jorge	Loguhuto Bay	Microgabbro	Opx; Cpx; Pl; Ol; Amphi
		16.21	NW San Jorge	Rata Bay	Granular to Coarse-grained Gabbro	
	Schists	16.07	SW San Jorge	Salavo Bay	Schist (Foliated)	Amphi, Qtz; Pl
	Lavas	16.13	NW San Jorge	Rata Pt (Offshore)	Columnar lava (microcrystalline)	Pl: Cpx
		16.14	NW San Jorge	Rata Bay	Dyke	Pl, Cpx
Santa Isabel	Gabbros	15.19	South of KKKFS	Mbadhambani Pt	Coarse-grained to Pegmatitic Gabbro	Pl; Amphi
		15.20	North of KKKFS	Vikenara rocks	Microgabbro	
		15.21	North of KKKFS	Vikenara rocks	Microgabbro	Opx; Pl; Ol; Amphi
		17.02	North of KKKFS	Mahighe Island (SE)	Foliated-Layered Gabbro	Opx; Cpx; Pl;
		17.10	North of KKKFS	Mahighe Island (SE)	Foliated-Layered Gabbro	Cpx; Pl
		17.13	North of KKKFS	Mahighe Island (NE)	Foliated-Layered Gabbro	
	Lavas	15.01	South of KKKFS	Lepi Bay	Pillow-basalt (microcrystalline)	Pl
		15.02	South of KKKFS	Lepi Bay	Pillow-basalt (microcrystalline)	Pl, Cpx, Amphi
		15.05	South of KKKFS	Lepi Bay	Pillow-basalt (microcrystalline)	Pl
		18.01	North of KKKFS	Kolare Island	Pillow-basalt (microcrystalline)	Pl

List of Abbreviations:

Cpx: clinopyroxene; Opx: orthopyroxene; Pl: plagioclase; Ol: olivine; Amphi: amphibole; Qtz: quartz.
KKKFS: Kia-Kaipito-Korighole Fault System

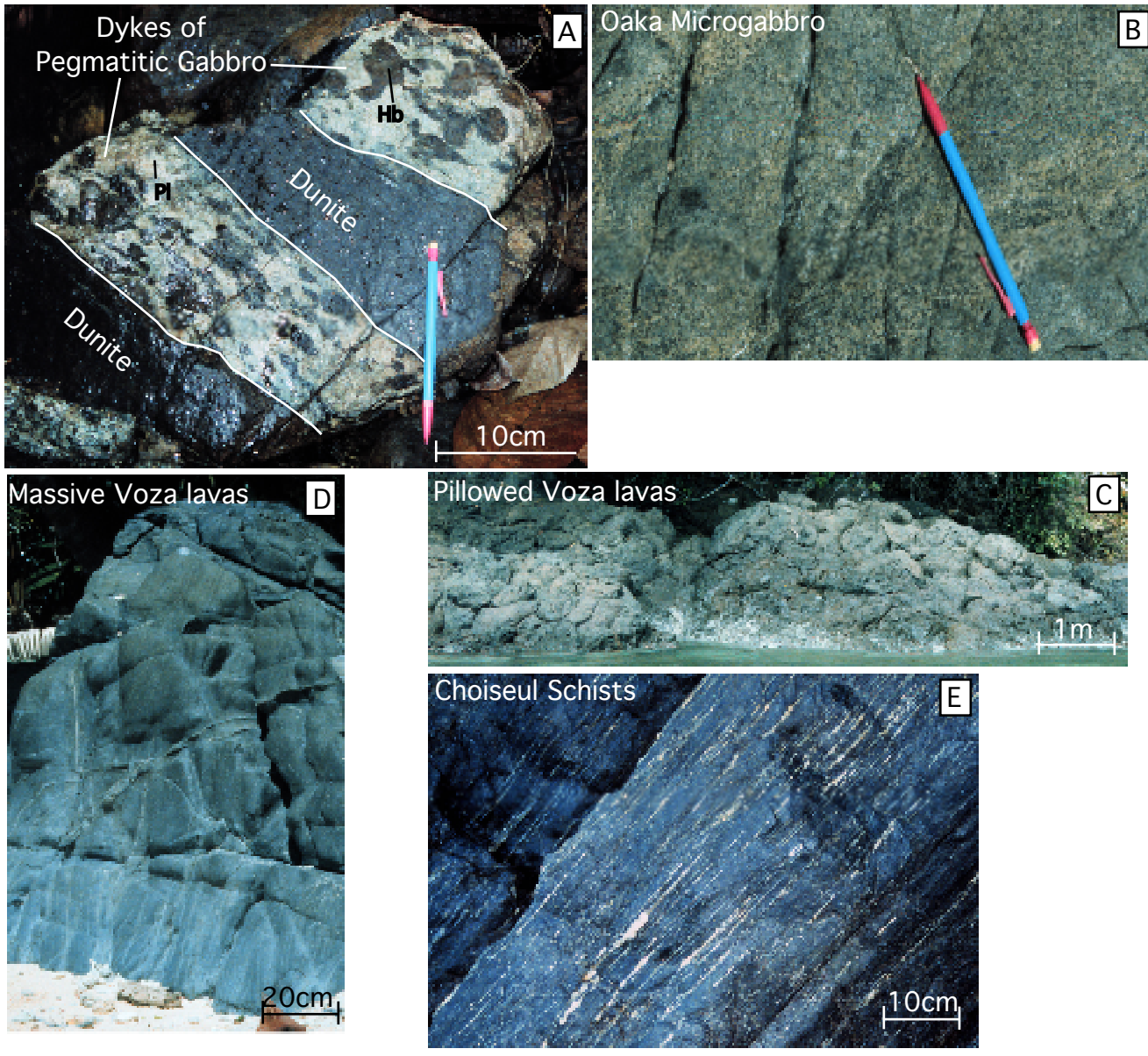

Fig. 5-3: Different types of Pre-Miocene mafic rocks from the Choiseul Island.
A: Dykes of Pegmatitic gabbro (Hb: Hornblende and Pl: Plagioclase) crosscutting dunites (Siruka River, southeast Choiseul) (Sample 22.08).
B: Modally-graded layering marked by appearance and disappearance of mafic and felsic minerals in the Oaka Metamicrogabbro (Munggarokoso Point, southeast Choiseul) (Sample 23.04).
C: Pillow lavas in the Voza lavas (Sisiata River, southeast Choiseul) (Sample 24.03).
D: Outcrop of massive Voza lavas (Kagau Island) (Sample 20.02).
E: Steeply dipping gneissic foliation in the Choiseul Schists (Mbembelana Island) (Sample 20.05).

3.2 San Jorge and Santa Isabel

The location of the samples from the islands of San Jorge and Santa Isabel is shown in Fig. 5-2. The description of these volcanic rocks and schists together with the gabbros is displayed in Table 5-2.
Massive and pillowed flows crop out abundantly on Santa Isabel (southeast coast). On the island of Kolare (Fig. 5-2), pillow basalts (sample 18.01) are overlain by peridotites with high angle NW-SE-trending faulted contacts against these two formations (Fig. 5-4A). This suggests that the ultramafic rocks were thrust over the basalts in this area. But most of time, the contact between the ultramafic rocks and the pillow-basalts cannot be observed (Fig. 5-4B) like at Tanabuli Point (Fig. 5-2). In the location of Lepi Bay, pillow basalts (15.01, 15.02 and 15.05) crop out on both sides of the KKKFS with a succession of ultramafic rocks - pillowed basalts - ultramafic rocks - pillowed basalts (Fig. 5-2) but the contacts between these formations are not exposed.
On the island of San Jorge, the only extrusive rocks were found at Rata Bay (Fig. 5-2): 1) a dyke (16.14) of lavas crosscutting serpentinised ultramafic rocks (Figure 5-4C) and 2) columnar lavas (16.13) cropping out on a small islet.
The gabbros from Santa Isabel are scattered on both sides of the KKKFS (Fig. 5-2) whereas the San Jorge gabbros were essentially collected from two locations (Loguhuto River and Salavo River) at southwest of San Jorge (Fig. 5-2). The San Jorge and Santa Isabel gabbros represent a large variety of gabbros. They range from massive to layered gabbros with undeformed to foliated and/or sheared fabric (Fig. 5-5). Like on Choiseul, dykes of coarse to pegmatitic gabbros are found crosscutting ultramafic rocks.
Schists are found in only one location of San Jorge (Fig. 5-4B). They locally outcrop at the north of the Salavo Bay in close proximity of tectonic contact with peridotites (Fig. 5-4A). Field relationships between these schists and the San Jorge gabbros could not be determined.

4 TEXTURAL AND PETROLOGICAL CHARACTERISTICS

4.1 The volcanic rocks and schists

The Voza Lavas from Choiseul have undergone variable metamorphism ranging from unmetamorphosed and low grade (Group 1) to highly metamorphosed amphibolites (Group 2) (Table 5-1). The Group 1, which was the most sampled, have variable textures ranging from microcrystalline through fine-grained to granular. The original igneous texture of the Group 1-basalts is dominant with only chlorite and zeolites as secondary minerals. In contrary, the Group 2 consists of granular metamorphosed lavas characterised by abundant amphibole but no foliation. Grain size of the Group 2-Voza Lavas varies from fine to coarse. Textures are dominantly heteroblastic and granoblastic with hornblende extensively replacing pyroxene. Plagioclase can occur abundantly (up to 50%) in mosaics of equant to xenomorphic grains. Retrograde metamorphism is obvious in some samples in which chlorite replaces the granular amphibole. The Choiseul Schists are mineralogically similar to the Group 2-Voza Lavas with the predominance of